



Development of novel correlative AFM-Fluorescent methods for the study of biological samples

Oscar Saavedra V.

► To cite this version:

Oscar Saavedra V.. Development of novel correlative AFM-Fluorescent methods for the study of biological samples. Agricultural sciences. Université Montpellier, 2021. English. NNT: 2021MONTT017 . tel-03346449

HAL Id: tel-03346449

<https://theses.hal.science/tel-03346449>

Submitted on 16 Sep 2021

HAL is a multi-disciplinary open access archive for the deposit and dissemination of scientific research documents, whether they are published or not. The documents may come from teaching and research institutions in France or abroad, or from public or private research centers.

L'archive ouverte pluridisciplinaire **HAL**, est destinée au dépôt et à la diffusion de documents scientifiques de niveau recherche, publiés ou non, émanant des établissements d'enseignement et de recherche français ou étrangers, des laboratoires publics ou privés.

THÈSE POUR OBTENIR LE GRADE DE DOCTEUR DE L'UNIVERSITÉ DE MONTPELLIER

En Biologie Santé

École doctorale Sciences Chimiques et Biologiques pour la Santé (CBS2)

Unité de recherche Centre de Biochimie Structurale (CBS), INSERM U1054

Development of novel correlative AFM-Fluorescence methods for the study of biological samples

Présentée par Oscar SAAVEDRA-VILLANUEVA

Le 03 Mai 2021

Sous la direction de Pierre-Emmanuel MILHIET
et Luca COSTA

Devant le jury composé de

Gladys MASSIERA, Professeur, Université Montpellier

Pieter DE BEULE, Chercheur,

International Iberian Nanotechnology Laboratory (INL)

Eric LESNIEWSKA, Professeur, Université Bourgogne

Lorena REDONDO-MORATA, Chargé de recherche, Institut Pasteur de Lille

Pierre-Emmanuel MILHIET, Directeur de Recherche, Université Montpellier

Luca COSTA, Chargé de recherche, Université Montpellier

Président du jury

Rapporteur

Rapporteur

Examinatrice

Directeur de thèse

Co-Directeur de thèse



UNIVERSITÉ
DE MONTPELLIER

Abstract

Biological membranes are flexible barriers that ensure cell permeability, delineating the cell boundaries and the intracellular compartments to organelles within the cell. They are composed mainly by phospholipids and proteins. Those components are the main ones responsible for membrane remodeling. The latter process is highly dynamic and requires observation at high spatial and temporal resolution. This thesis work focused on two main challenges in the study of membranes: i) Softness of biological membranes and their mechanical properties. Membranes are very soft and fragile materials, and determine their real morphology is highly complicated due to their softness. We have studied the maximal force exerted by an AFM tip that supported lipid bilayers can withstand before rupture, as well as their Young's modulus, both as a function of the tip size. ii) Chemical sensitivity and molecular recognition in microscopy. AFM can achieve the topography of the membrane. However, this technique cannot distinguish the molecule below the AFM tip. In order to overcome this barrier, we worked on developing a new fluorescence super-resolution technique combining AFM and confocal microscopies. First, we developed a correlated and synchronous confocal Fluorescence-lifetime imaging microscope (FLIM)-AFM setup. Finally, we developed a Metal Induced Energy Transfer (MIET)-AFM setup in order to measure molecular recognition, topography, and mechanical properties of biological samples simultaneously.

Keywords: Biological membranes, Atomic Force Microscopy (AFM), Metal Induced Energy Transfer (MIET), Correlative microscopies, Compression, Rupture forces.

Résumé

Développement de nouvelles approches de microscopie correlative AFM- Fluorescence pour l'analyse d'échantillons biologiques

Les membranes biologiques sont des barrières flexibles qui assurent la perméabilité des cellules, délimitant les frontières cellulaires et les compartiments intracellulaires aux organites à l'intérieur de la cellule. Elles sont composées principalement de phospholipides et de protéines. Ces composants sont les principaux responsables du remodelage des membranes. Ce dernier processus est très dynamique et nécessite une observation à haute résolution latérale et temporelle. Ce travail de thèse s'est concentré sur deux défis principaux dans l'étude des membranes : i) Les propriétés mécaniques. Les membranes sont des matériaux très mous et fragiles, et déterminer leur morphologie réelle est très compliqué en raison de leur mollesse. Nous avons étudié la force maximale exercée par une pointe AFM que les bicouches lipidiques supportées peuvent supporter avant la rupture, ainsi que leur module d'Young, tous deux en fonction de la taille de la pointe. ii) Sensibilité chimique lors de l'imagerie des membranes. L'AFM permet d'obtenir la topographie de la membrane. Cependant, cette technique ne peut pas distinguer la molécule située sous la pointe de l'AFM. Afin de surmonter cet obstacle, nous avons travaillé à la mise au point d'une nouvelle technique de fluorescence à super-résolution combinant l'AFM et les microscopies confocales. Tout d'abord, nous avons mis au point un microscope confocal synchrone et corrélé d'imagerie de fluorescence à vie (FLIM)-AFM. Enfin, nous avons mis au point un dispositif de transfert d'énergie induit par les métaux (MIET)-AFM afin de mesurer simultanément la reconnaissance moléculaire, la topographie et les propriétés mécaniques des échantillons biologiques.

This thesis is dedicated to
my family, especially to my mom,
for never limiting my curiosity and giving me freedom to explore the world.

Acknowledgements

First of all, I want to begin by thanking Hervé Elettro and Manouk Abkarian for all the help, advice, and guidance when I decided to start a new adventure out of Chile.

To Luca Costa, my co-supervisor, for his strong support, advice, and patience throughout my thesis. And Pierre-Emmanuel Milhiet, my supervisor, for sharing his knowledge and always being available when I required his advice. And to both of them for trusting me for this project.

To my two office mates. Thales Fernandes for providing a critical vision and redirecting the projects when it was necessary. Anthony Vial for his help anytime that I needed it. And to both of them for our office's discussions about anything, in addition to the excellent atmosphere.

To Viviana Clavería and Julián Gurgo for their honest and deep friendship, as well, my support in difficult moments.

To Amélie Vizeneuve, for sharing all these moments and experiences together.

To Constance Renault, Sara Rombouts, Amandine Pisoni, Jacqueline Valverde, Marion Clé, and Sergio Espinola for all these friendly and funny moments during these years.

To the SPM 2.0 people for the knowledge shared and fruitful discussions. But especially for their human qualities and group cohesion. I really enjoyed each of our meetings in both day and night activities.

To Martina di Muzio for all our discussion and long days exploring our ideas during secondments without leaving out the fun. David Tóth for being a friend, bringing joy at every moment.

To the CBS people for the friendly environment in the lab.

Now, I will shift to Spanish for the words to my family. Especialmente quiero agradecer a las personas a quienes esta tesis está dedicada, a mi familia. Gracias por siempre darme la

libertad de explorar sin limitarme, en especial a mi madre quien es la parte esencial en mi familia y mi vida, y quien motivo mi curiosidad desde el inicio de mi vida. A mi abuela y a mi tatá (QEPD) por su incondicional apoyo, a pesar de que muchas veces no entendían lo que yo hablaba. Y a mis tres hermanos (Maikol, Emerson y Marcos) porque a pesar de nuestras diferencias, siempre confiaron en mí y estuvieron cuando más los necesite. Gracias por todo, prometo visitarlos pronto.

Oscar Saavedra-Villanueva acknowledges Alexandra Elbakyan for breaking the ‘rules’ opening the science with Sci-Hub. My sincere thankfulness to everyone that was part of this step of my career and life. Oscar Saavedra-Villanueva acknowledges funding from the European Union’s Horizon 2020 research and innovation program under the Marie Skłodowska-Curie grant agreement No. 721874 (SPM2.0).

Contents

1	Cell membranes	2
1.1	Biological membranes	2
1.1.1	Membrane lateral segregation	4
1.1.2	Membrane curvature	6
1.1.2.1	Nanoscopic curvature	8
1.1.2.2	Microscopic curvature	10
1.1.2.3	Macroscopic curvature	11
1.1.3	Mechanical properties of cell membranes	12
1.2	Model membranes	13
1.2.1	Giant Unilamellar Vesicles	14
1.2.2	Large Unilamellar Vesicles	15
1.2.3	Supported Lipid Bilayers	16
1.2.3.1	Methods used to prepare SLBs	18
1.2.3.2	Mechanism of SLB formation	23
1.3	Main challenges in the study of membranes	24

1.3.1	1 st challenge: the membrane-AFM tip interaction force	24
1.3.2	2 nd challenge: Chemical sensitivity	25
1.3.3	3 rd challenge: Time resolution	27
2	Mechanical properties of Supported Lipid Bilayers	28
2.1	Mechanical properties	28
2.2	Quantifying membrane (or cell) mechanical properties	33
2.2.1	Optical Tweezers	35
2.2.2	Micropipette Aspiration	37
2.2.3	Surface Force Apparatus	38
2.2.4	Atomic Force Microscopy	40
2.2.4.1	AFM cantilever calibration	48
2.2.4.2	AFM operation modes	51
2.2.4.3	Guiding rules for AFM imaging	58
2.3	Rupture force measurements	59
2.4	Experimental Methods	61
2.4.1	Sample preparation	61
2.4.2	AFM imaging and Force Spectroscopy	62
2.4.3	Data Analysis	63
2.5	Results	66
2.5.1	Rupture of Supported Lipid Bilayers	66
2.5.2	Young's modulus of Lipid Bilayers	72

2.6	Conclusions	78
3	MIET-AFM	81
3.1	Necessity of Super-Resolution and morphology	81
3.1.1	Molecular Recognition	84
3.1.1.1	Fluorescence microscopy	84
3.1.1.2	Simultaneous topography and recognition imaging (Pico TREC)	85
3.1.1.3	Infrared (IR) spectroscopy	87
3.1.1.4	Förster Resonance Energy Transfer (FRET)	89
3.2	Metal Induced Energy Transfer (MIET)	93
3.3	MIET-AFM	95
3.3.1	MIET-AFM working principle	95
3.3.2	Experimental setup	98
3.3.3	Confocal-AFM cross-talk	101
3.3.4	Simultaneous FLIM-AFM	107
3.3.5	Preparation of a MIET-AFM probes	109
3.4	Experiments	113
3.4.1	Simultaneous force curve and nanodiamond lifetime on a flat gold surface	113
3.4.2	Simultaneous force curve and nanodiamond lifetime on a gold nanopar- ticle	117

3.4.3	The problem of many NV centers per nanodiamond when imaging 30 and 10 nm gold nanoparticles	121
3.5	Conclusions	123
4	Conclusions and Perspectives	126
4.1	Conclusions	126
4.2	Perspectives	128
A	Sample preparation: DOPC:DPPC (v:v 1:1) labeled with 0.1% BODIPY on glass coverslip	131
B	PhD's publications	133
	Bibliography	183

List of Figures

1.1	Schematics of Phospholipids structure.	4
1.2	General overview of lateral heterogeneity in the plasma membrane	7
1.3	Lipid-associated membrane domains	8
1.4	Local differences in membrane curvature are hallmarks of cellular membranes	9
1.5	Spontaneous membrane curvature induced by different lipid species	10
1.6	Membrane curvature induced by hydrophobic protein motifs' insertion . . .	10
1.7	Microscopic curvature of membranes	11
1.8	macroscopic curvature	12
1.9	Schematics of Giant Unilamellar Vesicle (GUV) and Multilamellar Vesicle (MLV)	14
1.10	Giant Unilamellar Vesicles (GUVs)	16
1.11	Schematics of Supported Lipid Bilayers (SLBs) onto a hydrophilic and hydrophobic substrates	17
1.12	Schematics of SLBs preparation by the method of Langmuir. Langmuir . .	20
1.13	Schematics of SLB preparation by the method of vesicle fusion.	21
1.14	Schematics of SLBs preparation by the method of spin coating.	22

1.15	Mechanisms of vesicle rupture schematics	23
1.16	Correlative Fluorescence-AFM of HeLa cells expressing HIV-1 Gag-GFP	25
1.17	AFM topography and molecular recognition by PICO TREC	26
2.1	Schematics of a mechanical deformation on a body of original length l	29
2.2	Schematics of Poisson's effect on a body	30
2.3	Length-scale, time-scale and elasticity-scale for different bio-materials	31
2.4	Schematic of Hertz's contact model for a spherical indenter in a flat surface	33
2.5	Schematic of an optical trap	36
2.6	Schematic of an micropipette aspiration setup	37
2.7	The Surface Force Apparatus	39
2.8	Schematic drawing of a Surface Force Apparatus	40
2.9	Schematics of an Atomic Force Microscope	41
2.10	Scanning electron microscope images of an AFM cantilever	43
2.11	Scanning electron microscope images of AFM cantilever shapes	43
2.12	Schematics of a rectangular AFM cantilever	44
2.13	Scanning electron microscope images of AFM tips	44
2.14	Schematic of sample stage and piezo stage AFM	46
2.15	Simplified scheme of the feedback loop circuitry in amplitude modulation AFM	47
2.16	Simplified scheme of the feedback loop circuitry in amplitude modulation AFM	49

2.17	Schematics of different AFM modes	52
2.18	Dependence of the amplitude and the phase shift as a function of the excitation frequency for a forced harmonic oscillator with damping	54
2.19	Amplitude and phase distance curves obtained in air with a silicon tip on a mica surface	55
2.20	Schematic representation of force-distance curve using AFM-FS	56
2.21	Unbinding force vs. loading rate	57
2.22	Typical approach force-distance curve of the SLB indentation process using AFM-FS	60
2.23	Algorithm developed to evaluate rupture forces from FS-AFM data	64
2.24	Force-Volume experiment on DOPC:DPPC (1:1) SLBs on mica	67
2.25	Picture representation of fluid- and gel-phase membranes with two different indenter sizes: 2 nm tip <i>versus</i> 10 nm tip radii	68
2.26	Force-distance curves of fluid- and gel-phase for different tip radii and tip chemical compositions	69
2.27	Rupture force F_B for DOPC and DPPC enriched domains for different tip radii and tip chemical compositions	70
2.28	AFM-DFS on DOPC:DPPC (1:1) SLBs	71
2.29	Evaluation of Young's modulus and Debye Length for DOPC and DPPC model membranes using an indenter with a radius of 20 and 50 nm	74
2.30	Young's modulus and Breaking Force distribution DOPC-enriched domains using a tip with a radius of 2 nm (MSNL-D cantilever)	75
3.1	Correlative AFM-dSTORM of CD9 recruitment at HIV-1 budding sites	83

3.2	Molecular recognition interaction forces	86
3.3	Simultaneous topography and recognition imaging (TREC)	87
3.4	AFM-IR correlative microscopy schematic view	88
3.5	Jablosky diagram	90
3.6	FRET efficiency in function of r/R_0	92
3.7	Metal-induced fluorescence lifetime modification in the presence of a gold layer	94
3.8	MIET-AFM working principle	96
3.9	Expected MIET-AFM maps by scanning a single gold nanoparticle	97
3.10	Fluorescent nanodiamonds	99
3.11	Simultaneous FLIM-AFM setup	100
3.12	Possible AFM tip and confocal spot interactions	102
3.13	Simultaneous photon counts and force scans for three different AFM can- tilevers.	104
3.14	Luminescence decay curves and variation of the measured force for three different AFM cantilevers	106
3.15	Lifetime analysis for DOPC:DPPC curves labeled with 0.1 % BODIPY . .	108
3.16	Simultaneous FLIM-AFM on DOPC:DPPC (1:1 molar ratio) SLBs on glass labeled with 0.1% of BODIPY	109
3.17	BODIPY lifetime distribution	110
3.18	Grafting a single and selected nanodiamond	112
3.19	Simultaneous force curve and nanodiamond lifetime measurements approach- ing and retracting a gold substrate	115

3.20 Nanodiamond lifetime measurements approaching and retracting from a gold substrate	118
3.21 MIET-AFM on two 100 nm gold nanoparticles	120
3.22 MIET-AFM on two 100 nm gold nanoparticles	120
3.23 Multi-NV centers on a nanodiamond	122
3.24 Sample prepared using a thin film of PDMS with two cavities on a glass coverslip.	125
4.1 DNA origami	130

List of Tables

1.1	Summary of the common supports employed to prepare SLBs	18
1.2	Summary of the most common methods used to prepare SLBs	22
2.1	Summary of techniques to measure cellular forces	34
2.2	Rupture force (F_B), activation volume (V) and associated number of molecules (n) for DPPC and DOPC membranes indented by silicon and carbon AFM tips	71
3.1	Emission/Excitation filters	100
3.2	Slopes of the fits in Figure 3.14.	107

Chapter 1

Cell membranes

In the present chapter biological membranes are presented. At first, we focus on membrane remodelling processes including lateral segregation of membrane constituents and the formation of membrane curvature at the nano- and macro- scales. In this frame, we introduce membrane mechanical properties and describe their relevance in the active remodelling of membranes. Subsequently, we introduce the most common procedures and methods to prepare model (artificial) membranes that will be used in this thesis. Finally, we report the main challenges in the study of biological membranes, which will be addressed in the present thesis manuscript.

1.1 Biological membranes

Biological membranes are flexible barriers that ensure cell permeability. They delineate the cell boundaries, as well, the intracellular compartments to organelles within the cell. Cellular membranes remodeling plays an importance role in most fundamental cellular processes such as growth, division, endo- and exocytosis, trafficking, signaling, and associated pathology at different lengthscale and timescale [1]. In this frame, an accurate localisation of membrane constituents at high spatial and temporal resolution is important to understand the molecular mechanisms associated to cellular processes.

Biological membranes are composed mainly by phospholipids and proteins. Oligosaccharides are present in a smaller quantity. In this thesis, we will refer to phospholipids as lipids. A phospholipid is an amphipathic molecule meaning it has both hydrophobic and hydrophilic components. A lipid molecule can be divided into two parts (see Figure 1.1a)): i) polar head or head, which is composed of a phosphate group (negatively charged), resulting in a hydrophilic polar head. ii) non-polar tails, or lipid tails, which are uncharged and nonpolar fatty chains, giving the molecule its hydrophobic properties. There are two types of lipid chains depending on its saturation: i) unsaturated ones have at least one double bond in their fatty acid chain- they are in liquid-phase at room temperature -, such as 1,2-dioleoyl-sn-glycero-3-phosphocholine (DOPC) seeing its structure in Figure 1.1b). ii) saturated ones have no double bounds resulting in saturated chains with hydrogen atoms, such as 1,2-dipalmitoyl-sn-glycero-3-phosphocholine (DPPC); its structure is shown in Figure 1.1c).

Biological membranes are naturally immersed in a aqueous environment. Due to their chemical properties, lipids form a continuous bilayer membrane consisting of two lipid layers where lipid tails are faced between each other, keeping the polar heads exposed to the liquid environment. Membrane layers are called inner and outer leaflets, depending on whether they are exposed to the cytoplasm or the extracellular medium [2]. In both leaflets, the components are distributed asymmetrically between the inner and outer sides [3]. Both the inner and outer layers are structurally and dynamically coupled in a way that is currently driving extensive research efforts [4].

As mentioned, lipids are mainly responsible of membrane permeability and lateral organisation, as shown in Figure 1.2. Remodeling of biological membranes is of high importance in most of the fundamental cellular processes such as growth, division, endo- and exocytosis, trafficking, signaling and associated pathology. The active modulation of membrane, here called **membrane remodeling** is achieved by several means including:

- **dynamics and lateral segregation of membrane components**
- **membrane curvature**
- **interaction with the cytoskeleton**

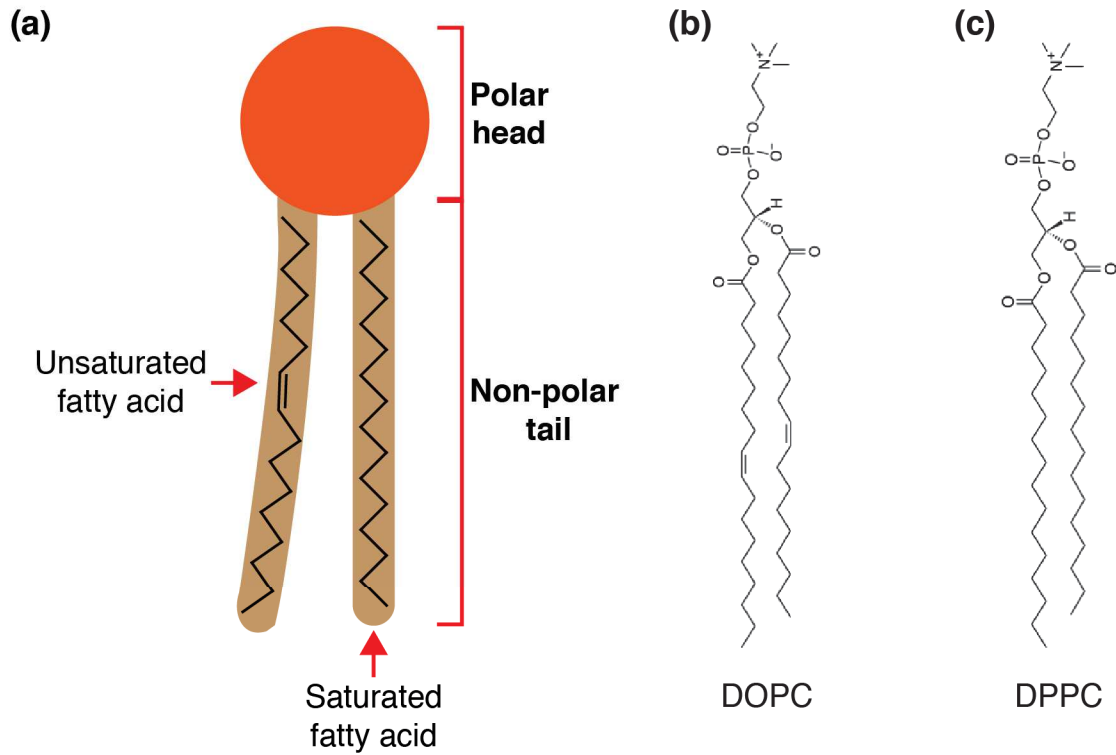


Figure 1.1: Schematics of Phospholipids structure. a) Schematics of a phospholipid molecule highlighting the polar head and nonpolar tails, where the two types of fatty acid chains are shown: unsaturated and saturated ones. b) DOPC molecule's structure as an example of unsaturated fatty acid. c) DPPC molecule's structure as an example of saturated fatty acid.

In the following subsection, membrane remodeling mechanisms are going to be described in details.

1.1.1 Membrane lateral segregation

Lateral membrane organization has been studied for several decades, where different studies suggest that the membrane diffusion process in the plasma membrane may be more complicated than a simple Brownian diffusion [5]. Based on experimental results, different models have been developed. The first theory that is analyzed in this thesis is the 'fluid-mosaic' model. This model was proposed by Singer and Nicholson in 1972 [6]. Here, membrane constituents are treated as a two-dimensional equilibrated fluid postulating that the membrane's components are in a mixed and homogeneous phase. Within

this model, the plasma membrane's multi-component lipid nature promotes the 'solvation' of various membrane proteins via specific interaction such as hydrophobic shielding, Van der Waals, hydrogen bonding, and electrostatics [7]. During the last decades, experiments suggest that the membrane appears to be partitioned into specific components over long and short spatial and temporal scales [8, 9, 7].

Lipid raft theory (or membrane raft) was introduced to explain the lateral membrane heterogeneity, proposing that the interaction between specific lipids (for example, cholesterol, saturated lipids, and glycosylated lipids) in the plane of the membrane could drive the formation of functionally important, relatively ordered, membrane regions. In turns, the latter can recruit other lipids and proteins [10, 11]. The theory was supported by several observations *in-vitro* in biomimetic membranes, providing clear evidence that specific lipids interact preferentially with one another, generating and inducing large-scale lateral domains[8].

However, a precise definition of lipid raft has been missing until 2006. The definition adopted is the following: "Membrane rafts are small (10–200 nm), heterogeneous, highly dynamic, sterol- and sphingolipid-enriched domains that compartmentalize cellular processes. Small rafts can sometimes be stabilized to form larger platforms through protein-protein and protein-lipid interactions" [12]. It should be mentioned that the term "lipid raft" was discarded in favor of "membrane raft" by this group of experts [12]. Figure 1.2b shows the plasma membrane as an assembly of different membrane components and membrane rafts. This was demonstrated by theoretical and experimental studies involving relatively saturated lipid, an unsaturated lipid, and cholesterol in artificial membranes. Moreover, it has been shown that clusters are induced by specific protein-protein and protein-lipid interactions [12, 11]. More recently, Sezgin et al. summarised the lipid-associated membrane domains [11], and we will focus on the following:

- a simple membrane domain can be a pure lipid cluster (Figure 1.3a)).
- in the most physiological relevant cases, membrane domains can also contain proteins which in turn might also be organized in clusters (Figure 1.3b)).
- by mixing a saturated lipid, an unsaturated lipid, and cholesterol in artificial membranes, they often result in liquid-liquid phase separation and the establishment

of two distinct phases (Figure 1.3c)), which are liquid-disordered (l_d) and liquid-ordered (l_o) phases, where the first is less viscous than the latter [11, 7].

Observations on both natural and model membranes show that phase segregation is highly dependent on temperature, the relative composition of lipid in both symmetric and the asymmetric leaflets, and the membrane tension.

Most membranes show fluidity, including rapid diffusion for some lipid and protein species within the membrane plane [13]. By using single-particle tracking, studies revealed a complex set of restrictions on protein lateral mobility, such as Brownian confined and directed motion, confined motion, or anomalous diffusion [14, 15]. Concluding, membrane dynamics plays a fundamental role in several cellular process and it is modulated by the interplay between lipids and proteins [1].

1.1.2 Membrane curvature

Membrane curvature also plays an essential role in fundamental cell functions. Cells need to bend membranes to perform processes such as division, motion/displacement, vesicle trafficking, exo- and endo-cytosis and signaling, [1]. As a consequence, the modulation of the biological membrane shape and curvature is central to eukaryotic life [16]. The cell membrane can be locally highly curved eventually for a limited timescale. Such a high curvature is essential for organelles' function and the control of fission and fusion in the cell [1]. Figure 1.4a) shows a cell cartoon, where different possible membranes curvatures are highlighted.

Membrane curvature at high resolution can not be observed under physiological conditions. Typically these observations are performed using electron microscopy, typically Electron Microscopy (EM) (see Figure 1.4b, c, and d). Despite outstanding advancements regarding environmental electron microscopy, EM still requires a dry sample under vacuum conditions. As a consequence, the biological specimen under observation is fixed (an irreversible process where the membrane is not dynamic anymore).

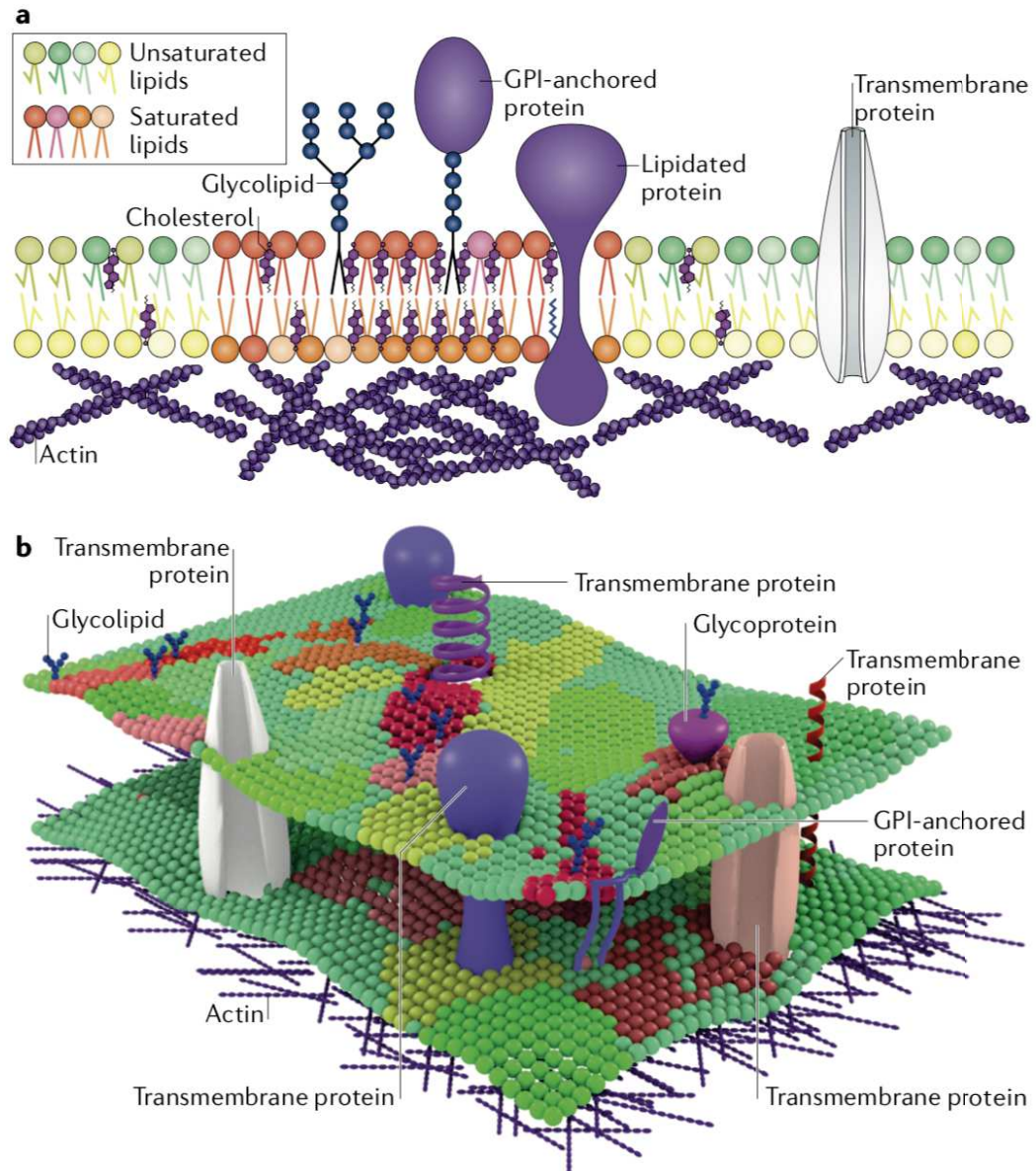


Figure 1.2: General overview of lateral heterogeneity in the plasma membrane. a) Side view of lateral membrane heterogeneity, where different lipids both unsaturated and saturated lipids, glycolipids besides different proteins. b) Top view of lateral membrane heterogeneity, where different membrane domains and liquid-liquid phase separation are shown. Adapted from [11].

Additionally, membrane curvature is highly dependent on the elastic properties of lipid bilayers (which will be addressed in chapter two of this thesis) depend on many parameters such as lipid composition, pH, ionic strength, temperature [17, 18, 19, 20, 21]. These properties make membranes resistant to spontaneous bending; therefore, active mechanisms are needed to change their shape. The spontaneous curvature of the bilayer is the

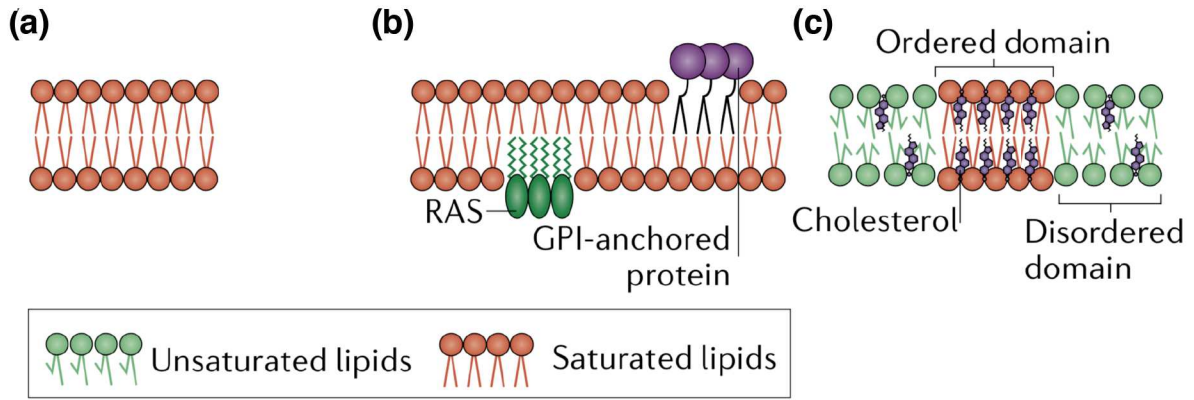


Figure 1.3: Lipid-associated membrane domains. a) Pure lipid clusters. b) Lipid-mediated protein cluster, such as GPI domains, RAS domains. c) Liquid-liquid phase separation of lipids, where cholesterol is preferentially linked to liquid-ordered (l_o) phase and no longer to liquid-disordered (l_d) phase. Adapted from [11].

difference in surface between its inner and outer leaflet, and the spontaneous curvature of each side is affected by the weighted average of the constituent lipids [22, 23, 1].

Membranes can get curved in many different ways:

1.1.2.1 Nanoscopic curvature

Membranes can get spontaneously curved due to their lipid composition. Lipids have intrinsic shapes depending on the size balance between the head group and tail chain compositions (length and saturation) [24, 1]. Such intrinsic properties determine their side-by-side packing imposing a shape on the leaflet, and consequently, the membrane. The local spontaneous curvature of lipids can be organized as follows [24]: (i) Cylindrical, which induces flat monolayer curvature, as shown in Figure 1.5a). (ii) Conical, which induces negative curvature, as shown in Figure 1.5b). (iii) Inverted-conical, which induces positive curvature, as shown in Figure 1.5c). By mixing the lateral organization of lipids within the previous local spontaneous curvature, membranes get different spontaneous curvature, as shown at the right-side of Figure 1.5. In addition to the spontaneous membrane curvature induced by lipid species, membranes can get curved by the insertion of a protein motif at the nanoscale. The insertion of small hydrophobic proteins motif in the membrane is a very efficient way to induce local membrane curvature. It can be a

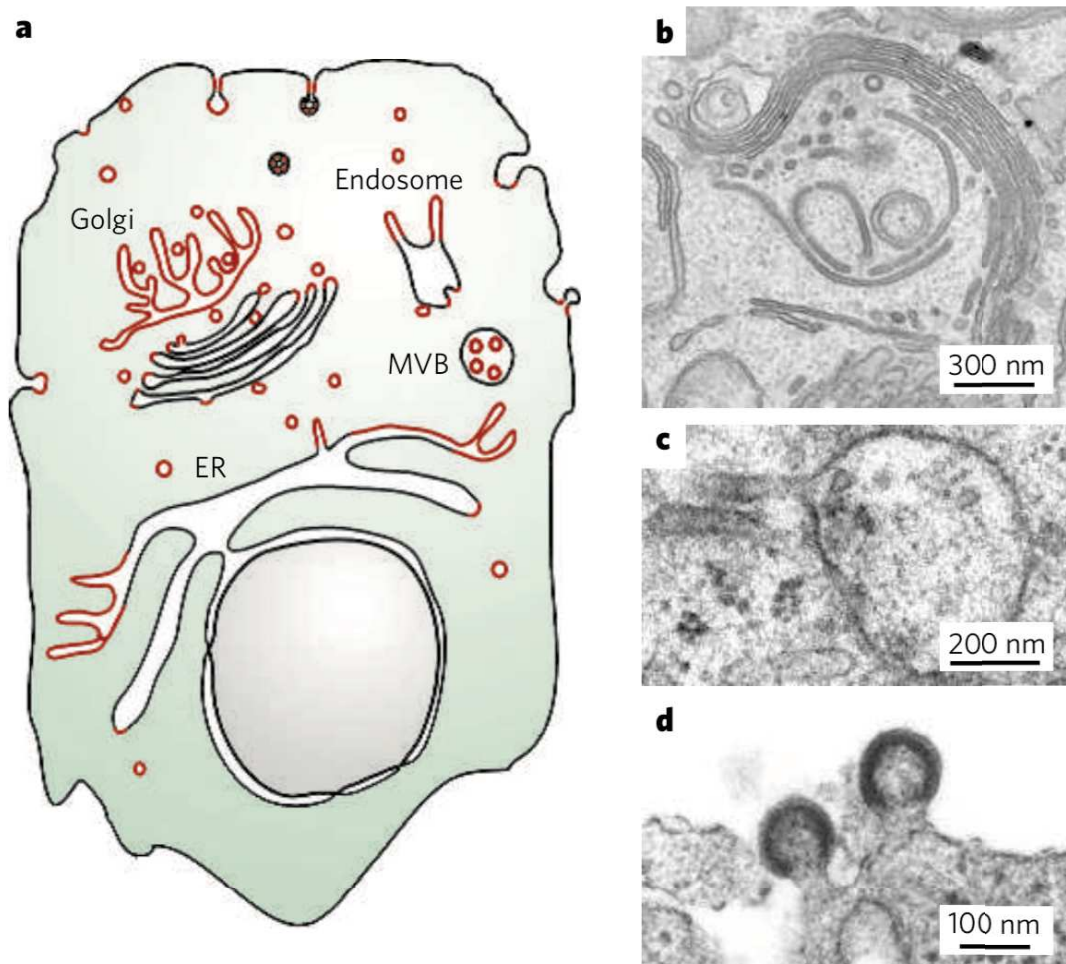


Figure 1.4: Local differences in membrane curvature are hallmarks of cellular membranes. a) Diagram of a cell, where cellular membrane and high local membrane curvature are highlighted in black and red lines, respectively. b) Fenestration in the Golgi (from C. Hopkins and J. Burden, Imperial College London). c) Tubule on endosomes (from P. Luzio and N. Bright, University of Utah). d) HIV-1 viral budding (from W. Sundquist and U. von Schwedler, University of Utah). Adapted from [1].

single insertion, where the bending of the membrane is dissipated rapidly in space. If the insertions are several and in a narrow space, the resulting membrane curvature is much more pronounced [25, 26, 1]. Figure 1.6 shows some examples of protein motifs' insertion.

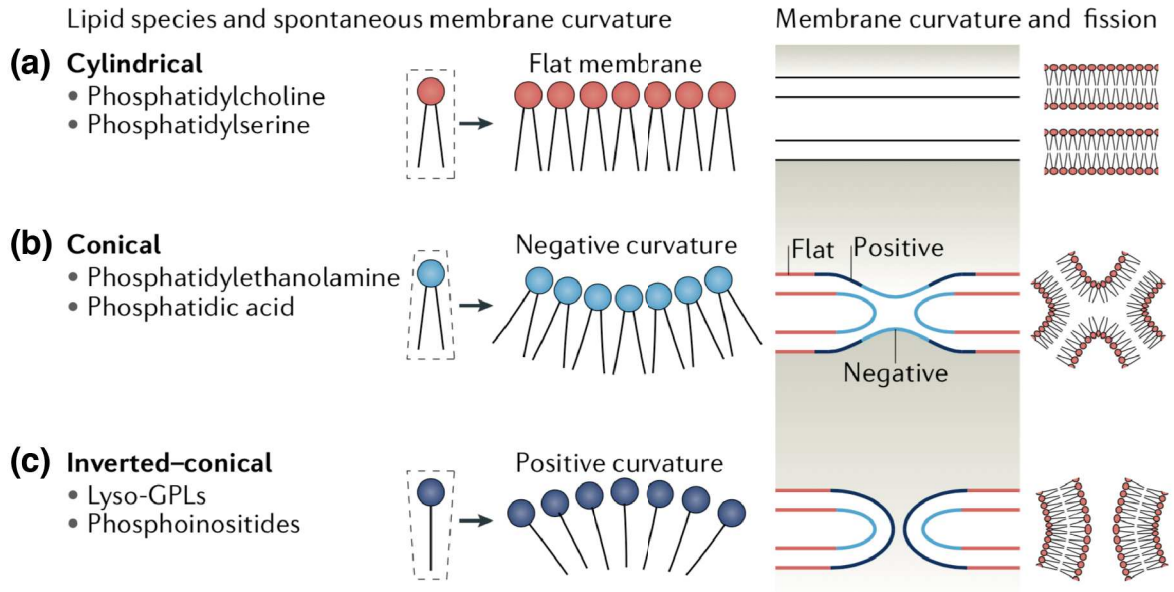


Figure 1.5: Spontaneous membrane curvature induced by different lipid species. The size balance between the head group and hydrophobic tails affects membrane spontaneous curvature. It can be organized in: a) Cylindrical forming flat monolayers such as phosphatidylcholine and phosphatidylserine. b) Conical giving negative curvature to the membrane such as phosphatidylethanolamine and phosphatidic acid. c) Inverted-conical giving positive curvature to the membrane such as lyso-GPLs and phosphoinositides. The membrane curvature and fission are shown on the right side of the figure. Colors illustrate changes in curvature. Adapted from [24].

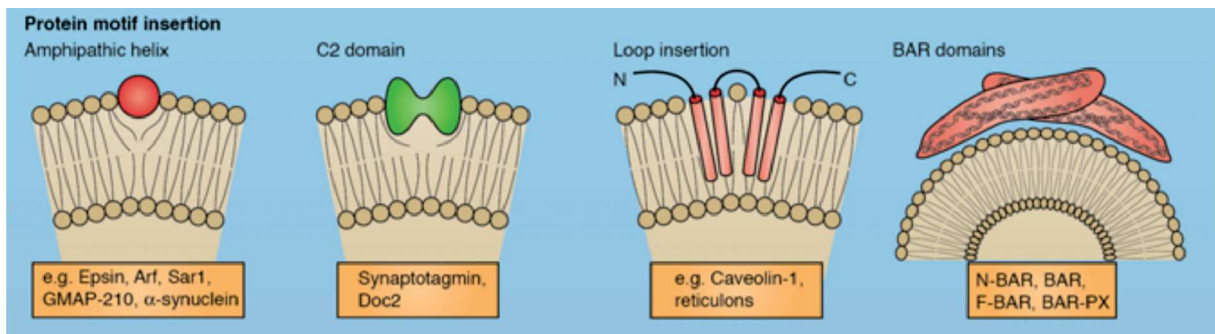


Figure 1.6: Membrane curvature induced by hydrophobic protein motifs' insertion. Adapted from [1].

1.1.2.2 Microscopic curvature

Biological membranes can get microscopically curved by the assembly of proteins into larger structures with a shape formed by the oligomer [1]. Two mechanisms can modulate

microscopic curvature:

- Protein scaffolding: some proteins do not bind to the membrane directly and rely on adaptor proteins (coat proteins) to link them to membranes. Among the adaptors, COPI [27], COPII [28, 27], and clathrin [29], as shown in Figure 1.7. Some proteins as dynamin GTPase superfamily can induce membrane curvature by self-polymerizing into spirals, although a pre-existing curvature is required to assemble efficiently, at least in the presence of membrane tension [1].
- BAR (Bin/Amphiphysin/Rvs) domains are crescent-shaped dimeric modules that bind to membranes [1]. Some BAR domains can oligomerize by forming 'tip-to-tip' or 'side-to-side' interactions (see Figure 1.7), increasing their local concentration, suggesting that they can impose their intrinsic curvature locally to the membrane [1, 30, 31].

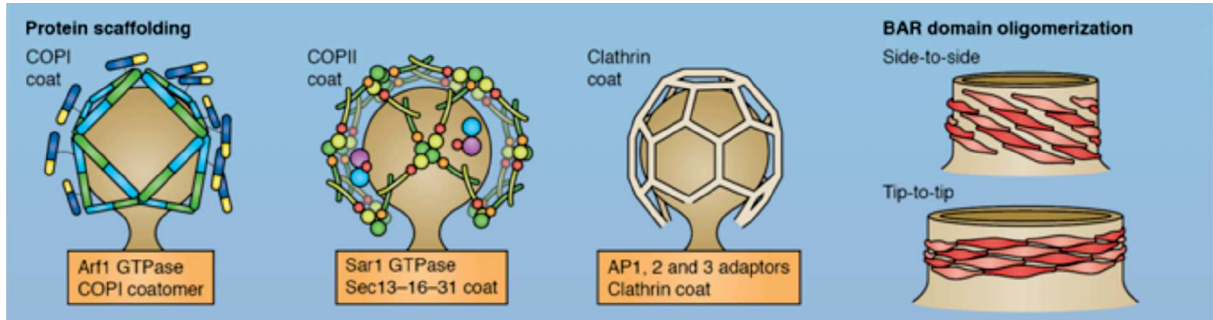


Figure 1.7: Microscopic curvature of membranes. Induced by: (i) protein scaffolding such as COPI, COPII, and clathrin coating. (ii) BAR domain oligomerization, showing the cases of 'side-to-side' and 'tip-to-tip'. Adapted from [1].

1.1.2.3 Macroscopic curvature

Finally, membranes can get curved over large length-scale by means of cytoskeletal scaffolding as in the case of filopodia or lamellipodia as shown in Figure 1.8

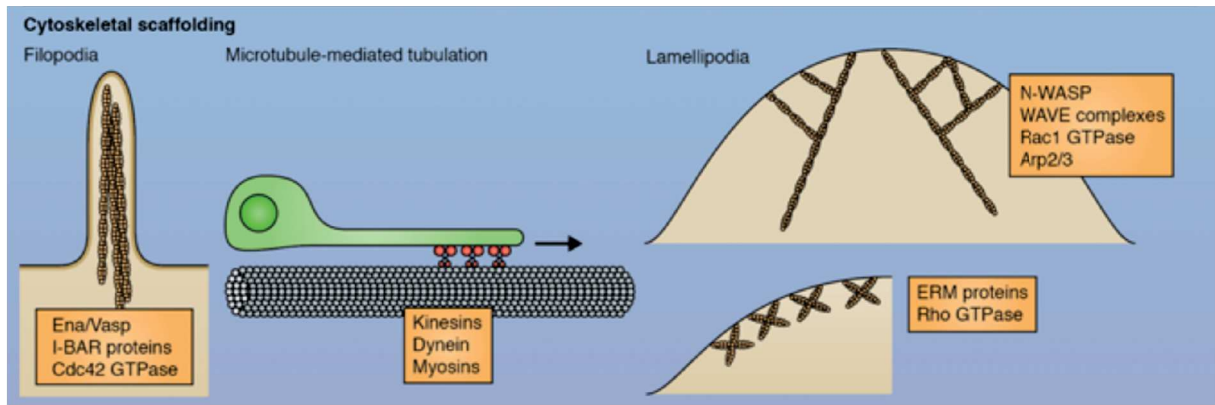


Figure 1.8: Macroscopic membrane curvature over large length-scales obtained by means of cytoskeletal scaffolding. Adapted from [1].

1.1.3 Mechanical properties of cell membranes

We have shown the importance of membrane remodeling within the cell processes and how they are related to the organization's membrane components. Also, membrane remodeling can be viewed through the prism of mechanical forces and cell deformations. A better understanding of how mechanical stresses and deformations regulate cellular functions requires detailed knowledge of the cell mechanical properties [32, 33]. It is well known that cells are viscoelastic bodies, meaning that cells store and dissipate mechanical energy, and their response to mechanical stimuli depends on the rate at which the stimulation is applied [34, 33]. However, the most common approach reported studying cell mechanics is determining the stiffness or an apparent elastic modulus[32].

We will roughly define some mechanical properties on biological. Then, a detailed overview of mechanical properties and different methods used and developed to study them will be provided in Chapter 2.

Various studies have been carried out to measure mechanical properties of cells. Rico et al. [35] have found for Alveolar epithelial cells (A549 cells) that their elasticity modulus is in the range of 0.3-1.4 kPa depending on the AFM tip used. More recently, Sokolov et al. [36] have developed a method to separate the elastic modulus of biological membranes from the one of the cytoskeleton by Atomic Force Microscopy (AFM) indentation experiments. Here, they consider the cellular brush, which is an essential inelastic part of the eukaryotic cells— finding that the elastic modulus of MFC-7 epithelial cells is approximately 0.4 kPa (without the cytoskeleton contribution).

Another important mechanical property of cell membranes is the membrane tension. Using the model proposed by Michael Sheetz [37], it is possible to quantify the membrane tension by pulling membrane tubes. The membrane tension for human melanoma M2 and A7 cells is 0.012 mN/m and 0.011 mN/m, respectively. Whereas the membrane-cytoskeleton adhesion force is ≈ 11 pN and ≈ 14 pN for M2 and A7 cells, respectively. We have briefly described the mechanical properties of biological membranes and how soft they are. However, those parameters are measured and/or evaluated with high dispersion because cells and biological membranes are highly heterogeneous and complex materials. This heterogeneity often makes difficult to infer conclusions from the experiments. As previously mentioned, all membrane remodeling effects are very challenging to be observed *in-vivo* in physiological conditions at high spatial and temporal resolution. Since cellular membranes are very soft, heterogeneous and dynamic, it is very challenging to observe them with the existing microscopies, because of their limitation. The present work aims at presenting a novel microscopy technique suited for the study of cellular membranes. At first, we will consider model membranes that can mimic more complex biological membranes.

1.2 Model membranes

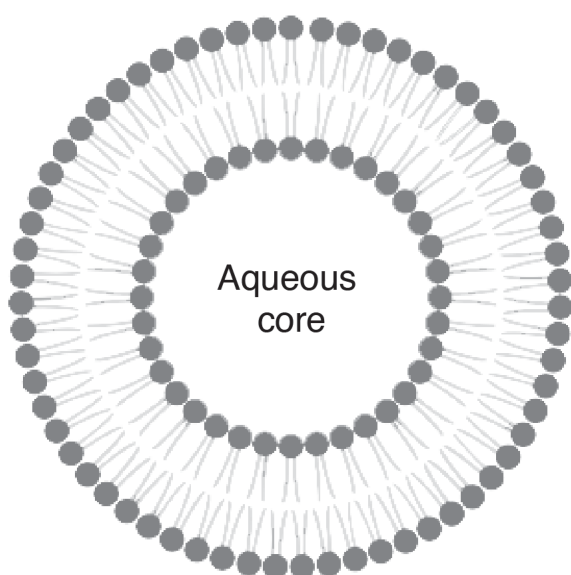
Due to its heterogeneity and the interplay between its constituents, mainly lipids and proteins, a biological membrane is very complex and challenging to study. Model membranes were developed to investigate the specific activity and interactions of a lower number of membrane constituents in a simplified scenario. They are an artificial assembly of lipids with fewer components, resulting in lower complexity than natural ones making them a suitable option to study. The lipids and proteins composition can be controlled in model membranes, allowing for the study of the functional role of specific lipids within cell membranes. Moreover, the environmental conditions, including surrounding medium, ion concentration, and temperature, can be precisely controlled. Model membranes have been extensively used to understand remodeling effects involving lateral lipid organization [38], and lipid-protein interactions.

During the last decades, different types of model membranes were developed. There are

currently two main categories of model membranes:

- Free-standing membrane as vesicles, which are subdivided in Unilamellar Vesicles (with an Aqueous core), and Multilamellar Vesicles (with onion-like membrane core) as shown in Figure 1.9.
- Planar model membranes.

(a) Unilamellar Vesicle



(b) Multilamellar Vesicle

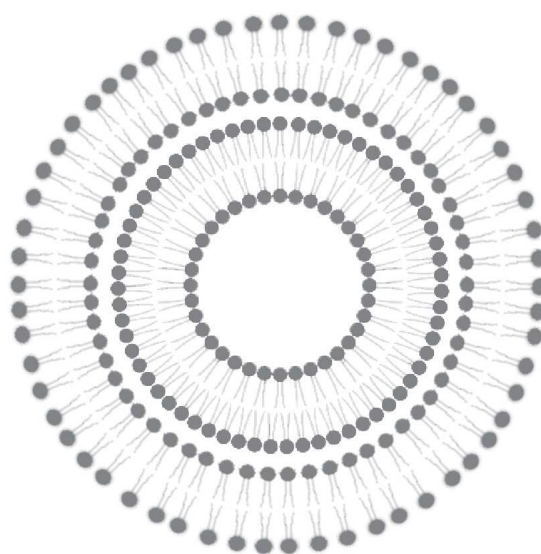


Figure 1.9: Schematics of Giant Unilamellar Vesicle (GUV) and Multilamellar Vesicle (MLV). a) Scheme of a GUV with a aqueous core. b) Scheme of a MLV. Both schematics are just a cartoon because lipids are not in scale with the vesicles.

1.2.1 Giant Unilamellar Vesicles

Giant Unilamellar Vesicles (GUVs) are simple free-standing bilayers whose size, geometry, and composition can be tailored with high precision [39]. They are cell-size (1-100 μm) vesicles. A vesicle membrane is a lipid bilayer wrapped into a spherical shell, enclosing an amount of liquid inside and separating it from the outside medium (see Figure 1.10a)), as a cell does. In addition to the fact that their size allows us to visualize them individually

with a simple optical microscope, GUVs have been widely used to probe bilayers' properties, such as heterogeneities in lipid composition, shape, mechanical and chemical properties [39]. In addition, these vesicles can be controlled and manipulated by microscopy techniques, such as micropipette aspiration [40, 41], membrane flickering analysis [42, 43], and fluorescence imaging of lateral membrane organization [44, 45, 46] (as shown in Figure 1.10b)). Concerning the lipid composition, they can be designed with high precision varying from a single lipid to mixtures of lipids (synthetic or natural lipid extracts) with added proteins, or even fragments from natural cell membranes [39]. In Figure 1.10b), a Gel- l_d coexistence is shown for a binary 18:0-SM:DOPC (1:1) label with LR-DPPE at 0.05 mol%. An essential characteristic of GUVs is that their top and lateral parts are substrate-free, meaning that any interaction with the substrate that might affect lipid diffusion, for instance, is avoided.

The most used method to prepare GUVs is electroformation. It is a method where lipids are deposited on conductive coated glass (typically indium tin oxide or ITO) instead of a Teflon ring employed as a spacer in vacuum conditions. Afterward, the dried lipids are rehydrated with buffer, and the first coverslip is sandwiched using a second conductive cover glass. Then, an electric field with a specific frequency and voltage is applied, inducing the formation of GUVs. The main drawback of this method relies on the significant oxidation effect that can be induced in the vesicles when they are composed of polyunsaturated lipids [47]. For more details, see the protocols described in Morales-Penningstong et al. 2010 [48] and Bhatia et al. 2015 [39].

1.2.2 Large Unilamellar Vesicles

Large Unilamellar Vesicles (LUVs) are smaller than GUVs, and have a size ranging between 0.1-1 μm of diameter. They offer high entrapment of hydrophilic materials in the liposome-internal aqueous space [49]. Reverse Phase Evaporation (RPE) is the most used method for LUVs preparation with 60-65% drug entrapment efficiency [49]. In this method, the lipid phase is dissolved in an organic solvent (typically methanol/chloroform). By adding an aqueous solution, a water-in-oil emulsion of the phospholipid is formed. The

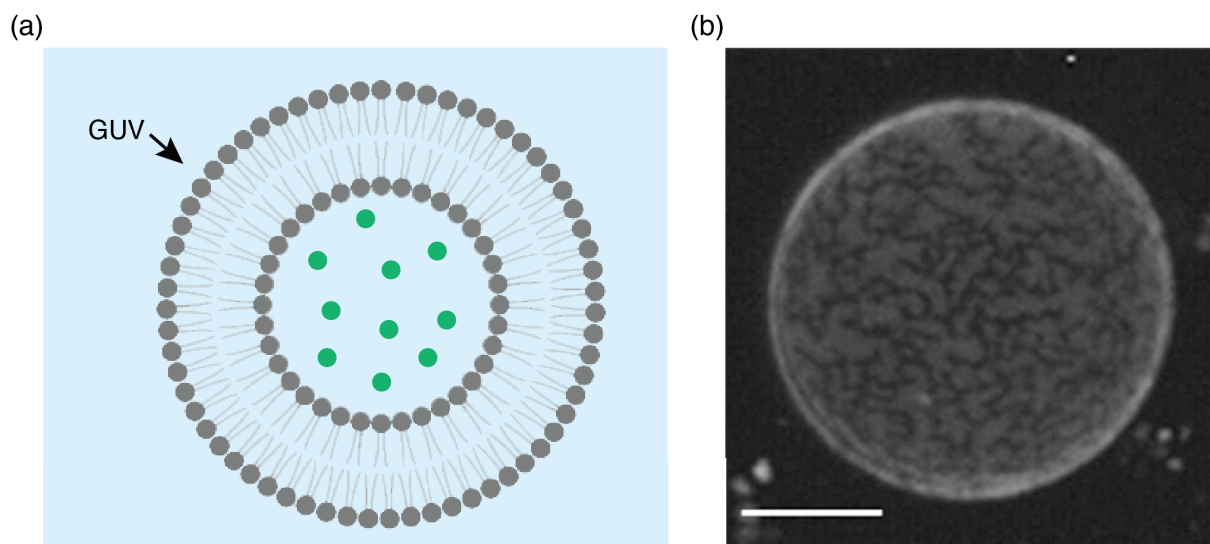


Figure 1.10: Giant Unilamellar Vesicles (GUVs). a) Scheme of a GUV, where both inside and outside mediums are different. b) 18:0-SM:DOPC (1:1) lipid composition GUV label with LR-DPPE at 0.05 mol%. Scale bar 10 μm . Adapted from [48].

organic solvent is removed under reduced pressure, and then water and lipid are sonicated to obtain a gel that contains the LUVs [50, 49]. Another suitable preparation method for LUVs is the formation of multilamellar vesicles from a dry lipid film by vortexing or by successive freeze/thaw cycles before extrusion or sonication that has been employed in the experiments presented in this manuscript (see the process detailed in Section 1.2.3.1).

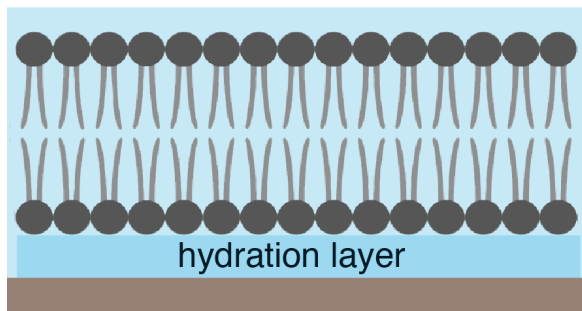
1.2.3 Supported Lipid Bilayers

Supported Lipid Bilayers (SBLs) are planar model membranes supported by a solid substrate. Several surfaces can be employed, mainly Muscovite mica, smooth glass coverslips, or Silicon. The lipid molecule orientation depends on the deposited surface affinity of its two sides with the solid: (i) for a hydrophilic substrate, the head-groups are facing the substrate or/and buffer (see scheme in Figure 1.11a)). In this case, a hydration buffer layer is in between the polar heads and the substrate. (ii) for a hydrophobic substrate, the phospholipid alkyl chain is in contact with the substrate forming a monolayer where the head-groups face the aqueous solution. This monolayer can withstand a bilayer on it, where one bilayer side will be facing the monolayer heads and the other hand the buffer

solution (see scheme in Figure 1.11b)). While the latter case does not produce an SLBs, we decided to include this short explanation to show why we will only focus on SBLs on hydrophilic surfaces from now.

A crucial difference between supported model membranes and free-standing model mem-

(a) Hydrophilic surface



(b) Hydrophobic surface

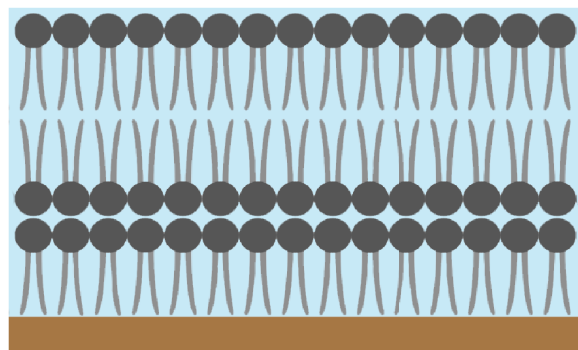


Figure 1.11: Schematics of Supported Lipid Bilayers (SLBs) onto a hydrophilic and hydrophobic substrates. a) SLBs deposited on a hydrophilic surface with a hydration layer in between inner membrane and substrate. b) SLBs deposited on a hydrophobic surface.

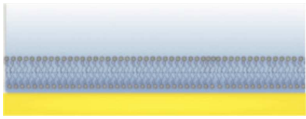
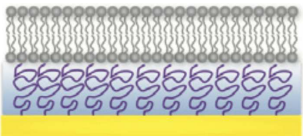
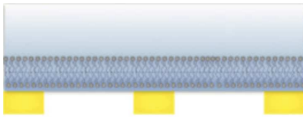
branes (vesicles) is that the inner-leaflet polar heads interact with the substrate in confined lipids. This interaction could be strong due to the short distance between the lower leaflet and the substrate, affecting free lipid diffusion. Such meaningful interaction has been highlighted in a few works inducing a decoupling of the two leaflets [51]. On the other hand, the hydration layer -with a typical thickness in the range of 1 to 3 nm [52]- plays a crucial role here separating the lipid polar head from the substrate and ensuring SLBs to have the essential feature of free-standing membranes. The latter has been demonstrated by measuring lipid diffusion using fluorescence recovery after photobleaching by McConnell's group [53], and confirmed by Fluorescence Correlation Spectroscopy (FCS) experiments [54, 55]. Other studies have been shown that this water layer can be tuned under different experimental conditions, such as the presence of calcium [56]. The surface treatment of glass slides could influence the hydration layer's viscosity affecting the lipid diffusion, and domain formation within the SLBs [57]. As well, numerous studies suggest that this interaction can be minimized using an appropriate buffer [58].

In order to preserve the quality of the membrane and its physicochemical properties, it is important that the substrate has few or no defects, and it has to be hydrophilic, smooth, and clean. Therefore, Muscovite mica [59], borosilicate glass [55], and oxidized silicon

[60, 61] are among the most frequently used. However, other materials such as metal as TiO_2 , gold, silver, and platinum have also been employed [62].

During the last few decades, the use and study of the supported model membranes have grown considerably. Consequently, many systems have been introduced and developed, including solid-supported lipid, polymer-cushioned lipid bilayer, hybrid bilayers, tethered lipid bilayers, suspended/free-standing lipid bilayers, and supported vesicular layers [63]. In Table 1.1, we focus on three types of substrates used to support SLBs with their main advantages and disadvantages: (i) solid substrate, (ii) polymer cushioned, and (iii) porous substrate.

Table 1.1: Substrates employed to support SLBs: solid substrates, polymer cushions and porous substrates. Main advantages and disadvantages are reported for each case. Adapted from [51].

	Solid support	Polymer cushion	Porous support
Schematic			
Advantages	Improved coverage Improved imaging resolution by Atomic Force Microscopy	Poor interaction with the support	Free spanning bilayer Absence of support interaction
Drawbacks	Interaction with the support needs to be controlled	Difficulties in imaging Restricted lateral diffusion	Difficult coverage
References	[63]	[64]	[65]

1.2.3.1 Methods used to prepare SLBs

Here we will present and describe the three most common methods employed to prepare SLBs with their main advantages and disadvantages. The methods are the followings:

Langmuir-Blodgett

This method is based on producing a single lipid monolayer at the air-liquid interface of a Langmuir-Blodgett cell, transferred to a hydrophilic substrate, and subsequently used to deposit another single lipid monolayer on it, forming an SLB by coupling of both leaflets. A general protocol is described as follows: lipids are dissolved in chloroform-methanol (2:1 v/v) solution at 1 mg/mL and deposited on a Langmuir-Blodgett cell filled with deionized water where a lipid monolayer is formed at the interface of the cell. The lipids on the interface are subsequently compressed using a barrier [66], as shown in Figure 1.12a), until a monolayer is formed; this process is controlled by measuring the surface tension on the monolayer with a Wilhelmy plate. Once this monolayer (first leaflet of the bilayer) is formed, it is transferred to a hydrophilic substrate (typically muscovite mica or silicon) with the lipid headgroups toward the substrate. Afterward, the process is repeated a second time to form another lipid monolayer (second leaflet of the bilayer), deposited on the sample with the lipid headgroups facing the aqueous phase [67], resulting in a single SLB as shown in Figure 1.12b).

This method has several advantages: both leaflets of the bilayers are transferred independently, and they can be tuned in terms of lipid composition, inducing an asymmetry of the leaflets, as shown in Figure 1.12c) and as it is the case in the cell plasma membrane. In addition, the surface tension of both leaflets can be controlled, resulting in an asymmetry of the lateral pressure. However, as the main disadvantages, both leaflets must be produced in two separate processes, resulting in time-demanding sample preparation. In addition, the Langmuir cell does not produce a homogeneous coverage of the lipid monolayer at the interface, resulting in incomplete coverage of SLBs.

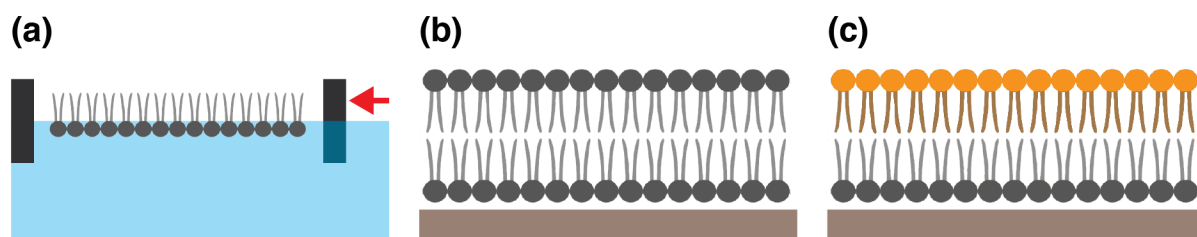


Figure 1.12: Schematics of SLBs preparation by the method of Langmuir. a) Diagram of a lipid monolayer laterally compressed in a Langmuir-Blodgett cell, b) Schematic of an SLB with symmetrical lipid composition leaflets, and c) Schematic of an SLB with two-asymmetrical lipid composition leaflets.

Vesicle fusion

This method is based on the adhesion of vesicles onto a generally flat and hydrophilic substrate and their rupture and spreading to produce a continuous SLB [38]. Here, lipids are individually dissolved in an organic solvent solution. MLVs are prepared by mixing the previously dissolved lipids and proteins in the desired molar ratio concentrations into a glass vial. The sample is evaporated to dryness under nitrogen flux for obtaining a thin film on the tube walls. After, the sample is rehydrated with buffer, producing vesicles. The solution is extruding in order to make LUVs in buffer solution. Finally, the LUVs solution is deposited on mica, where the LUVs break out, forming supported lipid bilayers (see [68] and Appendix A for more details).

We use this method to prepare SLBs because it offers us a simple preparation for a single SLB on a substrate, ensuring symmetric composition of both leaflets using a mixture of several lipids. A schematic and AFM topographical image of two lipid phase separations are shown in Figure 1.13b) and c), respectively.

Spin coating

In this method, a lipids mixture solution is spin-coated on a hydrophilic substrate. AC Simonsen and LA. Bagatolli showed in 2004 [69] that the hydrophilic substrate must be kept wet by the main spin coating solvent, hexane, during the entire procedure. The same

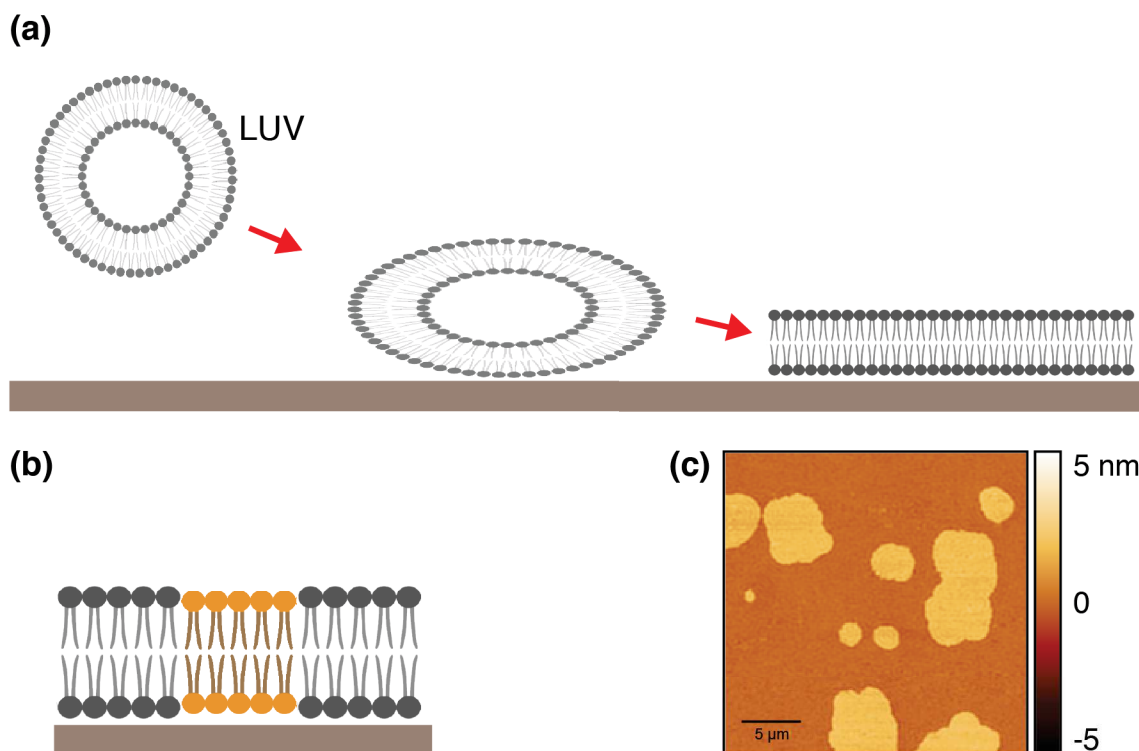


Figure 1.13: Schematics of SLB preparation by the method of vesicle fusion. a) Diagram of vesicle fusion to SLB formation. b) Schematic of 2-lipids composition SLB produced by the vesicle fusion method. c) topographical image of a two lipid separated-phase SLB on mica (DOPC: DPPC, 1:1) in DPBS buffer acquired by Atomic Force Microscopy. DOPC-domains (darker areas) in liquid phase, and DPPC-domains in gel phase.

authors found that the critical parameter for controlling the film thickness is the coating solution's concentration, finding that 7 mM is the optimal total lipid concentration for a mixture of lipids, typically sufficient to produce a complete coverage of the substrate [69]. Once the critical parameters are defined, the protocol is the following [69]: A freshly cleaved muscovite mica is placed into a spin-coater and spinning at 3000 rpm for 40 seconds upon application of the lipid solution - a volume of 15-20 μL is sufficient to cover a muscovite mica of 8x8 mm² fully. Afterward, the substrate is placed into a vacuum for 10-15 hours to ensure the solvent's complete evaporation, obtaining multilayers in air, as shown in Figure 1.14a). By re-hydrating and washing the sample with buffer, it is possible to switch between a stack of SBLs to a single SBLs (Figure 1.14b)). This process can be controlled by labeling the lipids with fluorescent probes and observe the SLBs formation using a fluorescence microscope.

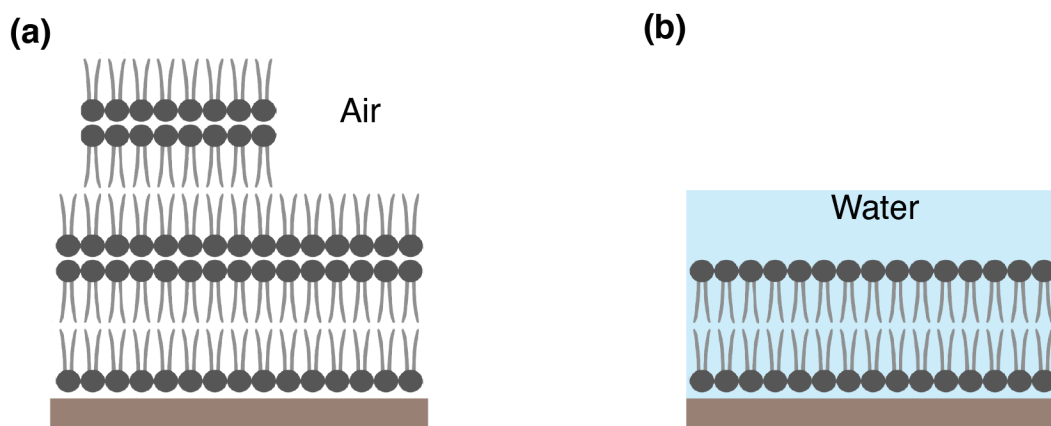


Figure 1.14: Schematics of SLBs preparation by the method of spin coating. a) Schematic of supported lipid multilayers produced by the spin coating method in air. b) Schematic of SLBs produced at the end of the spin coating method in liquid.

Table 1.2 presents the three methods usually employed to prepare SLBs and reports advantages and disadvantages for each case.

Table 1.2: Summary of the most common methods used to prepare SLBs. Adapted from [38].

	Langmuir-Blodgett	Vesicle fusion	Spin coating
Advantages	<ul style="list-style-type: none"> - Asymmetric bilayers (in composition and lateral pressure) 	<ul style="list-style-type: none"> - Simplicity (manipulation) and fast sample prep - Single bilayers (often) - Incorporation of proteins - Few defects 	<ul style="list-style-type: none"> - Full coverage - Absence of defects - Single or multi-bilayers
Drawbacks	<ul style="list-style-type: none"> - Leaflet decoupling - Uncompleted coverage - Defects (holes) - Time demanding sample prep 	<ul style="list-style-type: none"> - Symmetric bilayers - Equilibrium lateral pressure non-controlled 	<ul style="list-style-type: none"> - Symmetric bilayers - Requires exposition to organic solvents - Difficulty to control the number of layers
References	[67]	[70]	[69]

1.2.3.2 Mechanism of SLB formation

We have shown the most used method to prepare SLBs, but we did not describe how SLBs are formed in the vesicle fusion method. Based on the vesicle fusion method, studies combining quartz crystal microbalance with dissipation monitoring (QCM-D) and atomic force microscopy (AFM) suggest two main mechanisms for bilayers formation [38]: (i) a direct formation by fusion of vesicle after their contact with the surface [71, 63], (ii) the absorption of intact vesicles on the surface, followed by their rupture, eventually induced by neighboring activity, and finally bilayers formation [72, 63].

Ritcher et al. summarised the different mechanisms of SLB formation by the vesicle rupture [63], showing 4 cases in Figure 1.15.

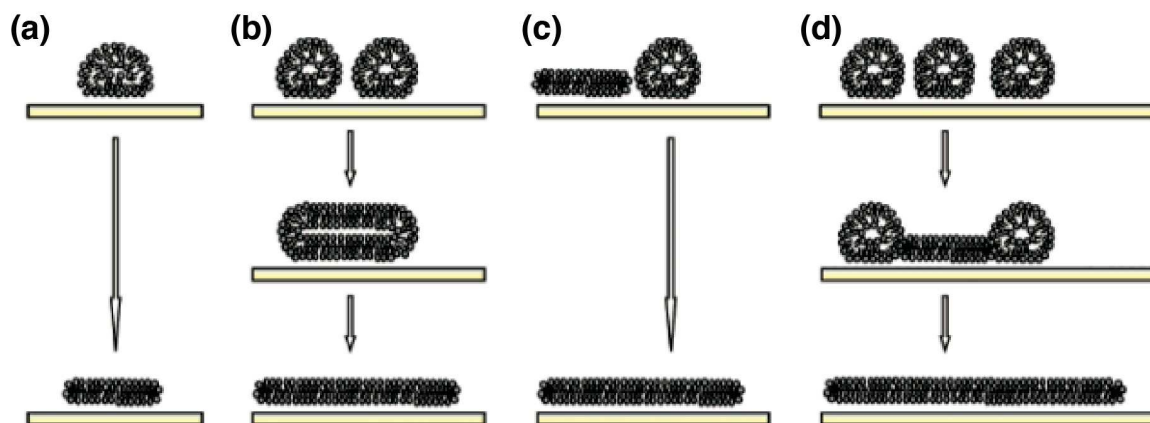


Figure 1.15: Mechanisms of vesicle rupture schematics. a) an isolated adsorbed vesicle ruptures spontaneously, driven by its support-induced deformation. b) neighboring adsorbed vesicles fuse, generating another vesicle for its eventual breaking. c) the active edge of a supported bilayer patch induces the rupture of a neighboring vesicle. d) the cooperative action of several adjacent vesicles leads to the rupture of a first vesicle (at the critical vesicular coverage), and the eventual rupture of the other vesicles by the active edge of the supported bilayer as in case c). Adapted from [63].

1.3 Main challenges in the study of membranes

In the present chapter, we have shown that membrane remodeling plays a fundamental role in many biological functions of the cell. In addition, we have shown that membrane constituents' activity is mainly modulated membrane remodeling. The latter is highly dynamic and requires observations at high lateral and temporal resolution. To achieve that in physiological conditions, we need to employ techniques that can work in liquid, including Atomic Force Microscopy (AFM) and fluorescence microscopy. However, both techniques have advantages and disadvantages for the study of cell membranes. The main disadvantage of fluorescence microscopy is the poor lateral resolution, which is limited by the Abbe limit (diffraction limit) [73], in practice to several hundreds of nanometers. However, several Super-Resolution fluorescence microscopies have recently been developed in the last decades [74], such as Structured Illumination Microscopy (SIM), Stimulated Emission Depletion (STED), Stochastic Optical Reconstruction Microscopy (STORM), Photo Activated Localization Microscopy (PALM), and MINFLUX. These Super-Resolution techniques can currently achieve resolutions below ten nanometers with an imaging rate ranging from tens of minutes to few seconds. However, unlike AFM, Super-Resolution fluorescence microscopies cannot measure the sample topography nor its mechanical properties.

Concerning AFM, there are several disadvantages we have to take into account when measuring cellular membranes:

1.3.1 1st challenge: the membrane-AFM tip interaction force

Biological membranes are very soft materials with a Young Modulus in the range of a few tens of kPa (for the case of a red blood cell's membrane [75]) to less than 100 MPa (for the case of supported lipid membranes on solid substrates [76]). As a consequence, they get largely deformed when a force is applied. AFM requires forces to image the topography, deforming, or even breaking the sample during AFM scanning. This problem will be described and studied in the second chapter of this thesis.

1.3.2 2nd challenge: Chemical sensitivity

AFM can achieve sub-nanometer vertical resolution obtaining high lateral and vertical images of the sample's topography. However, conventional AFM images do not have chemical sensitivity, which is essential to recognize single membrane constituents. However, some techniques have been developed in order to achieve specific molecular recognition. The main two are the following:

(i) correlative AFM - fluorescence microscopy, where specific membrane constituents can be labeled with a fluorescent probe and recognized within the fluorescence image. However, the constituents' localization resolution is limited by the fluorescence technique employed (a couple of hundreds of nanometers in Figure 3.1).

(ii) Simultaneous topography and recognition imaging (PICO TREC) can acquire si-

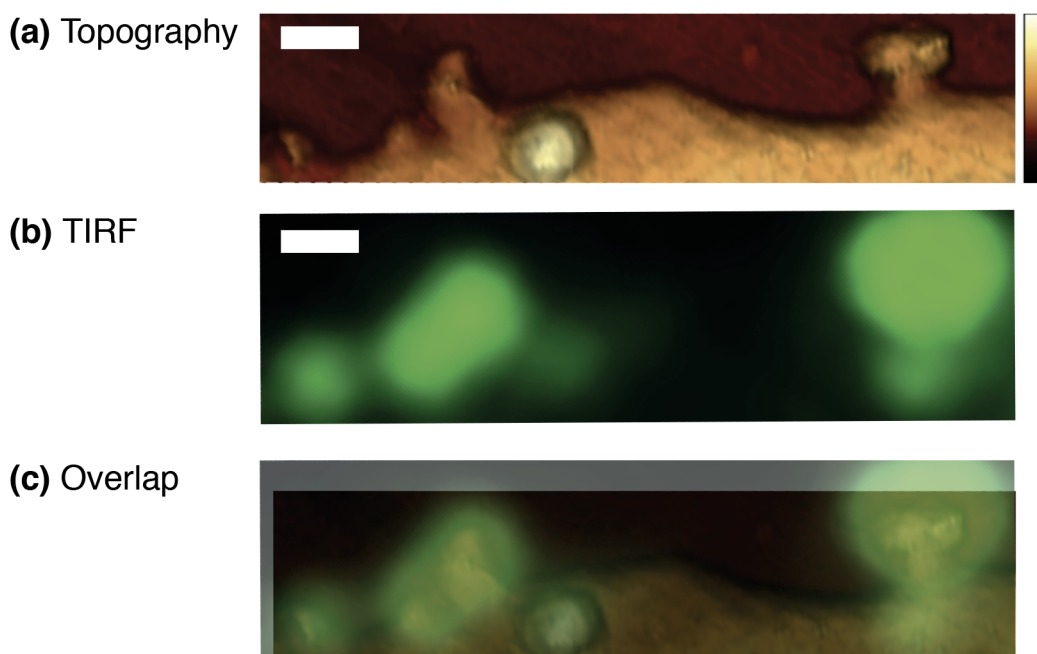


Figure 1.16: Correlative Fluorescence-AFM of HeLa cells expressing HIV-1 Gag-GFP. a) AFM-topography (color Z-scale is 300 nm). b) Total internal reflection fluorescence (TIRF) microscopy image of Gag-GFP. c) Overlay of a) and b). All scale-bars are 500 nm. Adapted from [77].

multaneous sample topography, and molecular recognition [78, 79], but it might fail to localize a part of the molecules of interest. Figure 1.17 shows a molecular recognition experiment using PICO TREC.

The problem of chemical sensitivity and molecular recognition in correlative fluorescence-

AFM studies will be addressed in the third chapter of the thesis: it presents a novel Super-Resolution technique developed combining an AFM with confocal microscopy using fluorescence spectroscopy and time-correlated single-photon counters. It is based on metal-induced energy transfer (MIET), and we called it MIET-AFM.

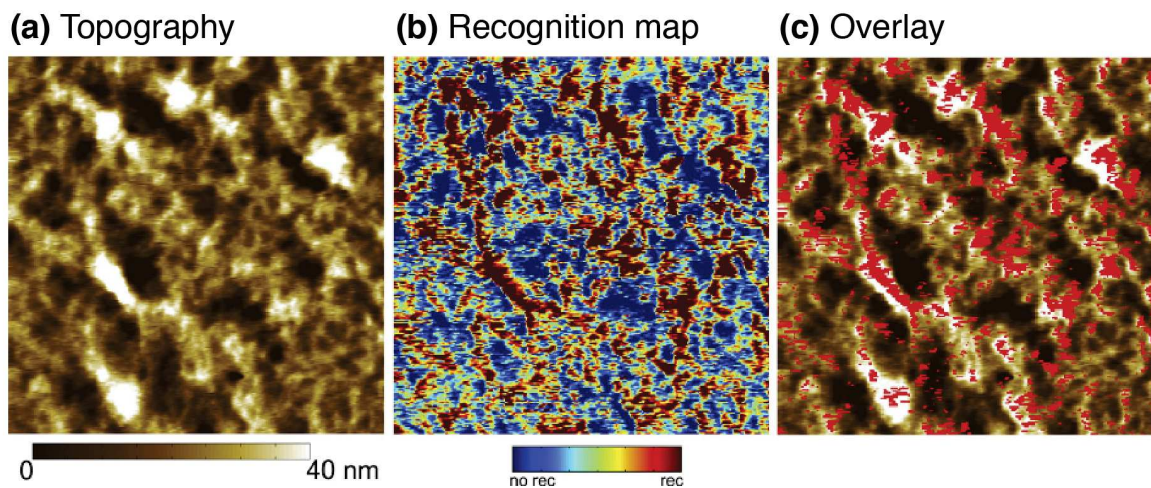


Figure 1.17: AFM topography and molecular recognition by PICO TREC. Nano-organization of the GnRH-Rs on the T24 cell surface. a) AFM Topography image. b) PICO TREC recognition map, where the red surfaces represent the GnRH-Hs. c) Overlay of a) and b). Adapted from [79].

1.3.3 3rd challenge: Time resolution

Because of the fast membrane dynamics, the slow AFM image acquisition time is an additional problem. A conventional AFM image takes at least a few minutes to be acquired. It represents an important limitation since cellular membranes are highly dynamic, at a timescale that in most cases cannot be assessed by conventional AFM.

Temporal resolution is out of this thesis' scope. However, this issue has been addressed by the High-Speed AFM (HS-AFM) [80], which can acquire topographical images of relatively flat samples at video rate (≈ 30 fps) [81, 82], with 2 nm of lateral resolution and 0.1 nm of vertical resolution [83].

Chapter 2

Mechanical properties of Supported Lipid Bilayers

In the previous chapter, we have shown that the mechanical properties of biological membranes play a fundamental role in many membrane remodeling processes and, therefore, in several fundamental cellular activities.

At first, this chapter introduces a basic membrane mechanics theory and some associated measurable observables.

Then, the most common instruments used to characterize membrane mechanics are introduced, especially focusing on Atomic Force Microscopy.

Finally, the problem of the formation of holes within model membranes indented by an AFM tip is accurately studied and discussed in the central part of this chapter.

2.1 Mechanical properties

The mechanical properties are quantified by measuring how a material responds to an applied mechanical stimuli. Starting from a simple case, a deformation: in the case of a parallelepiped, we consider a pressure σ applied perpendicularly onto one of the body faces. This pressure induces a deformation Δl of the body that is the consequence of the body compression. $\Delta l = l_0 - l$ is the change in body length obtained from the non

deformed length l_0 and the final deformed length l (see schematics in Figure 2.1a).

Considering the body as an elastic material, we can introduce elastic properties. By

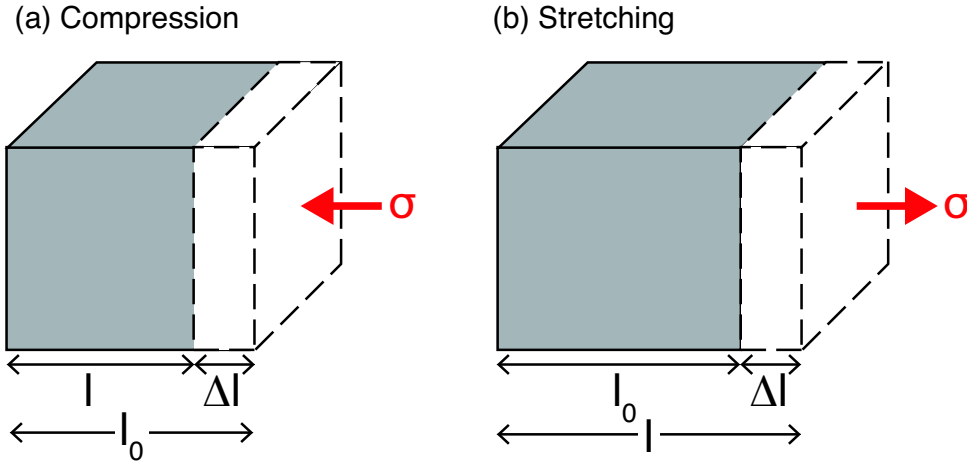


Figure 2.1: Schematics of a mechanical deformation on a body of original length l . a) compression and b) stretching.

definition, if a mechanical stimulus is applied to an elastic material, the latter is capable of returning to its original shape once the stimulus has been removed. The capability is described by the Hook's law that additionally states that when an elastic material is deformed, it is storing the energy applied. The elasticity of a body is characterized and quantified by the elasticity modulus E , in $[Pa]$, which is a fundamental property of solids that characterizes their ability to sustain their shape under mechanical stress [84]. The elasticity modulus E is also called Young's modulus. In a simple case such as the one in Figure 2.1, E is the scaling between stress σ (previously called pressure) and strain of the material as the following:

$$\sigma = E\varepsilon \quad (2.1)$$

Where ε is the normal strain defined as $\varepsilon = \frac{\Delta l}{l_0}$. Compression is defined when a stress σ is applied against one of the faces of the body (see Figure 2.1a). Otherwise, when the stress σ is applied outwards from one of the body's faces, the stimulus is called stretching (see Figure 2.1b). It is important to remark that 2.1 is valid for both compression and stretching but only for the linear elastic deformation.

E is an intrinsic property of the material, whereas the stiffness k , in $[N/m]$, is an extrinsic property, and it is the parameter that quantifies the body resistance to deformation ΔL

when a force F applied as:

$$F = k\Delta L \quad (2.2)$$

This parameter is typically used to characterize springs, and it is also commonly called "spring constant."

When a mechanical stimulus (compression or stretching) is imposed on a body, the latter

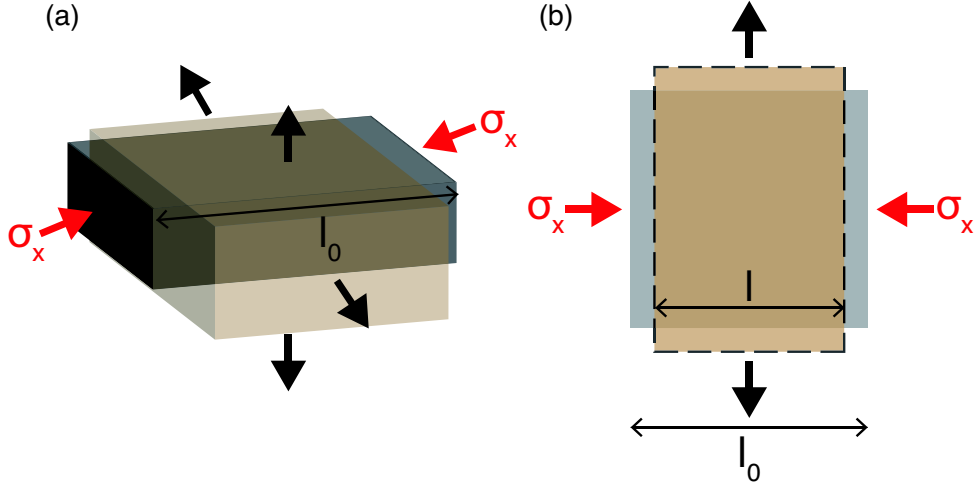


Figure 2.2: Schematics of Poisson's effect on a body. a) Isometric view, b) Top view.

is deformed both in the stress-axis direction as in the other axes. The off-axis deformations are described by the Poisson's ratio ν , which is defined as follows :

$$\nu = \frac{\varepsilon_{\parallel}}{\varepsilon_{\perp}} \quad (2.3)$$

Where ε_{\parallel} and ε_{\perp} are the strain in the direction of applied stress and perpendicular to applied stress, respectively; in other words, Poisson's ratio is the ratio of transverse expansion (or contraction) strain over the longitudinal extension strain in the direction of the applied stress [85]. Figure 2.2 shows a scheme showing that when a stress is applied in a direction, the deformed body also reacts in the other directions. Typical values for ν are in the range of -1 to 0.5: when a material has $\nu = 0.5$, it is known as a perfectly incompressible elastic isotropic material. This value is typically associated to SBLs [86, 87, 88]. While most materials have a positive coefficient, other materials have negative coefficient values[89], such as some foams, honeycomb, graphene[90], tendons[91], chain organic molecules[92].

Making a general overview of three relevant scales to take into account when studying

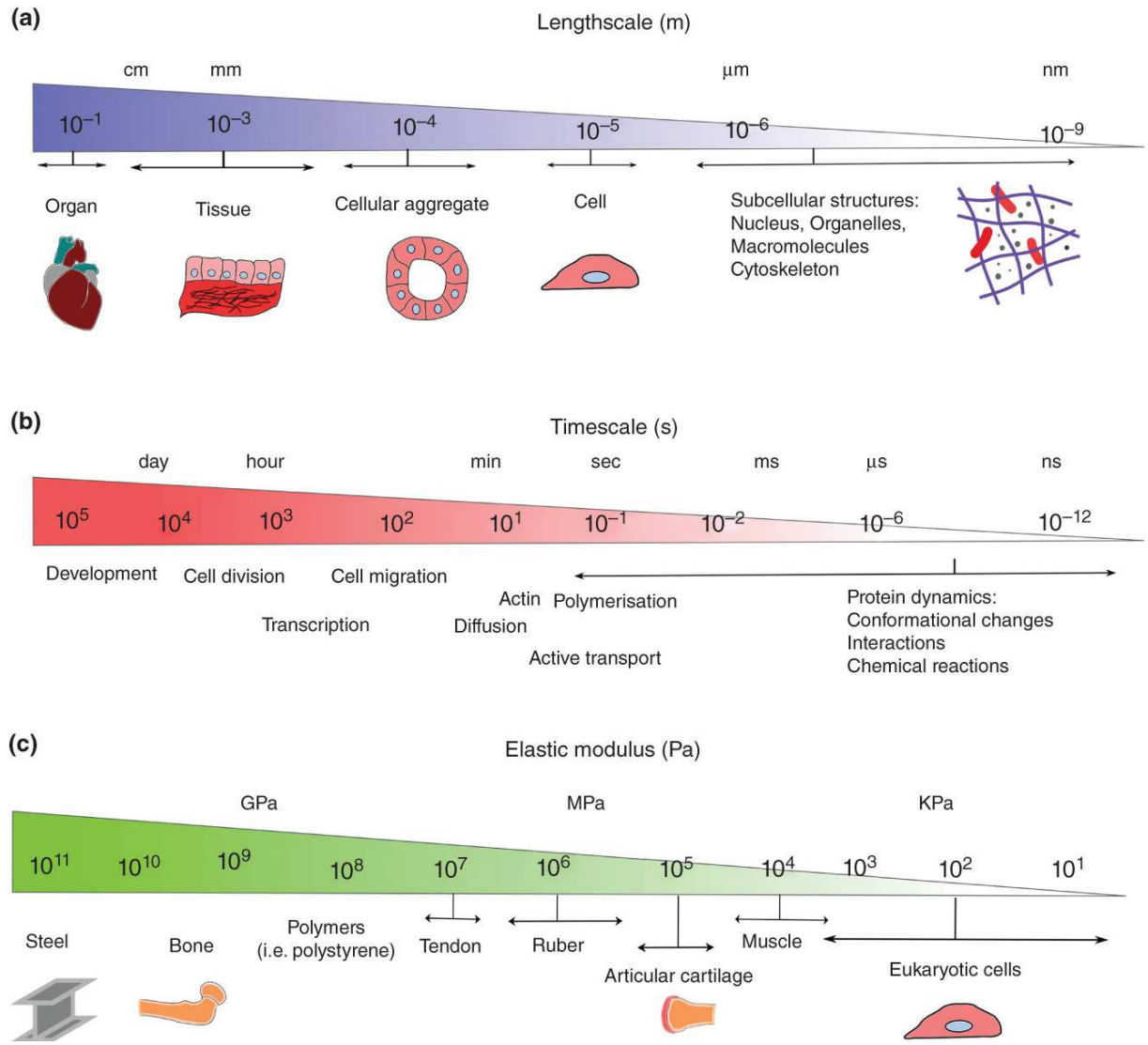


Figure 2.3: Length-scale, time-scale and elasticity-scale for different bio-materials. a) Length-scale, b) Time-scale and c) Elastic modulus scale. Adapted from [84].

mechanical properties of materials (or in our case, biomaterials), we can mention: length-, time- and elasticity modulus-scales, as shown in Figure 2.3. Biological materials are widely spread in all scales. Our subjects of interest, SLBs, are in the nanometer range in terms of length-scale, from minutes (diffusion) to nanosecond (lipids and proteins dynamics within the membrane) in the time-scale, and in the tens of kPa in the elastic modulus-scale.

It is important to note that a cell is a viscoelastic material. In a viscoelastic material, an imposed deformation simultaneously stores and dissipates mechanical energy, and thus, mechanical stress relaxes and deformation increases over time [84]. Biological membranes are represented as a thin layer, typically with a thickness h around 5 nm, composed of

two fluid lipid monolayers that a mechanical stimulus can deform. A membrane can be considered as a 2D material that can be stretched, and we can characterize such deformation using the areal expansion modulus K_A , which can be evaluated during micropipette aspiration experiments [93]. This parameter's typical values are in the range of 0.1-1 N/m [94], suggesting that lipid bilayers are essentially inextensible, tolerating only 4-6 % areal strain before rupture [93]. Based on the thin-plate theory, K_A can be written as follows [95]:

$$K_A = \frac{Eh}{2(1 - \nu)} \quad (2.4)$$

As previously mentioned, lipid membranes are composed by two non-fully coupled monolayers. Therefore, when a membrane is bent, one leaflet is differently stretched than the second one. The parameter representing the necessary amount of energy to deform a membrane from its natural curvature to a different one is known as bending modulus κ . In the thin-plate theory, for a continuous thin film, the bending modulus can be written as follows:

$$\kappa = \frac{Eh^3}{12(1 - \nu^2)} \quad (2.5)$$

Typical values found for κ are found to be on the order of $10 K_B T$ (K_B is the Boltzmann constant) or $10^{-19} - 10^{-20}$ J [93].

As shown so far in the present chapter, Young's modulus E is a fundamental parameter in determining and/or relating to many other properties. One of the most widely used methods to evaluate E is given by Hertz's contact model, which was proposed by H. Hertz in 1882 [96]. This model describes the elastic compression of a flat homogeneous and infinite extensive material induced by the force applied for a spherical indenter. In the absence of non-mechanical contact interaction forces, the model states:

$$F = \frac{4}{3} \frac{E}{1 - \nu^2} \sqrt{R\delta^3}, \quad (2.6)$$

Where R is the radius of the spherical indenter, ν is the Poisson ratio, δ is the indentation length, and E is the Young's modulus of the film, assuming the Young's modulus of the indenter E_I much higher than E . The indentation is pictorially reported in the Figure 2.4.

Once the theoretical background is defined, the following problem is how to measure

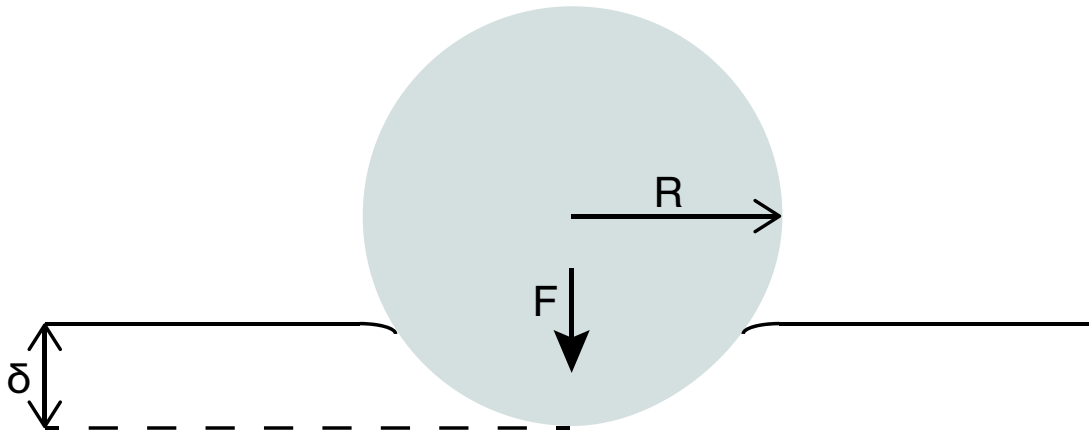


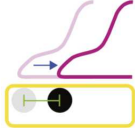
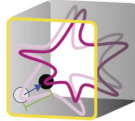
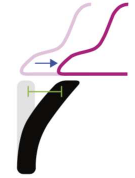

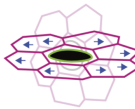

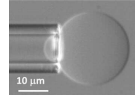
Figure 2.4: Schematic of Hertz's contact model for a spherical indenter compressing a flat surface. Contact between a rigid sphere of radius R and a flat surface, the sphere applies a force F over the flat surface.

these properties in such soft and small materials.

2.2 Quantifying membrane (or cell) mechanical properties

Novel technologies and methodologies have been developed to study the mechanical properties of biological membranes under different conditions and resolutions. They have all advantages and disadvantages. In table 2.1, a general overview of the techniques used to measure cellular forces is shown.

Table 2.1: Summary of techniques to measure cellular forces. Adapted from [97].

	Force range	Length scale	Measured quantity	Strengths	Limitations	References	Schematic
2D traction microscopy	$1-10^4$ Pa	$10^{-1}-10^3$ μm	Substrate displacement	<ul style="list-style-type: none"> + Absolute measurement + Tunability of substrate stiffness + Output is a 2D map 	<ul style="list-style-type: none"> - Computationally involved - High sensitivity to displacement noise 	[98, 99, 100, 101]	
3D traction microscopy	$10-10^4$ Pa	$10^{-1}-10^2$ μm	ECM displacement	<ul style="list-style-type: none"> + Cells in 3D environment + Output is a 3D map 	<ul style="list-style-type: none"> - Computationally very involved - Unknown ECM material properties close to the cell - Physiological ECM is non-linear 	[102, 103]	
Micropillars	$10^{-2}-10^2$ nN	$10^{-1}-1$ μm	Pillar displacement	<ul style="list-style-type: none"> + Absolute measurement + No reference image required + Simple force calculation 	<ul style="list-style-type: none"> - Discrete rather than continuous adhesion - Difficult to compare to physiological environments - Small stiffness range 	[104, 105, 106]	
Atomic Force Microscopy	$10-10^5$ pN	$10^{-3}-10^3$ μm	Cantilever displacement	<ul style="list-style-type: none"> + Possibility of imaging the sample + Simple and precise force measurements in real time + Wide force range + Point measurements 	<ul style="list-style-type: none"> - Requires contact - Requires surface considerations - Difficulties to implement some theoretical models 	[107, 108]	
Inserts	$10^{-1}-10^4$ Pa	$10-10^2$ μm	Insert deformation	<ul style="list-style-type: none"> + In vivo + Control of adhesion specificity + Versatile 	<ul style="list-style-type: none"> - Requires microinjection - No measurement of shear stress - No measurement of isotropic stress 	[109, 110, 111]	
Optical tweezers	$0.1-10^2$ pN	$10^{-3}-10^2$ μm	Colloidal displacement	<ul style="list-style-type: none"> + High signal-to-noise ratio + 3D tracking and forces + Multi-point measurements simultaneously + Point measurements + Non-contact 	<ul style="list-style-type: none"> - Narrow force range - Laser can damage the sample 	[112, 113]	
Micropipette Aspiration	$1-10^3$ pN	X μm	Sample deformation	<ul style="list-style-type: none"> + Point measurements 	<ul style="list-style-type: none"> - Requires contact - Requires surface considerations 	[114, 115, 116]	

2.2.1 Optical Tweezers

Optical Tweezers are a technique that makes use of a strongly focused laser beam to catch and hold dielectric particles in a size range from nanometers to micrometers. The focused light interacts with the colloidal particle applying a force toward the focus of the laser beam, with a magnitude proportional to the distance of the particle from the laser focus, under the assumption of small displacements away from the center of the trap [117]. The bead motion can be modeled as a stationary trap. Making use of the equipartition theorem, the average potential energy of the particle in the Hookean trap is equal to the thermal energy of the medium (without assuming a value for the local viscosity):

$$\frac{1}{2}K_B T = \frac{1}{2}k_{trap} \langle x^2 \rangle \quad (2.7)$$

where K_B is the Boltzmann's constant, T the medium absolute temperature, k_{trap} the equivalent stiffness of the optical trap, and $\langle x^2 \rangle$ is the mean square movement of the colloidal particle due to thermal vibrations. The k_{trap} values are in the range of $10^{-6} - 10^{-5} \text{ N/m}$. The optical force applies F_{trap} over the colloidal is:

$$F_{trap} = -k_{trap} \Delta x \quad (2.8)$$

where Δx is the distance of the sphere from the center of the optical beam (Figure 2.5), in an optical trap, F_{trap} is a restoring force due to the particle is attracted to the center of the beam. Optical tweezers provide a valuable tool for high precision measurements of small forces (in a range between $0.001 - 10^2 \text{ pN}$). There is an inherent limit on the amount of force that can be applied using this method. In order to increase the optical force, it is crucial to increase the laser power, potentially inducing local heating that might damage the cell structure and affect its mechanical properties [84].

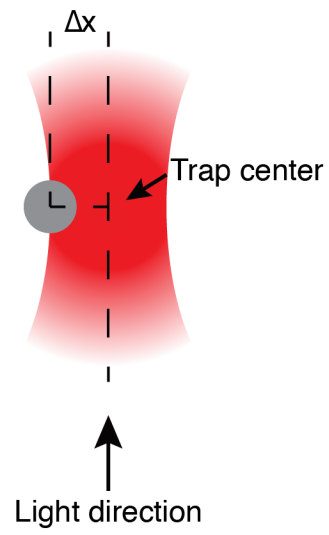


Figure 2.5: Schematic of an optical trap, where the colloidal particle is displaced Δx from the center of the optical trap.

2.2.2 Micropipette Aspiration

Micropipette aspiration is a technique employed to measure the mechanical properties of micrometric bodies, such as Liposomes, living cells, and tissues. It makes use of a micropipette to apply a suction pressure on the sample, and an optical microscope is used to quantify the sample deformation. Figure 2.6 shows the schematic of a typical microaspiration pipette setup. A pipette with a tip radius R_p , is connected to a water reservoir and applies a suction pressure ΔP on the specimen of interest. The pressure ΔP depends on the hydrostatic pressure and by the difference of height Δh between the pipette apex and reservoir water level, as:

$$\Delta P = \rho_{water} g \Delta h \quad (2.9)$$

where ρ_{water} is the water density (1 g/mL), g gravity acceleration. If there is a flow,

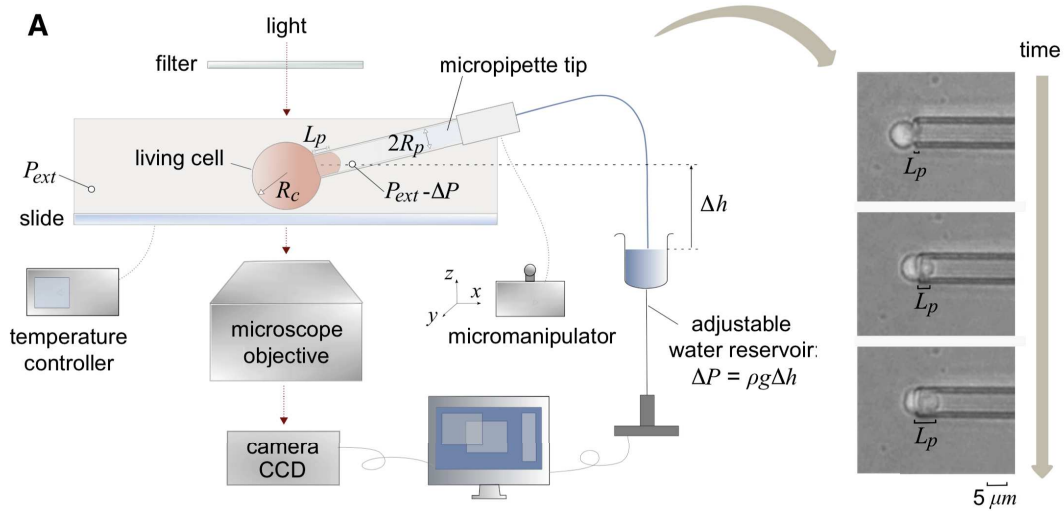


Figure 2.6: Schematic of an micropipette aspiration setup. Adapted from [114]

the pressure drop along the microcapillary must be taken into account [118], using the following equation:

$$\Delta P = \rho_{water} g \Delta h \left(1 - \frac{U}{U_f} \right) \quad (2.10)$$

where U is the velocity of the aspirated material, and U_f is the velocity for free flow. In order to probe biological samples, many models have been developed. The simplest model adopts continuum-modeling approaches. It was developed by Theret et al. [119],

without taking into account a direct link to subcellular components. This model provides one equation to compute the elastic modulus E of a sample by assuming a homogeneous incompressible linear-elastic half-space material:

$$\frac{\Delta P}{E} = \frac{2\pi}{3\phi_p} \frac{L_p}{R_p} \quad (2.11)$$

where L_p is the aspirated length (see Figure 2.6) and ϕ_p is a parameter that depends weakly on the thickness of the pipette wall, and the value $\phi_p \sim 2.1$ is typically used [114]. Micropipette aspiration is widely employed to evaluate interesting mechanical properties on biological samples, such as the Young's modulus E , Poisson rate ν , viscosity μ , diffusion coefficient [114]. With this technique, the spatial resolution depends on the correlated optical microscope employed, whereas the area that can be probed depends on the pipette radius size, typically higher than 1 μm . For this reason, the technique has a limited resolution for our objectives since we want to study biological membranes at the nanoscale.

2.2.3 Surface Force Apparatus

The Surface Force Apparatus (SFA) is a technique that quantifies the interaction force between two macroscopic and curved surfaces as a function of their separation distance. SFA can measure the absolute separation of the distance between molecules up to several hundred nanometers with an accuracy of 0.1 nm [115]. This separation between two interaction surfaces is determined directly by optical interferometry, typically, a Fabry-Perot interferometer [115]. J.N. Israelachvili established this technique in 1976, and it is currently capable of working in aqueous solutions such as KNO_3 [120]. SFA can directly measure long-range interaction forces, as a function of the distance between both surfaces, including van der Waals interactions[121], both repulsive and attractive forces, DLVO-type interaction, electrochemical surface forces [120, 122].

The figure 2.7 shows a schematic of the working principle of an SFA. Here, the samples are supported by two cleaved and atomically flat mica sheet surfaces (thickness $\sim 0.3\text{-}0.5 \mu\text{m}$), which are fixed to the surfaces of two crossed hemicylindrical and microscopic silica lenses (Figure 2.7(a) and (b)). The typical radii of these lenses are 1-2 cm. The mica

surface adjacent to the silica lens is coated with 50 nm silver film (reflective), which results in a resonant cavity for Fabry-Perot interferometry. The light transmitted by the interferometer consists of a series of interference fringes. Its wavelengths are determined by the thickness and refractive index of the various films between the two reflective silver surfaces. When a continuous white light is employed as a light source, the transmitted wavelength changes when the sample surfaces separation (D in Figure 2.7 (a)) changes. Finally, from those measured wavelength shifts, the distances D are determined within a resolution of 0.1 nm [115]. In the SFA, the separation D is controlled by a three-stage mechanism: an upper micro-driven rod, lower-driven rod, and a piezoelectric crystal, which are the coarse ($\sim 1\mu\text{ m}$), medium ($\sim 1\text{ nm}$), and fine distance controls ($< 1\text{ nm}$), respectively.

To measure the interaction forces between the two surfaces, one of the hemicylindrical

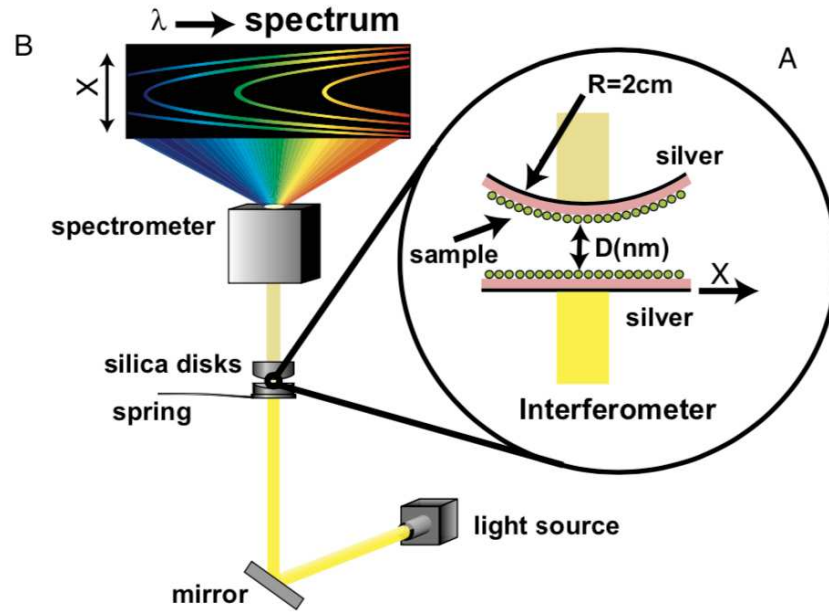


Figure 2.7: The Surface Force Apparatus. (a) samples in the SFA are supported on two hemicylindrical lenses oriented at right angles to each other. (b) Schematic diagram of the SPA working principle. Adapted from [115].

lenses is mounted at the end of a cantilever spring with a typical stiffness of $\sim 10^2\text{ N/m}$. Finally, the interaction forces are determined by a simple Hooke's law:

$$F_{int} = k_{eq}x \quad (2.12)$$

where F_{int} is the interaction force, k_{eq} the equivalent spring stiffness (lens-cantilever) and x the spring displacement. Clearly, the force resolution depends on cantilever stiffness. We have shown that SFA has many pros, but the main drawback for our purpose is that this technique cannot measure the properties at high lateral resolution since the surface employed has a radius of ~ 1 cm. The following technique notably improves this issue: in addition to the SFA force sensitivity capabilities, it can visualize the sample with nanometric lateral resolution.

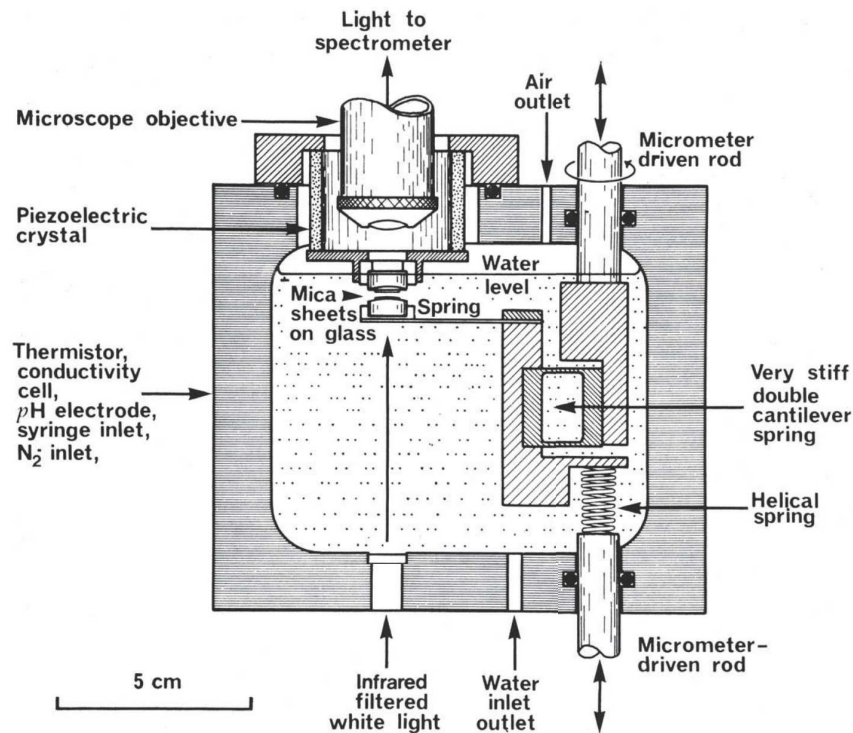


Figure 2.8: Schematic drawing of a Surface Force Apparatus. From [120].

2.2.4 Atomic Force Microscopy

Atomic Force Microscopy (AFM) is a very high-resolution Scanning Probe Microscopy (SPM) technique. AFM makes use of a micrometric cantilever with a nanometric tip to scan a sample and measure the sample topography at the nanoscale, as shown in Figure 2.9. It was invented in 1986 by G. Binnig, C. F. Quate and Ch. Gerber [123].

In order to better understand an AFM, we must describe the physics of the cantilever that is used to sense the surface and its properties. Physically, the AFM cantilever can

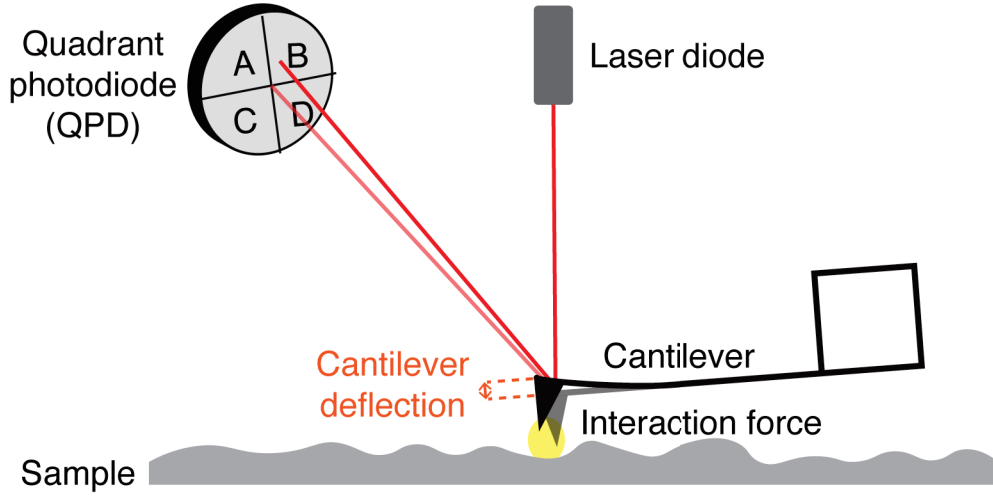


Figure 2.9: Schematics of an Atomic Force Microscope

be described as a single harmonic oscillator with a Point-Mass Model. In this model, the cantilever-tip system geometry is approximated by a spring with an effective mass (a fraction of the cantilever mass) located at the spring end, the AFM tip. In the presence of the tip-surface interaction forces F_{int} , the position of the tip is described by

$$m\ddot{z} + \gamma\dot{z} + kz = F_{int}(z) \quad (2.13)$$

where m is the effective cantilever mass, γ is linked to the viscosity of the medium surrounding the cantilever, and k is the cantilever spring constant. The equation 2.13 has different solutions depending on if the cantilever is excited or not (dynamic or static modes, respectively).

As mentioned in the previous chapter, this thesis aims to study biological samples, focusing on biological membranes. Biological samples are diverse, from nanoscale biomolecules such as lipid and proteins, up to the microscale when considering cells and tissues. AFM can reach tens of piconewtons (~ 10 pN) in force-resolution, 0.1 nm in vertical resolution, and a few Angstroms in lateral resolution.

We will now proceed to describe the main components of this instrument.

Cantilever

The AFM cantilever is the fundamental AFM component. An AFM cantilever is an elastic beam with a tip at the free end. This lever is used here for sensing the sample surface and its properties. Typically, this probe has a length of couple hundred microns, but more recently, fast cantilevers were developed for High-Speed AFM (HS-AFM) with a length of ten microns [82]. Commercially available AFM cantilevers are usually manufactured silicon, silicon nitride, and quartz-like materials. They are available in a wide range of shapes, spring constants, and resonant frequencies. In Figure 2.10 a cantilever and its tip are shown. Concerning the shape, they are rectangular or triangular, as shown in the Figure 2.11a) and b), respectively. The cantilever spring constant depends on its material and geometry. For a rectangular beam, the spring constant is given by

$$k = \frac{Ewt_c^3}{4(L-d)^3} \quad (2.14)$$

where E is the Young's modulus of the cantilever material, w and t_c are the cantilever width and thickness, respectively, L the length of the beam, d is the setback of the applied load from the cantilever free end. Another relevant parameter is the tip length h , spanning from the cantilever center until the end of the tip. h must be accurately chosen depending on the roughness of the studied sample. All dimensions are shown in Figure 2.12. The model of equation 2.14 is valid under the consideration that $w \ll L$, assuming that any bending effects of the beam along its width are negligible. Spring constant values of AFM cantilevers are typically in the range of 0.01 to 100 N/m.

Regarding the resonant frequency, it depends on the cantilever material, geometry, and also on the medium where the lever is immersed, such as liquid or air. For the same cantilever, the resonant frequencies in air and water, with low damping, are given by:

$$\omega_R^{air} = \sqrt{\frac{k}{m}} \quad (2.15)$$

$$\omega_R^{liq} = \sqrt{\frac{k}{m + m_{liq}}} \quad (2.16)$$

where ω_R^{air} and ω_R^{liq} are the angular resonant frequency in air and liquid, respectively, and m_{liq} is the liquid mass participating to the motion of the lever. As the equations 2.15 and 2.16 show, for the same cantilever, the resonant frequency is lower in a liquid than in air,

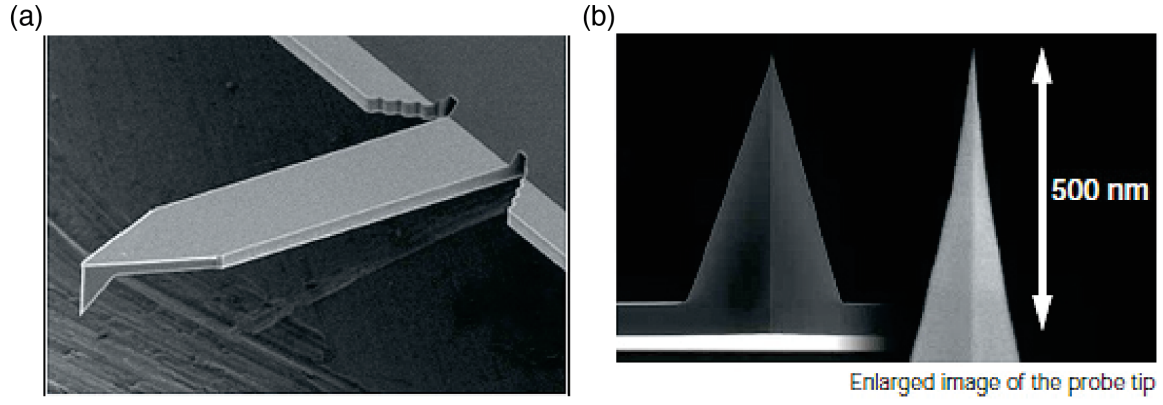


Figure 2.10: Scanning electron microscope images of an AFM cantilever. a) Cantilever, b) AFM tip. Adapted from [Olympus website](#).

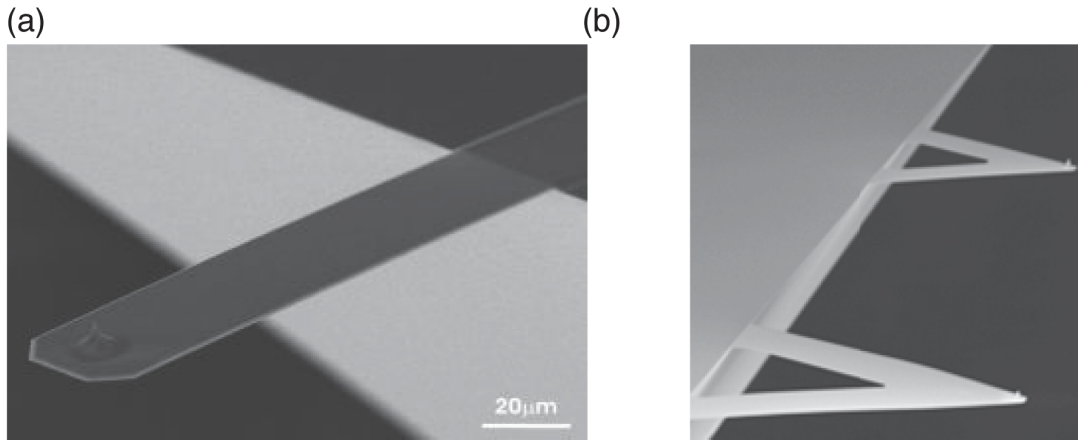


Figure 2.11: Scanning electron microscope images of AFM cantilever shapes. a) rectangular uniprobe™ [Nanosensors](#), b) triangular NSL from [Bruker](#).

typically

$$\frac{1}{3}\omega_R^{air} < \omega_R^{liq} < \frac{1}{2}\omega_R^{air} \quad (2.17)$$

AFM tips are available in a wide range of different shapes, including tips protruding at the end of the cantilever, pyramidal, conical and nano-spherical as shown in Figure 2.13 a), b) and c) respectively. Concerning the tip radius, the AFM tips are available from less than 2 nm up to tens of microns (colloidal probes). These characteristics allow for a wide variety of experimental indentation and microscopy schemes, i.e., from microspheres-tissue indentations to probing intra-molecular interactions between biomolecules[124].

In AFM, the lateral resolution depends on the effective interaction between the AFM tip and surface since the tip radius can be as small as 2 nm. It can probe the surface very locally. The tip aspect ratio has a defining role in determining the lateral resolu-

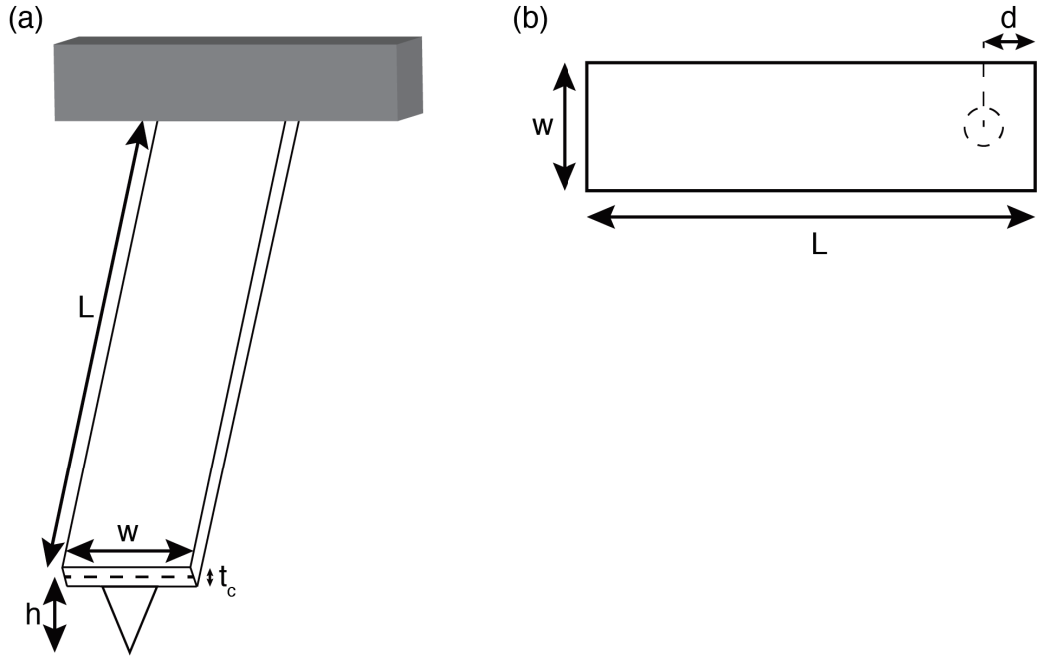


Figure 2.12: Schematics of a rectangular AFM cantilever.

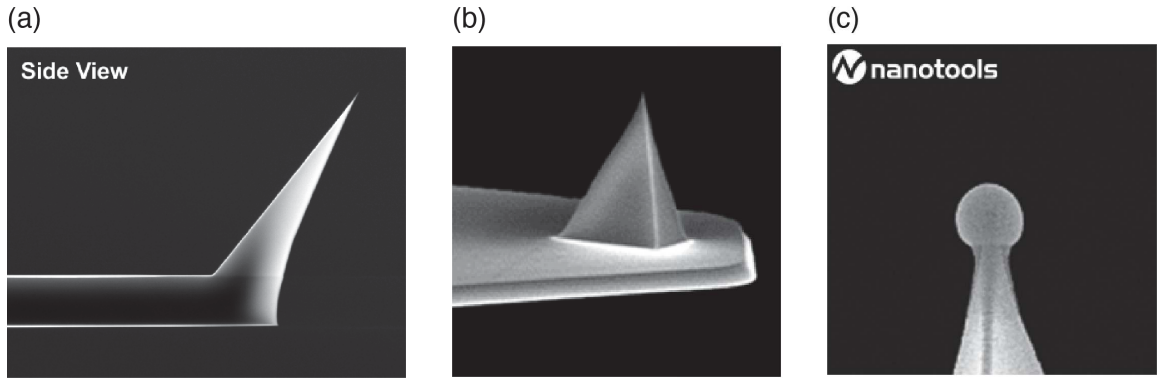


Figure 2.13: Scanning electron microscope images of AFM tips. a) ATEC-CONT from [Nanosensors](#), b) MSNL from [Bruker](#) and c) B20-FM from [Nanotools](#).

tion because it might compromise the lateral resolution when imaging surfaces with high roughness. During the last decades, several procedures have been developed to either reduce the tip radius and/or to get better aspect ratios [125], such as carbon nanotube AFM tips [126, 127]. The tip geometry might also be the source of several imaging artifacts, i.e., when the tip is asymmetrical, such as etched silicon. Choosing an appropriate combination of both AFM tip and cantilever is helpful in successfully image the target sample and achieving the highest resolution.

Detection system

One of the most widely used AFM detection systems is called optical beam deflection. It is composed of a laser and a photodetector, and it has the function of measuring and quantify the bending angle (deflection) of the AFM cantilever. A laser, typically a laser diode, is focused at the free end of the beam backside (where typically a reflective coating is deposited) and then reflected towards the photodetector, a position-sensitive photodiode array also called QPD. A QPD is a photodetector divided into four segments (see Figure 2.9): the reflected light needs to be aligned at the center of the QPD when the tip is far from the sample surface. The procedure is performed by maximizing the sum on the sensor, implying that a higher proportion of reflected photons is incident on the sensor. Mathematically the sum is described as

$$SUM = A + B + C + D \quad (2.18)$$

Where A , B , C , and D correspond to the current generated by the four QPD segments as described in Figure 2.9. In order to quantify both cantilever vertical deflection D_{ver} and lateral deflection D_{lat} as

$$D_{ver} = \frac{A + B - (C + D)}{SUM} \quad (2.19)$$

$$D_{lat} = \frac{A + C - (B + D)}{SUM} \quad (2.20)$$

The three signals are measured and expressed in Volts, and the system needs to be calibrated to convert D_{ver} , representing a deflection angle, into the vertical tip position (expressed in meters).

Scanners

AFM scanners are employed to vertically and laterally displace the sample in respect to the tip. They are typically made of piezoelectric materials, which can expand and contract when a voltage is applied, depending on both its polarity and intensity. Scanners are characterized by their sensitivity, which is the ratio of piezo movement per voltage

applied on the piezo, meaning how much the piezo material extends or contracts per applied voltage. However, the sensitivity is non-linear overscan size. Indeed, piezo scanners exhibit hysteresis between the forward and reverse scans. This issue can be corrected by adding a linear sensor to each stage to detect the real displacement of the piezo and, by applying a non-linear voltage to the piezo electrodes, the displacement can be controlled to be linear. The latter is known as a "closed-loop" AFM scanner, whereas, in the absence of this additional sensor, it is called an "open-loop" AFM scanner.

AFM can have two different stage configurations: sample stage or tip stage. In the sample stage, the tip is fixed in the XY-plane, and the sample moves under the AFM tip (Figure 2.14a)). In the tip stage, the sample is fixed while the AFM tip scans the surface (Figure 2.14b)). Additionally, the AFM has another relevant scanner, the Z-scanner (or

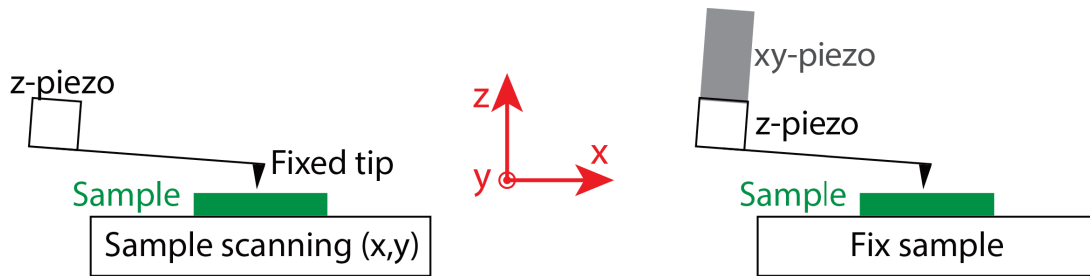


Figure 2.14: Schematic of a) sample stage and b) piezo stage AFM.

Z-piezo). It is in charge of moving the cantilever vertically, keeping constant amplitude in AFM-AM (see below) or deflection in static modes (see below) during XY Scan. Finally, an additional piezo, typically much smaller than Z-piezo, can drive the cantilever base at a defined frequency, such as the cantilever resonant frequency, as it is done in Dynamic mode AFM (described in the following subsection).

AFM control system

The AFM control system is in charge of the control of all instrument parts. The feedback control works both for dynamic and static AFM modes. In dynamic mode, the cantilever-tip system is excited at a single frequency by a piezo. The practical goal of the feedback loop is to keep the error signal (difference between the setpoint and desired tip deflection or tip oscillation amplitude) as small as possible. The error signal is treated in

the proportional-integral-differential (PID) system.

In dynamic mode, the cantilever deflection is measured by the QPD sensor and send to a lock-in amplifier, which processes the signal and returns a signal related to the oscillation amplitude and phase of the cantilever. The feedback loop maintains constant the amplitude while the tip is either scanned across the sample surface or kept still above a given surface region. The root mean square value of the oscillation signal measured in the QPD is kept constant in a process that involves the comparison between the instantaneous values of the amplitude A with respect to a reference value A_{SP} , called the setpoint amplitude, and the difference of both amplitudes ($A_{SP} - A_i$) is the error signal. The PID output sends a voltage signal to the piezo Z-scanner to either approach or withdraw the tip/sample in such a way as to minimize the error signal. The feedback loop set the upper limit for the maximum scanning speed of the microscope. Figure 2.15 shows the schematic of the feedback system described.

As mentioned, instead of keeping constant the oscillation amplitude in the case of static mode, the PID system keeps the static cantilever deflection constant during image acquisition.

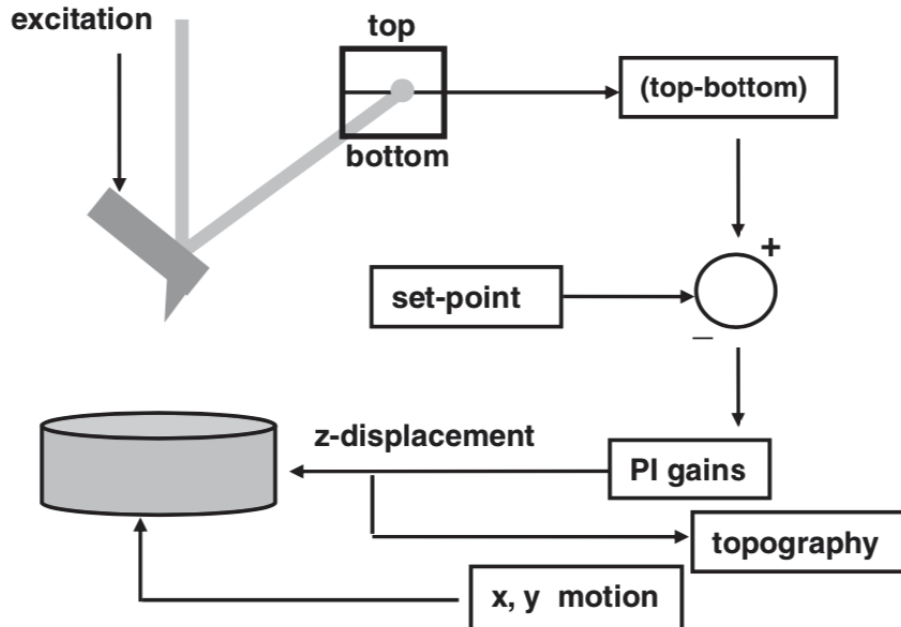


Figure 2.15: Simplified scheme of the feedback loop circuitry in amplitude modulation AFM. Adapted from [128].

2.2.4.1 AFM cantilever calibration

Quantitative AFM is crucial for a wide range of applications. For example, when performing topography measurements in contact mode, the knowledge of the lever stiffness allows control of the contact force, preventing possible damage of soft samples [129]. Applications, where high precision is desired require the AFM probe to be directly used as a force sensor. Using Hooke's law, the cantilever deflection can be converted into a force (only valid in the low deflection angle regime of the cantilever). When the cantilever deflection is acquired, the QPD is generated in a current converted into volts by a trans-impedance amplifier. Then, it must be converted into a force value. For this purpose, two calibrations have to be done: first, to determine the cantilever spring constant k and then the optical sensitivity converting the voltage at the output of the trans-impedance amplifier into a deflection angle, finally into a tip position in meters. Several calibrations methods have been proposed in the last decades. The most employed ones are the method to calibrate the *optical sensitivity* (detector calibration) and the *thermal method* and *Sader method* to calibrate the cantilever spring constant:

Optical sensitivity

As mentioned, using a trans-impedance amplifier, the current generated by the QPD four segments is converted into a voltage signal. However, we must quantify the cantilever deflection in length unity, and therefore a conversion factor is required. The Inverse optical lever sensitivity (*InvOLS*) calibration is based on the acquisition of a force-distance curve on a stiff sample, implying that the surface deformation upon tip-sample contact is negligible and assuming that the cantilever deflection is equal to the z-piezo displacement. The *InvOLS* is the scaling between the measured deflection voltage (D_{ver}) and the cantilever deflection Δz , as:

$$\text{InvOLS} \equiv \frac{\Delta z}{D_{ver}} \quad (2.21)$$

InvOLS is usually expressed in nm/V.

This value depends on the laser spot position along the cantilever axis, the cantilever

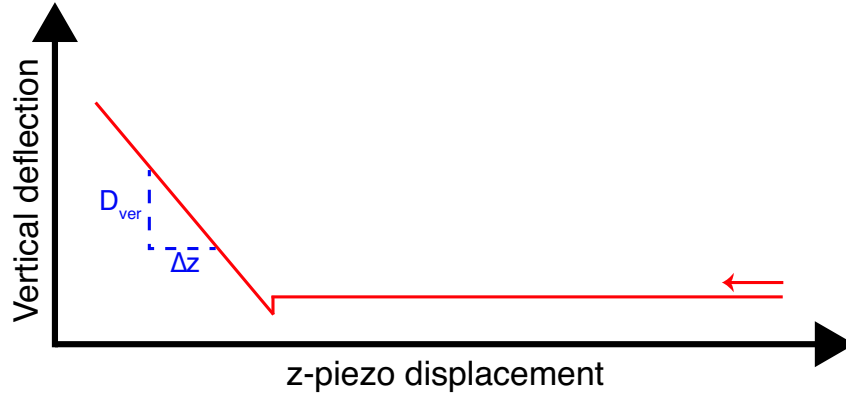


Figure 2.16: Operational scheme to acquire the *InvOLS* scaling factor to calibrate the cantilever deflection using an optical beam deflection system.

length, and the distance between the tip and the QPD. As a consequence, the sensitivity will depend on the cantilever length and the alignment procedure [128]. Additionally, this calibration depends on the refractive index of the medium surrounding the cantilever, such as air, water, or buffer. therefore, the calibration must be performed in the same medium, where the AFM measurements are carried out.

Thermal noise method

The thermal noise method relies on the fact that a harmonic oscillator in thermal equilibrium is mechanically vibrating due to thermal noise [130]. The Hamiltonian \hat{H} of a harmonic oscillator can be written as

$$\hat{H} = \frac{m\dot{z}^2}{2} + \frac{1}{2}kz^2 \quad (2.22)$$

Assuming that the harmonic oscillator is in thermal equilibrium with the environment, the equipartition theorem can be applied, obtaining the following relationship:

$$\frac{1}{2}k \langle z^2(\omega) \rangle = \frac{1}{2}k_B T \quad (2.23)$$

where $\langle z^2(\omega) \rangle$ is the mean square deflection of the cantilever due to thermal vibrations in all spectrum of frequencies, k_B is the Boltzmann's constant and T is the absolute temperature. Rewriting the equation 2.23, the spring constant of the cantilever k can be

expressed as

$$k = \frac{k_B T}{\langle z^2(\omega) \rangle} \quad (2.24)$$

The measurement of $\langle z^2(\omega) \rangle$ is therefore required over all frequencies. Butt and Jaschke [131] refined this method, demonstrating that the contribution of the first resonance to $\langle z^2(\omega) \rangle$ is 96 %. As a consequence, the measurement of PSD can be done just for the lowest eigenmode, and then, its dependence on the frequency is fitted with the dynamic response of a single-harmonic oscillator (a Lorentzian function), obtaining:

$$k_1 = \frac{4k_B T}{\omega_1 Q_1 A_1} \quad (2.25)$$

where k_1 is the cantilever spring constant of the first mode, Q_1 is the quality factor of the first mode and A_1 is the amplitude of the first mode. A relationship between the cantilever static and the first mode spring constant is derived by using the vibrational decomposition of the cantilever oscillations [128],

$$k = \frac{k_B T}{\langle z^2(\omega) \rangle} = \frac{12k_B T}{1.875^4 \langle z_1^2(\omega) \rangle} = 0.9707k_1 \quad (2.26)$$

showing that k and k_1 can be used as equivalents for tip calibrations.

Sader method

In the Sader method, the AFM cantilever is modeled considering the hydrodynamics of the fluid surrounding the lever, and the dissipation effects on the cantilever dynamics [132, 133]. In this method, the optical sensitivity calibration is not required. It has been developed to determine the spring constant k of a rectangular cantilever that is defined as [133]

$$k = 0.1906\rho_f w^2 L Q_f \Gamma_i(\omega_f) \omega_f^2 \quad (2.27)$$

Where ρ_f is the fluid density, w and L are the cantilever width and length, Q_f is the resonant quality factor of the lever immersed in the fluid, ω_f the cantilever resonant frequency in the fluid, and $\Gamma_i(\omega_f)$ is the imaginary component of the hydrodynamic function. The

$\Gamma(\omega_f)$ depends on the AFM cantilever geometry, and for a rectangular cross-section an analytic expression has been determined by Sader *et al.* [132]. ω_f and Q_f can be determined by fitting a simple harmonic oscillator model to the resonant spectrum of the cantilever. Lastly, since this method depends only on the cantilever plane-view dimensions, they are provided by the AFM cantilever manufacturer with good accuracy. Alternatively, they can be easily be determined with an optical microscope before mounting the cantilever or directly *in situ*.

Combined calibration strategies

Performing the previous calibrations in series, the AFM cantilever is calibrated both in optical sensitivity and spring constant k . The two most used strategies are the following:

1. Optical sensitivity + Thermal noise method: in this strategy, the optical sensitivity is employed to quantify the *InvOLS*, and the thermal noise to determine the cantilever stiffness k . The main disadvantage of this combination is that the optical sensitivity method requires mechanical contact between the AFM and a hard surface, and this procedure can induce tip damage and/or pollution.
2. Thermal noise method + Sader method: In this strategy, the equation 2.27 (Sader method) is used to evaluate the cantilever spring constant k , and after the thermal noise method is employed to obtain the *InvOLS* factor. In comparison with the previous one, the advantage of this method is that the cantilever is calibrated out of tip-sample mechanical contact, avoiding tip damage.

2.2.4.2 AFM operation modes

The AFM is a very versatile instrument that operates in several different modes for both imaging or force-distance curves. We will describe the most used AFM operational schemes, such as static and dynamic modes. All the following operational modes can work

in both air and liquid environments.

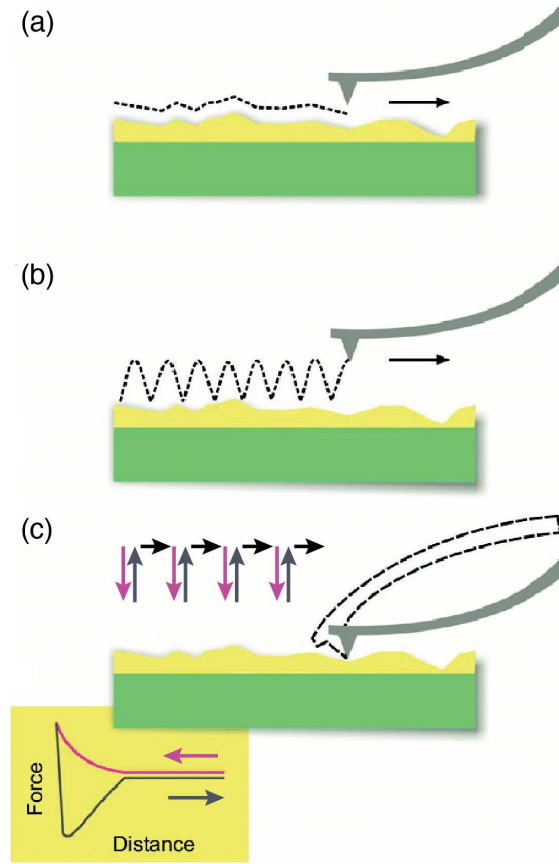


Figure 2.17: Schematics of different AFM modes. a) Contact mode, b) Dynamic mode and c) Fast force curves. Adapted from [134].

Contact imaging mode

Contact mode is the basis for all AFM modes. Here, the AFM probe is constantly in mechanical contact with the sample surface. By scanning the surface with the tip, since the AFM tip is close enough to the sample surface, any morphological variation within the sample induces a cantilever deflection. Using the AFM feedback loop to maintain the vertical deflection constant at a given force set-point, a sample topographical image can be generated, as shown in Figure 2.17a).

In contact mode, since the AFM cantilever is not excited at its resonance on the vertical z -axis ($\dot{z} = 0$ and $\ddot{z} = 0$, no speed and acceleration of the cantilever in the axial direction, respectively), equation 2.13 can be simplified as the Hook's law:

$$F_{int}(z) = k\Delta z \quad (2.28)$$

Where $F_{int}(z)$ is the force on the cantilever, k the cantilever spring constant, and Δz the cantilever deflection.

In this mode, the force set-point corresponds to the force permanently applied by the cantilever to the sample. This force can induce sample deformation and/or damage. Therefore, it is crucial to minimize force set-point when measuring soft biological specimens.

Dynamic imaging mode

In dynamic mode, a harmonic stimulus is imposed to the AFM tip exerting an external force $F_{ext}(t) = F_0 e^{i\omega t}$ at the cantilever base, where ω is the frequency of the stimulus. Rewriting the equation 2.13 for the Point-Mass model with the external force, the equation becomes:

$$m\ddot{z} + \gamma\dot{z} + kz = F_{int}(z) + F_0 e^{i\omega t} \quad (2.29)$$

If the cantilever is far from the surface, the tip-sample interactions are negligible, therefore, we can assume $F_{int} = 0$. Since the induced external force is harmonic, we look for a harmonic solution with the form $z(t) = z_0 e^{i\omega t}$. Introducing $z(t)$ into the equation 2.29, this becomes as,

$$(-m\omega^2 + i\gamma\omega + k) z_0 = F_0 \quad (2.30)$$

Solving for z_0 , we obtain:

$$z_0 = \frac{\frac{F_0}{m}}{i\frac{\omega}{m}\gamma + \frac{k}{m} - \omega^2} \quad (2.31)$$

Inserting the equation 2.15 ($\omega_R = \sqrt{\frac{k}{m}}$) into the last equation, the forced harmonic oscillator amplitude A and phase ϕ are the following:

$$A(\omega) = |z_0(\omega)| = \frac{\frac{F_0}{m}}{\sqrt{\frac{\omega^2 \gamma^2}{m^2} + (\omega_R^2 - \omega^2)^2}} \quad (2.32)$$

$$\phi(\omega) = \arctan\left(\frac{\gamma\omega}{m(\omega_R^2 - \omega^2)}\right) \quad (2.33)$$

The amplitude $A(\omega)$ and phase $\phi(\omega)$ of the forced harmonic oscillator are shown in

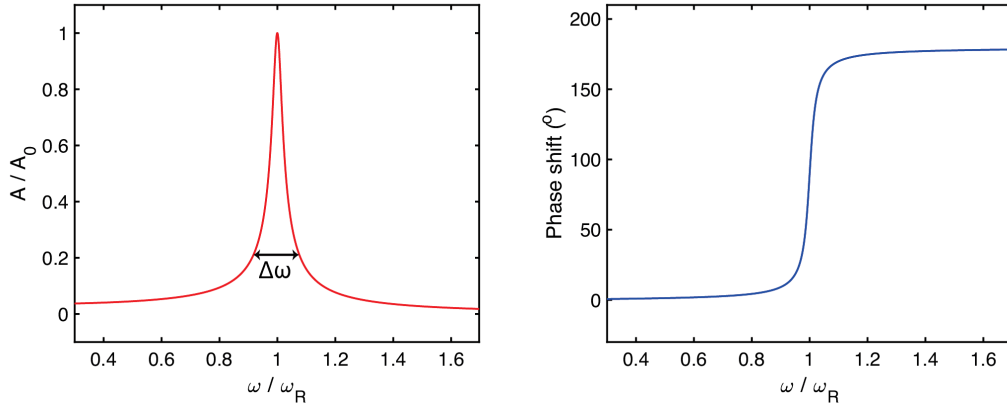


Figure 2.18: Dependence of the amplitude and the phase shift as a function of the excitation frequency for a forced harmonic oscillator with damping γ . Adapted from [135].

Figure 2.18. where Q can be expressed as :

$$Q = \frac{\omega_R}{\Delta\omega} \quad (2.34)$$

When the tip and sample are close enough, interaction forces F_{int} are not anymore negligible. These interaction forces change the oscillation of the cantilever in both amplitude $A(z)$ and phase $\phi(z)$ as shown in Figure 2.19, adapted from [135]. In this figure, the interaction forces are negligible at tip-sample distances larger than 28 nm because amplitude and phase do not vary with the tip-sample distance. When the tip is at a sample distance inferior to 28 nm, the interaction forces are not negligible, as the variation of amplitude and phase clearly shows it. In the case of the amplitude, when the AFM tip approaches the surface, the amplitude decreases due to the presence of these interaction forces.

Dynamic mode AFM has two main variables, Amplitude Modulation AFM (AM-AFM) and Frequency Modulation AFM (FM-AFM). In AM-AFM, the excitation frequency is usually set at the first resonance frequency of the cantilever, and the response amplitude is adjusted to be constant by a feedback loop [136], as shown in Figure 2.17b) and described

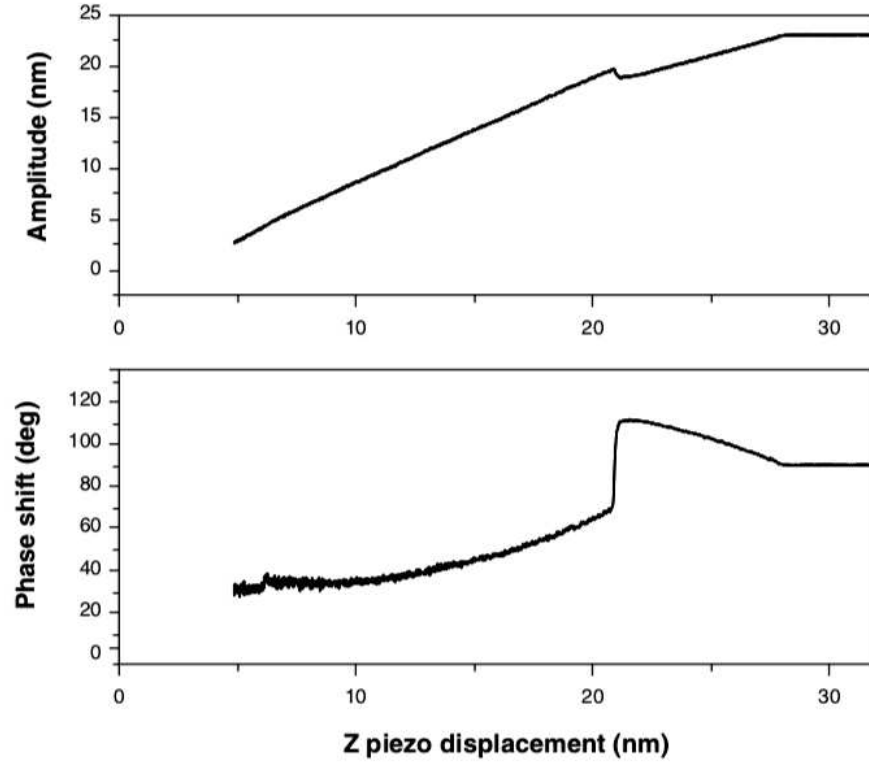


Figure 2.19: Amplitude and phase distance curves obtained in air with a silicon tip on a mica surface. Adapted from [135].

in the previous section (Figure 2.15).

The main advantage of this operation mode (AFM-AM) is that the AFM cantilever is in intermittent contact with the sample. It results in minor damage for the sample, especially when it is soft, due to decreased friction present when the tip is in contact with the sample.

AFM-Force Spectroscopy

AFM-Force Spectroscopy (AFM-FS) is a technique based on the AFM static mode. The AFM tip is approached to the surface at constant approaching speed v . The cantilever deflection is measured as a function of the tip-sample distance. At large distances, tip-sample interaction forces are negligible. At a short distance, the tip can be used as an indenter to induce a local sample deformation up to the desired force (force threshold). The operational scheme is described in Figure 2.20:

(a) the non-contact regime is shown.

(b) jump to contact, the jump shown here is due to attractive forces bending the cantilever towards the sample in cases where the force gradient is higher than the cantilever spring constant.

(c) local compression of the sample by the AFM tip. It is the repulsive interaction forces regime. Interesting samples' mechanical properties can be measured, such as Young's modulus.

(d) once the threshold force is established, the AFM tip is retracted from the surface. In this regime, adhesion and capillary forces dominate the interactions. Often the tip remains in contact with the sample due to tip-sample adhesion forces. In this case, the cantilever is deflected downwards. At this stage, interesting sample properties can be measured, such as adhesion tip-sample forces, unbinding processes, and SLBs pulling tubes [59].

(e) the AFM tip is retracted far away from the surface.

In addition to the sample mechanical properties, this mode can be used to quantify

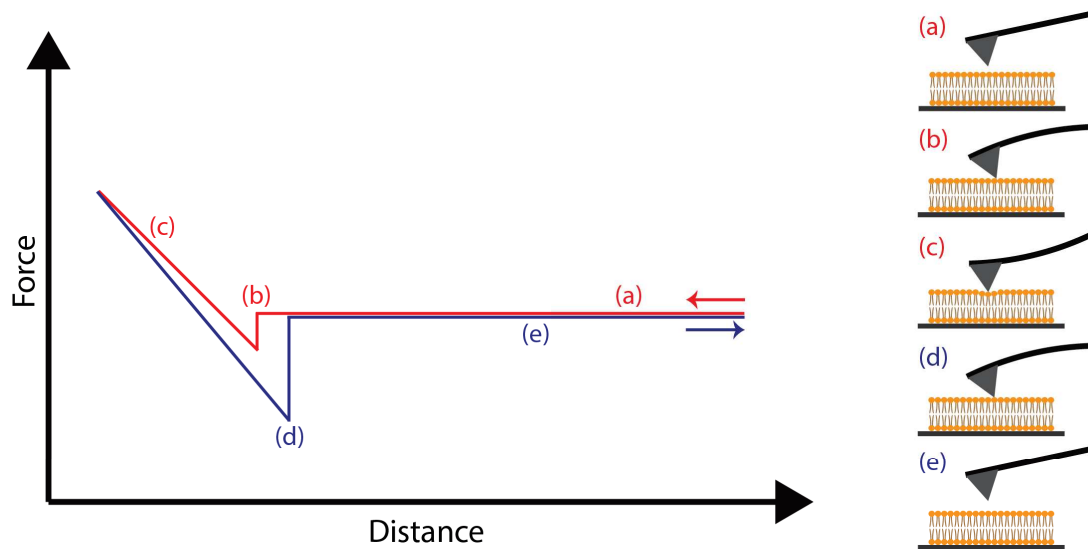


Figure 2.20: Schematic representation of a force-distance curve using AFM-FS, showing the different steps: a) approaching, b) jump to contact (attractive interaction forces) c) compression of the sample (repulsive contact interaction forces), d) tip-sample adhesion and capillarity forces e) retracting. The red line corresponds to the approach trace and the blue line to the retraction trace.

distance-dependent sample properties as Van der Waals interaction, surface charge properties as double-layer interaction, protein unfolding, and stretching of molecules between tip and surfaces. A critical remark: force-distance curves are more sensitive when the

cantilever spring constant roughly matches the stiffness of the tip-sample contact.

AFM-Dynamic Force Spectroscopy

AFM-FS has evolved in the AFM-Dynamic Force Spectroscopy (AFM-DFS). In this technique, the measurements are performed with the same procedure as in AFM-FS, but different sets of data are acquired at variable loading rates v (the approach-retract speed between tip and sample). AFM-DFS is used to characterize the dynamic response of a specimen within different loading rates v , such as unbinding forces in ligand-receptor bonds [137, 138, 139] as shown in Figure 2.21. Also, SLBs rupture forces depend on the loading rate v [140, 141], as will be discussed in the following sections of the chapter.

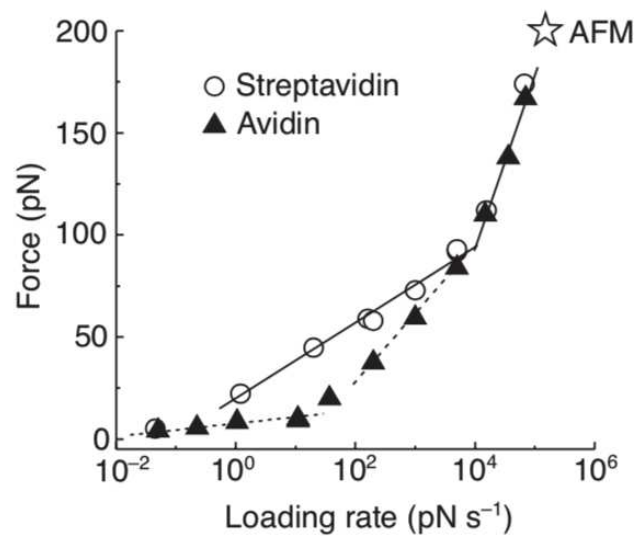


Figure 2.21: Biding force vs. loading rate. Dynamic strength spectra for biotin-streptavidin (circles) and biotin-avidin (triangles) bonds. Adapted from [139].

Fast force curves mode

Fast force curves mode is a static and easy imaging mode where the tip is approached and retracted from the sample surface as in AFM-FS. It is based on acquiring force-distance

curves in each pixel of the AFM image, as shown in Figure 2.17c) (a force-distance curve is shown in the inset). Using the approach force curve, the tip-sample distance is evaluated at the position of the maximal force reached, and if this process is applied to each pixel, the sample topography can be inferred. The main advantage of this operation mode is the ability to generate simultaneously a topographical image and mechanical properties images (including elasticity, adhesion, and any other properties that can be generated from a force-distance curve). This operation mode is a "below-resonance" (quasi-static) intermittent contact method. Therefore, the sample damage is reduced, and it is suited to study very soft samples such as cells and biological membranes.

This method has been developed around 2010 and has several names depending on the AFM company: i.e., it is called Quantitative-Imaging (QI) by JPK (Berlin, Germany) and PeakForce Quantitative Nanoscale Mechanical (PeakForce QNM) by Bruker (Santa Barbara, CA). The main difference between the different imaging modes relies in the fact that in QI mode, the tip-sample distance is modulated by a triangle wave whereas in PeakForceQNM is modulated by a sinusoidal wave. Additionally, in QI any approach-retract cycle frequency can be selected by the AFM user, whereas in PeakForceQNM frequencies are limited to a discrete number of options (up to 8 kHz).

2.2.4.3 Guiding rules for AFM imaging

As shown here, the lateral resolution in AFM depends on several parameters: guiding rules were proposed by Professor Ricardo García [125] to simplify the experimental task of achieving high-resolution images. They are the followings:

1. The instrumental noise should be smaller than the aimed resolution.
2. In general, the lateral resolution cannot be smaller than the size of the tip apex. However, in some cases, the AFM lateral resolution can be smaller than the tip size due to tip imperfection and roughness.
3. The decay length of the tip-surface interaction should be smaller than the tip apex.

4. Imaging isolated three-dimensional objects imposes limits on the lateral resolution.
5. The adhesion energy should be minimized. This is usually achieved by using sharp tips or biological samples, inserting a buffer with a salt concentration.
6. The applied force should be as small as possible.
7. Under identical conditions (tip radius and applied force), the stiffer the sample, the better the lateral resolution.

Having considered the different techniques that can probe the mechanics of biological membranes, we decided to use AFM for probing the mechanical properties of cellular membranes because this technique can work under physiological conditions with both *in-vitro* biomimetic model membranes or in cells. Additionally, AFM has the peculiarity to probe very local membrane mechanics, which is advantageous since membranes are heterogeneous at the nanoscale.

Being interested in the mechanics of biological membranes, we have mainly employed AFM-FS to investigate the mechanics of model membranes, as discussed in the following section.

2.3 Rupture force measurements

With the exception of the lipid tube pulling case, in all AFM-FS experiments, the radius of the AFM tip used as indenter plays a significant role. Therefore, the knowledge of the AFM tip radius is essential to properly define the force and indentation length range of the AFM-FS curve to be used to accurately evaluate the mechanical properties of the sample, such as E . Indeed, the maximal force and, consequently, the indentation length to be considered to properly evaluate E , avoiding substrate contributions, will change with the indenter size. If higher forces are applied during the indentation cycle, membrane rupture can be achieved [141, 142] as shown in Figure 2.22. This membrane's rupture is observed as a jump in the force-distance curve and can be interpreted as a penetration of the AFM tip through the membrane film, as shown in Figure. 2.22d).

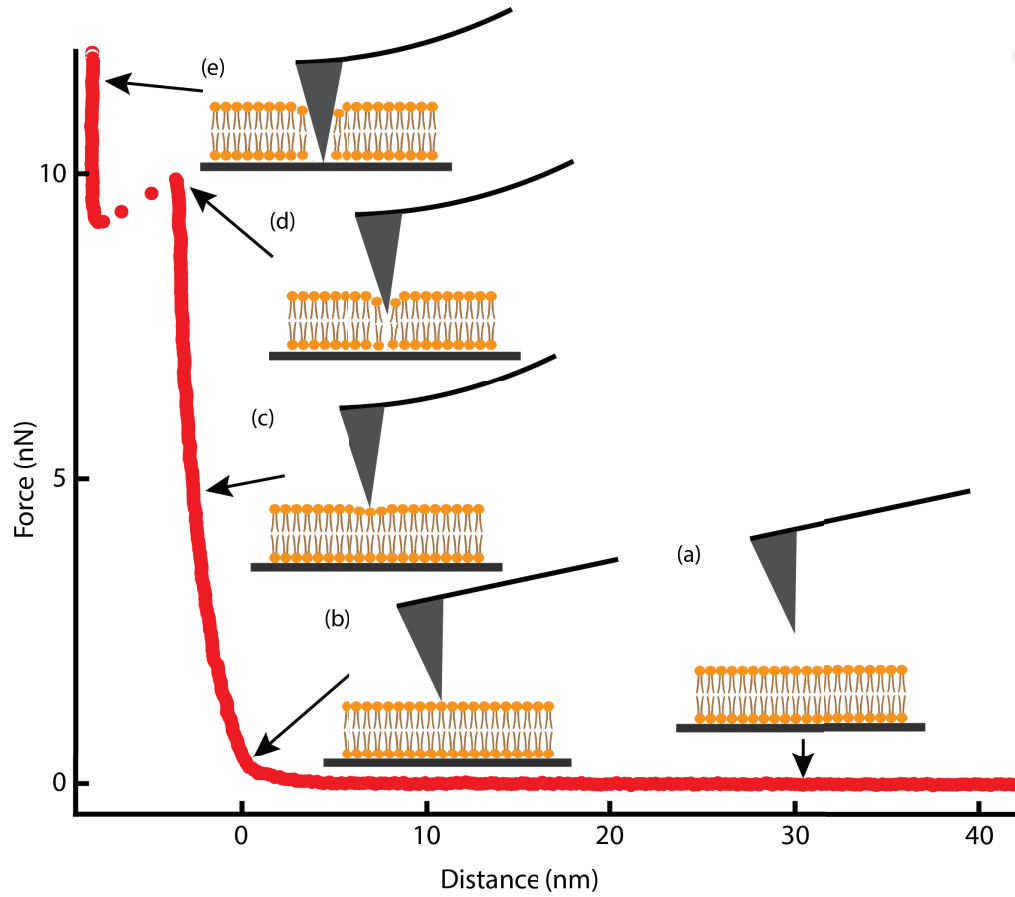


Figure 2.22: Typical approach force-distance curve of the SLB indentation process using AFM-FS, showing the different steps: a) approaching, b) first tip-sample contact (contact point), c) vertical compression of the SLB, d) SLB's rupture point, and e) tip-rigid substrate interaction. The membrane rupture's scheme is pictorially presented in the insets.

The rupture process of thin film has been extensively studied because of its importance for both natural and industrial processes such as the rupture of lubricant films, poration of biological membranes, where several mathematical models have been proposed and successfully applied to describe these processes. However, a model for the rupture of solid-supported thin films by an AFM tip was not reported until 2002, when Butt *et al.* [143, 144, 145] proposed a discrete molecular model capable of predicting the threshold rupture force F_B as follows

$$F_B = F_T \ln \left(\frac{0.693vK}{k_0 F_T} + 1 \right), \quad (2.35)$$

with F_T the thermal force

$$F_T = \frac{2\pi h R k_B T}{\alpha V}, \quad (2.36)$$

where v is the loading rate (approach speed of the AFM tip), K is the cantilever spring constant, k_0 is the probability of observing a film rupture due to thermal fluctuation, and h is the membrane thickness. V is defined as the activation volume occupied by the critical number of lipid molecules that can escape from the mechanical contact with the tip during the indentation, therefore, triggering the starting point of the hole formation within the membrane. As a consequence, the equation (2.35) predicts the rupture force F_B to increase with the AFM tip radius R .

In the following sections, we will show the model's efficiency in predicting the rupture force of the liquid phase and gel phase model membranes as a function of different AFM tip radii.

2.4 Experimental Methods

2.4.1 Sample preparation

DOPC and DPPC were individually dissolved in a chloroform-methanol (2:1) solution to a final concentration of 10 mM each. 10 μ L of each phospholipid solution were mixed, poured in a glass vial and evaporated to dryness under nitrogen flux for 2 hours to form a thin film on the tube walls. Afterwards, the dried phospholipid film was hydrated with 1 mL of DPBS buffer solution, previously heated at 70 °C, subjected to three minutes

vortex cycle and finally extruded for 15 passages with 0.1 μm membrane filter (Whatman International). The final solution was immediately used to prepare SLBs by vesicles fusion method: 50 μL of lipids final solution were deposited onto freshly cleaved mica disks (9.5 mm diameter), previously glued on top of larger Teflon disks that were in turn placed onto metallic disks. Disks were incubated for 30 minutes at 70 $^{\circ}\text{C}$ in an oven. In order to prevent the evaporation of the solution, disks were kept inside a petri dish placed in a larger petri filled with water, ensuring the necessary humidity level during incubation. Afterwards, disks were incubated at room temperature for 10 minutes before being carefully rinsed ten times with buffer solution in order to remove intact lipid vesicles. Membranes were kept overnight in buffer and protected from light exposure at room temperature. AFM measurements were carried out 24 hours after membrane preparation.

2.4.2 AFM imaging and Force Spectroscopy

AFM images and AFM-FS measurements were performed using a JPK NanoWizard 4 AFM (Berlin, Germany) using the following cantilevers: V-shaped Si_3N_4 cantilevers MSNL-D, MSCT-E and MLCT-Bio-DC-F from Bruker (Bruker AFM Probes, Camarillo, CA) and spherical-shaped carbon AFM tips mounted on rectangular cantilevers, Biosphere B20-CONT, B50-FM and B100-FM purchased from Nanotools GmbH (München, Germany). For each cantilever, the optical lever sensitivity was calibrated, acquiring a force curve on a rigid mica substrate (nm/V), whereas the spring constant was calibrated using the thermal noise method [146]. Both calibrations were performed in DPBS buffer at the end of the AFM-FS experiments to preserve the AFM tip radius from possible damage that can occur during the acquisition of the force curve on rigid mica.

AFM-FS curves were recorded by approaching the tip to the membranes at a constant loading rate of 1 $\mu\text{m}/\text{s}$ with a sampling frequency of 7 kHz at room temperature. For dynamic force spectroscopy (AFM-DFS) experiments, the loading rate was varied between 0.5 $\mu\text{m}/\text{s}$ and 50 $\mu\text{m}/\text{s}$, and MSCT-F cantilevers were used.

Force *versus* distance curves were acquired using a grid of 15×15 , 20×20 or 25×25 points (Force-Volume experiments) over regions ranging from $25 \times 25 \mu\text{m}^2$ to $80 \times 80 \mu\text{m}^2$ depending on tip radius size. Once AFM-FS data were recorded, all regions were imaged

in contact or quantitative-imaging (QI) modes. We acquired AFM topographical images at the end of the Force-Volume experiments to protect the AFM tip from contamination and damage that can occur during image acquisition. To ensure an accurate evaluation of the rupture force and Young's modulus and avoid data collected in the presence of tip damage (i. e. resulting in a different tip radius), we have monitored the increase of the rupture force measured with the same probe for each experimental session. Data showing an increase of the rupture force during acquisition were discarded.

2.4.3 Data Analysis

Rupture forces and Young's modulus evaluations from AFM-FS curves were obtained with custom-made MATLAB and Python programs.

Rupture force:

We developed an algorithm to properly determine the corresponding rupture force F_B for each force-distance curve acquired. This algorithm works as follows (Figure 2.23):

- First, the force curve is low-pass filtered (Figure 2.23a).
- The algorithm performs a first numerical derivative (Figure 2.23b). A threshold, the green dashed line, is used to discard non-relevant values, and the local minimum of the derivative is identified (eventually the maximum, if data orientation is inverse).
- The minimum of the derivative corresponds to a position in the force curve that is represented by a red dot in Figure 2.23c. A region defined by 20 to 30 data points centered in the red dot is then considered: it is shown in Figure 2.23d with two vertical green dashed lines.
- The maximal local force in the region is identified and corresponds to the rupture force F_B (red dot in Figure 2.23d).

With the AFM-FS curve, we can correlate each curve to a specific pixel and create a Force map (Figure 2.24d) that can be correlated with a topography AFM image (Figure 2.24c)

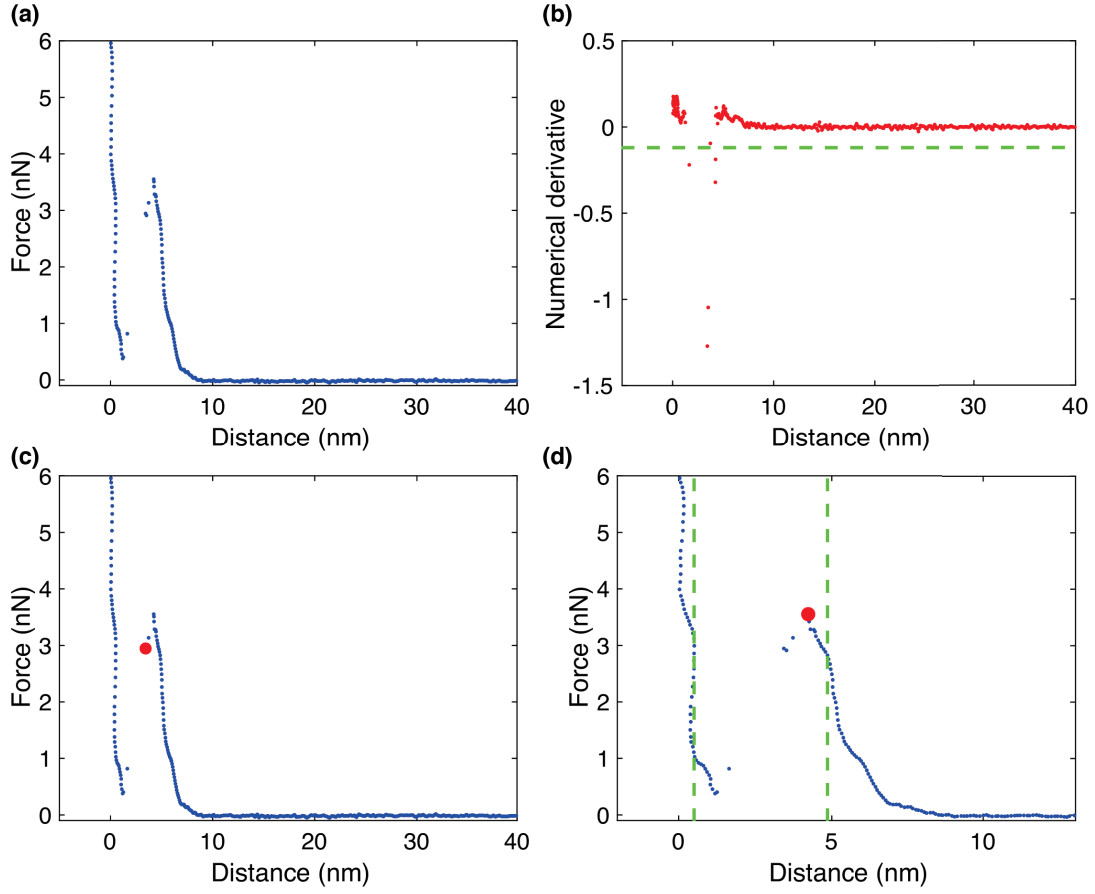


Figure 2.23: Algorithm developed to evaluate rupture forces from FS-AFM data. (a) Low-pass filtered force curve. (b) Numerical first derivative of (a). (c) Position of the minimum of (b) in the force curve, represented by a red dot. (d) The local maximum of the force curve, corresponding to the breaking force F_B , is evaluated over a region (green dashed lines) centered in the position of the minimum of the numerical derivative.

of the same region of interest. Therefore, we can associate each rupture force F_B to the corresponding lipid enriched domain visible from the AFM image.

For each AFM-FS experimental session, we built histograms reporting the F_B distribution for both fluid and gel phase membranes. From each histogram, we evaluated the average F_B . Joining data from different experimental sessions, we averaged all mean F_B values in a unique F_B , and we evaluated its standard deviation for each membrane phase and AFM tip radius experimental conditions.

Young's modulus:

AFM-FS experiments were performed on DOPC:DPPC (1:1) SLBs at a loading rate

of $v = 1 \text{ } \mu\text{m/s}$ using B20-CONT cantilevers with a tip radius of 20 nm and B50-FM cantilevers with a tip radius of 50 nm (both purchased from Nanotools). The membrane Young's modulus was evaluated with a numerical fit of the indentation cycles using the Hertz model (2.37b). The contact point between tip and membrane was determined assuming the presence of 2.7 nm of water layers plus 3.6 and 4.6 nm as DOPC and DPPC thickness, respectively [52].

The total thickness was added to the absolute position of the mica substrate, evaluated from the position of mechanical contact between tip and mica. Our data show the presence of the Electric Double-Layer (DL) interaction in the tip-membrane non-contact part of the curve, resulting in non-negligible forces of a few hundreds of pN once the contact is established. We took the DL effect into account, modeling the tip as a sphere near a flat surface [147] (Equation 2.37a). As a consequence, we have fitted the AFM-FS force *versus* distance curves independently with two different interactions as follows:

$$F_{DL}(z) = \frac{RF_Z}{\lambda_D} e^{-z/\lambda_D}, \quad \text{for } 0.1 \text{ nm} \leq z \leq 10 \text{ nm} \quad (2.37a)$$

$$F_H(z) = \frac{4}{3} \frac{E}{1-\nu^2} \sqrt{R} (-z)^{\frac{3}{2}} + F_0, \quad \text{for } -\delta_{max} \leq z \leq 0 \text{ nm} \quad (2.37b)$$

where z is the tip-membrane distance, λ_D is the Debye length, R is the tip radius, F_Z is an interaction constant with unity of force, E is Young's modulus, F_0 is the interaction force at the contact point between tip and membrane and δ_{max} the maximal indentation of the SBLs. ν is assumed as 0.5 (meaning a perfectly elastic uncompressed material), data were fitted with the Hertz model until a maximal indentation δ_{max} of 1.5 nm for DOPC and 1 nm for DPPC. DL fit was limited to tip-membrane distances higher than 1 Å to avoid taking into account non-ubiquitous short-range Van der Waals (VdW) attractive interactions (\approx to 10–20 pN, at the limit of our instrumental sensitivity). Concluding, for Equation 2.37a, we left F_Z and λ_D as free parameters, whereas for Equation 2.37b, only E was left as a free parameter.

2.5 Results

2.5.1 Rupture of Supported Lipid Bilayers

As previously mentioned, the AFM tip radius influences the measurements of the membrane mechanical properties. For that, we focus here on the influence of the AFM tip radius when measuring membrane rupture in the case of both fluid-phase and gel-phase SLBs.

Acquiring AFM-FS curves for both DOPC and DPPC as was described in the Experimental Method section, we determined the rupture force (F_B) for both DOPC and DPPC for different tips radii and tip chemical compositions. Typical force-distance curves recorded in a single grid with an MSCT cantilever with a tip radius of 10 nm at a loading rate of $v = 1 \mu\text{m/s}$ are reported in Figure 2.24a: we observe two different rupture force (F_B) regimes, a lower one for DOPC domains (blue curves) and a higher one for DPPC-enriched domains (red curves).

In our study for the case of DOPC enriched domains, we show the presence of two tip radii regimes: when the size of the tip ($\approx 1\text{--}2 \text{ nm}$) is in the range of the area occupied by a few lipid molecules, the tip can penetrate through the membrane encountering low resistance, here referred as a puncture mechanism. We interpret the latter case as an in-plane lateral perturbation of few molecules surrounding the AFM tip in a non-compressive regime. Finally, we show that larger tip radii ($> 2 \text{ nm}$) indentation always show a vertical lipid compression followed by membrane rupture, confirming experimentally the discrete molecular model introduced by Butt and Franz where the activation volume V is observed to be constant and independent of the tip radius [143]. In the DOPC case (Figure 2.25a and b), a vertical compression of the membrane is observed with the 10 nm tip (blue curve) while the 2 nm tip indentation (red curve) suggests a different physical mechanism is occurring (Figure 2.25d). Both AFM tips vertically compress the DPPC-enriched domains.

For better clarity, Figures 2.26b and c show indentation cycles performed with

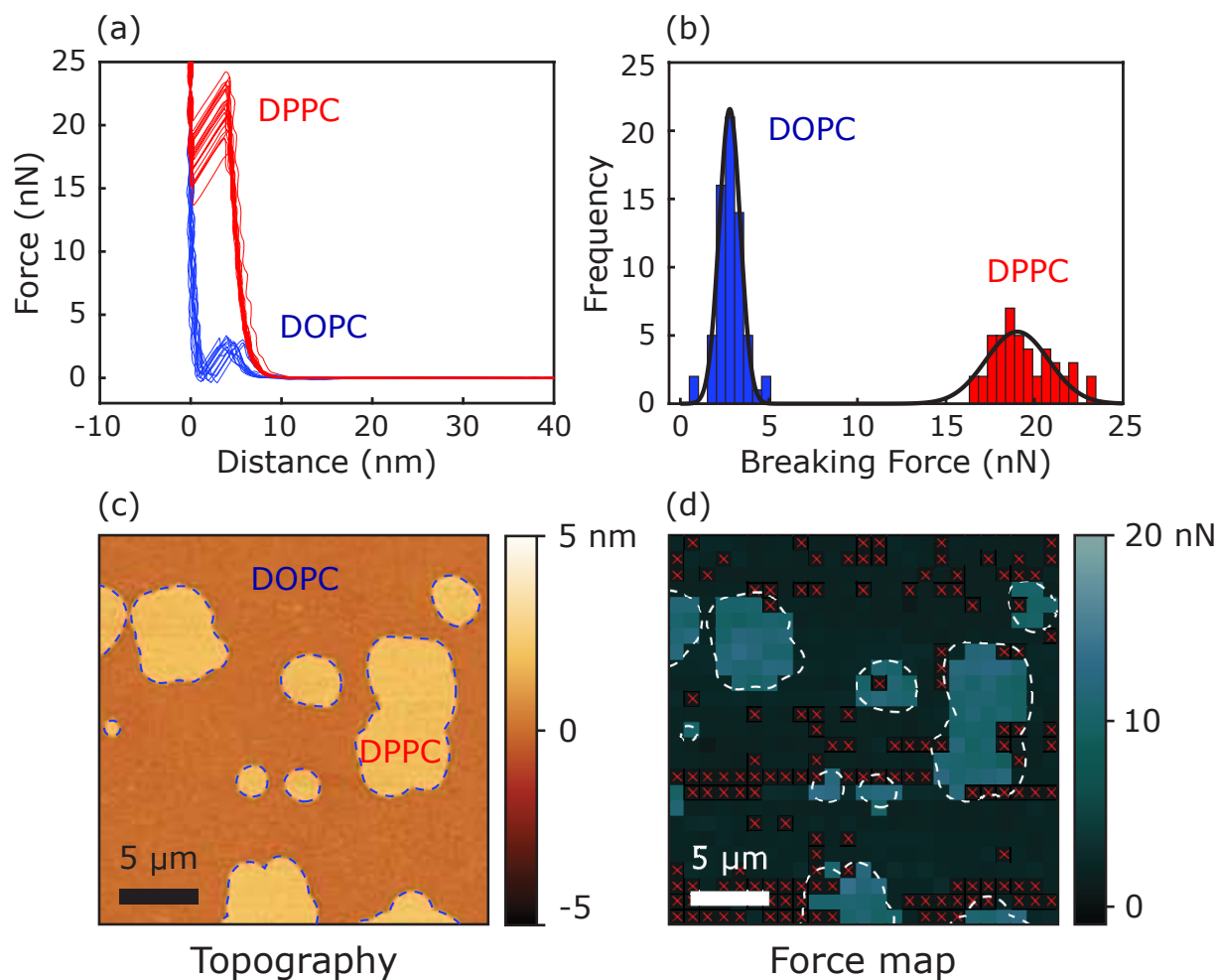


Figure 2.24: Force-Volume experiment on DOPC:DPPE (1:1) SLBs on mica in DPBS buffer. (a) Force *versus* tip-sample distance curves (blue, DOPC domains; red, DPPE domains) recorded with a tip with radius of 10 nm at a loading rate of $v = 1 \mu\text{m/s}$ over a region of interest of $25 \times 25 \mu\text{m}^2$. (b) Rupture force F_B distributions, (c) topographical image showing both DOPC- and DPPE-enriched domains obtained in QI AFM mode. DPPE domains are characterized by a higher thickness compared to DOPC domains. (d) F_B XY distribution map that well correlates with (c). Red crosses highlight the discarded curves. The dashed-line in (c) and (d) indicates the boundary between the DOPC and DPPE domains.

carbon probes with dashed lines and rupture force obtained with silicon and silicon nitride probes with continuous lines. Figure 2.27 presents all values for the rupture force observed on both DOPC and DPPE enriched domains as a function of the indenter radius. In agreement with previous data [144], we observe a variation of F_B with the tip chemical composition: this is evident comparing F_B values obtained with 20 nm radius Si_3N_4 and

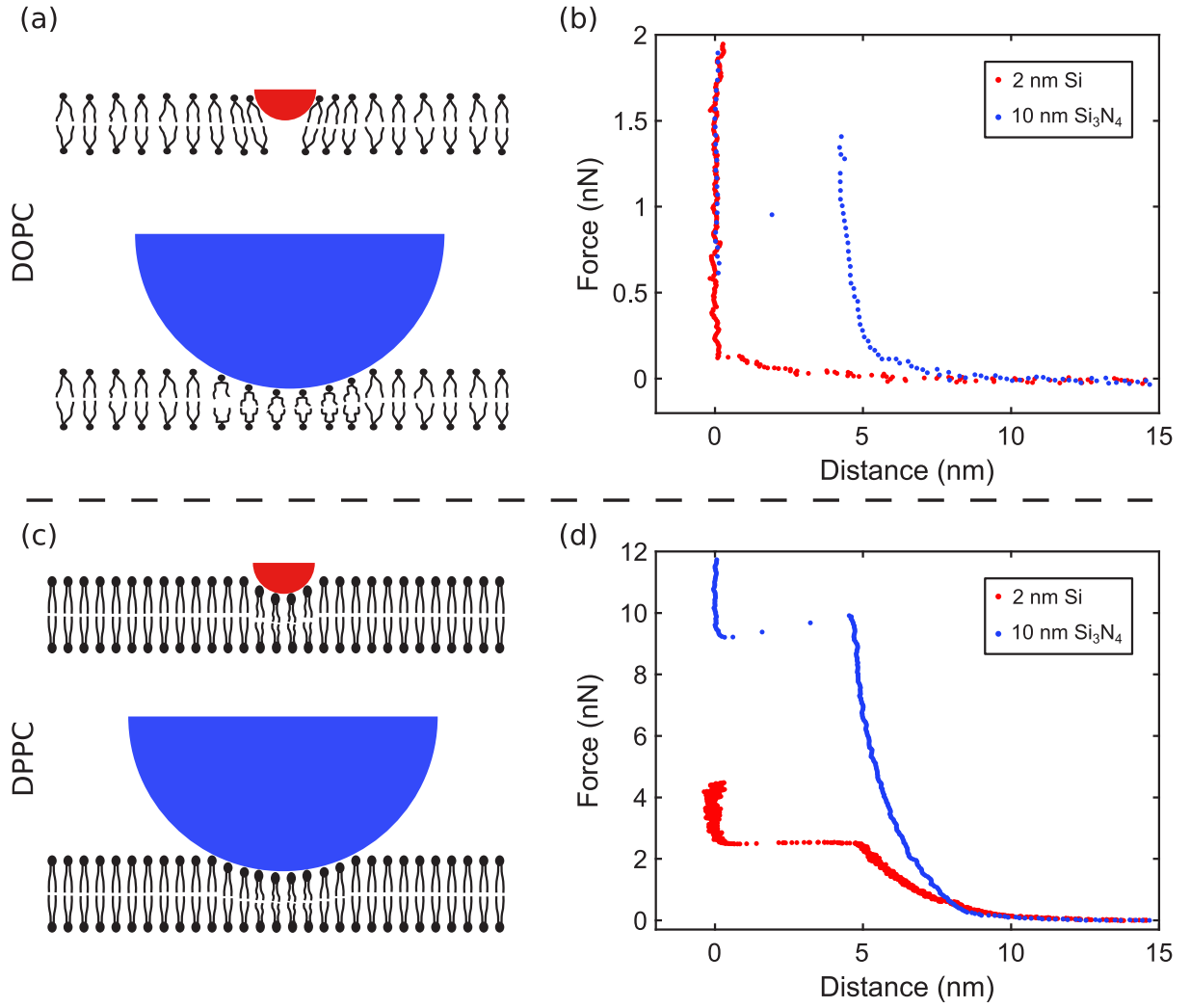


Figure 2.25: Pictorial representation of fluid-phase (a, DOPC) and gel-phase (c, DPPC) membranes indentations with two different indenter sizes: 2 nm tip *versus* 10 nm tip radii. While in both DOPC and DPPC the 10 nm tip (blue curve) induces a vertical compression of the lipid molecules (b,d), a 2 nm tip (red curve) can penetrate the fluid-phase membrane inducing a local perturbation of the molecules surrounding the tip in absence of membrane rupture. Measurements were performed in DPBS buffer.

carbon AFM tips.

Our data can be used to evaluate the activation volume V in (2.35) and consequently the associated number of molecules involved at the beginning of the rupture process. To do so, we have evaluated k_0 for both DOPC and DPPC from dynamic force spectroscopy (AFM-DFS), as proposed by Butt *et al.* [144]. We measured F_B as a function of the loading rate v (between 0.5 and 50 $\mu\text{m/s}$) for both DOPC and DPPC (Figure 2.28a

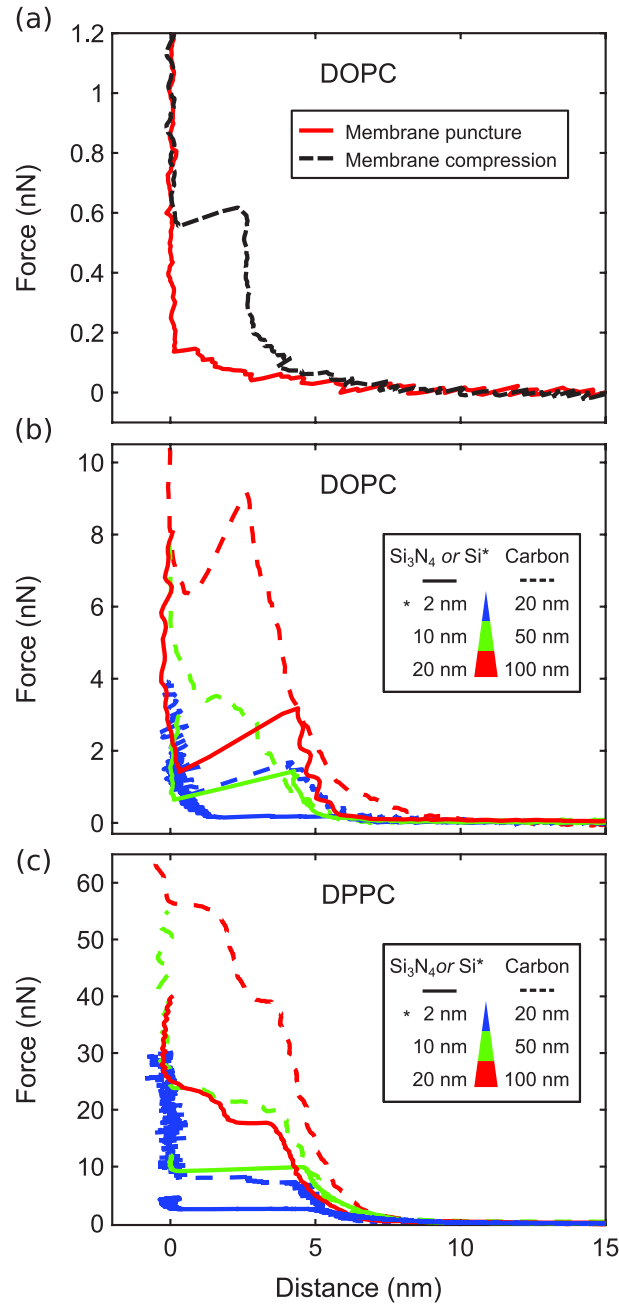


Figure 2.26: Force-distance curves of fluid- and gel-phase for different tip radii. (a) coexistence of vertical compression (black) and membrane puncture (red) when indenting a fluid-phase membrane (DOPC) with a 2 nm indenter. (b) and (c) indentation cycles on fluid (DOPC, b) and gel (DPPC, c) phase membranes measured with different tip radii in DPBS buffer. The maximal force the membrane can withstand before rupture for both DOPC and DPPC increases with the tip radius.

and b, respectively) using MSCT-F cantilevers. Data were fitted using

$$F_B = \alpha + \beta \log_{10} \frac{v}{v_0}, \quad (2.38)$$

where F_B , α and β are in nN and $v_0 = 1 \mu\text{m/s}$. The free fit parameters α and β lead to

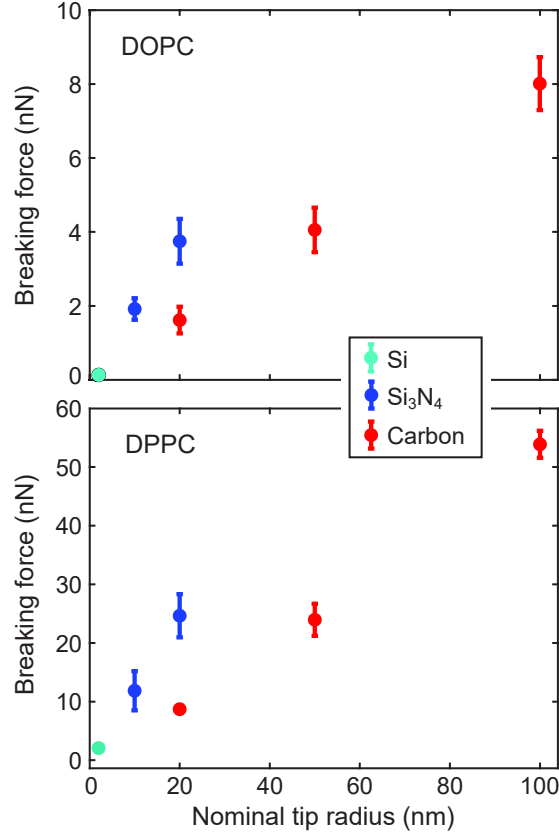


Figure 2.27: Rupture force F_B for DOPC and DPPC enriched domains indented by silicon, silicon nitride and carbon AFM tips at a constant loading rate $v = 1 \mu\text{m/s}$ in DPBS buffer. The rupture force increases with the tip radius, suggesting that the number of molecules involved in the onset of the rupture process is independent of the tip radius.

the evaluation of k_0 as follows

$$k_0 = 1.596 \frac{K v_0}{\beta} 10^{-\frac{\alpha}{\beta}}. \quad (2.39)$$

We evaluated $k_0^{DPPC} = 4.1 \text{ MHz}$ (close to the value reported by reference [148]) and $k_0^{\text{DOPC}} = 297 \text{ MHz}$.

V is found to be essentially constant with the indenter radius for both DOPC- and DPPC-enriched domains but dependent on the tip chemical composition (Table 2.2). We can associate to each activation volume the number of molecules n triggering the rupture process defined as $n \approx V/(Ah)$. Assuming the head to head distance h to be 3.6 nm and 4.5 nm for DOPC [52] and DPPC [149], respectively, Table 2.2 reports the measured activation volumes and the corresponding number of molecules n including their errors, evaluated from the dispersion of each rupture force, for DOPC and DPPC membranes indented by silicon and carbon AFM tips. As a consequence, since the total

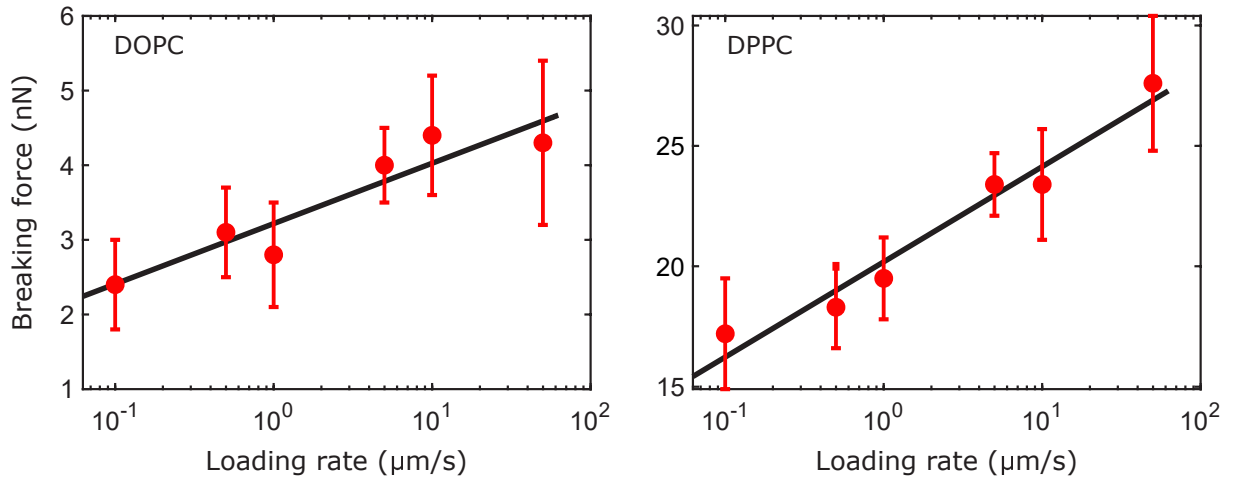


Figure 2.28: AFM-DFS on DOPC:DPPC (1:1) SLBs, in DPBS buffer. Mean rupture force *versus* loading rate v (error bars denote standard deviation) for DOPC and DPPC enriched domains. In black the fit with (2.38). The free parameters obtained from the fit are: $\alpha = (3.22 \pm 0.41)$ nN and $\beta = (0.81 \pm 0.43)$ nN (DOPC) and $\alpha = (20.2 \pm 1.1)$ nN and $\beta = (3.95 \pm 0.56)$ nN (DPPC).

number of molecules N elastically compressed by the tip increases with the tip radius, for a given tip chemistry, n is observed to be independent of N .

Table 2.2: Rupture force (F_B), activation volume (V) and associated number of molecules (n) for DPPC and DOPC membranes indented by silicon and carbon AFM tips

DPPC			DOPC			Tip material	Radius [nm]
F_B [nN]	V [nm ³]	n	F_B [nN]	V [nm ³]	n		
2.21 ± 0.08	2.3 ± 0.1	1.0 ± 0.1	0.12 ± 0.02	-	-	Si	2
12.0 ± 3.3	1.8 ± 0.3	0.8 ± 0.1	1.9 ± 0.3	5.7 ± 1.0	2.2 ± 0.4	Si ₃ N ₄	10
24.8 ± 3.7	2.1 ± 0.2	0.9 ± 0.1	3.7 ± 0.6	7.9 ± 0.8	3.1 ± 0.3	Si ₃ N ₄	20
8.8 ± 0.6	6.1 ± 0.3	2.7 ± 0.1	1.6 ± 0.4	18.4 ± 3.2	7.1 ± 1.2	carbon	20
24.1 ± 2.7	6.2 ± 0.5	2.8 ± 0.2	4.0 ± 0.6	21.5 ± 3.1	8.3 ± 0.8	carbon	50
54.0 ± 2.3	5.1 ± 0.7	2.3 ± 0.1	8.0 ± 0.7	19.9 ± 1.4	7.7 ± 0.5	carbon	100

It is remarkable that in the case of DPPC enriched domains, the use of probes with a tip radius larger than 20 nm induces a two-step rupture process (Figure 2.25c).

Several scenarios that remain to be elucidated can be involved explain the mechanism: 1) two different rupture events involving at first the DPPC molecules compressed at the very end of the tip apex and subsequently other molecules compressed by the tip side at higher indentation length; 2) a limiting maximal DPPC hole size inferior to 20 nm; 3) tip approach and hole formation comparable speeds ($k_0 \approx 4$ mHz for DPPC membranes; 4) discrete rupture of the upper membrane leaflet subsequently followed by the rupture of the bottom leaflet. To evaluate F_B and V , we have considered the breaking event characterized by the highest rupture force only.

2.5.2 Young's modulus of Lipid Bilayers

In addition to the rupture force, the elasticity can be used to characterize biological membranes. This section is devoted to the characterization of the elastic properties of SLBs in terms of Young's modulus. In addition, in the rupture force experiments reported previously, we reported observing a different mechanism in the case of indentation of DOPC-enriched domains with a small tip radius ($\approx 1\text{--}2$ nm). In order to check whether such indentation is compatible with vertical compression of the membrane, we have evaluated the Young's modulus for DOPC-enriched domains for small tip indenters and compared it with the one evaluated for large and well-defined tip radii. As the Young's modulus is an intrinsic property of a material, meaning that it does not depend on the indenter size, we expect to observe a Young's moduli values considerably different, justifying the existence of a novel mechanism, occurring when using small probes, not involving mechanical compression of the sample.

AFM-FS experiments were performed on DOPC:DPPC (1:1) SLBs at a loading rate of $\nu = 1 \mu\text{m/s}$ using two different well-defined tip radii 20 and 50 nm by using the B20-CONT and B50-FM AFM cantilevers (both purchased from Nanotools), respectively, previously introduced. The manufacturer of these cantilevers measured each cantilever's tip radius individually in order to ensure its size with a precision of ± 1 nm, being the ideal tip for our experiments. Assuming ν as 0.5 (perfectly elastic uncompressed material), data were fitted with the Hertz model previously described in equation XX, until a maximal indentation δ_{max} of 1.5 nm for DOPC and 1 nm for DPPC. DL fit was limited to tip-membrane

distances higher than 1 Å to avoid taking into account non-ubiquitous short-range Van der Waals (VdW) attractive interactions (\approx to 10–20 pN, at the limit of our instrumental sensitivity). Concluding, for Equation XY, we left F_Z and λ_D as free parameters, whereas for Equation XX, only E was left as a free parameter. We have evaluated $E^{DOPC} = (34 \pm 19)$ MPa and $E^{DPPC} = (48 \pm 15)$ MPa (Figure 2.29 c and e, respectively) for the 20 nm carbon probe and $E^{DOPC} = (36 \pm 19)$ MPa and $E^{DPPC} = (58 \pm 28)$ MPa (Figure 2.29 g and i, respectively) for the 50 nm carbon probe. Our values are consistent with the fact that the Young’s modulus constitutes an intrinsic mechanical property of a material; therefore, it is independent of the indenter size. Moreover, our values are in agreement with data reported in the literature [87]. In addition, we have determined $\lambda^{DOPC} = (1.6 \pm 1.4)$ nm and $\lambda^{DPPC} = (1.5 \pm 1.4)$ nm (Figure 2.29 d and f, respectively) for the 20 nm probe and $\lambda^{DOPC} = (1.3 \pm 0.6)$ nm and $\lambda^{DPPC} = (1.7 \pm 0.7)$ nm (Figure 2.29 h and j, respectively) for the 50 nm probe. This suggests that DOPC and DPPC head-groups have similar Debye length values close to 1.5 nm in DPBS buffer.

Sharp probes were previously used to evaluate the Young’s modulus of DOPC membranes using Peak-Force Tapping AFM (indentation cycles in between one and two orders of magnitude faster) in buffer containing $MgCl_2$ [86, 87]. By analyzing the Young’s modulus of the AFM-FS data acquired for the sharpest probes (MSNL-D), where the breaking force was studied within the literature. We have observed the Young’s modulus for DOPC-enriched domains when the size of the tip is small (\approx 1–2 nm), the molecular vertical compression in fluid phase membranes is a rare event, in favor of cases where the tip can puncture the membrane in the absence of rupture events (Figure 2.26, red curve).

Fitting indentation cycles on DOPC (number of curves= 175) with the Hertz’s model ((2.37b)), assuming 2 nm as tip radius (MSNL-D cantilever, Bruker), we observe that a large majority of the curves leads to Young’s modulus consistently lower (\approx 2–3 MPa, Figure 2.30 a, red region) than the values reported in Figures 2.29c and g and, more generally, in the literature [87].

It imposes a limit to the use of the Hertz model since the vertical compression of the lipid molecules rarely occurs (the green region in Figure 2.30a). Figure 2.30b shows the distribution of maximal force the membrane can withstand for the same dataset.

The large majority of indentation cycles show a force that is maximal at the contact point between the tip and mica (see the red curve in Figure 2.26a), suggesting that the physical

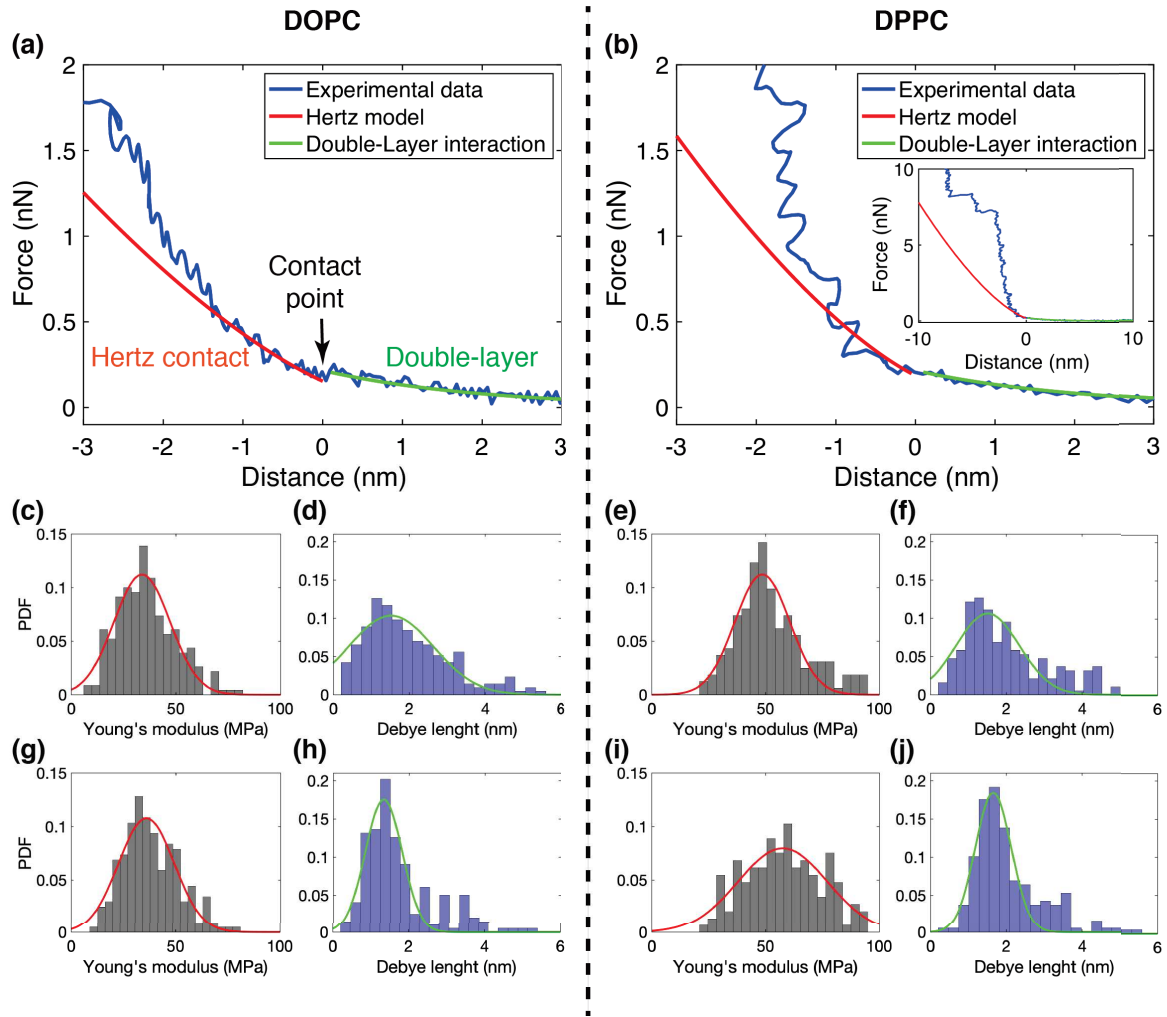


Figure 2.29: Evaluation of Young's modulus and Debye Length for DOPC (a) and DPPC (b) model membranes using an indenter with a radius of 20 nm (a,b,c,d,e,f) and 50 nm (g,h,i,j). In red the fit with Hertz model (Equation S1.2), in green the fit with DL model (Equation S1.1), the tip-membrane contact point is fixed at $z = 0$. The free parameters E and λ_D distributions over 200 curves, for both DOPC and DPPC, are displayed in the histograms. For the 20 nm indenter, $E^{\text{DOPC}} = (34 \pm 19)$ MPa and $\lambda_D^{\text{DOPC}} = (1.6 \pm 1.4)$ nm, (c) and (d), respectively and $E^{\text{DPPC}} = (48 \pm 15)$ MPa and $\lambda_D^{\text{DPPC}} = (1.5 \pm 1.4)$ nm (e) and (f), respectively. For the 50 nm indenter, $E^{\text{DOPC}} = (36 \pm 19)$ MPa and $\lambda_D^{\text{DOPC}} = (1.3 \pm 0.6)$ nm, (g) and (h), respectively and $E^{\text{DPPC}} = (58 \pm 28)$ MPa and $\lambda_D^{\text{DPPC}} = (1.7 \pm 0.7)$ nm, (i) and (j), respectively.

mechanism involved during the indentation does not lead to a membrane rupture event anticipated by a molecular vertical compression. In other words, the tip can easily puncture the membrane, therefore encountering lower resistance (red region in Figure 2.30b).

Our data suggest that small indenters should not be used to quantify the DOPC Young's

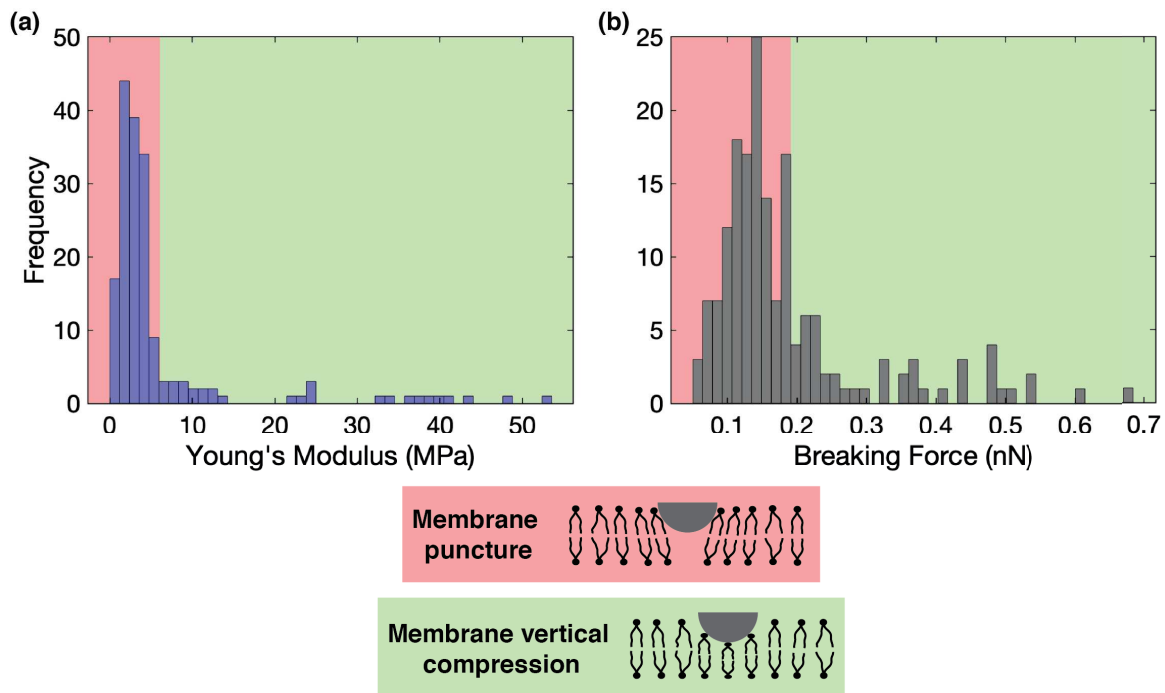


Figure 2.30: (a) Young’s modulus distribution evaluated from indentation cycles on DOPC membranes, fitted with the Hertz contact model, using a tip with a radius of 2 nm (MSNL-D cantilever). The measured Young’s modulus is ≈ 1 order of magnitude lower than the reported value of $\approx 20 - 30$ MPa. (b) Maximal force the membrane can withstand for the same dataset of (a): in most cases (red region) it was evaluated at the contact point between the tip and the mica because the molecular vertical compression leading to membrane rupture is absent. In both (a) and (b), the green region consists of the approach curves where molecules are vertically compressed. The red region highlights the indentation cycles showing membrane puncture.

modulus using the Hertz contact model, and any other model, with an indentation speed of $\approx 1 \mu\text{m/s}$ in experiments carried out in the absence of MgCl_2 .

While for the DPPC case, the use of equation (2.6) provides a Young’s modulus in the range of few tens of MPa, close to what has been reported in the literature for both AFM tips [88, 87], this applies to the DOPC only for the larger tip case. Indeed, indentation curves performed with the 2 nm tip on DOPC membrane show a much softer indentation regime where the Hertz fit would provide a Young’s modulus of ≈ 2 MPa [124], far too low for DOPC membrane since it has been reported to be in the range of 20–30 MPa [88, 87]. The unrealistic Young’s modulus and the absence of rupture events suggest a different indentation mechanism is occurring. Moreover, since the tip radius

we used for the fit (≈ 2 nm) is smaller than the membrane thickness, the surface of the tip in contact with the membrane at large indentation is underestimated and, therefore, the obtained small Young's modulus is even overestimated, further confirming its unrealistic value. According to Tristram-Nagle and co-authors, the area occupied by a DOPC molecule is $A \approx 70 \text{ \AA}^2$ [52]. The area occupied by a DPPC molecule has been reported to be $A \approx 47 \text{ \AA}^2$ [150, 151]. Approximating the tip as a sphere, for indentations δ smaller than tip radius R , the contact area, also known as the spherical cap, is given by $S = 2\pi\delta R$. The contact area S can be related to the area A occupied by a single lipid by multiplying the latter times the number of lipids N and dividing by the coverage/packing factor Φ .

$$2\pi\delta R = \frac{NA}{\Phi} \quad (2.40)$$

The densest packing assumes a value of ≈ 0.9069 in two-dimensional space (hexagonal packing), which is the case here. As a consequence, for an indentation δ of 0.5 nm there are approximately $N_{DOPC} = 8$ DOPC molecules in mechanical contact with the 2 nm AFM tip, whereas the molecules increase to approximately $N_{DPPC} = 12$ in the DPPC case. The low number of molecules involved can justify the probability of a physical indentation mechanism where a vertical molecules compression is minimized in favor of a lateral molecules tilt/displacement, here referred to as puncture mechanism. However, it is remarkable that the latter occurs only in DOPC-enriched domains, despite a number of molecules below the tip similar to the DPPC case. Eventually, the higher diffusion coefficient characterizing DOPC molecules ($\approx 4 \text{ \mu m}^2/\text{s}$ [152]) compared to DPPC molecules ($\approx 10^{-3} \text{ \mu m}^2/\text{s}$ [153]) can play an additional role favouring such mechanism. In other words, the use of a small AFM indenter induces an in-plane local perturbation in the absence of elastic compression followed by membrane rupture. Indentations with the high-speed AFM (HS-AFM) or eventually correlative fluorescence correlation spectroscopy (FCS)-AFM experiments can further explore the contribution of lipid diffusion to the mechanical response of the membrane. During all experimental sessions for fluid-phase membranes using the 2 nm AFM tip, we observed a prevalence of indentation cycles where the tip can penetrate the membrane in the absence of molecular vertical compression in respect of cycles where compression is present, as shown in Figure 2.26a. When using larger AFM tip indenters, molecular vertical compression always occurs. Figures 2.26b and c show indentation cycles on DOPC- and DPPC-enriched domains acquired with tip

radii varying from 2 nm to 100 nm. In addition, the curves presented in Figure 2.26 clearly show that the maximal force F_B the membrane can withstand before rupture for both DOPC and DPPC increases with the tip radius as predicted by (2.35).

In the case of thin films, Dimitriadis *et al.* [154] have shown that the Hertz model must be corrected to take into account the finite thickness of the film (equation (8) in reference [154]) that would otherwise induce an apparent material stiffening. The correction function is proportional to the square root of the tip radius, and this model considers the membrane's thickness. However, it cannot explain the apparent membrane softening observed for fluid phase membranes indented by a 2 nm AFM sharp tip (Figure 2.26a, and Figure 2.30). The Hertz model itself (2.6) describes indentation cycles in the approximation of the a radius $R \gg \delta$, leading to the Hertz contact radius $a \approx \sqrt{R\delta}$ [96]: in the 2 nm tip radius case, the approximation does not hold, but the use of the non-simplified Hertz radius $a = \sqrt{R\delta - \delta^2}$ does not lead to the expected Young's modulus E^{DOPC} value either. Therefore, indentation cycles performed with such a small tip radius, with a contact area compared with the surface occupied by few lipid molecules, reveal a physical indentation mechanism that minimizes molecular vertical compression. While the use of small AFM tips could be extended to a large variety of thin films constituted by diffusive and dynamic molecules, in practice, it represents a limit to the conventional Hertz contact mode because, with this indenter size, the membrane is not being vertically compressing what is required to probe Young's modulus under any compression model. Additionally, the acquisition of AFM images is particularly challenging because of the films' small rupture force.

Indentation cycles performed with larger indenters can be used to probe membrane mechanical stability. Interestingly, the activation volume associated with the onset of the rupture process is essentially constant in the range of the indenter sizes we tested in this work. Suggesting that the activation volume, together with the probability to observe a film rupture due to thermal fluctuation k_0 , are the quantities that should be considered when comparing variations of membrane mechanical stability due to the presence of external factors or due to changes in membrane composition.

2.6 Conclusions

In the first chapter, we discussed the relevance of the lipid organization on biological membranes' mechanical properties. We have also discussed how model membranes such as supported lipid bilayers play a crucial role in approaching and understanding membrane remodeling on biological membranes. In order to probe mechanical properties of membranes, within this chapter, we used AFM - a well-establish technique to image the lateral organization of biological membranes in both homogeneous and phase separation- to probe and image supported lipid bilayer with phase separation, distinguishing both lipids present on the membrane. Moreover, we used AFM-FS to probe the mechanical properties of the membranes at the nanoscale, correlating them with each lipid-enriched domain. We have shown that the indenters' size to probe membrane mechanics through AFM-FS is crucial to properly quantify intrinsic properties such as the Young's modulus and the number of molecules involved at the onset of a hole formed within the membrane. These intrinsic properties help us to distinguish and show the presence of two different effects- vertical compression and puncture of the membranes- by evaluating one intrinsic property (Young's modulus) on the data acquired for this novel effect called puncture. We have shown for the first time that, for small indenters, the membrane Young's modulus cannot be assessed due to the puncture mechanism, where the tip passes through the membrane with less resistance than in a compression regime. Resulting in the erroneous estimation of the Young's modulus due to the membrane is not being compressed, at least for the case of DOPC-enriched domains. For larger indenters, our results are in good agreement with Butt and Franz's theory [143] and confirm that the rupture force increases with the indenter radius. Although the critical number of molecules involved in the AFM tip breakdown process is material-dependent, it remains constant regardless of the indenter size.

We have shown that AFM is a versatile tool to probe membranes because it provides the membrane morphology with high lateral resolution. At the same time, we can probe and characterize membranes mechanically with nanoscale resolution, correlating the membrane topography with local mechanics. A crucial advantage of AFM, compared with other techniques that can probe membranes' mechanical properties, such as optical

tweezers, micropipette aspiration, and surface force apparatus, is that AFM can achieve both mechanical properties and topography the nanoscale, and even simultaneously, with nanoscale resolutions. In this frame, a new technique called Phonic Force Microscopy was recently developed [155] (initially proposed in 1997 by Florin et al. [156]) in order to image biological samples without force-induced artifact. At the core of the technique, there is a sharp probe scanned by an optical tweezer. The latter can measure the interaction force acting on the scanning probe with sub-pN resolutions. However, this technique can not apply more than few tens of pN. Consequently, this technique can not probe membrane mechanics as we did with AFM due to the force range limitations.

The physics of hole formation within a membrane is contained in equation (7) of reference [143], where the energy is dictated by an interplay of line tension, spreading pressure, and the membrane elastic energy. In our case, we are interested in the process of hole formation where the latter term is absent. Additionally, it is remarkable that one cannot assume constant line tension and spreading pressure, first and second terms of equation (7) in reference [143], in the process of hole formation, where our data suggests that they are indentation dependent. We propose to use this novel puncture effect on membranes as a possible way to measure the line tension of membranes. However, it is challenging to adequately describe the dependency of line tension and spreading pressure as a function of the indentation from our data: besides the very small forces measured (\approx tens of pN), several questions arise concerning the way single molecules are tilted/laterally displaced and how the two leaflets differently participate to the hole formation at different indentation lengths.

We have shown that the AFM tip can be very invasive with the membrane and even break it with a low force if a small indenter is used. We emphasize the importance of correctly choosing both the AFM tip size and force applied to the membrane. Indeed, even without membrane breakage, the latter can get curved and deformed by the AFM tip's mechanical constraints during the sample scan. As a possible solution for this issue, we will propose in the next chapter a new Scanning Probe Microscopy technique that aims at using a fluorescence signal as the feedback signal, meaning that, in a long term perspective, the topography will be reconstructed without measuring the interaction force with an AFM cantilever.

We have shown that supported lipid bilayers can be characterized and distinguished by

their mechanical properties like Young's modulus and breaking forces. However, a more exhaustive characterization of a membrane requires the recognition of the components of the membrane. As mentioned in the first chapter, in most cases, AFM cannot recognize a molecule by itself, and it requires a correlation with another technique/instrument that can achieve molecular recognition. The novel Scanning Probe Microscopy technique introduced in the next chapter is based on the correlation of an AFM with confocal microscopy. This development aims at measuring membrane topography, mechanical properties, and chemical molecular recognition with a high lateral resolution in a correlative and simultaneous way.

Chapter 3

MIET-AFM

In the present chapter we discuss the necessity of a novel correlative AFM-Super Resolution instrument. At first, we report and discuss the main techniques employed for molecular recognition when studying biological membranes. Then, we introduce the MIET-AFM operational scheme and report the relevant instrumental work necessary to develop such a technique. The synchronous and cross-talk free use of an AFM with a confocal microscope is here crucial. Finally, we report the first MIET-AFM images obtained with a resolution inferior to the diffraction limit, making of MIET-AFM a new Super Resolution technique.

3.1 Necessity of Super-Resolution and morphology

In the two previous chapters, we have presented the most relevant lipids characteristics and their mechanical properties. We have shown that different lipids can be distinguished thanks to their topography and their mechanical properties, such as Young's modulus and rupture force. As mentioned in the first chapter, biological membranes and supported model membranes are composed of many components, including lipids but also proteins which are heterogeneously distributed on both leaflets. As those membrane constituents are small (in the nanometer range), AFM cannot recognize a molecule. However, if the molecules of interest are labeled with fluorescent probes, fluorescence microscopy

can be used for molecular recognition. Although conventional fluorescence microscopy is limited by the diffraction limit, which is a problem if we aim to address fundamental biological questions, it can be used to characterise membrane remodeling, as we have shown in the first chapter. However, given the size of membrane constituents, the localization of interest molecules at high spatial resolution is crucial.

A potential approach to fully describe a membrane is the correlative AFM with Super-Resolution Fluorescence Microscopy, as shown in Figure 3.1. There, a correlative AFM-dSTORM - it is a Super-Resolution Fluorescence Microscopy technique that will be later described in this chapter- approach was used to investigate the organization of tetraspanins HIV-1 on HeLa cells [77]— highlighting the necessity of a more complete description of the membranes at high resolution.

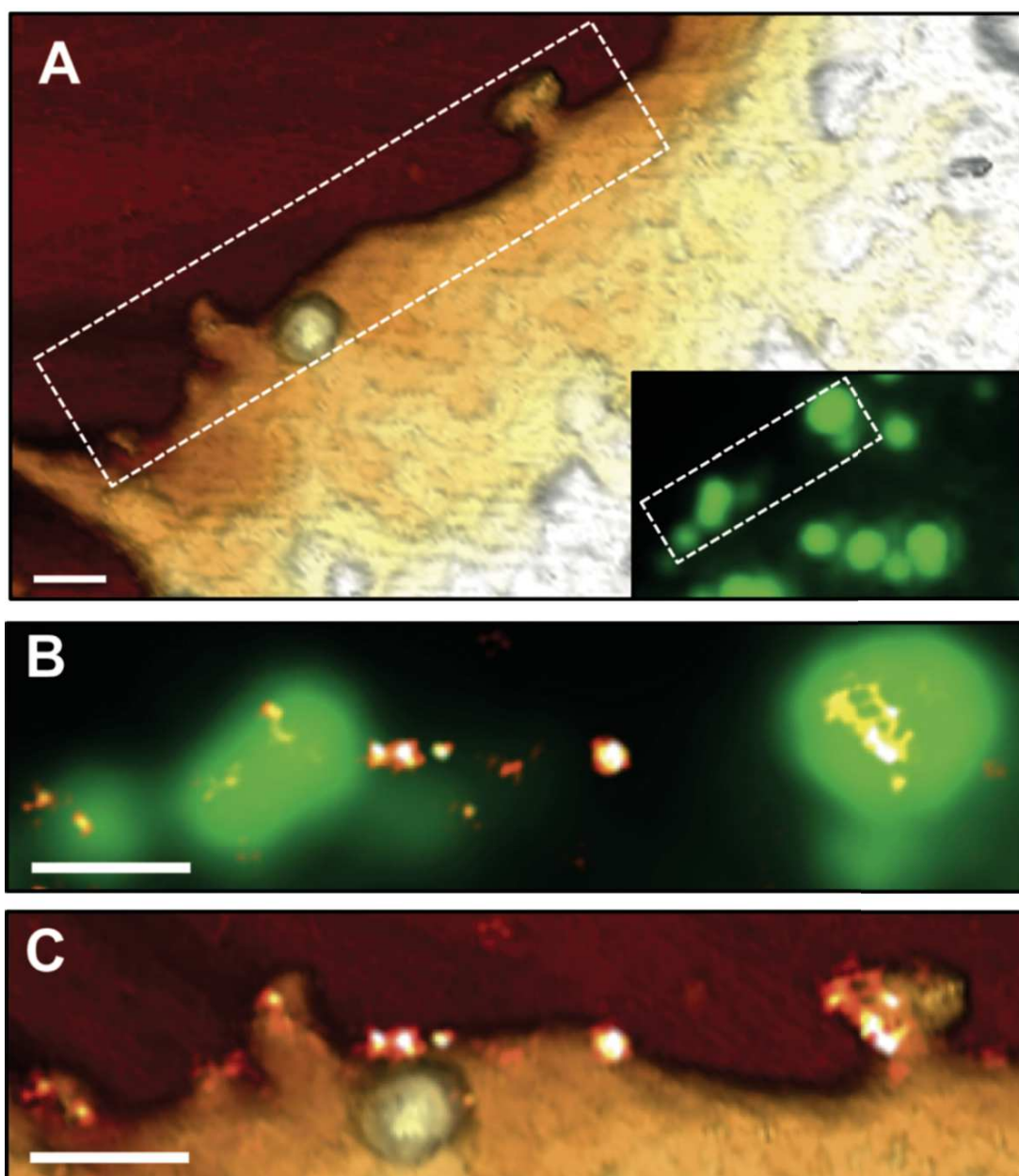


Figure 3.1: Correlative AFM-dSTORM of CD9 recruitment at HIV-1 budding sites. HeLa cells expressing HIV-1 Gag-GFP were immuno-stained with anti-CD9 coupled to Alexa-647. a) AFM 3D images of a HeLa cell (the dotted lines delineate the zoomed areas shown below, and the insets are corresponding Gag-GFP signal fluorescence images). The scale bar is 500 nm. b) overlays of the Gag-GFP picture with the reconstructed dSTORM image of the tetraspanin CD9. c) Overlays of the reconstructed dSTORM image of the tetraspanin CD9 with the AFM topography image. The scale bar is 200 nm in b) and c). AFM color z-scales are 300 nm. Adapted from [77].

Concluding, the full membrane characterization requires to measure its morphology, determine its components, and describe them mechanically.

3.1.1 Molecular Recognition

In the frame of molecular recognition, diverse techniques have been developed during the last decades and are currently well-established and available, allowing characterization at different lengths and timescales. We focus on the following techniques:

3.1.1.1 Fluorescence microscopy

Historically, fluorescence microscopy was limited by the diffraction limit. However, some recently developed super-resolution techniques have bypassed the diffraction limit and improved the lateral resolution (depending on the technique) down to a few nanometers [157]. Some of these super-resolution techniques are Stimulated Emission Depletion Microscopy (STED) [158], Stochastic Optical Reconstruction Microscopy (STORM) [159], Photoactivated Localization Microscopy (PALM) [160], and MINFLUX [161]. The main drawbacks are: (i) the photo-toxicity due to the laser power that some of them need for measuring. (ii) acquisition speed, taking until tens of minutes per image, becoming a problem due to the high dynamics of membrane constituents (for PALM and STORM). Concerning the coupling of AFM and Fluorescence microscopy, many setups were developed during the last decade, using super-resolution fluorescence. However, the laser power required for super-resolution fluorescence affects the AFM measurement, as we have shown for Confocal Laser Scanning Microscopy (CLSM) in Fernandes et al. 2020 [157]. Because of that, the AFM and fluorescence images are acquired in series, and the correlation between images is generated afterward [162, 163]. Finally, concerning the long acquisition time of some super-resolution fluorescence, a temporal delay between the molecular recognition's image and mechanical properties' maps makes it difficult to follow dynamical biological processes.

3.1.1.2 Simultaneous topography and recognition imaging (Pico TREC)

Pico TREC is a technique where the AFM tip is chemically functionalized to detect molecules during AFM-AM mode scanning. This technique was developed by Peter Hinterdorfer's group in Austria.

The AFM tip functionalization is the key parameter in this technique. The tip surface is functionalized with ligands in order to bind them with the receptors at the sample. The tip chemical functionalization has been extensively studied, establishing well-defined protocols for the surface chemistries most used for modifying AFM tips for single-molecule recognition studies. However, chemical protocols should be carefully developed and tested in order to achieve strong biomolecules attachment at low surface density [78].

Pico TREC offers the possibility to study molecular recognition in two different ways:

(i) recognition forces, probing the interaction forces between the modified tip and the sample surface, or ligand-receptor interaction forces. The interaction force (unbinding) can be probed and measured in a force-distance curve during the tip retraction by approaching an AFM tip with ligand functionalization on a sample with receptors, as shown in Figure 3.2a), where the force-jump due to the interaction force is highlighted. If the same process is done on a sample where the receptors are blocking, no force-jump will be acquired on the force-distance curve, as shown in Figure 3.2b). By sequentially repeating this procedure, the study of the ligand-receptor unbinding force can be characterized by statistics. As these measurements are performed in an AFM, the force is measured with few picoNewtons of resolution [78].

(ii) molecular recognition maps, it is based on AFM-AM mode where a ligand functionalized tip scans the surface, detecting the molecular recognition signals by properly analyzing the signal. The topography and recognition images are simultaneously obtained using an electronic circuit (Pico TREC) [164, 165]. Here, the sinusoidal signal from the cantilever deflection (AFM-AM mode) is separated into two maxima (U_{up}) and minima (U_{down}) (Figure 3.3a)), which are used to evaluate the Recognition and Topography image, respectively (Figure 3.3b)).

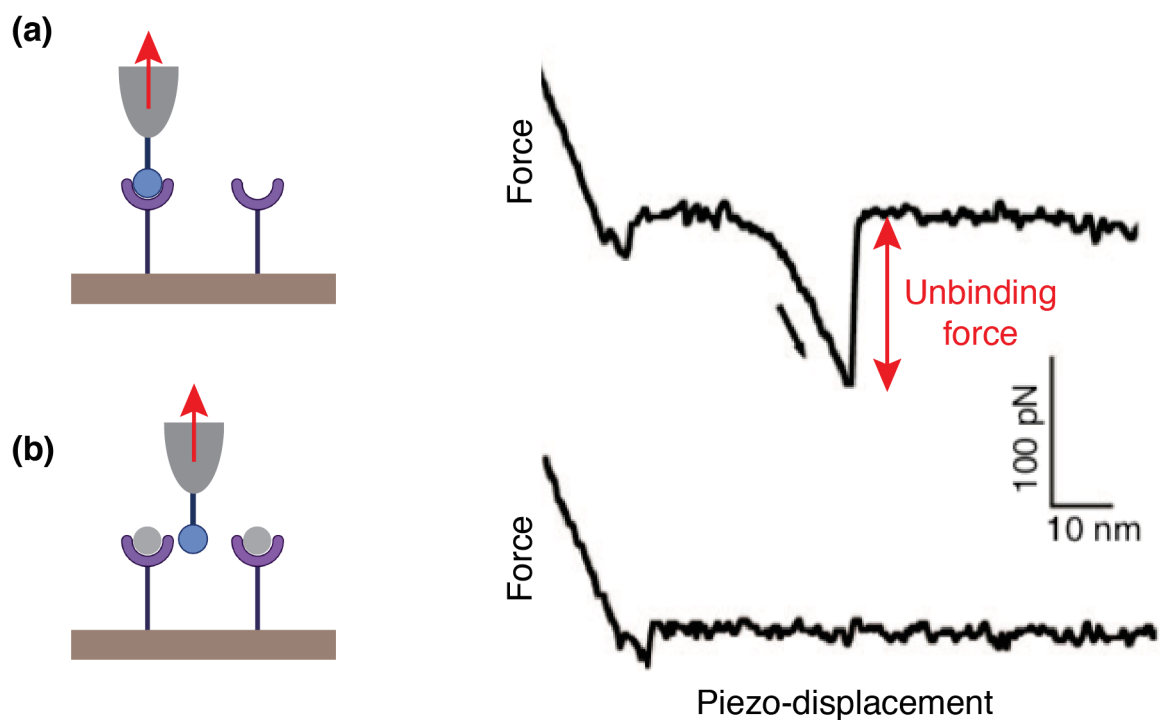


Figure 3.2: Molecular recognition interaction forces. a) Typical force-displacement curve obtained upon retracting an AFM tip functionalized with oligoglucose carbohydrates (ligands) from a surface modified with the lectin concanavalin A (receptors), where the unbinding force is highlighted. At the left, a schematic of the process is shown. b) Typical force-displacement curve obtained upon retracting an AFM tip functionalized in the same conditions of a) and where the receptors are blocked. No unbinding force was measured. At the left, a schematic of the process is shown. Adapted from [78].

The main drawbacks of this technique are: (i) the lifetime of a functionalized tip may be very short because of tip contamination or damage [78]. Indeed, in AFM experiments tip contamination and damage constitute often a problem. In Pico TREC it is even more crucial because the chemical functionalization under the tip can be easily altered during data acquisition, making only a few maps should be acquired with the same tip in order to ensure proper interaction forces. (ii) Accurate data collection and interpretation often require strong expertise, especially when dealing with complex specimens such as living cells [78].

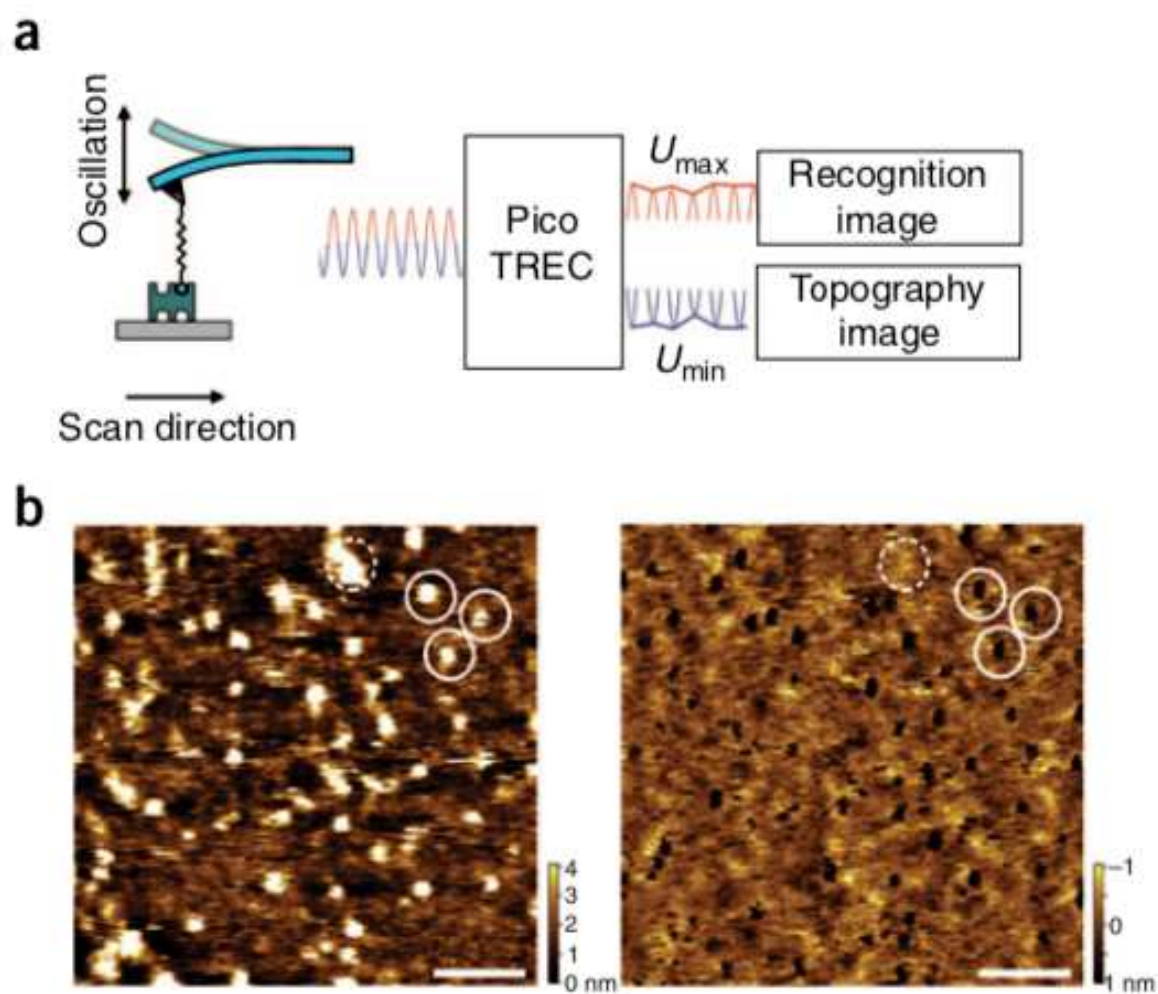


Figure 3.3: Simultaneous topography and recognition imaging (TREC). Adapted from [78].

3.1.1.3 Infrared (IR) spectroscopy

Infrared (IR) spectroscopy, called vibrational spectroscopy, is a technique that analyzes the interaction of molecules with infrared light. It is based on the theory that molecules tend to absorb specific light frequencies (energy) depending on their structure. More specifically, it depends on the shape of the molecular potential energy surfaces, the associated vibronic coupling, and the mass of the molecule's atoms. This spectroscopy technique deals with the electromagnetic spectrum's infrared region, i.e., light having a longer wavelength and lower energy than visible light. The pattern of absorption peaks in the IR spectra serve as a fingerprint that can be used to characterize and/or identify chemical species [166], making this technique one of the most widely used methods for chemical analysis.

The main advantage of this technique is that it is a label-free technique, i.e., the molecules do not have to be tagged with another molecule, therefore permitting study them without any external agents. However, its major limitation is the lateral resolution due to the long-wavelength of IR light because of the diffraction limit. Most commercial Fourier transform infrared (FT-IR) microscopes based on a thermal IR source have a practical spatial resolution limited from λ to 3λ (in the range of 2.5 - 75 μm), depending on the specific technique and configuration employed [167, 168]. Recently, a spatial resolution close to 1 μm even with a thermal source was reported [169, 170, 166].

AFM and IR spectroscopy have been early combined and commercial setups are now

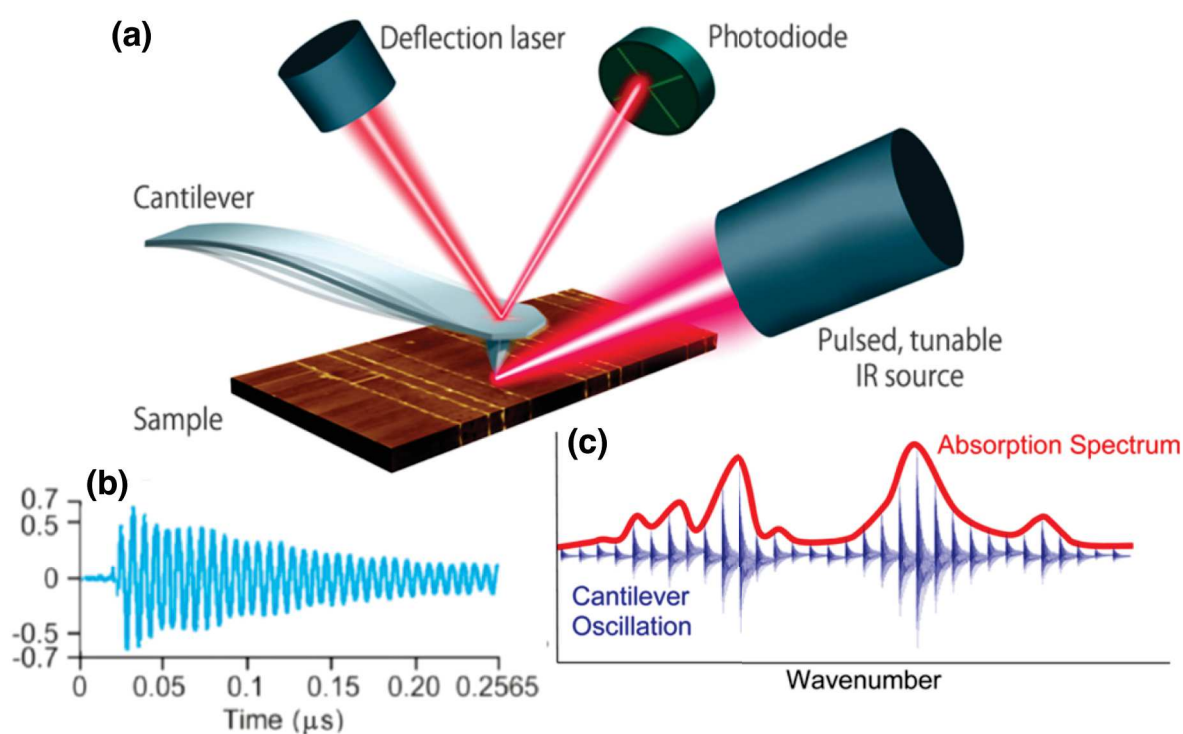


Figure 3.4: AFM-IR correlative microscopy schematic view. a) Schematic of AFM-IR, where a pulsed tunable IR laser source is focused on a sample near the AFM tip. When the sample absorbs the IR light, it induces a thermal expansion, which is measured by the AFM tip. b) The sample's photothermal expansion induces a transient cantilever oscillation proportional to the IR absorption. c) Measuring the AFM cantilever oscillation amplitude as a function of the wavelength results in a local absorption spectrum with nanoscale spatial resolution. Adapted from [166] and Anasys Instruments.

available. AFM-IR employs a pulsed tunable laser source focused near the AFM tip, which scans the sample, as shown in Figure 3.4a. The light is absorbed by the specimen

producing a photothermal expansion of its absorbing regions, detected by the AFM tip, here the IR detector, as an induced transient on the cantilever oscillation, which is linearly dependent on the IR absorption [171, 172, 166] as shown in Figure 3.4c. As the AFM tip is used as the thermal expansion detector, AFM-IR can overcome conventional IR microspectroscopy’s spatial resolution limits [166]. The most common method to perform correlative AFM-IR maps is by measuring the AFM probe response to IR absorption as a wavelength function. Additionally, by fixing the wavelength and measuring the absorption, it is possible to create a chemical recognition map where the distribution of chemical species is shown across the sample and correlate this chemical map with the AFM topography.

We have shown that IR is a powerful technique to recognize chemical compositions on the sample. However, it is hard for this technique to work in liquid conditions due to the water absorbance. The latter represents a significant limitation for the study of biological samples under physiological conditions. Most of the experiments with cells are performed with dried samples [173, 174], in non physiological conditions, without cell and membrane dynamics.

3.1.1.4 Förster Resonance Energy Transfer (FRET)

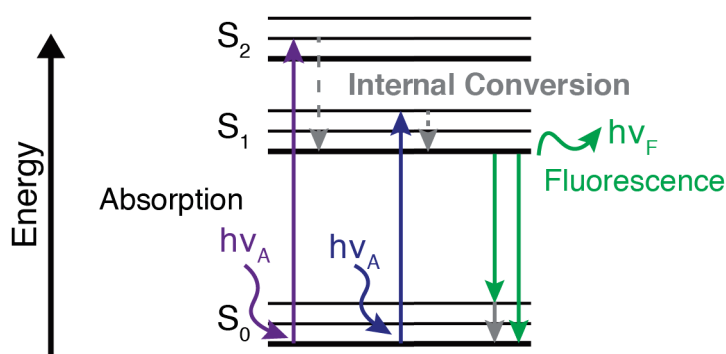
FRET is a technique widely used to measure the relative distance between two light-sensitive molecules (chromophores) with sub-nanometer resolution. Theodor Förster developed the theory behind it in the late 1940s [175, 176]. However, FRET was not applied to biological experiments until the 1970s.

When a fluorophore is illuminated by the light in the energy that it can absorb, by absorbing a photon, it increases its electron’s energy resulting that the electron in the excited orbital is paired (by opposite spin) to a second electron in the ground-state orbital [177]. However, this excited state is not stable for longer, and the molecule returns to its ground state by two mechanisms: (i) internal conversion, where vibrational relaxations decrease this excess of energy. (ii) emission of a photon (with lower energy than the absorbed one), which has a typical emission rate of around $10^8 s^{-1}$, resulting in a typical fluorescence life-

time near 10 ns [177]. The process described is called 'florescence,' and it is described graphically by the Jablonski diagram (see Figure 3.5a)). While fluorescence lifetime (τ) of a fluorophore is the average time between its excitation and return to the ground state, in other words, the average time between a photon is accepted and emitted as fluorescence.

Coming back to FRET, it is based on an electrodynamic phenomenon, where a first

(a) Fluorescence



(b) Energy Transfer

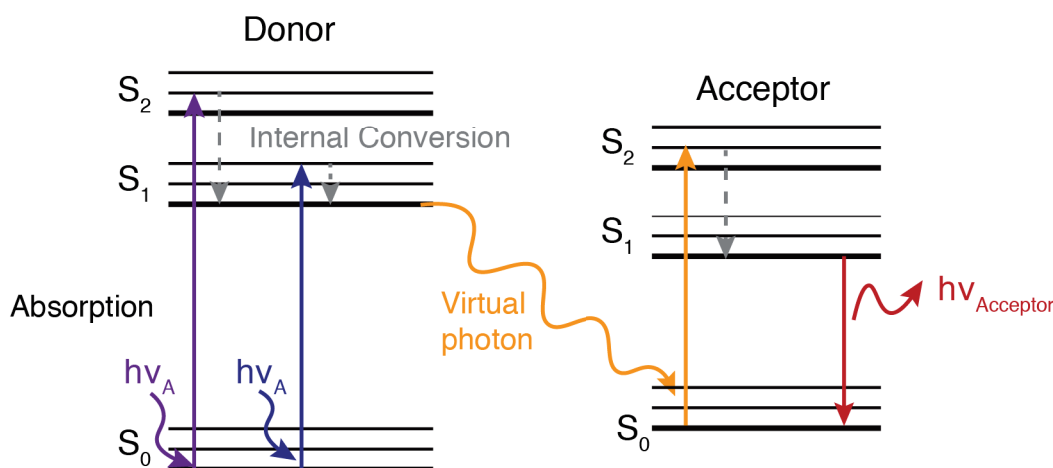


Figure 3.5: Jablosky diagram.

fluorophore (donor) is initially in its electronic excited state and transfers its energy to a second fluorophore (acceptor). This energy transfer is done without a photon's emission from the donor (Figure 3.5b)) but instead due to long-range dipole-dipole interaction between the donor and acceptor [178]. The latter is based on a fluorophore concept as an oscillating dipole, which can exchange energy with another dipole with a similar resonance frequency [179, 180, 178]. The energy transfer rate from donor to acceptor depends on (i) the extender spectra overlap of the donor's emission spectrum with the acceptor's absorption spectrum. (ii) the quantum yield of the donor. (iii) the relative orientation

of the donor and acceptor transition dipoles is also called orientation factor (κ^2), which is assumed $\kappa^2 = 2/3$ when at least one of the molecules is free to rotate (random orientation). (iv) the donor-to-acceptor distance. The rate of energy transfer $k_T(r)$ is given by:

$$k_T(r) = \frac{1}{\tau_D} \left(\frac{R_0}{r} \right)^6 \quad (3.1)$$

Where τ_D is the decay time of the donor in the absence of receptor (in the same medium), R_0 is the Förster distance, and r the distance between the donor and acceptor. Concerning R_0 , it is defined as the distance where the transfer efficiency is 50%. At this distance, the donor emission would be decreased to half its intensity compared to when the donor is in the same condition but the absence of acceptors.

We mentioned the energy transfer efficiency (E_{ET}) without defining it. It is defined as the fraction of photons absorbed by the donor which are transferred to the acceptor [178], and it is given by:

$$E_{ET} = \frac{k_T(r)}{\tau_D^{-1} + k_T(r)} \quad (3.2)$$

Replacing the equation 3.1 into 3.2, E_{ET} is given by:

$$E_{ET} = \frac{R_0^6}{r^6 + R_0^6} \quad (3.3)$$

It shows that the transfer efficiency depends strongly on the donor-to-acceptor distance, as shown in Figure 3.6. Showing that the highest variation on the efficiency is around to $r = R_0$.

If a fixed distance separates the donor-acceptor pairs, the transfer efficiency can be expressed as [178]:

$$E_{ET} = 1 - \frac{F_{DA}}{F_D} \quad (3.4)$$

where I_{DA} and I_D are the relative fluorescence intensity of the donor in the presence and the absence of the acceptor, respectively. The last equation can be written in an analogous form in the function of the lifetimes as:

$$E_{ET} = 1 - \frac{\tau_{DA}}{\tau_D} \quad (3.5)$$

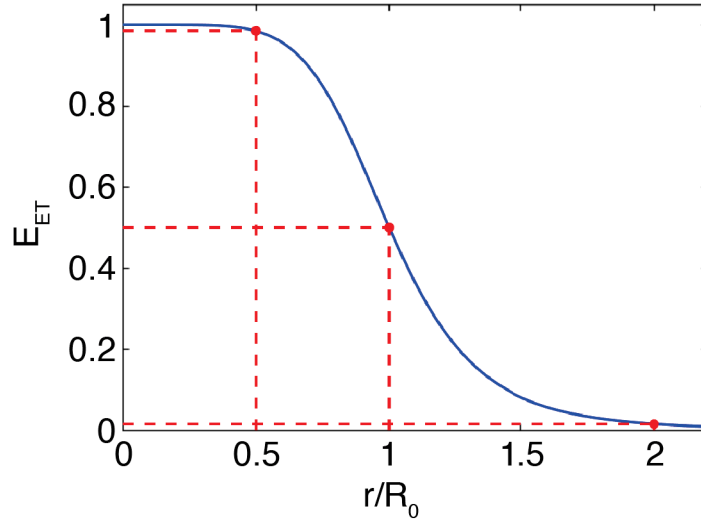


Figure 3.6: FRET efficiency in function of r/R_0 .

where τ_{DA} and τ_D are the donor's fluorescence lifetime in the presence and absence of the acceptor, respectively.

In an operational scheme where the AFM tip is used as donor or acceptor, the main problems to use FRET as a molecular recognition technique are: i) photobleaching and ii) the Förster distances (R_0) are typically in the range of few nanometers. If we analyze more in details the equation 3.3 and Figure 3.6, they show that the highest variation on the efficiency is around to $r = R_0$. The efficiency at $r = R_0/2$ is 98.5% and at $r = 2R_0$ is only 1.5%. Assuming an $R_0 = 5$ nm, the efficiency for $r = 2.5$ nm should be 98.5%, and for $r = 10$ nm is 1.5%. There, we can see how small variations in distance result in a considerable efficiency change. However, these short interaction distances are tricky to control, resulting in a instrumental complex problems when combining FRET with AFM for simultaneous molecular recognition and mechanical properties on biological samples.

The ideal instrument would require the use of AFM combined with a fluorescence technique that is sensitive to distances larger than just a few nm. It is the case for Metal Induced Energy Transfer (MIET). Therefore, this chapter is devoted to the development of the MIET-AFM, which can synchronously provide AFM and super-resolution images.

3.2 Metal Induced Energy Transfer (MIET)

Metal Induced Energy Transfer (MIET) is a technique based on energy transfer like FRET, but the acceptor molecule is replaced with a metallic surface (layer or nanoparticle) measuring the energy transfer efficiency from the donor to metal surface plasmons [181, 182]. The main advantage of MIET is that the axial-distance between the fluorophore and the metal surface can be determined with nanometers accuracy, but the interaction range over which efficient energy transfer is an order of magnitude larger than for conventional FRET [182] - given us a possible solution to the problem with the short interaction range of FRET.

Enderlein proposed this technique theoretically at the end of the 1990's [183] and demonstrated experimentally in 2014 [182, 184], showing that the fluorescent lifetime of a fluorophore can be tuned by the presence of a metallic surface depending on the distance between them with nanometer precision [184].

MIET is based on the modulation of a luminescent molecule's de-excitation rate to the ground state by the near-field coupling to surface plasmons in a thin metal film deposited on the substrate surface [182, 185] or metallic nanoparticles [186]. This modulation of the luminescent molecule can be measure as a change in its fluorescence lifetime, which can be converted into height values. For a fluorophore positioned to a distance z from a flat metallic surface, the fluorescent lifetime of the fluorophore $\tau(z, \theta)$ is given by:

$$\frac{\tau(z, \theta)}{\tau_0} = \frac{1}{1 - \Phi + \Phi \cdot [S_{\perp}(z) \cos^2\theta + S_{\parallel}(z) \sin^2\theta] / S_0} \quad (3.6)$$

where z is the distance between the dipole and metal, θ orientation of the emission dipole moment, τ_0 is the fluorescent lifetime of the fluorophore in the absence of the metal, Φ is the free-space quantum yield, S_0 is the total amount of energy emitted by the fluorophore per time in free space. S_{\perp} and S_{\parallel} are, respectively, the perpendicular and parallel components of the emission rate, which are independent on θ and depends on the wavelength (λ) of the virtual photon emitted by the fluorophore, and on the complex reflective index of the metal, for more details see the theoretical background proposed by Jörg Enderlein in 1999 [183]. As the complex reflective index (n_m) for silver and gold, at 670 nm, are $n_m = (0.16 + i4.07)$ and $n_m = (0.17 + i3.61)$, respectively, resulting in that $S(S_{\perp}, S_{\parallel})$

is almost identical for both metal [183]. On the other hand, if n_m is much different, aluminum $n_m = (1.45 + i7.7)$, resulting in S different from the previous cases. Showing that the S_{\perp} and S_{\parallel} , and therefore $\tau(z, \theta)$, highly depend on the complex refractive index of the metallic material. Recently, it has been shown that if a layer of graphene is used as the substrate, MIET still occurs on fluorophores. In this case, graphene has a $n_m = (2.77 + i1.41)$ (at $\lambda = 680\text{nm}$) resulting in a shorter interaction range than the shown for a gold substrate [187]. We can then conclude that the MIET resolution and interaction range highly depend on the substrate material.

The dipole lifetime change in the presence of a gold film of 20 nm thickness function

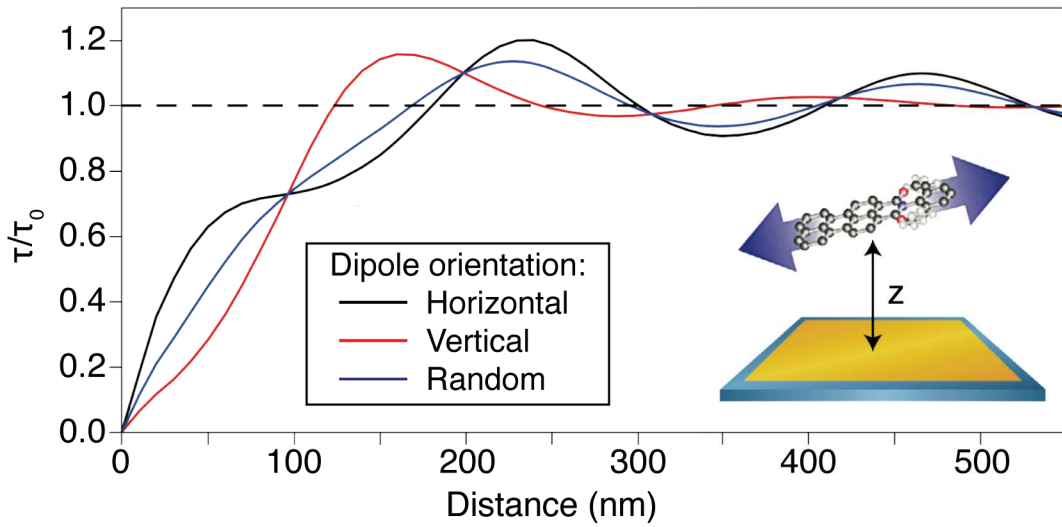


Figure 3.7: Metal-induced fluorescence lifetime modification in the presence of a gold layer. Calculated dependence of fluorophore lifetime in the function of the dipole-gold film separation (z). Gold thickness of 20 nm. Three cases are shown: horizontal, vertical, and random dipole orientation. Adapted from [182].

of the distance- for different dipole orientations- is shown in Figure 3.7. It is worth to mention that equation 3.6 is only valid for a dipole-plane interaction. However, our case is different; we will use a metallic sphere interacting with a dipole.

3.3 MIET-AFM

MIET-AFM is a novel technique that correlates AFM morphology measurements with MIET as Super-Resolution fluorescence microscopy in a synchronous way. The use of MIET is dedicated to molecular recognition taking advantage of its high spatial resolution. We chose MIET, rather than another similar technique like FRET, due to its interaction range. As previously mentioned, MIET occurs over larger interaction distances than FRET (up to one order of magnitude higher). On the other hand, MIET-AFM has a competitive advantage in comparison to some of the Super-Resolution fluorescence techniques, since it is compatible with confocal fluorescence microscopy, allowing us to probe locally, simultaneously, and synchronously the mechanical properties and molecular recognition on the sample. The latter is crucial in biological membranes due to high dynamics and heterogeneity, as discussed in the first chapter. As this technique is probing the sample in a synchronous and simultaneous approach, we do not need to correlate both topographically and recognition maps after the acquisition as most of the correlatives techniques, avoiding to deal with mechanical drift and membrane dynamics.

The following section is devoted to the MIET-AFM working principle. Then, we will explain the FLIM-AFM setup developed for the MIET-AFM operational scheme, the troubles encountered during the development, and how we solved them. Finally, we will introduce the MIET-AFM probes that we fabricated and used in our experiments, emphasizing why they are crucial for a successful experiment.

3.3.1 MIET-AFM working principle

MIET-AFM requires synchronous and simultaneous FLIM-AFM. As we have shown before, the fluorophore lifetime change depends on its distance from the metal surface and which metal is involved in the energy transfer. If the metallic surface is a nanoparticle, the distance and efficiency of this energy transfer also depend on the nanoparticle size. The setup employed is a simultaneous and synchronous AFM-FLIM, where the fluorophore is located at the AFM tip apex, in such a way that its position can be controlled by the

AFM setup and the sample scanner, ensuring high vertical and lateral precision. The fluorophore is excited by a supercontinuum laser, and the photons emitted are collected by an avalanche photodiode (APD) and the information is transferred to the TCSPC card. Then, if a metallic nanoparticle is at the sample, the fluorophore can be precisely approached to this nanoparticle. There are two cases: (i) if the relative distance between the fluorophore and metallic nanoparticle is larger than the energy transfer range, the fluorophore fluorescence lifetime will not be affected. We call it 'low MIET' regime, as shown in Figure 3.8a). (ii) On the other hand, if the relative fluorophore-metallic nanoparticle distance is in the energy transfer range, the fluorophore fluorescence lifetime will decrease. We call it 'high MIET', and a schematic is shown in Figure 3.8b).

By using this working principle, molecular recognition maps can be obtained by scanning

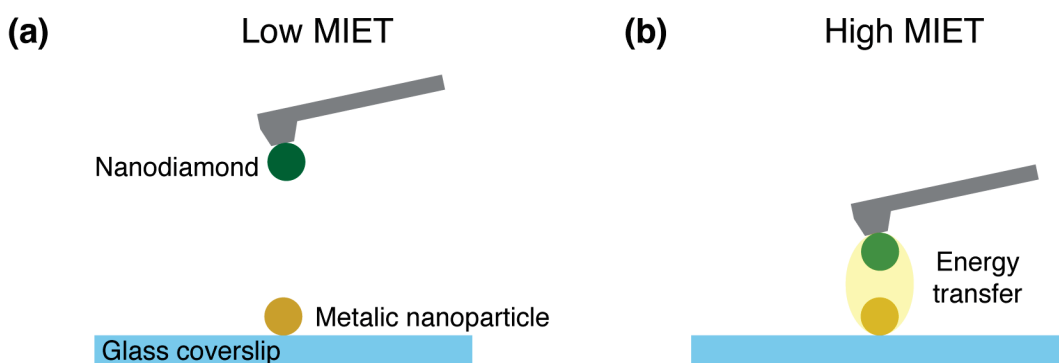


Figure 3.8: MIET-AFM working principle. a) Low MIET, and b) High MIET.

by AFM a sample where the molecules of interest are labeled with a metallic nanoparticle, in our case, gold nanoparticles. In this operational scheme, the MIET-AFM setup can address simultaneous and synchronous measurements of the sample morphology (and its mechanical properties) and molecular recognition maps by monitoring the change of the fluorophore lifetime located at the AFM tip apex as shown in Figure 3.9. Since MIET is a technique with axial resolution inferior to the diffraction limit, we expect for our MIET-AFM to have tens of nanometers as lateral resolution, as discussed in Section 3.2.

The choice of the fluorophore to place at the AFM tip apex is a tricky one. The two main characteristics that this fluorophore must have are the following:

- Capable to transfer energy to the metallic nanoparticle: here we focus on gold nanoparticles.

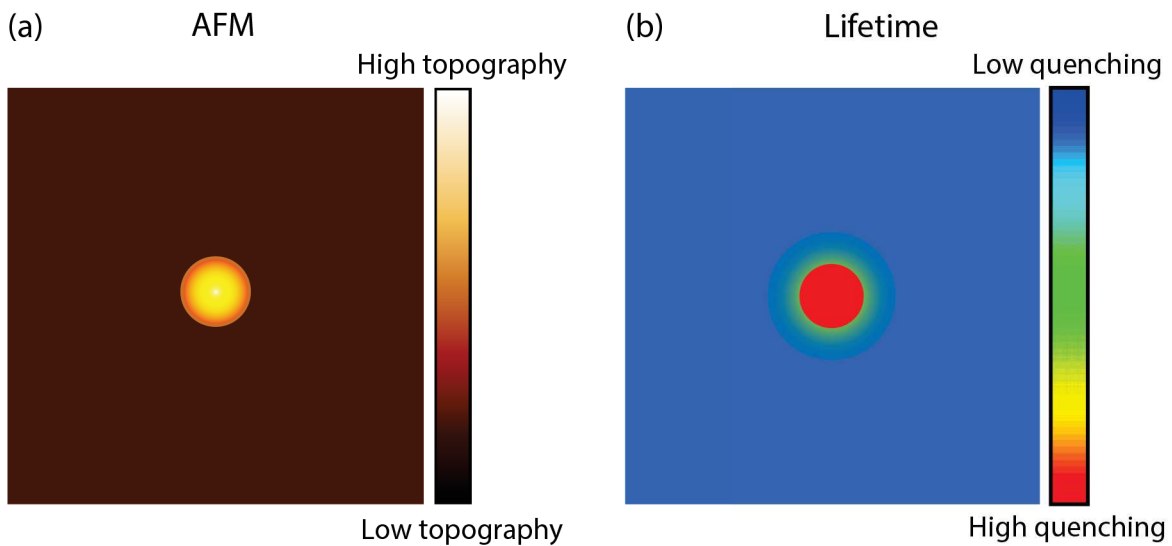


Figure 3.9: Expected MIET-AFM maps by scanning a single gold nanoparticle. a) AFM morphology, and b) lifetime of the fluorescent emitter located at the AFM tip apex.

- Photostability, the fluorophore is continuously exposed to the excitation light, which, in most of fluorophores, produces photochemical alteration resulting mainly in molecule photobleaching and blinking. Both effects do not permit a stable MIET-AFM acquisition. One of the possible solutions to this problem is to work at a lower laser power as possible. However, a single MIET-AFM image could take a couple of minutes, which is a long time for most of the fluorophore, even at low laser power.

The solution that we propose is the use of fluorescent nanodiamonds, which contain defects (color centers) in their structure providing interesting fluorescent properties. In the fluorescent nanodiamond's structure, two adjacent carbon atoms are replaced by a nitrogen atom and a vacancy, as shown in Figure 3.10a. This defect site is called a nitrogen-vacancy (NV) center [188]. There are two different types of NV, depending on its charged state: NV^0 state, which is neutrally charged. On the other hand, NV^- is negatively charged. We decided to use the NV^- due to its photophysics properties. One of the most relevant characteristics is its unlimited photostability meaning that nanodiamonds with NV centers never bleach (any detectable change in their fluorescence emission in function of time). In addition, most of the NV centers do not blink, as shown in the graph of Figure 3.10c. The latter makes the nanodiamonds more suitable for our instrument than the quantum dots (QDs) because of the random blinking exhibited on QDs [189]. This makes QDs tricky to use as the fluorescent probe at the AFM tip apex because this behavior can induce

artifacts and fluorescence variations that are not sample-dependent, imposing complexity to the interpretation of the QDs emission. Therefore, we preferred nanodiamonds over QDs.

Nanodiamonds have a large absorption and emission spectrum, as shown in Figure 3.10b, where the zero-phonon line of NV^- is located at 637 nm, and the resulting fluorescence emission is between 600 and 850 nm [190, 188]. Nanodiamonds have a long fluorescence lifetime of around 15 ns in DPBS solution, as shown in Figure 3.10d. This outstanding photostability makes NV centers- in nanodiamonds excellent candidates to be used as fluorophore for MIET-AFM. In this scheme, we have to address how to bind them at the tip apex in order to maximize the energy transfer that highly depends on the fluorophore-metal surface distance. This will be addressed in the next subsections, after having described the correlative FLIM-AFM experimental setup.

3.3.2 Experimental setup

We developed a synchronous and simultaneous Fluorescence Lifetime Imaging Microscopy (FLIM)-AFM setup. This setup is based on Nanowizard 4 AFM (JPK Instruments, Bruker) equipped with a Tip Assisted Optics (TAO) module (JPK Instruments, Bruker) and a Vortis-SPM control unit. The AFM cantilever detection system was custom-modified employing an infrared low-coherence light source, with emission centered at 980 nm and further long-pass filtered at 850 nm with a Schott RG850 filter. The AFM head was mounted on custom-made confocal microscopy based on a Zeiss inverted optical microscope with an oil immersion objective with a 1.4 numerical aperture (Plan-Apochromat 100x, FWD = 0.17 mm, Zeiss) and a pinhole of 100 μm diameter size (P100D, Thorlabs). The excitation source is a Rock-PP supercontinuum pulsed laser (Leukos), which operates at 20 MHz (50 ns pulses of width < 100 ps). On the detection side, we used an avalanche photodetector (SPCM-AQR-15, PerkinElmer) connected to an SPC-150 (Becker & Hickl) TCSPC card to collect fluorescence signals. To filter out the photons from the AFM detection system in the fluorescence emission path, we used an ET800sp short-pass filter (Chroma). The excitation laser power was measured after the objective at the sample

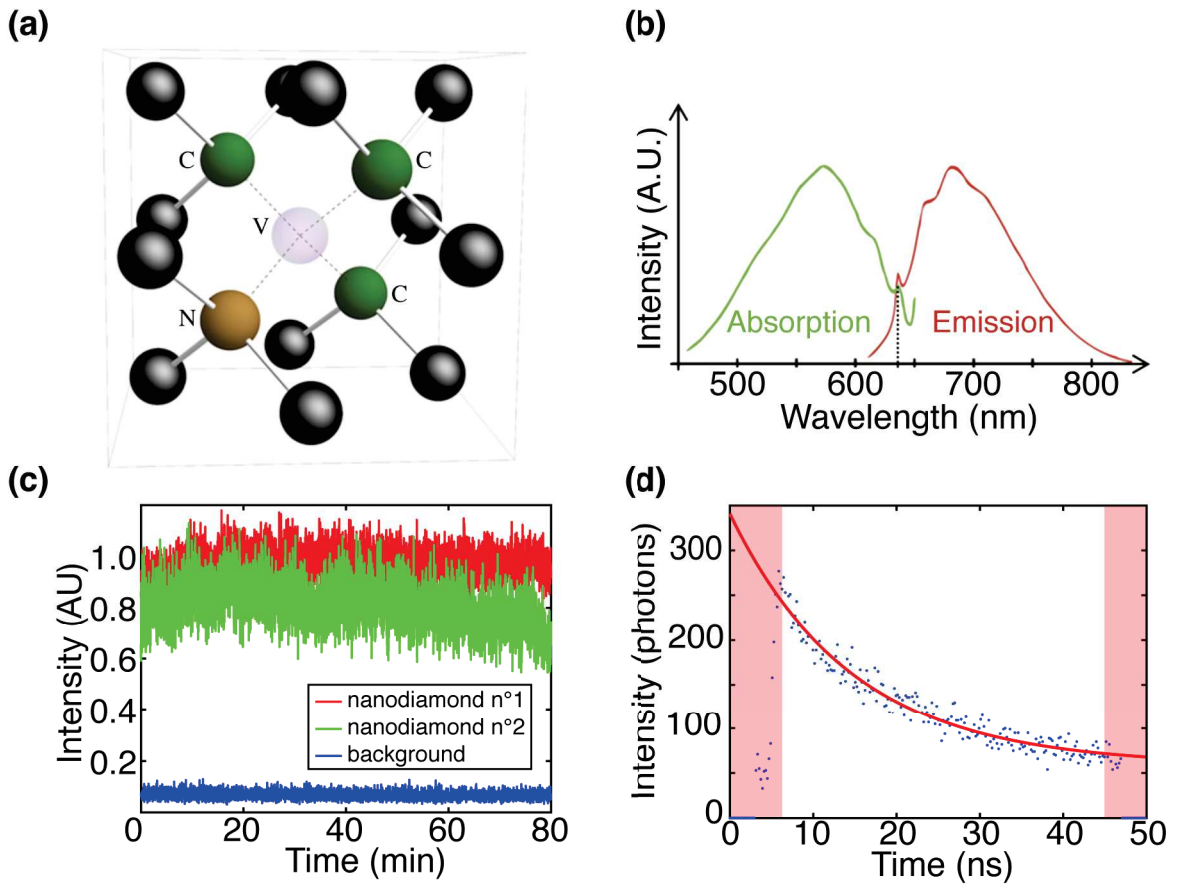


Figure 3.10: Fluorescent nanodiamonds. a) Schematic of the nitrogen-vacancy center and diamond lattice depicting the vacancy (transparent purple), the nearest neighbor carbon atoms to the vacancy (green), the substitutional nitrogen atom (brown), and carbon atoms in the defect's proximity (black). Adapted from [191]. b) Optical absorption and emission spectrum of the fluorescent nanodiamonds, where the dash line corresponds to the zero phonon line (ZPL) at 637 nm. Adapted from [192]. c) Photostability of nanodiamonds acquired in TIRF microscopy with a 562 nm excitation laser, 700/50 nm emission filter, and 1 frame/s. d) Fluorescence lifetime of a nanodiamond using a 532/10 nm excitation filter, 100 μ W of power, and a 709/167 nm emission filter. The transparent red areas represent the excluded data from the fit. The nanodiamond lifetime is 14.7 ± 1.7 ns.

level with an S170C microscope slide power sensor and a PM 100 energy meter interface (both purchased from Thorlabs). Both emission and excitation filters utilized are shown in Table 3.1. Our setup can be adapted and optimized to different fluorophores and dyes by merely exchanging the emission and excitation filter. A schematic and a photo of the setup are shown in Figure 3.16 a) and b), respectively.

The main advantage of our setup is the capability to acquire FLIM/AFM images simul-

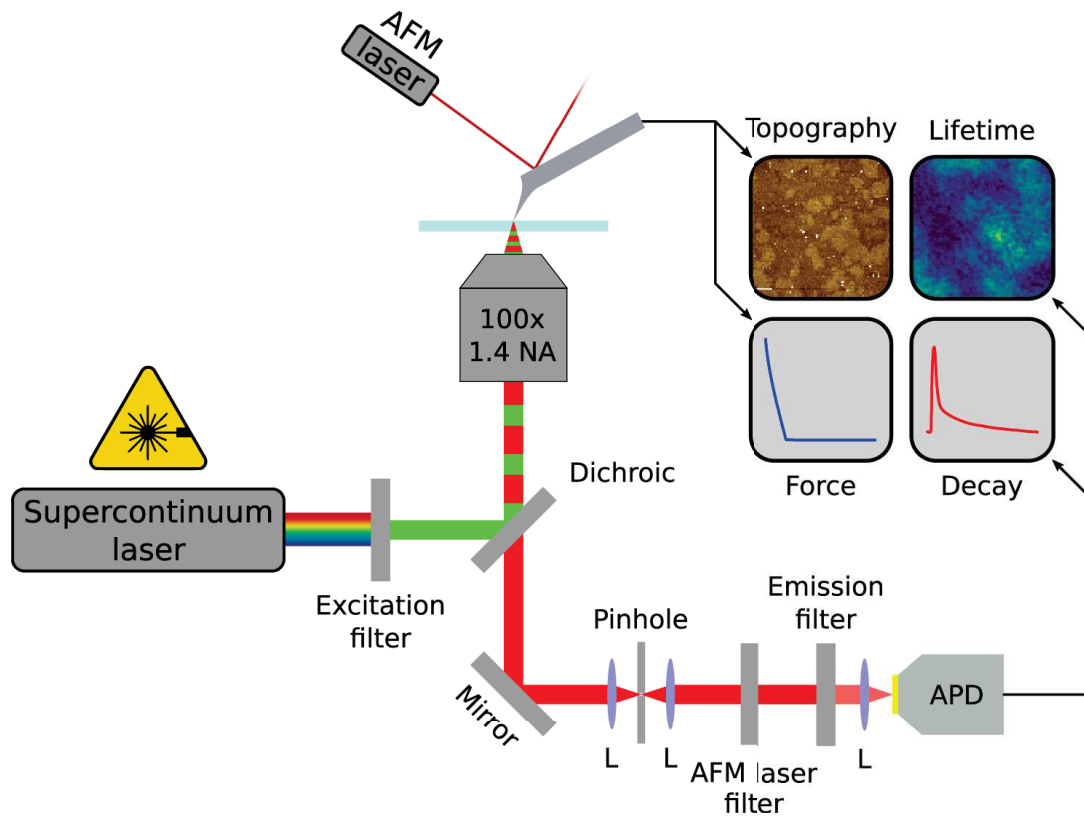


Figure 3.11: Simultaneous FLIM-AFM setup.

Table 3.1: Emission/Excitation filters

	Model	Wavelength [nm]	Brand
Excitation	ZET488/10x	448/10	Chroma
	ZET532/10x	532/10	Chroma
Emission	FF01-525/39	525/39	Semrock
	AT690/50m	690/50	Chroma
	FF01-709/167- 25	709/167	Semrock

taneously. By aligning the AFM tip to the confocal spot and fixing the tip position. Full alignment is obtained in two steps:

1. The tip is at first roughly aligned using white field illumination, and then the alignment is fine-tuned using the increase of tip luminescence.

2. The sample is imaged, and any mismatch between topography and FLIM image is adjusted by correcting the tip position.

After the alignment process, we keep the AFM tip always at the center of the confocal spot. To image the sample, the tip is fixed in position, and we scan the sample using the TAO as sample scanner.

Keeping the confocal spot and AFM tip aligned during data acquisition has the advantage of maintaining constant all spurious effects resulting from the synchronous operation. In addition to the tip/cantilever luminescence background and the optomechanical deflection, we mention the mirror-like effect that is due to the reflection of the incoming excitation light by the metallic coating at the cantilever backside: this results in a higher excitation intensity that is constant all over the image acquisition if confocal spot and tip are aligned, whereas it is not in case of wide-field epifluorescence or confocal spinning disk operational schemes.

3.3.3 Confocal-AFM cross-talk

The combination of confocal microscopy and AFM has some troubles that need to be investigated and quantified as the photothermal induced deflection resulting from metal coating at the cantilever backside [193], radiation pressure exerted on the tip [194] due to the scattering of the confocal spot and finally perlever luminescence [195].

The phenomena that affect the AFM tip due to the focused excitation light interaction are two: optomechanical forces and/or tip/cantilever luminescence, where the former branches into radiation pressure and photothermal effect. Radiation pressure (Figure 3.12a) will always be present in all cases since the scattering of the incoming light will generate forces due to the change in momentum of light. Momentum conservation dictates that the cantilever will be deflected upwardly by this force. Photothermal deflection (Figure 3.12b) is present if the cantilever is composed of two different materials (similar to bimetallic strip), which is the case of metal-coated cantilevers, where a thin layer of metal is deposited onto the cantilever backside to improve reflectivity. For visible light, gold will absorb more than either silicon or silicon nitride (due to the higher extinction coefficient), and due to

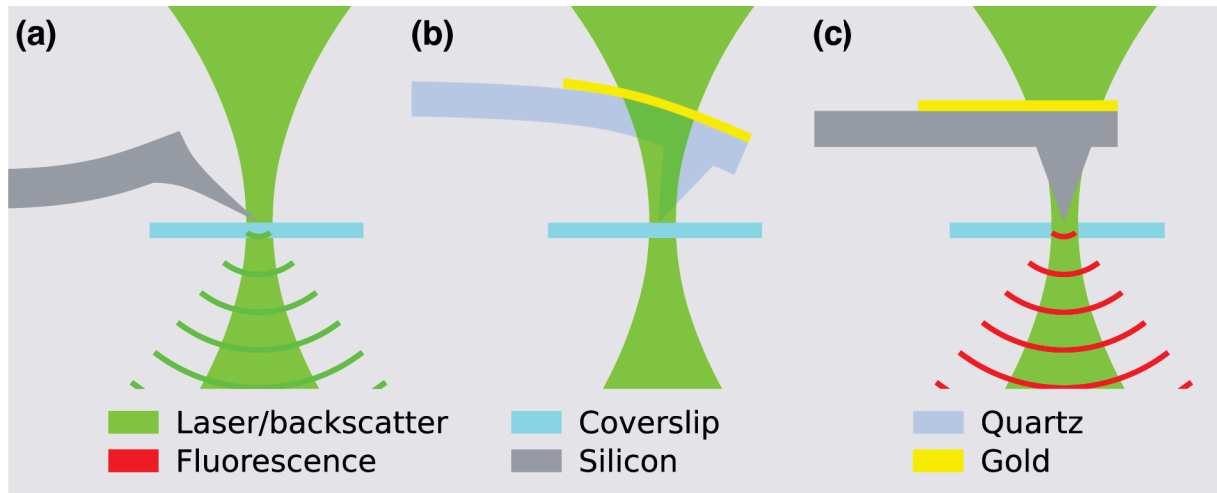


Figure 3.12: Possible AFM tip and confocal spot interactions. a) Radiation pressure. b) Photothermal induced deflection. c) Cantilever/tip luminescence.

its higher thermal expansion coefficient, it will expand more when heated by the laser. This differential expansion will cause a downwards bending of the cantilever. Spurious luminescence (Figure 3.12c) can arise from two sources:

1. The tip/cantilever material itself can present luminescence properties, as in the case of amorphous silicon nitride, particularly important at wavelengths higher than 800 nm [195].
2. The coating on the cantilever backside can be luminescent as well, as for example, gold that emits in the red region of the spectrum [196].

It is worth to notice that backscattered light will occur in all possible configurations since the tip will always scatter the incoming light of the confocal spot in all directions and, therefore, for the same reason, radiation pressure will always be present. However, most of the backscattered light can be easily eliminated by a notch filter when it is not already sufficiently reflected by the emission filter.

We characterized and quantified these effects by operating the AFM in the reverse-tip imaging configuration [197]. The confocal spot is focused 4 μm from a glass coverslip and held in place throughout the measurement. Using the 'hover mode' of the AFM, the tip scans the glass coverslip in the trace scan, and then, in the retrace scan, the tip follows the retrace topography vertically displaced in z by a given distance specified by the user.

In this way, it is possible to make a constant height image even if the sample is inclined. In this mode, the cantilever's deflection is monitored in the retrace scan without active feedback. Deflection (force) and intensity (photon counter) images are acquired during the scan, as shown in Figure 3.13. The resulting images will be of the confocal spot's interaction with different regions of the tip for different focal planes. In this operational scheme, the confocal spot is steady and operates as a "probe," while the AFM tip and cantilever are the samples to be measured, hence the name, reverse-tip imaging. We used three AFM cantilevers with different specifications: a protruding silicon tip (Figure 3.13a), a quartz-like tip with gold coating on the cantilever backside (Figure 3.13b), and silicon nitride (Si_3N_4) with a gold-coated cantilever (Figure 3.13c), commercially available as ATEC-CONT (Nanosensors), qp-BioAC (Nanosensors), and MLCT-BIO-DC (Bruker), respectively. The images were acquired both with the tip in focus and out-of-focus positions to observe the different interactions of the confocal spot (300 μW power, 532/10 nm wavelength) with the AFM tip and cantilever body.

Given the broad emission spectra of silicon [198], silicon nitride, and the metallic coating on the cantilever backside, in our case gold, the choice of the emission filter is not crucial if compared to fluorescence imaging of conventional organic fluorophores characterized by narrow emission spectra. In Figure 3.13, we used a 690/50 nm emission filter. Panels 1, 3, and 5 show the photon intensity signal, whereas panels 2, 4, and 6 display the vertical force acting on the AFM cantilever. Figure 3a shows that the ATEC-CONT has a bright central spot in the photon intensity channel due to tip luminescence and presents a positive force in the range of a few hundred of piconewtons. By inserting a notch filter in the emission path, no significant change in the photon intensity channel is observed, which shows that backscattering contribution is minimal, and the band-pass emission filters completely filter it out. Such a positive force is a direct consequence of the radiation pressure acting on the cantilever due to the backscattered light. With the qp-BioAC (Figure 3.13b), the situation is consistently different: the force is negative, and it has a maximum modulus of ≈ 7 nN. The confocal spot interacts strongly with the gold reflective coating on the cantilever backside, as shown in the photon intensity images, Figure 3.13b panels 1, 3, and 5. Consequently, the interaction induces a differential heating that bends the cantilever downwards due to photothermal effects. The intensity signal presents no direct correlation with force observed and is highly dependent on the

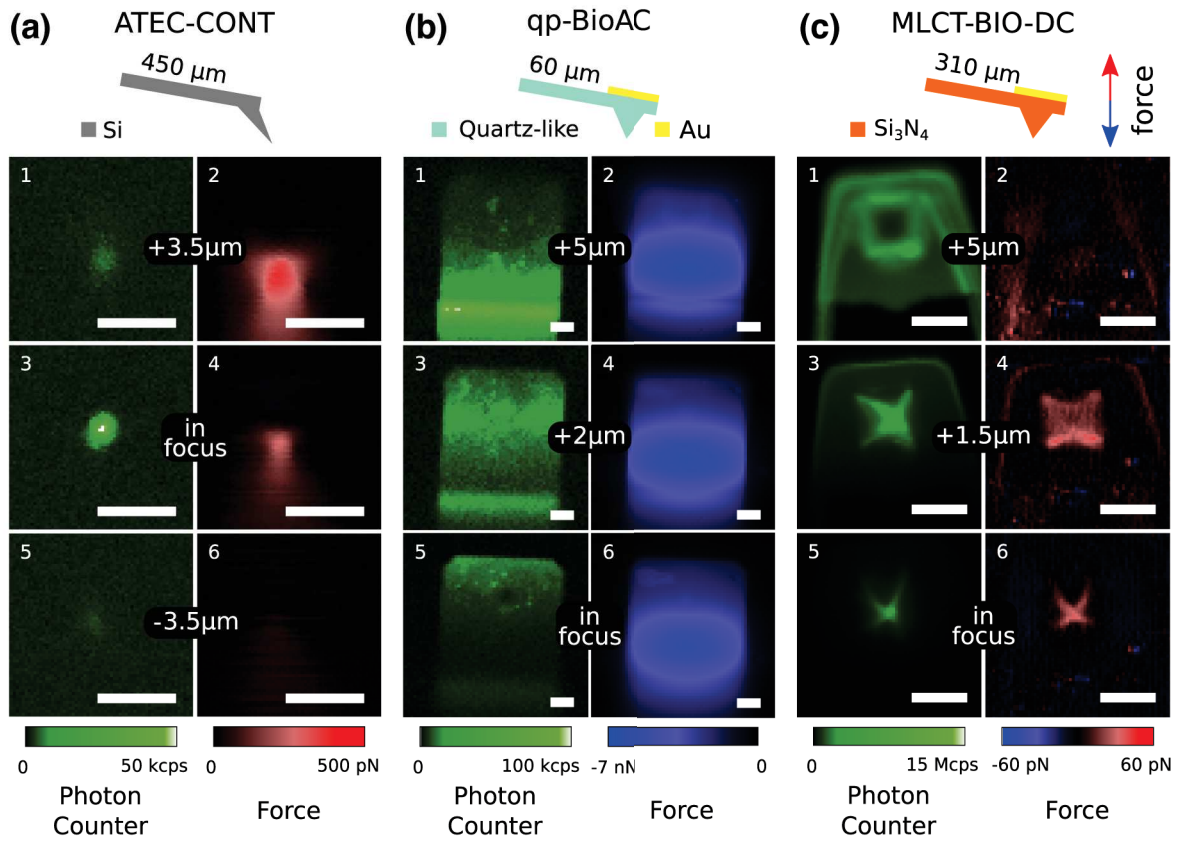


Figure 3.13: Simultaneous photon counts (panels 1, 3, and 5) and force (2, 4, and 6) scans for three different AFM cantilevers. a) ATEC-CONT, b) qp-BioAC, and c) MLCT-BIO-DC. The images were acquired utilizing the reverse-tip image operational scheme where the confocal spot is a probe, and the AFM tip and cantilever are the samples to be measured. Data were performed with a 532/10 nm excitation filter, a 690/50 nm emission filter, with a laser power of 300 μ W. Subfigures 1-2, 3-4, and 5-6 were acquired at different distances from the confocal spot focal plane. The scale bar is 5 μ m for all images. In the schematic of the cantilevers, the nominal cantilever length and the red and blue arrows indicate positive and negative force directions, respectively, corresponding to the color scale in panels 2, 5, and 6. Intensity (photon counter) images (panels 1, 3, and 5) are given in counts per seconds (cps) and were recorded directly from the APD. The cantilever used for the qp-BioAC is the CB2 (0.1 N/m of nominal spring constant), while the one for MLCT-BIO-DC is the cantilever C (0.01 N/m of nominal spring constant). The Point Spread Function (PSF) of the confocal spot is \approx 400 nm.

cantilever bending angle. In contrast with the previous case, the tip position is characterized by a darker spot in the photon intensity image (Figure 3.13b panel 5) that is due to the fact that both excitation light and gold emission have to pass through the tip,

therefore through a higher quantity of material. As a consequence, we collect less fluorescence emitted by the reflective gold coating material when the tip and confocal spot are aligned. The MLCT-BIO-DC (Figure 3.13c) shows a mix of radiation pressure and mild photothermal deflection contributions in the force signal. In this case, it is also possible to observe the interaction with the tip's gold-coating, but the thermal effects are not as drastic as before, leading to a totally positive force acting on the cantilever when the tip and confocal spot are aligned. The small deflection of the MLCT-BIO-DC, despite the presence of a gold coating at the cantilever's end, could be attributed to its manufacturing process, optimized to minimize probe bending due to elevated temperatures.

Given the data presented in Figure 3.13, the arising question is what cantilever is worth using to reduce cross-talk between AFM and time-resolved fluorescence acquisitions in correlative experiments. Figure 3.14a presents time-resolved fluorescence decay curves acquired for the three AFM cantilevers of Figure 3.13 with a high laser power of $300\text{ }\mu\text{W}$ to maximize signal to noise ratio for the less luminescent ones. MLCT-BIO-DC (yellow curve) has the highest intensity signal by two orders of magnitude and presents a long lifetime in comparison with the qp-BioAC (red curve) and the ATEC-CONT (green curve).

While ATEC-CONT and qp-BioAC will affect the measured lifetime of fluorescent probes characterized by a short ($\approx 1\text{ ns}$) lifetime, the MLCT-BIO-DC will affect a larger variety of fluorophores presenting even longer lifetimes. Besides, we monitored the spurious force's variation as a function of the incident laser power (see Figure 3.14b). The force scales linearly with the power, and the different cantilevers branch in the two categories depending on the nature of the optomechanical interaction: radiation pressure and photothermal induced deflection.

It is worth to notice that the photothermal deflection computed in this case, for a laser power of $300\text{ }\mu\text{W}$, is inferior in modulus to the 7 nN shown in Figure 3.13b because in the latter case, the maximum force is measured with the confocal spot focused on gold-coated cantilever backside and not on the AFM tip as in Figure 3.14b, as previously mentioned. Table 3.2 reports the slopes from Figure 3.14b, force versus laser power, which indicates the force's significance for a given probe.

Concluding, according to our results, low laser power should be used, and the relative position between the tip and the confocal spot should be held constant, leading to a change of the cantilever equilibrium position while avoiding a change of relative deflec-

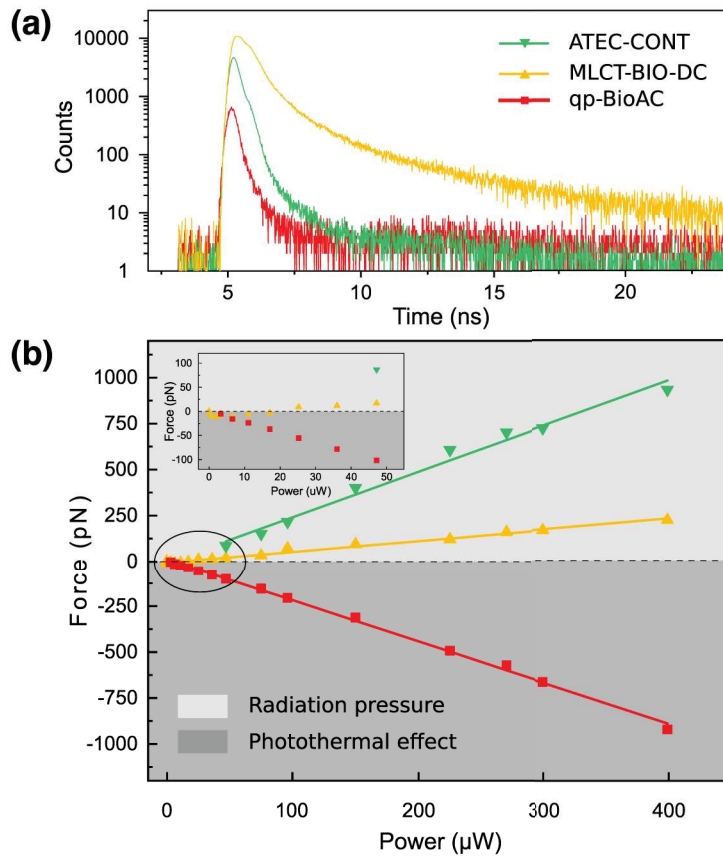


Figure 3.14: Luminescence decay curves and variation of the measured force for three different AFM cantilevers. The cantilevers used are qp-BioAC (red), MLCT-BIO-DC (yellow), and ATEC-CONT (green). a) Luminescence decay curves for different AFM cantilevers. b) variation of the measured force as a function of the laser power. The inset shows a zoom of the region of low power, highlighted by the ellipse. Positive force is characterized as radiation pressure (light grey region), while negative force is photothermal induced deflection (dark grey region). All curves in a) were acquired with 532/10 nm excitation filter, 690/50 nm emission filter, and 300 μW .

tions. Besides, our data suggest (Figure 3.14a) that the qp-BioAC cantilevers should be employed to accurately evaluate the lifetime of the fluorescent probes within the sample. Instead, MLCT-BIO-DC cantilevers, presenting lower spurious force, are more suited for experiments where low AFM interaction forces have to be measured and in the presence of a large number of fluorophores in the excitation volume, ensuring a high signal to noise ratio to properly evaluate their lifetime.

Table 3.2: Slopes of the fits in Figure 3.14.

Cantilever	Brand	Optomechanical constant [pN/ μ W]
ATEC-CONT	Nanosensors	2.47 ± 0.13
qp-BioAC	Nanosensors	-2.24 ± 0.03
MLCT-BIO-DC	Bruker	0.59 ± 0.02

3.3.4 Simultaneous FLIM-AFM

The advantage of the correlative AFM-FLIM imaging mode relies on the complementarity of the two techniques. In order to test our setup, we imaged fluid and gel phases enriched domains in biological model membranes correlating their morphology (AFM) with their local viscosity (FLIM). We prepared a sample of DOPC:DPPC (v:v 1:1) labeled with 0.1 % BODIPY in volume on round glass coverslips (28 mm diameter, 165 μ m thick, purchased from Marienfeld) as described in Appendix A.

For the simultaneous acquisition of AFM, confocal microscopy, and FLIM, we used: AFM images of the membrane were acquired in contact mode using a rectangular qp-BioAC cantilever (Nanosensors) with a stiffness of 0.3 N/m at a constant force of 1.5 nN at a line imaging rate of 0.25 Hz with 128 lines x 128 pixels and with a scan size of 15 μ m x 15 μ m. Images were acquired using a 488/10 nm excitation filter and a 535/39 nm emission filter with a laser excitation power of 120 nW, ensuring the highest accuracy for BODIPY lifetime evaluation while minimizing the spurious force during AFM acquisition. The measurements were performed at room temperature.

Lifetime analysis: The FLIM image has a lifetime curve per pixel acquired. They are processed in the SPCM software (Becker & Hickl). The presence of the tip, qp-BioAC in this case, in the confocal spot results in a signal of a low lifetime, < 1 ns, as shown in Figure 3.15a. In Figure 3.15a, a decay curve from DOPC region from Figure 3.16c is shown, while Figure 3.15b) shows the respective phasor plot. The decay curve presents no peak with low lifetime, indicating that the tip does not contribute with any spurious signal. This is further corroborated by the phasor plot showing data that belong to a single population and close to the semi-circle.

Both topography (Figure 3.16a))and fluorescence intensity (Figure 3.16b)) shown that

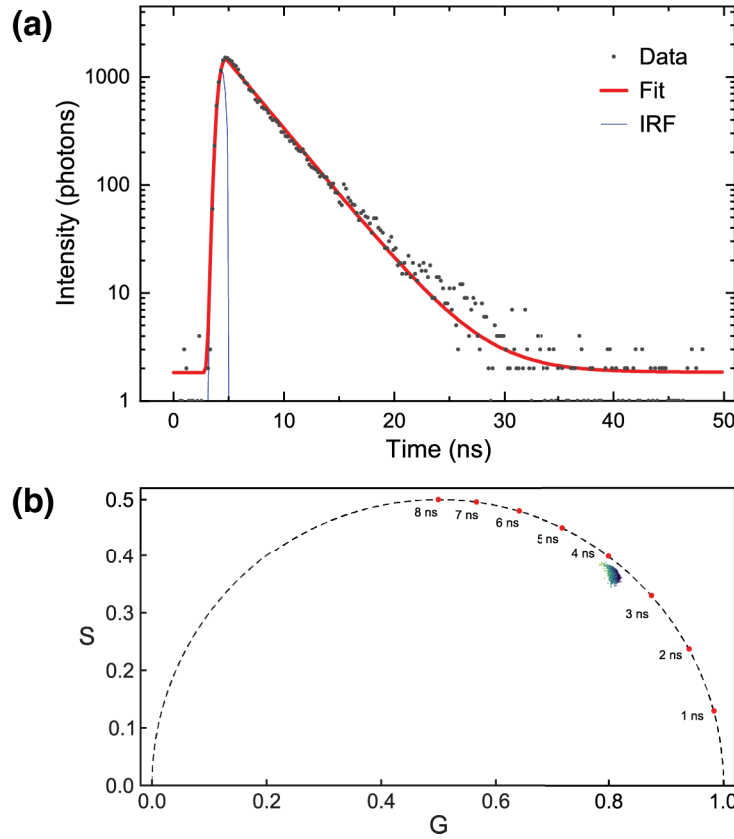


Figure 3.15: Lifetime analysis for DOPC:DPPC curves labeled with 0.1 % BODIPY. a) Decay curve from a DOPC enriched region, where the blue curve is the Instrumental Response Function (IRF), black dots are experimental data, and the red curve is the experimental data fit. b) phasor plot of all DOPC/DPPC enriched regions. The power used was 120 nW, with an excitation filter of 488/10 nm and a band-pass emission filter of 525/39 nm. A qp-BioAC cantilever was employed.

DPPC enriched regions (higher thickness) have lower BODIPY concentration than DOPC enriched regions. Wu et al. showed in GUVs that high viscosity lipids present higher BODIPY's lifetime. Hence BODIPY's lifetime can be used to probe the viscosity of the lipid directly [199]. Figure 3.16c) shows that DPPC enriched domains have a higher lifetime when compared with DOPC domains, 3.71 ± 0.09 ns and 3.55 ± 0.07 ns, respectively, as shown in the histograms of Figure 3.17; this is expected since DPPC is a gel-phase lipid (at room temperature), hence more viscous than DOPC (fluid-phase lipid). The higher lifetime, above 3 ns, when compared to Wu et al. ≈ 1.8 ns [199], can be attributed to the fact that SLBs are formed on top of a substrate (glass), inducing different physical behaviors in terms of lipid diffusion and potentially local viscosity when it is compared to free-standing bilayers in the GUVs case. Indeed, even if the presence of a layer of buffer

(2-3 nm thickness) between the lipid polar heads and the substrate generally prevents an important hindrance in lipid diffusion [38], it is known that the latter can be reduced as compared to giant unilamellar vesicles [200]. The tip luminescence, dominated by a low lifetime (<1 ns), is not present in the simultaneous AFM-FLIM imaging.

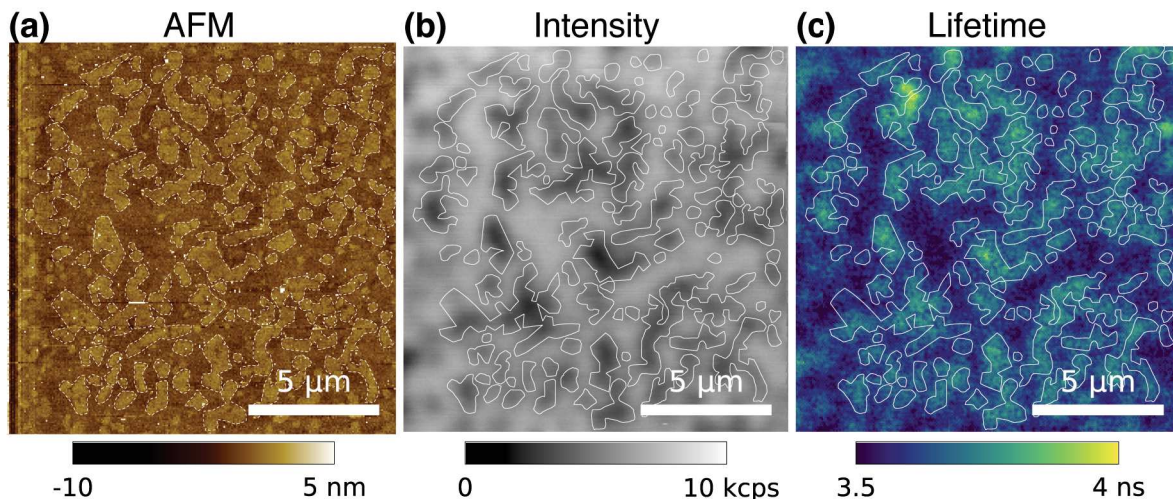


Figure 3.16: Simultaneous FLIM-AFM on DOPC:DPPC (1:1 molar ratio) SLBs on glass labeled with 0.1% of BODIPY. a) AFM morphology, b) fluorescence intensity, c) lifetime. The scale bar is $5 \mu\text{m}$, the power used was 120 nW with a 488/10 nm excitation filter and a 525/39 nm emission filter. An a qp-BioAC tip was employed. The dashed white lines serve as a visual aid for the separation of the two lipid enriched domains.

3.3.5 Preparation of a MIET-AFM probes

MIET-AFM makes use of a nanodiamond at the tip apex as fluorophore. As previously shown in this chapter, nanodiamonds are fluorescent stable nanoparticles due to their NV center, which means they never bleach and do not blind, making them ideal candidates for experiments that require long photostability as MIET-AFM experiments. However, all nanodiamonds are different in terms of size and number of NV centers. Then, we need to grab a single nanodiamond at the AFM tip apex selectively, which is a problem because we can not use functionalization methods that graft a random nanoparticle from a sample. In order to address this problem, we have tested different methods such as tip chemical functionalization and deposition of a thin film of optical glue functionalization to graft a nanodiamond selectively. However, we did not achieve a sufficient reproducibil-

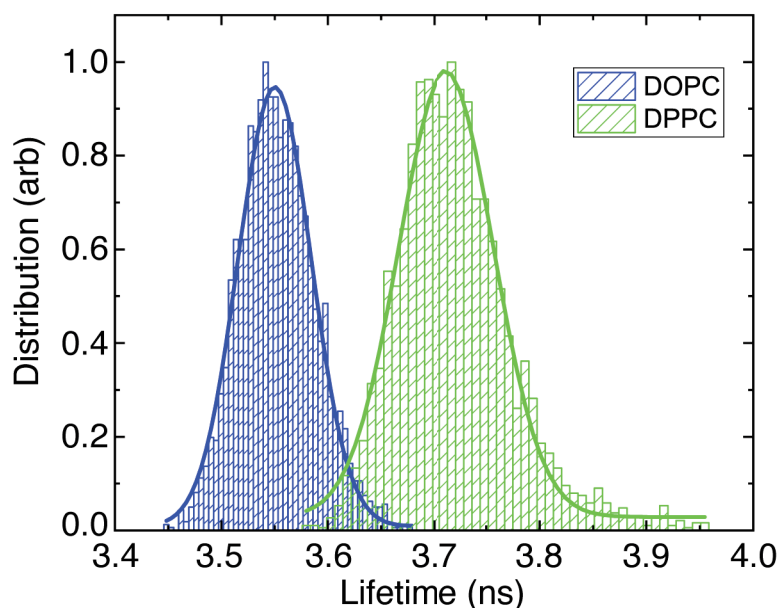


Figure 3.17: BODIPY lifetime distribution from DOPC (blue) and DPPC (green) domains from Figure 3.16. The lifetimes of DOPC and DPPC are 3.55 ± 0.07 ns and 3.71 ± 0.09 ns, respectively.

ity with those protocols. Finally, we developed a protocol where a custom-made plateau cantilever - based on a qp-BioAC cantilever- is functionalized with Poly-L-Lysine (PLL) coating. In this way, we can glue a nanodiamond by electrostatic forces due to the fact that nanodiamonds are negatively recharged, and PLL is positively recharged. Custom qp-BioAC tips, presenting a plateau at the tip apex, were purchased from Nanoworld: they were fabricated, modifying a qp-BioAC cantilever (see Figure 3.18e)). An electron beam deposited carbon tip was grown on top of a thin layer of gold, and through Field Ion Beam (FIB), a flat circular plateau of ≈ 50 nm diameter was obtained. The advantage of the modified qp-BioAC plateau tip is that the plateau increases the nanoparticle-tip contact area.

Fluorescent Nanodiamonds (FNDs) were purchased from FND Biotech (Taiwan). A solution of 40 nm diameter nanodiamonds, each containing in average 15 NV centers, at a concentration of 0.1 mg/mL was sonicated for 15 min and subsequently diluted to 0.1 μ g/mL in deionized water. 5 μ L were deposited on a round glass coverslip (28 mm diameter, 165 μ m thick, purchased from Marienfeld) that was previously cleaned by a cycle of sonication in KOH for 15 min, followed by a second cycle of sonication in deionized water for 15 min, and subsequently dried under nitrogen flow. Once the deposited nanodia-

monds solution is dried, the sample is mounted and mechanically fixed in an Attofluor chamber (Thermofisher) and rehydrated with DPBS solution.

Concerning the AFM tip functionalization, a modified qp-BioAC plateau tip (Nanosensors) was coated with Poly-L-lysine hydrobromide (P0879) purchased from Sigma-Aldrich, depositing 2 μL of PLL solution at 1 mg/mL on the tip for 15 min. Afterward, the tip is removed from the PLL drop and left to dry.

The PLL-coated tip was mounted in the AFM and calibrated using a combination of a Sader [201] and thermal [146] methods (called "contact-free" method in the JPK AFM instruments). The fundamental peak was used with a correction of 0.817 at room temperature and in a liquid environment (DPBS). Subsequently, the AFM tip and confocal spot were aligned as described in the experimental setup of this chapter. Fluorescence images were acquired without AFM tip to pre-localize nanodiamond candidates on a glass coverslip for the grafting process, as shown in Figure 3.18c). Consequently, an AFM image with a low force setpoint ($\ll 1$ nN) and few pixels (32 pixels x 32 pixels) in the same area in AFM dynamic mode avoiding tip pollution and damage, obtaining the nanodiamond morphology and profile as shown in Figure 3.18a) and 3.18b), respectively. The PLL-coated was then pressed on the selected nanodiamond for 1 minute with a 1 nN setpoint [197]. Afterward, a fluorescence image of the same area was acquired to check if the selected nanodiamond was grafted; it will not be present in this image, as shown in Figure 3.18d). The use of PLL permanently sets the nanodiamond to be at the tip apex if low forces are used to avoid dislodging events.

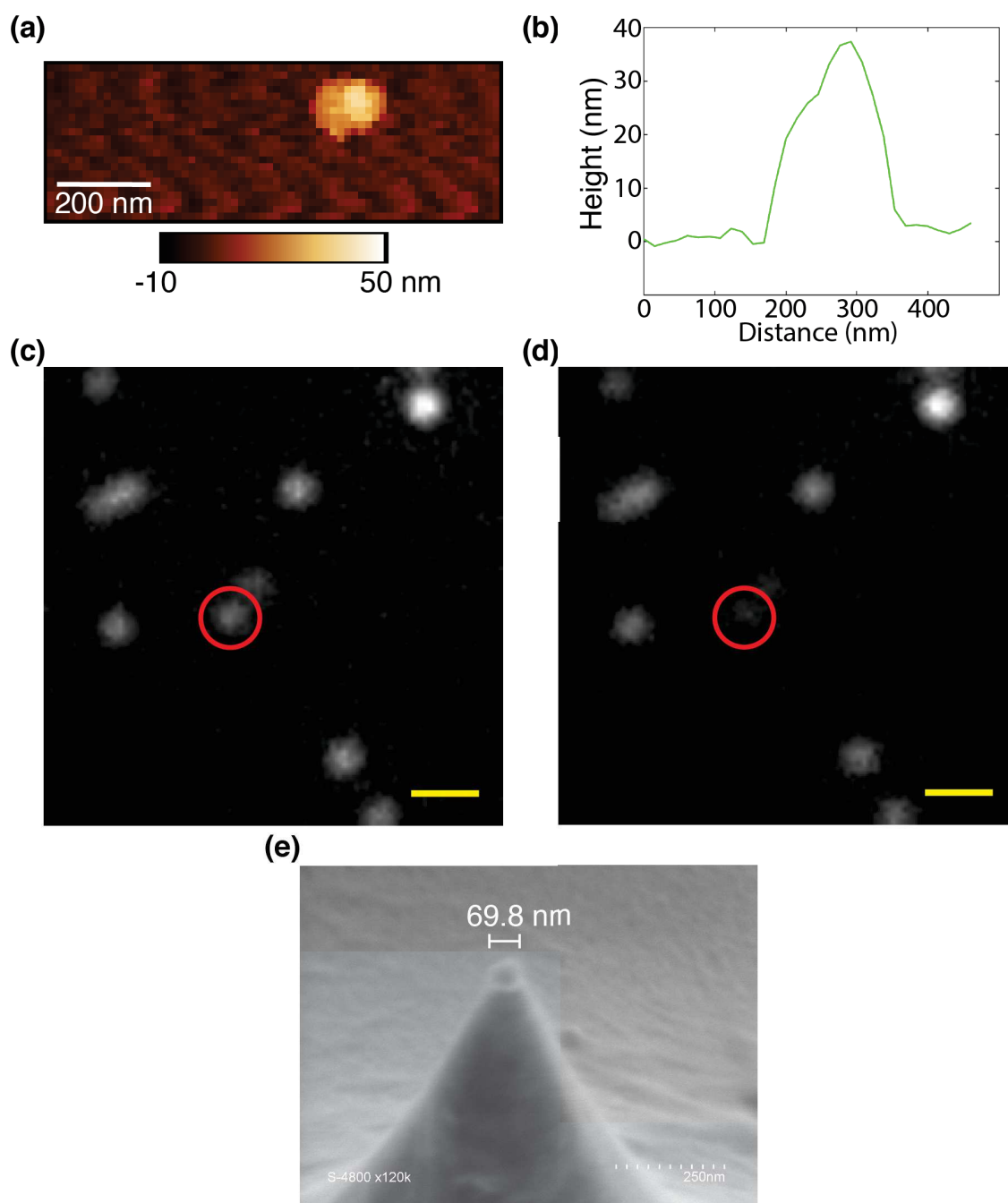


Figure 3.18: Grafting a single and selected nanodiamond. a) AFM topography image of the nanodiamond to graft measured with the functionalized plateau tip. b) Nanodiamond's profile from a). c) TIRF image of nanodiamonds sample on a glass coverslip: the selected nanodiamond to be grabbed by the AFM tip is highlighted by a red circle. d) TIRF image of nanodiamonds sample on a glass coverslip once the nanodiamond has been grabbed by the AFM tip. The scale bar in c) and d) are 5 μm . e) SEM image of a modified qp-BioAC plateau tip.

3.4 Experiments

Having tested the FLIM-AFM experimental setup and having developed a method to prepare and fabricate MIET probes, the MIET-AFM setup must be experimentally tested. In this subsection we describe different experiments that will quantify and set up the crucial parameters required to carry on MIET-AFM on biological membranes. The first experiment aims at testing the NV centers (on the MIET probe) as a fluorescent dipole, quantifying the change of its lifetime in the presence of a metallic substrate. After, we will measure the shift of the nanodiamond lifetime in the presence of metallic nanoparticles of different sizes. Once the dependency on the distance is understood, we will perform MIET-AFM experiments on the same metallic nanoparticles deposited on a glass coverslip in order to acquire MIET-AFM molecular recognition images on the most straightforward system possible. We chose gold as the material for all these experiments because of its refractive index, as discussed in section 3.2. As a perspective, MIET-AFM will be tested on DNA origami functionalized with two nanoparticles separated at a well-defined distance to evaluate the minimal separation that MIET-AFM can distinguish.

3.4.1 Simultaneous force curve and nanodiamond lifetime on a flat gold surface

To test the efficiency of NV centers on a nanodiamond in the presence of a metallic surface in the function of the distance. We adapted our setup to perform AFM-FS and fluorescence spectroscopy experiments synchronously. In this novel operational scheme, the AFM tip has fluorescent properties- due to the nanodiamond grafted at the tip apex- that can be correlated with the force measured by AFM while being approached or retracted from the sample. The force readout can be used to define the mechanical contact position between the sample and the fluorescent probe. Subsequently, the latter can be accurately placed with nanometric precision at a given distance from the sample, and its lifetime can be probed. In this approach, we can characterize the NV centers' efficiency in the function of the distance (in all distance range) within a nanometric resolution.

Gold-coated coverslips were prepared. 24 mm diameter circular glass coverslips (Marienfeld) were subjected to sonication cycles in acetone (5 minutes) and ethanol (5 minutes) and subsequently dried under nitrogen flow. 5 nm or 10 nm of gold were evaporated on top of coverslips by thermal evaporation method at a rate of 1 Å/s (AS053 Oerlikon thermal evaporating source). The sample was mounted and mechanically fixed in an Atof fluor chamber (Thermofisher) and hydrated with Dulbecco's Phosphate Buffer Solution (DPBS), purchased from GIBCO, without MgCl_2 and CaCl_2 (GIBCO ref. 14190-094). AFM and photons collected were synchronized by tagging each photon read by the TC-SPC card with the TTL signal from the AFM instrument, which enables the acquisition of decay curves for every z-position of the tip. We acquired approach-retract curves with the simultaneous collection of force, photon intensity (photon counter), and fluorescent nanodiamond lifetime was performed using 532/10 nm as excitation filter and 709/167 nm as emission filter with a laser excitation power of 90 μW . In order to analyze only the photons emitted by the nanodiamond, the photons with a lifetime below 6 ns were discarded due to the dominance of IRF and the gold luminescence, as explained in the previous section. Afterward, the number of photons emitted by the nanodiamond is in the order of tens of counts per second (cps), whereas normal acquisition speed in modern AFM can reach hundreds of kHz [202]. Since hundreds to thousands of photons are needed to evaluate the lifetime properly, our acquisition bandwidth must be reduced to a few tens/hundreds of Hz. Faster acquisition rates would result in the collection of too few photons (or even none), and the lifetime evaluation would be impossible. For this reason, we have fixed our acquisition bandwidth to 20 Hz and performed forced curves in a quasi-static mode at a speed of 5 nm/s.

Lifetime was evaluated by amplitude weighting the decay curve for times greater than 6 ns. All measurements were performed at room temperature and under liquid conditions in DPBS. The tip was held constant, and the sample was approached to the tip using the axial sample piezo of the TAO module. The tip-confocal alignment was performed similarly to the method described above with a critical change: we focused the confocal spot when the tip is in mechanical contact with the sample surface. Hence the maximum signal from the nanodiamond/gold happens at the contact point (Figure 3.19).

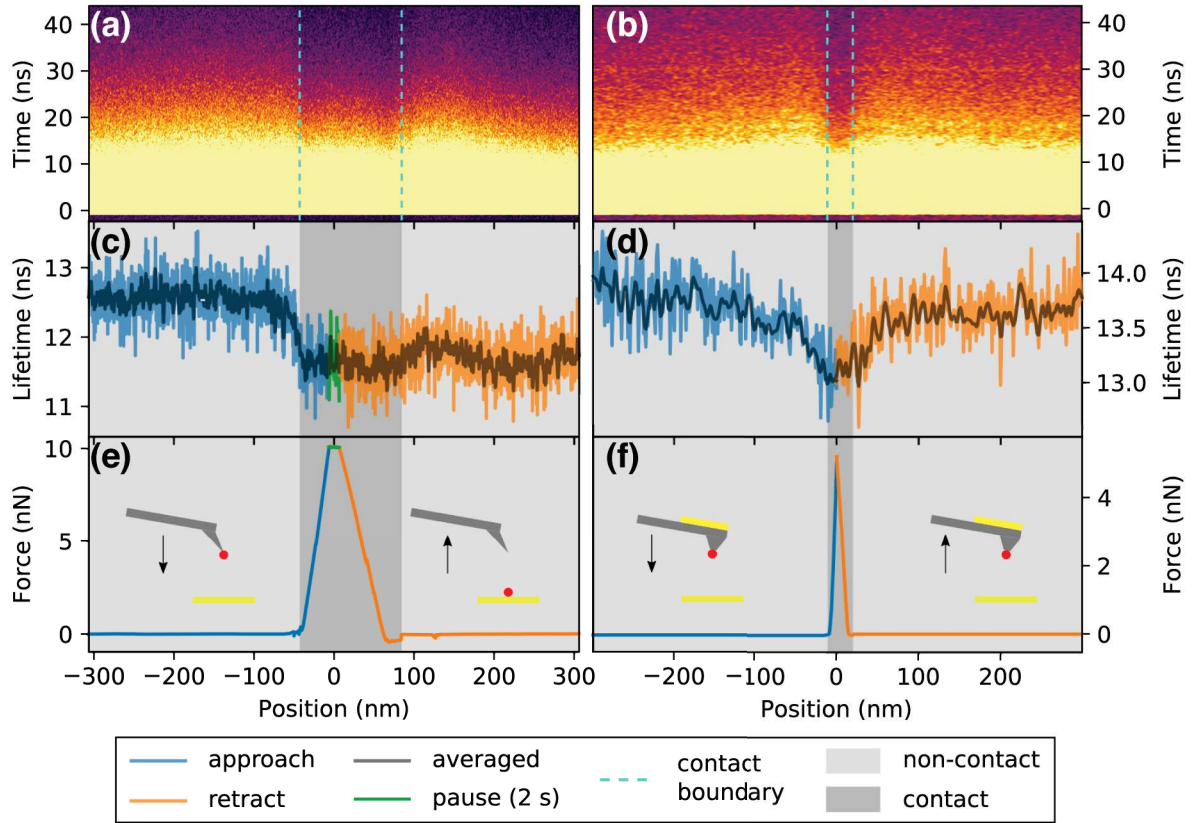


Figure 3.19: Simultaneous force curve and nanodiamond lifetime measurements approaching and retracting a gold substrate. Photons are synchronized with TTL from the AFM enabling the acquisition of decay curves for every z-position of the tip. (a,b) Show the tip z-position versus time (decay curves), where the color scale represents the number of photons collected (brighter means more photons and vice versa)

. (c,d) Show the lifetime of the nanodiamond in function of the tip position. (e,f) Show the standard force curves unfolded so approach and retract curves are separated in the negative and positive axis, respectively. The blue curves in (c-f) consists of the approach whereas orange region the retract. The green curves in (c,e) constitute a region where the tip was paused for 2 seconds. The light gray region displays the non-contact (zero force) interactions whereas the darker gray consists of the contact regime. A 532/10 nm excitation filter was used with a 709/167 nm emission filter with power of 90 μ W. The dark gray curves in (c,d) show the data with spatial (9 neighbors) and temporal (4 neighbors) binning (filter). The same binning is also applied to (a,b) to aid visualization. An ATEC-CONT was used in (a,c,f) whereas in (b,d,f) a modified qp-BioAC red (CB1) with a plateau was used. Tip schematics in (e,f) show an AFM tip with a nanodiamond (in red) and the gold substrate (yellow). In the retract curve of (e) the nanodiamond is left on the surface whereas in (f) it is kept at the tip's end.

By approaching and retracting the nanodiamond to the gold-coated coverslip, we show the decrease of the lifetime of NV centers in a diamond nanoparticle due to MIET [203]. Figure 3.19 shows an example of nanopositioning and nanomanipulation of a nanodiamond attached to the apex of an AFM tip. Figure 3.19a and b show a plot of the decays for every pixel (z-position, axis). The color scale represents the number of 3.19e and f. Firstly, we approached an ATEC-CONT tip holding a nanodiamond at its apex to a gold substrate, pressed with a high force (10 nN), and held in place for 2 seconds (Figure 3.19a, c, and e). This allowed the nanodiamond to dislodge from the tip and to stay permanently on the gold. The tip was then retracted without the nanodiamond. This can be clearly seen from Figure 3.19c, where the lifetime decreases, approaching the gold, and never recovers back during tip retraction from gold. The lifetime of the nanodiamond changes from 12.60 ± 0.28 ns to 11.69 ± 0.30 ns, which corresponds to a quenching efficiency of $\approx 7.2\%$. In a second experiment, showed in Figure 3.19b, d, and f, we used a custom qp-BioAC tip (CB1) with a plateau at its end, holding a stable nanodiamond at the tip's apex. In this configuration, the fluorescent nanodiamond is approached, pressed with lower force (5 nN), and retracted from the gold substrate without being dislodged from the AFM tip. The lower force is a requirement to avoid the loss of the nanodiamond upon contact. The lifetime and force curves are symmetric, Figure 3.19d, and f, showing that the interaction is reversible. The nanodiamond lifetime changes from 13.86 ± 0.27 ns to 13.13 ± 0.23 ns upon contact with the gold, which corresponds to a quenching efficiency of $\approx 5.5\%$. The quenching in lifetime when approaching gold, or any metal, is expected due to MIET [203]. The radiation rate will change due to the coupling of the nanodiamond electromagnetic near-field with the gold's plasmons. In the vertical position (x-axis) of Figure 3.19e and f the approach and retract curves have been "unfolded", where approach/retract have negative/positive position values.

In Figure 3.19, we have shown that the lifetime decrease occurs in the absence of mechanical contact between the fluorescent probe and the gold substrate, at short distances where the AFM is not sensitive enough to detect any interaction force. In perspective, this enables the possibility to obtain topographical images in liquid acquired in the absence of AFM tip-sample mechanical contact. It represents a significant advance when it is to image soft, fluorescently-labeled samples that are largely deformed by conventional AFM due to their extreme softness as it occurs in the case of living cell membranes.

In our case, only a small drop (7% and 5%) in nanodiamond lifetime is observed in Figure 3.19c and d, respectively. Although the change is small, uncertainty in lifetime characterization is in order of hundreds of picoseconds; therefore, the change observed is still significant. Tisler et al. have observed a 35% MIET efficiency when approaching a single NV center 25 nm nanodiamond attached to an AFM tip on top of graphene, a material that behaves like metal [204] as described in Section 3.2. In our case, the small MIET efficiency observed in Figure 3.19 could be attributed to either the larger nanodiamond size (≈ 40 nm) or the more abundant number of NV centers (≈ 15) that are randomly oriented in the nanodiamond core. In the case of the experiment shown by Tisler et al. [204] a complete lifetime spectroscopical change with respect to the nanodiamond-sample distance is not reported. Indeed, in their case, the lifetime variation was measured only when the nanodiamond was in mechanical contact with graphene or the underlining substrate.

We have shown that MIET can be achieved in our setup by approaching a nanodiamond to a gold flat substrate. However, our goal is to image membrane components and to achieve that, we should label the biomolecules of interest with small metallic nanoparticles to detect and show that we can localize them by MIET-AFM. Next subsection is devoted to metallic nanoparticles imaging by MIET-AFM

3.4.2 Simultaneous force curve and nanodiamond lifetime on a gold nanoparticle

Next, we tested evaluated the energy transfer between NV centers and metallic nanoparticle as a function of their reciprocal the distance: the geometry corresponds to the one of MIET-AFM experiments (nanoparticle-nanodiamond interaction).

A nanodiamond was grafted at the tip apex of a custom plateaux qp-BioAC cantilever. Gold nanoparticles were deposited on a glass coverslip. 24 mm diameter circular glass coverslips (Marienfeld) were subjected to sonication cycles in KOH solution at 1 M concentration (15 minutes) and deionized water (15 min) and subsequently dried under nitrogen flow. 100 nm diameter gold nanoparticles in 0.1 mM PBS solution were purchased from

Sigma (Sigma ref. 753688). Gold nanoparticles solution was diluted 100 times, and 2 μL of the diluted solution was deposited on the cleaned coverslip and let it dried. Once it is dried, the sample was mounted and mechanically fixed into an Attofluor chamber (Thermofisher) and hydrated with DPBS, purchased from GIBCO, without MgCl_2 and CaCl_2 (GIBCO ref. 14190-094).

First, we perform AFM-FS and fluorescence spectroscopy experiment synchronously, as reported in the previous experiments. The AFM acquisition bandwidth was fixed to 20 Hz, and force curves were performed in a quasi-static mode at a speed of 5 nm/s, for the reasons explained in the previous experiment. The tip was held constant, and the sample was approached to the tip using the axial sample piezo of the TAO module. The tip-confocal alignment was performed, focusing the confocal spot when the tip is in mechanical contact with the sample surface. Hence the maximum signal from the nanodiamond/gold nanoparticle happens at the contact point (Figure 3.20).

By approaching and retracting the nanodiamond to a 100 nm gold single nanoparticle,

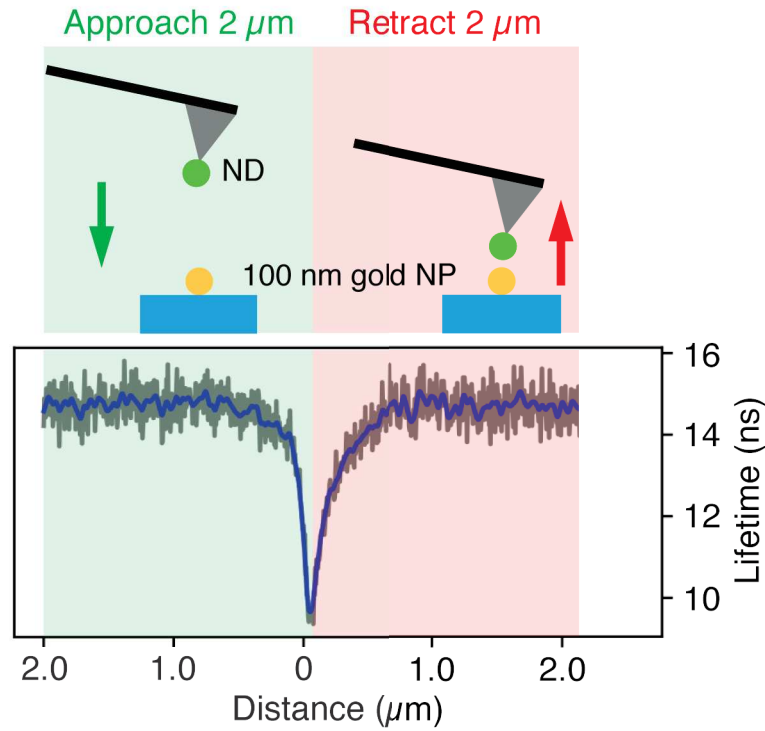


Figure 3.20: Nanodiamond lifetime measurements approaching and retracting from a gold substrate.

we show the decrease of the lifetime of the NV centers in the nanodiamond due to MIET [203]. Figure 3.20 shows the change of the nanodiamond fluorescent lifetime as a function

of the distance with the 100 nm gold nanoparticle. When the tip is approached to the nanoparticle, the lifetime starts to decrease in the absence of mechanical contact, shifting from 15 ns to 9.5 ns upon contact with the gold nanoparticle. The latter corresponds to a quenching efficiency of $\approx 33\%$. Once the tip is retracted from the nanoparticle, the lifetime fully recovered its fluorescent lifetime. Figure 3.20 shows that the approaching-retracting curves for the nanodiamond lifetime are symmetrical, confirming that MIET-AFM can be achieved axial-resolutions below the diffraction limit between the NV centers and gold nanoparticles.

The following step is to test if MIET-AFM can produce images with lateral resolution inferior to the diffraction limit. In order to test the lateral resolution on the MIET-AFM scheme, we performed MIET-AFM images of the 100 nm gold nanoparticles deposited on a glass coverslip. By scanning the previous sample (100 nm gold nanoparticles deposited on a circular glass coverslip) using the TAO module. AFM image was performed on QI mode (the JPK below resonance image mode described in the previous chapter), using a 35 nm nanodiamond grafted at the plateau qp-BioAC tip (CB1), 5 $\mu\text{m/s}$ of tip speed, and 40 ms per pixel. The image was recorded in an area of 1.0 μm x 1.0 μm with 64 px x 64 px. The confocal image was performed using 532/10 nm as excitation filter and 709/167 nm as emission filter with a laser excitation power of 100 μW . The nanodiamond fluorescent lifetime was calculated only for photons with a lifetime above 6 ns in each pixel of the image in order to avoid the IRF and gold luminescence (tip coating and nanoparticle) contributions as explained in the previous subsections. The experiments were performed in a liquid condition in DPBS.

Figure 3.21 shows the MIET-AFM images for the topography (AFM), the nanodiamond intensity (confocal image), and the nanodiamond fluorescent lifetime (FLIM), which were acquired simultaneously for two 100 nm gold nanoparticle. We can ensure that they are two different nanoparticles and not a tip artifact due to tip contamination, or due to the grafted nanodiamond not at the tip apex, because the AFM topography profile shown in Figure 3.21a shows two bumps with the same height, which will be not the case in the case of a double tip/tip artifact. Figure 3.21c shows that the nanodiamond fluorescent lifetime shifted from 15 ns to 12 ns when it is at the top of each gold bead (see Figure 3.22a). The same image shows that the two gold nanoparticles can be distinguished in the lifetime image (Figure 3.21c), proving that we are below the diffraction limit in the

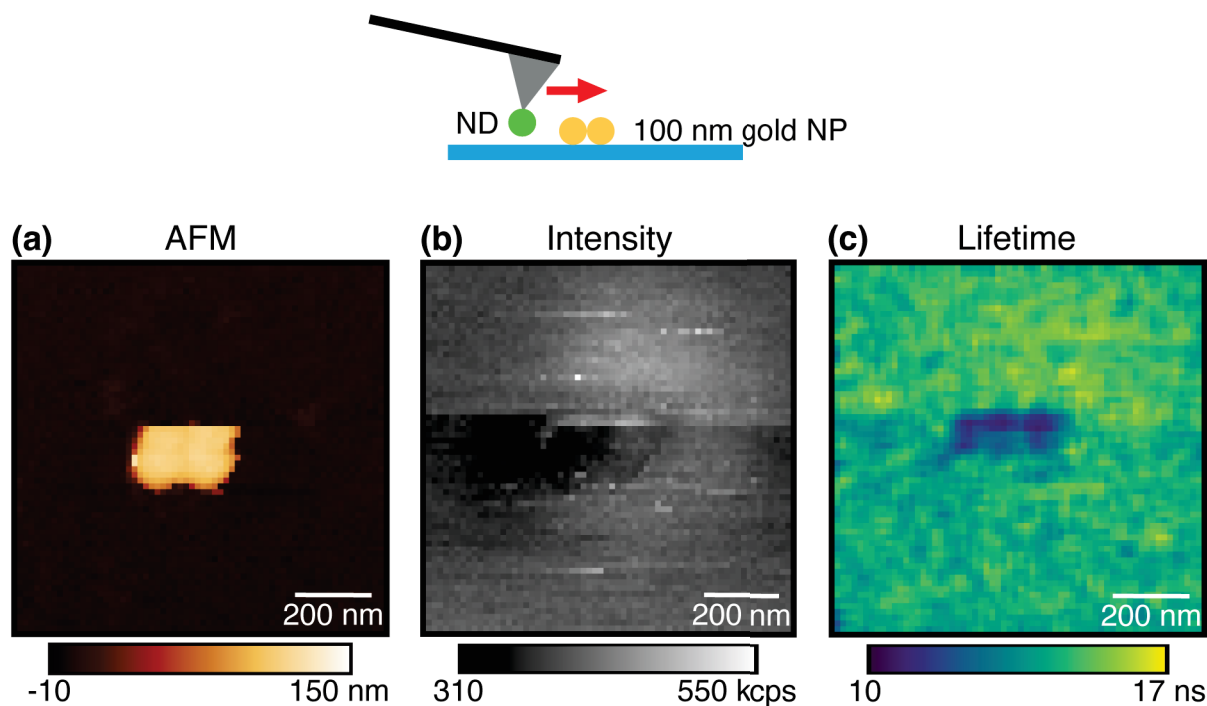


Figure 3.21: MIET-AFM on two 100 nm gold nanoparticles.

molecular recognition map (Figure 3.21c). With this experiment, we demonstrated that our MIET-AFM setup can achieve Super-Resolution molecular recognition maps simultaneously with topographical maps of the sample. However, 100 nm nanoparticles are still large probes to label a molecule. In order to overcome this issue, in perspective, we plan to probe MIET-AFM with smaller gold nanoparticles using the same operational scheme.

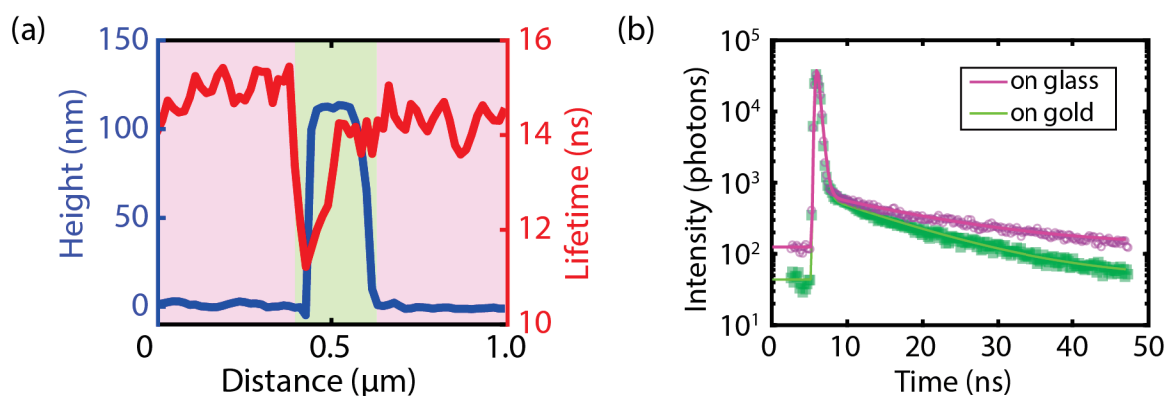


Figure 3.22: MIET-AFM on two 100 nm gold nanoparticles.

3.4.3 The problem of many NV centers per nanodiamond when imaging 30 and 10 nm gold nanoparticles

The natural following step is to perform MIET-AFM using smaller gold nanoparticles on the sample. However, when we approach a MIET-AFM probe with a nanodiamond at the tip apex to a 10 nm gold nanoparticle, any change in the nanodiamond lifetime is detected. We can ensure that our nanodiamond is at the tip apex because this nanoparticle is dislocated after couple of images scanning. The only possibility for this to happen during MIET-AFM scanning (as in Figure 3.21) is that the nanodiamond is positioned at the AFM tip apex. Then, by carefully analyzing the different factors that can affect the nanodiamond quenching, we determined that it is due to the following two:

- The MIET interaction range between a metallic nanoparticle and a fluorescent dipole depends on the nanoparticle size. A smaller metallic bead results in a shorter MIET interaction range and vice versa. As we switched from 100 to 10 nm gold nanoparticles, the quenching range should also decrease by roughly one order of magnitude.
- Our nanodiamonds are 35 nm ones from FND Biotech (Taiwan)- According to the manufacturer, this nanoparticle has 15 NV centers on average. Assuming that the NV centers are randomly allocated on the nanodiamond, some calculations can be done in order to understand the influence of these many color centers. For simplicity, the nanoparticle is replaced by a metallic layer in Figure 3.23. Here, the green dots represent the NV centers, if the z-position of each of them is described as:

$$x_i(z) = z + \delta_i^{NV} \quad (3.7)$$

where z is the minimal distance between the nanodiamond and metallic layer, and δ_i^{NV} the relative z-position of the NV center from the bottom of the nanodiamond. The lifetime of the nanodiamond is the measured lifetime (τ_M), which can be described in function of the lifetime for each NV center as:

$$\tau_M(z) = \left(\frac{1}{n}\right) \sum_n \tau_i(z) \quad (3.8)$$

where n is the total number of NV centers and $\tau_i(z)$ is the lifetime of the i -th NV center. As x_i is always larger than z , the effective distance for MIET is always underestimated. As well, a single nanodiamond has many NV centers, and all of them are randomly allowed on the nanoparticle, resulting in a different lifetime in each one. The closest ones to the metallic surface present a higher quenching than the ones that are positioned at longer distances. Then, if the MIET interaction range is short (due to the use of a smaller metallic nanoparticle), some of the NV centers could not change their lifetime, screening the quenching of the closer ones.

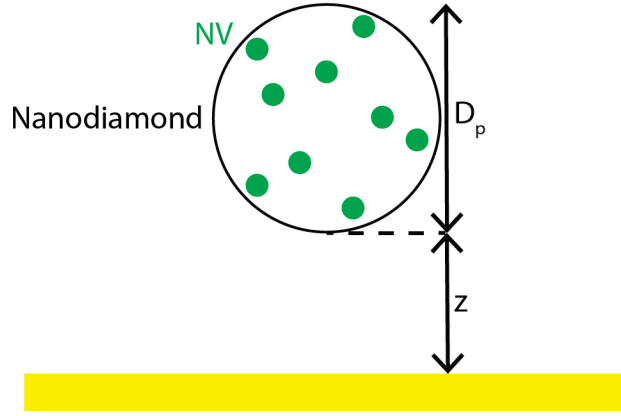


Figure 3.23: Multi-NV centers on a nanodiamond. Schematic of a nanodiamond of diameter D_p with multiples NV centers (in green) randomly distributed. The nanodiamond is separated a distance z from a metallic surface (in yellow).

According to the literature, the MIET quenching distances are in the order of the metallic nanoparticle size. Then, if we use a gold nanoparticle in the same range of size as the nanodiamond, we will measure a small decrease in the nanodiamond lifetime due to the screening of the NV centers quenching. The latter represents the central issue of why we did not measure any change in lifetime when we approached these nanodiamonds on small gold nanoparticles, in particular 30 and 10 nm ones.

A possible solution for that is the use of nanodiamonds with less NV centers, ideally a single NV center per nanodiamond. In this case, when the color center is approached to the metallic nanoparticle the measured lifetime corresponds to the only one present in the

nanodiamond, therefore avoiding any lifetime screening.

3.5 Conclusions

In this section, we have analyzed the second challenge in the study of biological membranes, the chemical sensitivity. In the second chapter, we used AFM to measure and evaluate the mechanical properties of supported lipid bilayers (SLBs) and their morphology at the nanoscale with high lateral resolution. However, as said earlier, AFM cannot distinguish the probed molecules, but AFM can be correlated with another microscopy technique to overcome this issue. Then, in order to achieve molecular recognition, we have developed a home-made confocal FLIM-AFM setup that allows us to measure the morphology and mechanical properties (AFM) and molecular recognition (Fluorescence/FLIM) simultaneously and synchronously. One of this setup's main advantages is its synchronicity because biological membranes are highly dynamic, as previously explained (see Chapter 2 for more details). In this manner, we evaluate the same molecules by both techniques regardless of the membrane diffusion, providing our approach a valuable and competitive advantage over other correlative methods where the sample is scanning sequentially and without synchronization, comparing two different snap of the sample due to the membrane diffusion.

We proposed a new super-resolution technique called Metal Induced Energy Transfer (MIET)-AFM combining MIET and AFM. When a fluorescent dipole is approached a metallic surface, the fluorescent dipole is quenched, shifting its fluorescent lifetime depending on the dipole-metallic surface distance. We proposed using this effect to simultaneously prove the sample's topography and mechanical properties (AFM) and the quenching signal as molecular recognition of a sample previously functionalized with gold nanoparticles.

We designed and developed MIET-AFM probes. They were done fabricating a custom-made plateau tip based on a qp-Bio AC (CB1) cantilever and using them to selectively grafting a single nanodiamond at the plateau tip apex. Concerning the analysis of the fluorescent lifetime of the nanodiamond as MIET-AFM probe, we decided to fit the lifetime

using a tail enhancement method to avoid the system's short lifetime contributions (AFM tip reflections and luminescence). In addition, we fitted our experimental data assuming a mono-exponential decay, which sometimes is not entirely correct, but due to the limited photon budget acquired during the MIET-AFM scan at each point, we were not in the position to distinguish multi-exponential decays. Therefore, this assumption could affect the sensitivity and resolution of our MIET-AFM super-resolution performance. However, our setup can simultaneously detect the topography and changes in the fluorescent lifetime on gold nanoparticles according to our experimental data. The latter confirms that, in first approximation, our data treatment is sufficient to provide super resolved images. Using our MIET-AFM probes, we can achieve molecular recognition images with lateral resolution below the diffraction limit on 100 nm gold nanoparticles deposited on a glass coverslip. Simultaneously with the molecular recognition maps, the MIET-AFM setup is capable of measuring the sample morphology with nanometric resolution. However, when we have tried MIET-AFM scan on smaller gold nanoparticles, 30 and 10 nm, we were not able to detect any quenching. We demonstrated that this can be due to the large number of NV centers (15 per particle on average) randomly distributed in the bead. This issue should be overcome using nanodiamonds with fewer NV centers (a single one in the best case). We also have tested 10 nm nanodiamonds from Adamas nano (North Carolina, US), but most of them are not fluorescent, and a high percentage of them blink and bleach. Indeed, when we tried to selectively graft a single 10 nm sized nanodiamond, our tip got easily polluted with non-fluorescent nanodiamonds.

Another solution could be the use of other fluorescent nanoparticles of small size. By searching in the literature, we have found FluoSphere[™] (FS) commercially available from ThermoFisher in different colors and sizes, from 20 nm up to 15 μm . They do not blink, and the solution does not contain other particles contamination that might pollute our MIET-AFM probes. Additionally, their fluorescent properties, such as the lifetime, are well-reproducible according to our preliminary tests. However, they show photobleaching, which could affect the total acquisition time budget. A possible solution is the sequential grafting of a new FS each time the old one has bleached. Here, we prepare the sample to study using a thin film of PDMS with two holes (made with micro-punches), as shown in the Figure 3.24. The PDMS film is mounted on top of a clean coverslip. A volume of FS

is deposited on one cavity while the sample to study (preliminarily gold nanoparticles) is deposited on the second hole. This sample preparation allows us to switch easily between the sample to investigate by MIET-AFM and the grafting of a new FS when the previous one has bleached. In this way, we can overcome the bottleneck induced by FS bleaching.

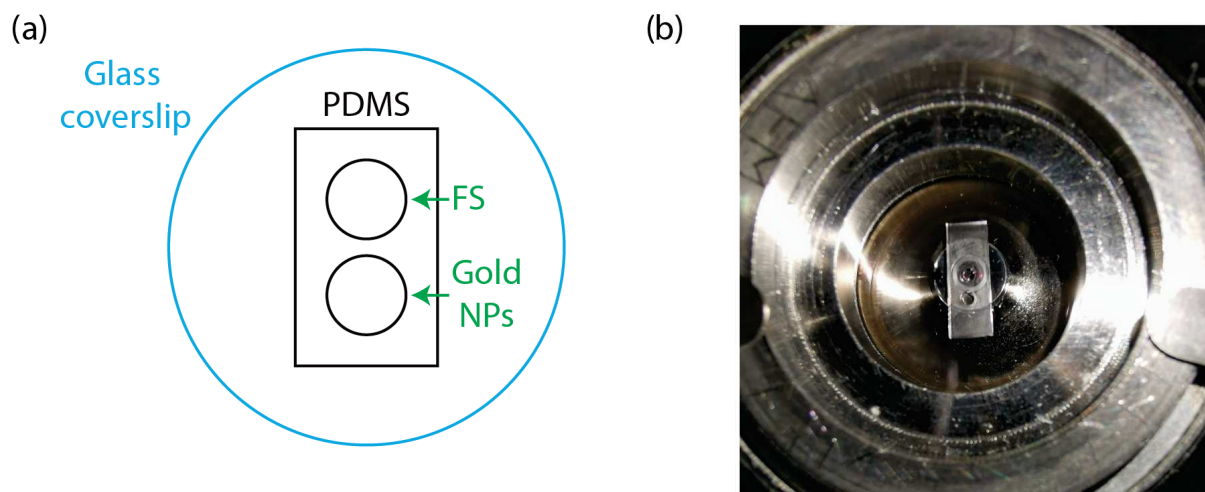


Figure 3.24: Sample prepared using a thin film of PDMS with two cavities on a glass coverslip. a) Schematic of the sample. b) Sample fixed on an Attofluor chamber (Thermofisher) and mounted on our microscope. In both cases, one cavity contains FluoSphere[™] (FS) and the other gold NPs. Each cavity is 1.2 mm in diameter in b).

Chapter 4

Conclusions and Perspectives

4.1 Conclusions

This thesis addressed biological membranes' mechanical stability and developed a novel AFM-Super Resolution technique, MIET-AFM, potentially capable of imaging them using an optical signal (fluorescence lifetime) replacing a mechanical one. The membrane constituents -essentially phospholipids and proteins distributed heterogeneously in the membrane- mainly regulate membrane remodeling processes, which are highly dynamic and require observations at high lateral and temporal resolutions. In perspective, we aim at using the MIET-AFM to characterize those processes.

In this frame, we have presented the three main challenges in the study of membranes:

The membrane-AFM tip interaction force

AFM is a well-established technique for imaging the lateral organization of membranes - in both homogeneous and phase separation- due to its high spatial resolution, achieving few nanometers in the lateral resolution and sub-nanometer in the vertical resolution. However, AFM employs a nanometric tip to interact with the surface, therefore applying a force. Since membranes are very soft materials (with a Young's Modulus ranging from

10 kPa to 100 MPa), they can get easily deformed, bend, and even break during AFM scanning. We have shown that we can distinguish two different lipids-enriched domains by AFM topographic images. Moreover, AFM-FS was used to probe the mechanical properties of membranes at the nanoscale, correlating them with each lipid-enriched domain. Our results show that the size of indenters used to probe membrane mechanics through AFM-FS is crucial to properly quantify intrinsic properties, such as the Young's modulus and the number of molecules involved at the onset of a hole formed within the membrane. We have used one of these intrinsic properties, the Young's modulus, to distinguish and show the presence of two different effects: vertical compression and puncture of membranes. The puncture is a novel effect where we have shown for the first time that, for small indenters, the tip pass-through the membrane with less resistance than in a compression regime. If puncture occurs, the membrane Young's modulus cannot be assessed with small indenters because the membrane is not vertically compressed, at least for the case of DOPC-enriched domains.

On the other hand, when larger indenters probe membranes, our results are in good agreement with Butt, and Franz's theory [143], confirming that the rupture force increases with the indenter radius. However, the number of molecules involved in the AFM tip breakdown process is material-dependent. It remains constant regardless of the indenter size. Finally, we have shown that the AFM tip can be very invasive with the membrane and even break it with a low force if a small indenter is used. Indeed, even without membrane breakage, the membrane can bend and be deformed by the AFM tip mechanical constraints. Therefore, it is essential to correctly choose both the AFM tip size and the force applied to the membrane.

Chemical sensitivity

Biological membranes are constituted by many components distributed heterogeneously. An exhaustive characterization of the biomolecules constituting the membranes requires both their localization and recognition. One of the disadvantages of AFM for probing biological membranes is that it cannot achieve chemical sensitivity. To overcome this problem, we proposed to correlate AFM with another technique to achieve molecular recog-

nition. Consequently, we have decided to combine AFM with fluorescence microscopy, particularly with Metal Induced Energy Transfer (MIET). We have proposed a new Super Resolution technique called MIET-AFM, where a fluorescent dipole positioned at the AFM tip apex is approached to a metallic nanoparticle, which is labeling the molecule of interest. Depending on the dipole-nanoparticle distance, the dipole can get quenched, and its lifetime decreases. In order to develop the MIET-AFM, we have assembled a custom-made confocal Fluorescent Lifetime Imaging Microscopy (FLIM)-AFM setup. It allows measuring the morphology and the nanomechanical properties (by AFM) and molecular recognition (by fluorescence quenching, MIET) simultaneously. We have designed and developed MIET-AFM probes by fabricating a custom-made plateau tip based on a qp-Bio AC cantilever and selectively grafting a single nanodiamond at the tip apex. We have shown that MIET-AFM can achieve topographical images simultaneously with molecular recognition maps, reaching lateral resolution below the diffraction limit on 100 nm gold nanoparticles. However, when we have tried MIET-AFM scan on smaller gold nanoparticles (30 and 10 nm), we could not detect any quenching. We argued that this could be explained by the large number of NV centers located in the nanodiamonds. In order to overcome this issue, we have proposed to replace the nanodiamonds with FluoroSphere[™] (FS). Unfortunately, due to lack of time, the experiments are ongoing, and they are proposed as perspectives for this novel technique.

4.2 Perspectives

Our perspectives for the work done during this Ph.D. thesis are the following: We have shown that the Young's modulus is a crucial parameter to characterize a material. Even more, it can allow us to distinguish between two different materials. Here, the physical models for different configurations are established for decades. However, in the literature, the Young's modulus of supported lipid bilayers is evaluated with the Hertz model, assuming that the material thickness is infinite compared with the indenter size. The latter is not the case during indenting supported lipid bilayers by AFM since the tip radius is comparable with the membrane thickness. Therefore, the model is not accurate, resulting in an overestimation of the elasticity modulus of these membranes. We propose the use of

models developed to correct this issue as the model proposed by Chadwick [154] almost 20 years ago. Indeed, the Hertz model is improved here because the thickness of the sample is taken into account.

We propose to further work on the novel effect called puncture to probe the intermolecular interaction within the membrane. A better understanding of this effect requires the investigation of the lipids' lateral diffusion influence.

Our manuscript mainly focused on membrane Young's modulus and the rupture force. However, we are currently further analyzing our data to investigate additional membrane mechanical properties, such as the presence of double rupture forces and membrane adhesion. Indeed, double rupture forces, largely ignored in the literature, occur in DPPC-enriched domains when: i) the tip radius is larger than 20 nm, and ii) the loading rate is higher than 10 $\mu\text{m/s}$. Currently, a manuscript based on our dataset is being prepared in the frame of an international collaboration.

Regarding the MIET-AFM setup, we plan to use 20 nm FluoroSpheresTM (Thermofisher) to replace the 35 nm FND on the MIET-AFM probes. Consequently, we plan to perform MIET-AFM maps on 30 and 10 nm gold nanoparticles on glass coverslips to improve the lateral resolution. Measuring a variation in the FluoroSphere's lifetime would allow MIET-AFM to work on labeled membrane molecules with reasonable nanoparticle size. Finally, in order to test the MIET-AFM resolution, we plan to use a DNA nanoruler with two 10 nm gold nanoparticles separated at a fixed distance (see Figure 4.1). We purchased these DNA nanorulers from GattaQuant, with two gold beads separated 30, 60, and 90 nm (depending on the sample), to test the smallest separation distance at which the two gold spheres can be distinguished.

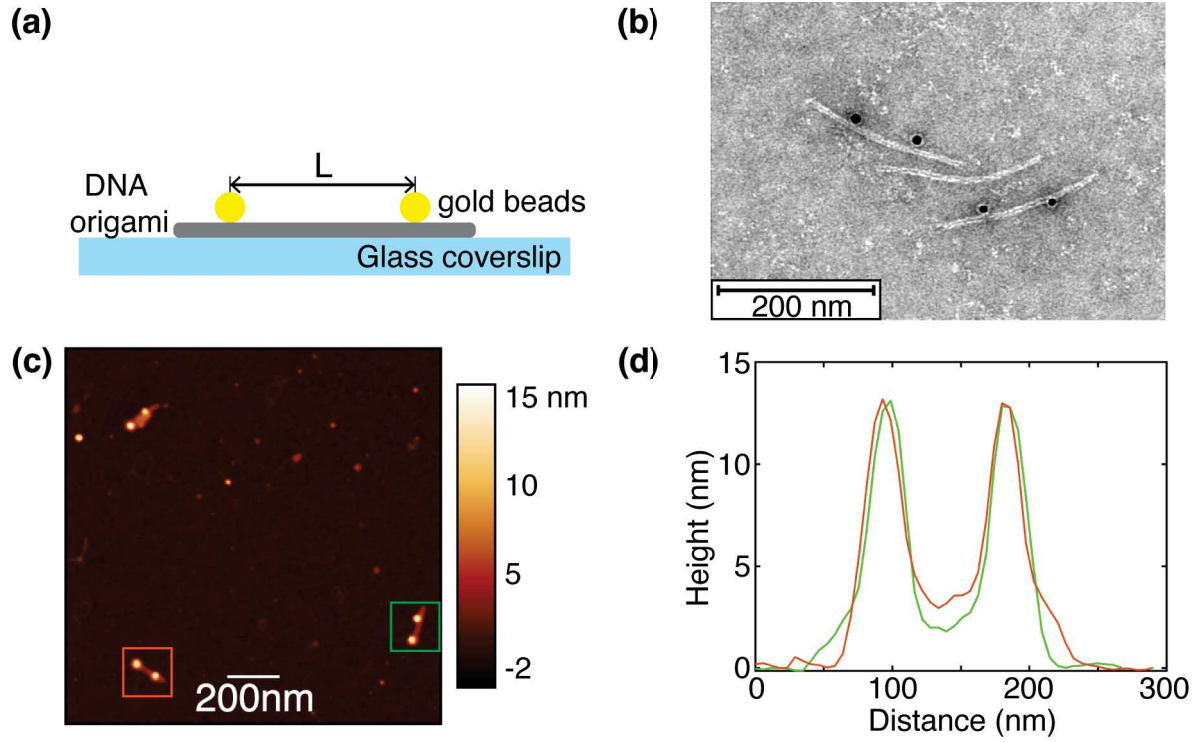


Figure 4.1: DNA origami. a) Schematic of the DNA origami with two gold nanoparticles of 10 nm of diameter separated by a distance L . b) TEM images of DNA origamis (Gat-taQuant), where the two gold beads are separated 90 nm. c) AFM image of DNA origami on mica in air for DNA origami where the nominal separation between the gold spheres is 90 nm. d) z-profile of the two DNA origamis highlighted in a color box in c). Both nanorulers show a separation between the gold nanoparticles of 87.1 nm, being consistent with the designed distance.

Appendix A

Sample preparation: DOPC:DPPC (v:v 1:1) labeled with 0.1% BODIPY on glass coverslip

1,2-dipalmitoyl-sn-glycero-3-phosphocholine (DPPC) and 1,2-dioleoyl-sn-glycero-3-phosphocholine (DOPC) were purchased from Avanti Polar Lipids Inc. 2-(4,4-difluoro-5,7-dimethyl-4-bora-3a,4a-diaza-s-indacene-3-dodecanoyl)-1-hexadecanoyl-sn-glycero-3-phosphocholine (BODIPY) was purchased from Thermofisher. Chloroform and methanol were purchased from Sigma-Aldrich. Membrane experiments were performed in DPBS buffer solution filtered before use with an inorganic membrane filter (0.22 μm pore size, Whatman International Ltd). DPPC and DOPC were individually dissolved in chloroform:methanol (v:v 1:1) and supplemented with 0.1% BODIPY. The solvent was then evaporated to dryness under nitrogen flow to obtain a thin film spread in a glass tube. The dried lipids films were hydrated with DPBS buffer solution, previously heated at 60°C, until a final total concentration of 0.2 mM. The tube was later subjected to cycles of vortex mixing and heating at 60°C. The vesicle suspension was extruded with a polycarbonate membrane filter (100 nm pore size, Whatman, purchased from Avanti Lipids). Circular glass coverslips (2.8 cm diameter, 165 μm thick, purchased from Marienfeld) were cleaned by a cycle of sonication in KOH for 15 min, followed by a second cycle of sonication in deionized water for 15 min. Then, the glass coverslips were exposed to plasma (Expanded Plasma Cleaner

PDC-002, Harrick Scientific Corporation) at high RF power level for 15 min. Supported lipid bilayers (SLBs) were obtained by vesicles fusion method [66, 151, 124, 157]. 300 μL of vesicles suspensions were deposited onto cleaned glass coverslips, previously mechanically fixed in an Attofluor chamber (Thermofisher), and incubated for 30 min at 70°C. Afterwards, the samples were rinsed several times with buffer solution to avoid unfused vesicles, always keeping the substrates hydrated and imaged by correlative confocal-AFM after 24 hours.

Appendix B

PhD's publications

Compression, Rupture, and Puncture of Model Membranes at the Molecular Scale

Oscar Saavedra V., Thales F. D. Fernandes, Pierre-Emmanuel Milhiet,* and Luca Costa*



Cite This: <https://dx.doi.org/10.1021/acs.langmuir.0c00247>



Read Online

ACCESS |



Metrics & More

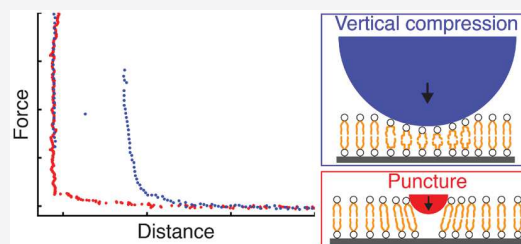


Article Recommendations



Supporting Information

ABSTRACT: Elastic properties of biological membranes are involved in a large number of membrane functionalities and activities. Conventionally characterized in terms of Young's modulus, bending stiffness and stretching modulus, membrane mechanics can be assessed at high lateral resolution by means of atomic force microscopy (AFM). Here we show that the mechanical response of biomimetic model systems such as supported lipid bilayers (SLBs) is highly affected by the size of the AFM tip employed as a membrane indenter. Our study is focused on phase-separated fluid-gel lipid membranes at room temperature. In a small tip radius regime (≈ 2 nm) and in the case of fluid phase membranes, we show that the tip can penetrate through the membrane minimizing molecular vertical compression and in absence of molecular membrane rupture. In this case, AFM indentation experiments cannot assess the vertical membrane Young's modulus. In agreement with the data reported in the literature, in the case of larger indenters (>2 nm) SLBs can be compressed leading to an evaluation of Young's modulus and membrane maximal withstanding force before rupture. We show that such force increases with the indenter in agreement with the existing theoretical frame. Finally, we demonstrate that the latter has no influence on the number of molecules involved in the rupture process that is observed to be constant and rather dependent on the indenter chemical composition.



INTRODUCTION

Biological membranes are cellular flexible barriers that ensure the cell permeability. Spatial and geometrical remodeling of biological membranes is of high importance in most fundamental cellular processes such as growth, division, endo- and exocytosis, trafficking, signaling, and associated pathology.¹ While the active modulation of the membrane is achieved by several means, including membrane composition and underlying cytoskeleton activity, its mechanical properties (i.e., bending stiffness, stretching modulus, and membrane tension) are crucial parameters in all remodeling processes. Membrane mechanics can be assessed with a large variety of techniques including atomic force microscopy (AFM), surface force apparatus (SFA),² optical tweezer,³ and micropipette aspiration^{4,5} on both *in vitro* biomimetic model membranes or *in cellulo*. The peculiarity of AFM is the unique capability to probe very local membrane mechanics which is an advantage when membranes are heterogeneous at the nanoscale. When using AFM force spectroscopy (AFM-FS) on biomimetic membranes such as supported lipid bilayers (SLBs), the AFM tip is used to compress elastically the underlying lipid molecules and the Young's modulus can be extracted using Hertz contact model.^{6–8} In addition, AFM-FS can be used to evaluate the stretching modulus.⁹ If a higher force is applied, a well-defined jump of the tip through the membrane is observed.^{10–16} If the tip is brought in mechanical contact with the membrane and then it is retracted, a lipid tube can be pulled off and membrane tension can be assessed.¹⁷ AFM-FS

curves acquired on free-standing (pore-spanning) lipid bilayers show instead a mechanical response that scales initially linearly with the indentation: depending on the pore size, membrane prestress, stretching and bending contribute differently to the mechanical response and important quantities such as membrane tension can be evaluated.^{18,19} With the exception of the lipid tube pulling case, in all AFM-FS experiments the radius of the AFM tip used as an indenter plays a major role. For instance, the Hertz contact model²⁰ describing the force inducing an elastic compression of a flat homogeneous film by a spherical indenter, in absence of nonmechanical contact interaction forces, is the following

$$F = \frac{4}{3} \frac{E}{1 - \nu^2} \sqrt{R\delta^3} \quad (1)$$

where R is the radius of the indenter, ν is the Poisson ratio, δ is the indentation length, and E is the Young's modulus of the film, assuming the Young's modulus of the indenter is much higher than the SLB E . The knowledge of the AFM tip radius is, therefore, essential to properly define the force and

Received: January 28, 2020

Revised: May 6, 2020

indentation length range of the AFM-FS curve to be used to accurately evaluate E . Indeed, the maximal force and, consequently, the indentation length to be considered to properly evaluate E , avoiding substrate contributions, will change with the indenter size. If higher forces are applied during the indentation cycle, membrane rupture can be achieved.^{12,21} Butt et al.^{13,22,23} proposed a discrete molecular model capable to predict the threshold rupture force F_B as follows

$$F_B = F_T \ln \left(\frac{0.693vK}{k_0 F_T} + 1 \right) \quad (2)$$

with F_T the thermal force

$$F_T = \frac{2\pi h R K_B T}{\alpha V} \quad (3)$$

where v is the loading rate (approach speed of the AFM tip), K is the cantilever spring constant, k_0 is the probability to observe a film rupture due to thermal fluctuation, and h is the membrane thickness. V is defined as the activation volume occupied by the critical number of lipid molecules that can escape from the mechanical contact with the tip during the indentation, therefore, triggering the starting point of the hole formation within the membrane. As a consequence, (2) predicts the rupture force F_B to increase with the AFM tip radius R .

In this frame, we focus here on the influence of the AFM tip radius when measuring membrane mechanical properties in the case of both fluid-phase and gel-phase SLBs. We show the presence of two tip radii regimes: when the size of the tip (≈ 1 – 2 nm) is in the range of the area occupied by few lipid molecules, the tip can penetrate through the membrane encountering low resistance, here referred as a puncture mechanism. We interpret the latter case as an in-plane lateral perturbation of few molecules surrounding the AFM tip, in a noncompressive regime. Finally, we show that larger tip radii (>2 nm) indentation always show a lipid vertical compression followed by membrane rupture, confirming experimentally the discrete molecular model introduced by Butt and Franz where the activation volume V is observed to be constant and independent of the tip radius.²²

EXPERIMENTAL SECTION

Materials. 1,2-Dioleoyl-*sn*-glycero-3-phosphocholine (DOPC) and 1,2-dipalmitoyl-*sn*-glycero-3-phosphocholine (DPPC) were purchased from Avanti Polar Lipids (Alabaster, AL). Chloroform ($\geq 99\%$) and methanol ($\geq 99.8\%$) were purchased from Sigma-Aldrich (St. Louis, MO). All experiments were performed in buffer solution of Dulbecco's phosphate-buffered saline (DPBS) ($1 \times$) purchased from Gibco (Grand Island, NY) and filtered before use using an inorganic membrane filter of $0.20 \mu\text{m}$ pore size from Whatman International (England, UK). Muscovite mica was purchased from GoodFellow (France).

Sample Preparation. DOPC and DPPC were individually dissolved in a chloroform–methanol (2:1) solution to a final concentration of 10 mM each. Ten microliters of each phospholipid solution were mixed, poured in a glass vial, and evaporated to dryness under nitrogen flux for 2 h to form a thin film on the tube walls. Afterward, the dried phospholipid film was hydrated with 1 mL of DPBS buffer solution, previously heated at 70°C , subjected to a 3 min vortex cycle, and finally extruded for 15 passages with a $0.1 \mu\text{m}$ membrane filter (Whatman International). The final solution was immediately used to prepare SLBs by the vesicles fusion method: $50 \mu\text{L}$ of lipids final solution were deposited onto freshly cleaved mica

disks (9.5 mm diameter), previously glued on top of larger Teflon disks that were in turn placed onto metallic disks. Disks were incubated for 30 min at 70°C in an oven. In order to prevent the evaporation of the solution, disks were kept inside a Petri dish placed in a larger Petri filled with water, ensuring the necessary humidity level during incubation. Afterward, disks were incubated at room temperature for 10 min before being carefully rinsed ten times with buffer solution in order to remove intact lipid vesicles. Membranes were kept overnight in buffer and protected from light exposure at room temperature. AFM measurements were carried out 24 h after membrane preparation.

AFM Imaging and Force Spectroscopy. AFM images and Force Spectroscopy (AFM-FS) measurements were performed using a JPK NanoWizard 4 (Berlin, Germany) using the following cantilevers: V-shaped Si_3N_4 cantilevers MSNL-D, MSCT-E, and MLCT-Bio-DC-F from Bruker (Bruker AFM Probes, Camarillo, CA) and spherical-shaped carbon AFM tips mounted on rectangular cantilevers, Biosphere B20-CONT, B50-FM, and B100-FM purchased from Nanotools GmbH (München, Germany). For each cantilever, the optical lever sensitivity was calibrated acquiring a force curve on a rigid mica substrate (nm/V), whereas the spring constant was calibrated using the thermal noise method.²⁴ Both calibrations were performed in DPBS buffer at the end of the AFM-FS experiments to preserve the AFM tip radius from possible damage that can occur during the acquisition of the force curve on rigid mica.

AFM-FS curves were recorded by approaching the tip to the membranes at a constant loading rate of $1 \mu\text{m/s}$ with a sampling frequency of 7 kHz at room temperature. For dynamic force spectroscopy (AFM-DFS) experiments, the loading rate was varied between $0.5 \mu\text{m/s}$ and $50 \mu\text{m/s}$ and MSCT-F cantilevers were used. Table 1 reports all cantilevers and tips used in this study.

Table 1. AFM Cantilevers, with Tip Chemical Composition, Employed and Total Number of Indentation Curves Recorded in This Study^a

cantilever	nominal tip radius (nm)	tip material	nominal stiffness (N/m)	number of probes used	curves collected
MSNL-D	2	Si	0.03	4	3125
MSCT-E	10	Si_3N_4	0.1	4	4375
MSCT-F	10	Si_3N_4	0.6	3	5000
MLCT-F	20	Si_3N_4	0.6	5	4600
B20-CONT	20	carbon	0.2	4	3625
B50-FM	50	carbon	2.8	4	6075
B100-FM	100	carbon	2.8	3	5225
			TOTAL	27	32025

^aMSCT-F cantilevers were used to acquire AFM-DFS data.

Force versus distance curves were acquired using a grid of 15×15 , 20×20 , or 25×25 points (force-volume experiments) over regions ranging from $25 \times 25 \mu\text{m}^2$ to $80 \times 80 \mu\text{m}^2$ depending on tip radius size. Once AFM-FS data were recorded, all regions were imaged in contact or quantitative-imaging (QI) modes. We acquired AFM topographical images at the end of the force-volume experiments to protect the AFM tip from contamination and damage that can occur during image acquisition. To ensure an accurate evaluation of the rupture force and avoid data collected in the presence of tip damage (i.e., resulting in a different tip radius), we have monitored the increase of the rupture force measured with the same probe for each experimental session. Data showing an increase of the rupture force during acquisition were discarded. Typical force–distance curves recorded in a single grid with a MSCT cantilever with tip radius of 10 nm at a loading rate of $v = 1 \mu\text{m/s}$ are reported in Figure 1a: we observe two different rupture force (F_B) regimes, a lower one for DOPC domains (blue curves) and a higher one for DPPC-enriched domains (red curves).

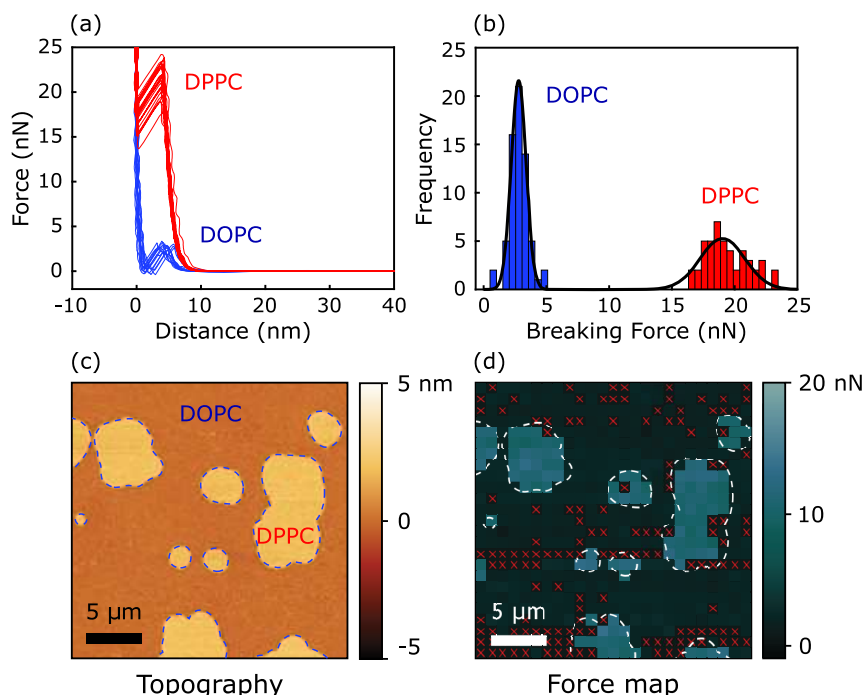


Figure 1. Force-volume experiment on DOPC:DPPC (1:1) SLBs on mica in DPBS buffer. (a) Force versus tip–sample distance curves (blue, DOPC domains; red, DPPC domains) recorded with a tip with a radius of 10 nm at a loading rate of $\nu = 1 \mu\text{m/s}$ over a region of interest of $25 \times 25 \mu\text{m}^2$. (b) Rupture force F_B distributions and (c) topographical image showing both DOPC- and DPPC-enriched domains obtained in the QI AFM mode. DPPC domains are characterized by a higher thickness compared to DOPC domains. (d) F_B XY distribution map that correlates well with panels (c). Red \times : discarded curves. Scale bar: $5 \mu\text{m}$.

Figure 1b shows the F_B distribution where each peak was fitted with a Gaussian function to determine the mean F_B and its standard deviation. The region of interest observed by AFM-FS was subsequently imaged by AFM in the QI AFM mode to observe DPPC- and DOPC-enriched domains (Figure 1c). Figure 1d shows the in-plane F_B distribution over the region of interest which highly correlates with the topographical AFM image in Figure 1c. A small in-plane drift is observed between (c) and (d) in Figure 1, most likely due to the AFM-FS long acquisition time. Red crosses in Figure 1d highlight the discarded curves which were affected by local and temporary tip contamination, occurring frequently in this kind of experiment.

Data Analysis. Rupture forces and Young's modulus evaluations from AFM-FS curves were obtained with custom-made MATLAB and Python programs. We developed an algorithm that makes use of a low pass-filter of the force curve, followed by a numerical first derivative. Finally, with a threshold method we identify the rupture force event, evaluated over a region surrounding the minimum of the numerical derivative (or maximum, depending on the orientation of the data). Section 1 of the Supporting Information reports an example of the efficiency of the algorithm for one force curve. The corresponding rupture force F_B is then considered. The algorithm has high precision if the rupture event induces an abrupt change of the force curve slope. For milder slopes, alternative methods should be taken into consideration. For each AFM-FS experimental session, we built histograms reporting the F_B distribution for both fluid and gel phase membranes. From each histogram we evaluated the average F_B and the standard deviation as a result of the histogram fit with a normal distribution. Statistical mean and standard deviation were observed to be comparable with fit outputs. Joining data from different experimental sessions, we averaged all mean F_B values in a unique F_B and we evaluated its standard error of the mean for each membrane phase and AFM tip radius experimental conditions. Membrane Young's modulus was evaluated with a numerical fit of the indentation cycles using (1). In addition, we evaluated the electric double layer contribution.²⁵ We report DOPC and DPPC Young's

moduli evaluated using both B20-CONT and B50-FM cantilevers. To do so, we fixed the contact point between the AFM tip and the membrane, defining the lower limit of the indentation curve to be considered for the fit. It was fixed considering 2.7 nm of water between the polar heads and the substrate, a constant DOPC and DPPC membrane thickness (3.6 and 4.6 nm for DOPC and DPPC, respectively),²⁶ and the position of the mica substrate evaluated from the mechanical contact between tip and mica. More details concerning the Young's modulus evaluation can be found in the second section of the Supporting Information (Figure S2).

RESULTS

The comparison between AFM-FS indentation cycles performed on DOPC fluid-phase and DPPC gel-phase domains with a 2 nm and a 10 nm AFM tip radius is pictorially and experimentally presented in Figure 2.

In the DOPC case (Figure 2a,b), we observe a vertical compression of the membrane by the 10 nm tip (blue curve) while the 2 nm tip indentation (red curve) suggests that a different physical mechanism is occurring (Figure 2b). DPPC-enriched domains are vertically compressed by both AFM tips. While for the DPPC case the use of (1) provides a Young's modulus in the range of a few tens of MPa, close to what has been reported in the literature for both AFM tips;^{6,8} this applies to the DOPC only for the larger tip case. Indeed, indentation curves performed with the 2 nm tip on the DOPC membrane show a much softer indentation regime where the Hertz fit would provide a Young's modulus of ≈ 2 MPa (see section 3 of the Supporting Information), far too low for the DOPC membrane since it has been reported to be in the range of 20–30 MPa.^{6,8} The unrealistic Young's modulus and the absence of rupture events suggest that a different indentation mechanism is occurring. Moreover, since the tip radius we

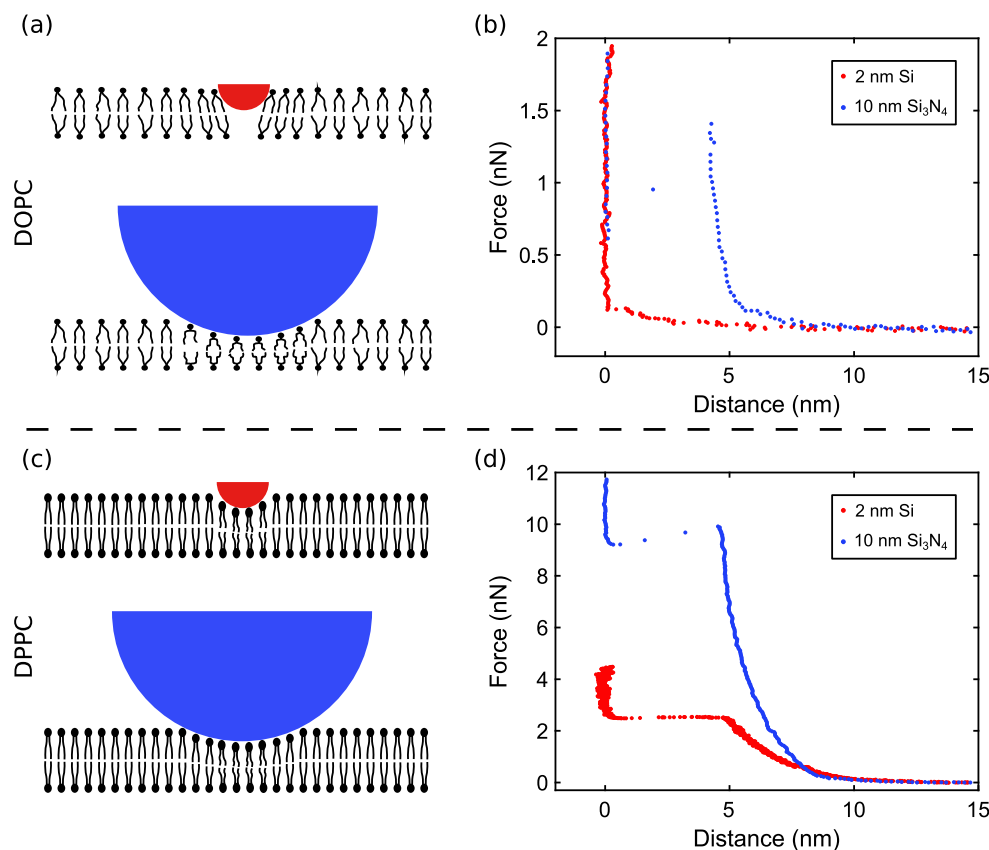


Figure 2. Pictorial representation of fluid-phase (a, DOPC) and gel-phase (c, DPPC) membrane indentations with two different indenter sizes: 2 nm tip versus 10 nm tip radii. While in both DOPC and DPPC, the 10 nm tip (blue curve) induces a vertical compression of the lipid molecules (b,d), a 2 nm tip (red curve) can penetrate the fluid-phase membrane inducing a local perturbation of the molecules surrounding the tip in absence of membrane rupture. Measurements were performed in the DPBS buffer.

used for the fit (≈ 2 nm) is smaller than the membrane thickness, the surface of the tip in contact with the membrane at large indentation is underestimated and, therefore, the obtained small Young's modulus is even overestimated, further confirming its unrealistic value. According to Tristram-Nagle and coauthors, the area occupied by a DOPC molecule is $A \approx 70 \text{ \AA}^2$.²⁶ The area occupied by a DPPC molecule has been reported to be $A \approx 47 \text{ \AA}^2$.^{27,28} Approximating the tip as a sphere, for indentations δ smaller than tip radius R , the contact area, also known as a spherical cap, is given by $S = 2\pi\delta R$. The contact area S can be related to the area A occupied by a single lipid by multiplying the latter times the number of lipids N and dividing by the coverage/packing factor Φ .

$$2\pi\delta R = \frac{NA}{\Phi} \quad (4)$$

The densest packing assumes a value of ≈ 0.9069 in two-dimensional space (hexagonal packing), which is the case here. As a consequence, for an indentation δ of 0.5 nm there are approximately $N_{\text{DOPC}} = 8$ DOPC molecules in mechanical contact with the 2 nm AFM tip, whereas the molecules increase to approximately $N_{\text{DPPC}} = 12$ in the DPPC case. The low number of molecules involved can justify the probability of a physical indentation mechanism where a vertical molecules compression is minimized in favor of a lateral molecules tilt/displacement, here referred to as puncture mechanism. However, it is remarkable that the latter occurs only in the case of DOPC membranes, despite a number of molecules

below the tip similar to the DPPC case. Eventually, the higher diffusion coefficient characterizing DOPC molecules ($\approx 4 \mu\text{m}^2/\text{s}$)²⁹ compared to DPPC molecules ($\approx 10^{-3} \mu\text{m}^2/\text{s}$)³⁰ can play an additional role favoring such mechanism. In other words, the use of a small AFM indenter induces an in-plane local perturbation in absence of elastic compression followed by membrane rupture. Indentations with the high-speed AFM (HS-AFM) or eventually correlative fluorescence correlation spectroscopy (FCS)-AFM experiments can further explore the contribution of lipid diffusion to the mechanical response of the membrane. During all experimental sessions for fluid-phase membranes using the 2 nm AFM tip, we observed a prevalence of indentation cycles where the tip can penetrate the membrane in absence of molecular vertical compression with respect to the cycles where compression is present, as shown in Figure 3a (see also Figure S3). Sharp probes were previously used to evaluate the Young's modulus of DOPC membranes using Peak-Force Tapping AFM (indentation cycles in between one and 2 orders of magnitude faster) in buffer containing MgCl_2 .^{7,8} Our data suggest that small indenters should not be used to quantify the DOPC Young's modulus using the Hertz contact model with an indentation speed of $\approx 1 \mu\text{m/s}$ in experiments carried out in the absence of MgCl_2 .

When using larger AFM tip indenters, molecular vertical compression always occurs. Figure 3b,c shows indentation cycles on DOPC and DPPC domains acquired with tip radii varying from 2 to 100 nm. All curves can be fitted with (1) leading to an estimation of both DOPC and DPPC Young's

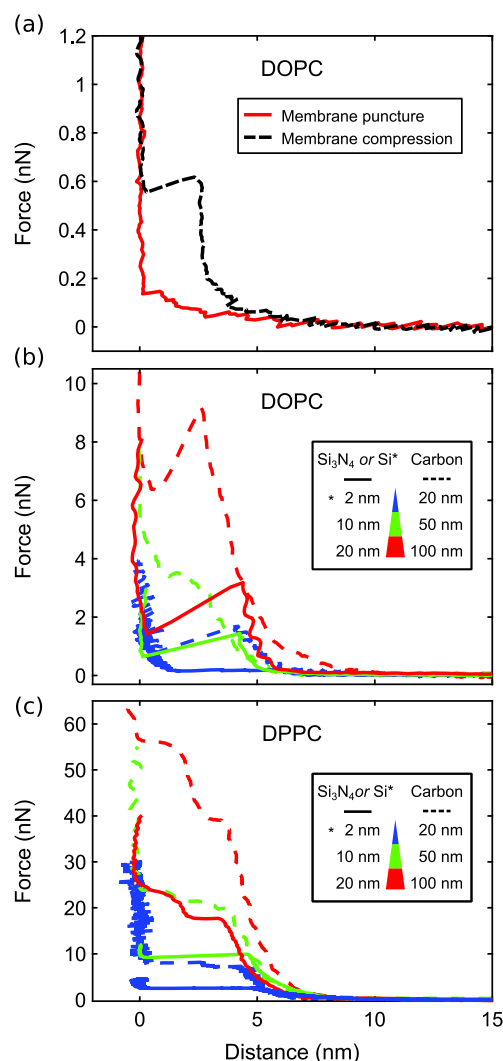


Figure 3. (a) Coexistence of vertical compression (black) and membrane puncture (red) when indenting a fluid-phase membrane (DOPC) with a 2 nm indenter. Panels (b) and (c) indentation cycles on fluid (DOPC, b) and gel (DPPC, c) phase membranes measured with different tip radii in DPBS buffer. The maximal force the membrane can withstand before rupture for both DOPC and DPPC increases with the tip radius.

moduli: the second section of the [Supporting Information](#) reports data obtained with 20 nm radius spherical indenters leading to $E^{\text{DOPC}} = (34 \pm 19)$ MPa and $E^{\text{DPPC}} = (48 \pm 15)$ MPa, in agreement with values reported in the literature.^{6,8} The use of a larger, 50 nm radius, spherical indenter leads to $E^{\text{DOPC}} = (36 \pm 19)$ MPa and $E^{\text{DPPC}} = (58 \pm 28)$ MPa, values comparable with the ones obtained with the 20 nm probe. This is consistent with the fact that the Young's modulus constitutes an intrinsic mechanical property of a material and therefore is independent of the indenter size.

In addition, the curves presented in [Figure 3](#) clearly show that the maximal force F_B the membrane can withstand before rupture for both DOPC and DPPC increases with the tip radius as predicted by (2). For better clarity, [Figure 3b,c](#) shows indentation cycles performed with carbon probes with dashed lines and rupture force obtained with silicon and silicon nitride probes with continuous lines. [Figure 4](#) presents all values for the rupture force observed on both DOPC- and DPPC-

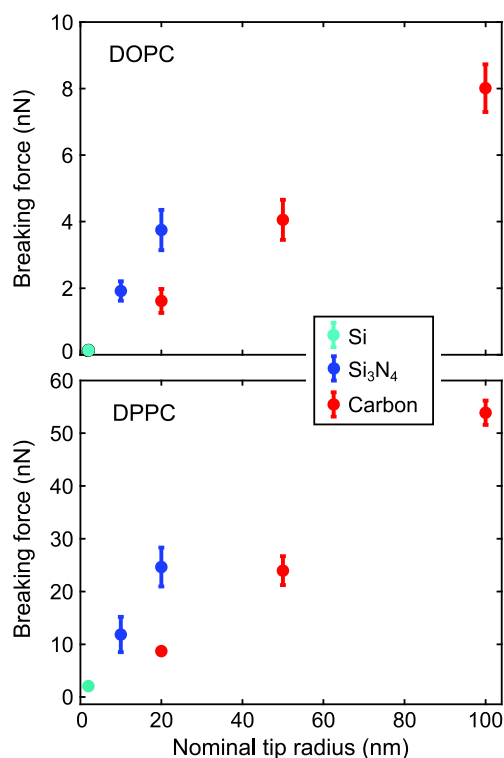


Figure 4. Rupture force F_B for DOPC- and DPPC-enriched domains indented by silicon, silicon nitride, and carbon AFM tips at a constant loading rate of $v = 1 \mu\text{m/s}$ in DPBS buffer. The rupture force increases with the tip radius, suggesting that the number of molecules involved in the onset of the rupture process is independent of the tip radius.

enriched domains as a function of the indenter radius. In agreement with previous data,¹³ we observe a variation of F_B with the tip chemical composition: this is evident comparing F_B values obtained with 20 nm radius Si_3N_4 and carbon AFM tips.

Our data can be used to evaluate the activation volume V in (2) and consequently the associated number of molecules involved in the beginning of the rupture process. To do so, we have evaluated k_0 for both DOPC and DPPC from dynamic force spectroscopy (AFM-DFS) data, as proposed by Butt et al.¹³ We measured F_B as a function of the loading rate v (between 0.5 and 50 $\mu\text{m/s}$) for both DOPC and DPPC ([Figure 5a,b](#), respectively) using MSCF cantilevers. Data were fitted using

$$F_B = \alpha + \beta \log_{10} \frac{v}{v_0} \quad (5)$$

where F_B , α , and β are in nN and $v_0 = 1 \mu\text{m/s}$. The free fit parameters α and β lead to the evaluation of k_0 as follows

$$k_0 = 1.596 \frac{K v_0}{\beta} 10^{-\alpha/\beta} \quad (6)$$

We evaluated $k_0^{\text{DPPC}} = 4.1$ mHz (close to the value reported by ref 31) and $k_0^{\text{DOPC}} = 297$ mHz.

V is found to be essentially constant with the indenter radius for both DOPC- and DPPC-enriched domains but dependent on the tip chemical composition ([Table 2](#)). We can associate to each activation volume the number of molecules, n , triggering the rupture process defined as $n \approx V/(Ah)$.

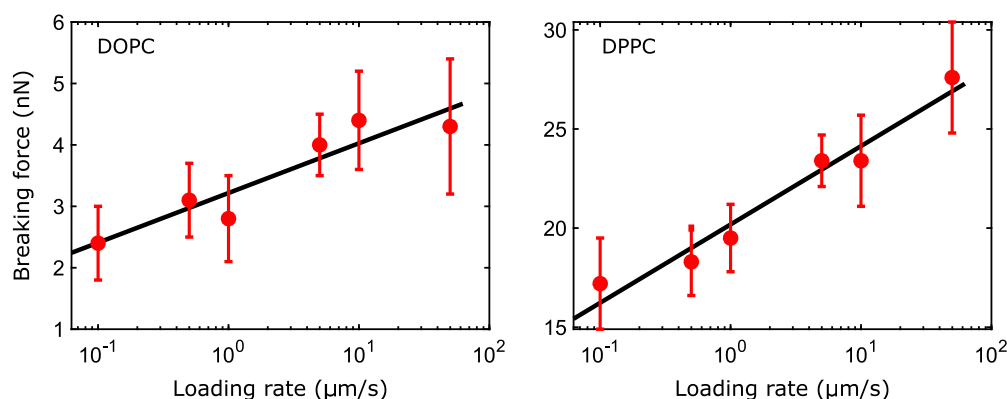


Figure 5. AFM-DFS on DOPC:DPPC (1:1) SLBs, in DPBS buffer. Mean rupture force versus loading rate ν (error bars denote standard deviation) for DOPC- and DPPC-enriched domains. The black line is the fit with eq 5. The free parameters obtained from the fit are $\alpha = (3.22 \pm 0.41)$ nN and $\beta = (0.81 \pm 0.43)$ nN (DOPC) and $\alpha = (20.2 \pm 1.1)$ nN and $\beta = (3.95 \pm 0.56)$ nN (DPPC).

Table 2. Rupture Force (F_B), Activation Volume (V), and Associated Number of Molecules (n) for DPPC and DOPC Membranes Indented by Silicon and Carbon AFM Tips, Expressed As the Mean Value \pm Sem

DPPC			DOPC				
F_B [nN]	V [nm ³]	n	F_B [nN]	V [nm ³]	n	tip material	radius [nm]
2.21 ± 0.08	2.3 ± 0.1	1.0 ± 0.1	0.12 ± 0.02	—	—	Si	2
12.0 ± 3.3	1.8 ± 0.3	0.8 ± 0.1	1.9 ± 0.3	5.7 ± 1.0	2.2 ± 0.4	Si ₃ N ₄	10
24.8 ± 3.7	2.1 ± 0.2	0.9 ± 0.1	3.7 ± 0.6	7.9 ± 0.8	3.1 ± 0.3	Si ₃ N ₄	20
8.8 ± 0.6	6.1 ± 0.3	2.7 ± 0.1	1.6 ± 0.4	18.4 ± 3.2	7.1 ± 1.2	carbon	20
24.1 ± 2.7	6.2 ± 0.5	2.8 ± 0.2	4.0 ± 0.6	21.5 ± 3.1	8.3 ± 0.8	carbon	50
54.0 ± 2.3	5.1 ± 0.7	2.3 ± 0.1	8.0 ± 0.7	19.9 ± 1.4	7.7 ± 0.5	carbon	100

Assuming the head to head h to be 3.6 and 4.5 nm for DOPC²⁶ and DPPC,³² respectively, Table 2 reports the measured activation volumes and the corresponding number of molecules n , including their errors, evaluated from the dispersion of each rupture force for DOPC and DPPC membranes indented by silicon and carbon AFM tips. For each tip radius, F_B and its associated standard error of the mean (sem) are evaluated joining single rupture forces obtained using several AFM probes over different experimental sessions. Since the total number of molecules N elastically compressed by the tip increases with the tip radius, for a given tip chemistry, n is observed to be independent of N .

It is remarkable that, in the case of DPPC-enriched domains, the use of probes with a tip radius larger than 20 nm induces a two-step rupture process (Figure 3c). Several scenarios, that remain to be elucidated, can be involved to explain the mechanism: (1) two different rupture events involving at first the DPPC molecules compressed at the very end of the tip apex and subsequently other molecules compressed by the tip side at higher indentation length; (2) a limiting maximal DPPC hole size inferior to 20 nm; (3) tip approach and hole formation comparable speeds ($k_0 \approx 4$ MHz for DPPC membranes); and (4) discrete rupture of the upper membrane leaflet subsequently followed by the rupture of the bottom leaflet. For the evaluation of F_B and V , we have considered the breaking event characterized by the highest rupture force only.

DISCUSSION

In the case of thin films, Dimitriadis et al.³³ have shown that the Hertz model must be corrected to take into account the finite thickness of the film (eq 8 in ref 33) that would otherwise induce an apparent material stiffening. The correction factor is proportional to the square root of the tip

radius but cannot explain the apparent membrane softening observed for fluid phase membranes indented by a 2 nm AFM sharp tip (Figure 3a and Figure S3). The Hertz model itself (1) describes indentation cycles in the approximation of the a radius $R \gg \delta$, leading to the Hertz contact radius $a \approx \sqrt{R\delta}$ ²⁰; in the 2 nm tip radius case, the approximation does not hold, but the use of the nonsimplified Hertz radius $a = \sqrt{R\delta - \delta^2}$ does not lead to the expected Young's modulus E^{DOPC} value either. Therefore, indentation cycles performed with such a small tip radius, with contact area comparable with the surface occupied by few lipid molecules, reveal a physical indentation mechanism that minimizes molecular vertical compression. While the use of small AFM tips could be extended to a large variety of thin films constituted by diffusive and dynamic molecules, in practice it represents a limit to the conventional Hertz contact model. Additionally, the acquisition of AFM images is particularly challenging because of the small rupture force of the films.

The physics of hole formation within a membrane is contained in eq 7 of ref 22, where the energy is dictated between an interplay of line tension, spreading pressure and the membrane elastic energy. In our case, we are interested in the process of hole formation where the latter term is absent. Additionally, it is remarkable that one cannot assume constant line tension and spreading pressure, first and second terms of eq 7 in ref 22, in the process of hole formation, where our data suggests that they are indentation-dependent. However, it is challenging to properly describe the dependency of line tension and spreading pressure as a function of the indentation from our data: besides the very small forces measured (\approx tens of pN), several questions arise concerning the way single molecules are tilted/laterally displaced and how the two leaflets

differently participate to the hole formation at different indentation lengths.

Indentation cycles performed with larger indenters can be used to probe membrane mechanical stability. Interestingly, the activation volume associated with the onset of the rupture process is essentially constant in the range of the indenter sizes we tested in this work. This suggests that the activation volume, together with the probability to observe a film rupture due to thermal fluctuation k_0 , are the quantities that should be considered when comparing variations of membrane mechanical stability due to the presence of external factors or due to changes in membrane composition.

In conclusion, in this work, we have shown that the size of indenters used to probe membrane mechanics, by means of AFM-FS, is crucial to properly quantify intrinsic properties such as the Young's modulus and the number of molecules involved at the onset of a hole formation within the membrane. Measurable observables such as the interaction force versus indentation length and the membrane rupture force are indeed highly dependent on the AFM tip radius. While the theoretical background has been well-established for decades, we have shown for the first time that, for small indenters, the membrane Young's modulus cannot be assessed due to the puncture mechanism, where the tip passes-through the membrane with less resistance than in a compression regime. This results in an erroneous underestimation on the Young's modulus if the Hertz model is employed. For larger indenters, our results are in good agreement with Butt and Franz's theory²² and confirm that the rupture force increases with the indenter radius. Although the critical number of molecules involved in the AFM tip breakdown process is material-dependent, it remains constant regardless of the indenter size.

■ ASSOCIATED CONTENT

SI Supporting Information

The Supporting Information is available free of charge at <https://pubs.acs.org/doi/10.1021/acs.langmuir.0c00247>.

Algorithm to evaluate the rupture force, Young's modulus and debye length evaluations, and coexistence membrane puncture and vertical compression for small tip indenters (PDF)

■ AUTHOR INFORMATION

Corresponding Authors

Pierre-Emmanuel Milhiet – Centre de Biochimie Structurale (CBS), CNRS, INSERM, Univ. Montpellier, 34090 Montpellier, France; Email: pem@cbs.cnrs.fr

Luca Costa – Centre de Biochimie Structurale (CBS), CNRS, INSERM, Univ. Montpellier, 34090 Montpellier, France; orcid.org/0000-0002-4527-0034; Email: luca.costa@cbs.cnrs.fr

Authors

Oscar Saavedra V. – Centre de Biochimie Structurale (CBS), CNRS, INSERM, Univ. Montpellier, 34090 Montpellier, France

Thales F. D. Fernandes – Centre de Biochimie Structurale (CBS), CNRS, INSERM, Univ. Montpellier, 34090 Montpellier, France

Complete contact information is available at:

<https://pubs.acs.org/doi/10.1021/acs.langmuir.0c00247>

Author Contributions

O.S., L.C., P.-E.M., and T.F.D.F. designed the research. O.S. acquired the data. O.S. and L.C. analyzed the data. O.S., L.C., T.F.D.F., and P.-E.M. wrote the article.

Notes

The authors declare no competing financial interest.

■ ACKNOWLEDGMENTS

The CBS is a member of the France-BioImaging (FBI) and the French Infrastructure for Integrated Structural Biology (FRISBI), 2 national infrastructures supported by the French National Research Agency (ANR-10-INBS-04-01 and ANR-10-INBS-05, respectively). O.S.V. acknowledges funding from the European Union's Horizon 2020 research and innovation program under the Marie Skłodowska-Curie Grant agreement no. 721874 (SPM2.0). This work was partially supported by the CNRS Momentum program (2017). The authors acknowledge Manouk Abkarian and Marina Ines Giannotti for fruitful discussions.

■ REFERENCES

- (1) McMahon, H. T.; Gallop, J. L. Membrane curvature and mechanisms of dynamic cell membrane remodelling. *Nature* **2005**, *438*, 590.
- (2) Orozco-Alcaraz, R.; Kuhl, T. L. Interaction forces between DPPC bilayers on glass. *Langmuir* **2013**, *29*, 337–343.
- (3) Li, Z.; Anvari, B.; Takashima, M.; Brecht, P.; Torres, J. H.; Brownell, W. E. Membrane tether formation from outer hair cells with optical tweezers. *Biophys. J.* **2002**, *82*, 1386–1395.
- (4) Rawicz, W.; Olbrich, K.; McIntosh, T.; Needham, D.; Evans, E. Effect of chain length and unsaturation on elasticity of lipid bilayers. *Biophys. J.* **2000**, *79*, 328–339.
- (5) Dieluweit, S.; Csiszar, A.; Rubner, W.; Fleischhauer, J.; Houben, S.; Merkel, R. Mechanical properties of bare and protein-coated giant unilamellar phospholipid vesicles. A comparative study of micropipet aspiration and atomic force microscopy. *Langmuir* **2010**, *26*, 11041–11049.
- (6) Et-Thakafy, O.; Delorme, N.; Gaillard, C.; Mériade, C.; Artzner, F.; Lopez, C.; Guyomarc'h, F. Mechanical Properties of Membranes Composed of Gel-Phase or Fluid-Phase Phospholipids Probed on Liposomes by Atomic Force Spectroscopy. *Langmuir* **2017**, *33*, 5117–5126.
- (7) Picas, L.; Rico, F.; Scheuring, S. Direct Measurement of the Mechanical Properties of Lipid Phases in Supported Bilayers. *Biophys. J.* **2012**, *102*, L01–L03.
- (8) Redondo-Morata, L.; Sanford, R. L.; Andersen, O. S.; Scheuring, S. Effect of statins on the nanomechanical properties of supported lipid bilayers. *Biophys. J.* **2016**, *111*, 363–372.
- (9) Das, C.; Sheikh, K. H.; Olmsted, P. D.; Connell, S. D. Nanoscale mechanical probing of supported lipid bilayers with atomic force microscopy. *Phys. Rev. E* **2010**, *82*, 041920.
- (10) Gumí-Audenis, B.; Costa, L.; Carlá, F.; Comin, F.; Sanz, F.; Giannotti, M. I. Structure and nanomechanics of model membranes by atomic force microscopy and spectroscopy: insights into the role of cholesterol and sphingolipids. *Membranes* **2016**, *6*, 58.
- (11) Redondo-Morata, L.; Giannotti, M. I.; Sanz, F. Influence of cholesterol on the phase transition of lipid bilayers: a temperature-controlled force spectroscopy study. *Langmuir* **2012**, *28*, 12851–12860.
- (12) Garcia-Manyes, S.; Oncins, G.; Sanz, F. Effect of ion-binding and chemical phospholipid structure on the nanomechanics of lipid bilayers studied by force spectroscopy. *Biophys. J.* **2005**, *89*, 1812–1826.
- (13) Loi, S.; Sun, G.; Franz, V.; Butt, H.-J. Rupture of molecular thin films observed in atomic force microscopy. II. Experiment. *Phys. Rev. E: Stat. Phys., Plasmas, Fluids, Relat. Interdiscip. Top.* **2002**, *66*, 031602.

- (14) García-Sáez, A. J.; Chiantia, S.; Salgado, J.; Schwille, P. Pore formation by a Bax-derived peptide: effect on the line tension of the membrane probed by AFM. *Biophys. J.* **2007**, *93*, 103–112.
- (15) Seghezza, S.; Diaspro, A.; Canale, C.; Dante, S. Cholesterol drives A β (1–42) interaction with lipid rafts in model membranes. *Langmuir* **2014**, *30*, 13934–13941.
- (16) Attwood, S.; Choi, Y.; Leonenko, Z. Preparation of DOPC and DPPC supported planar lipid bilayers for atomic force microscopy and atomic force spectroscopy. *Int. J. Mol. Sci.* **2013**, *14*, 3514–3539.
- (17) Gumí-Audenis, B.; Costa, L.; Ferrer-Tasies, L.; Ratera, I.; Ventosa, N.; Sanz, F.; Giannotti, M. I. Pulling lipid tubes from supported bilayers unveils the underlying substrate contribution to the membrane mechanics. *Nanoscale* **2018**, *10*, 14763–14770.
- (18) Janshoff, A.; Steinem, C. Mechanics of lipid bilayers: What do we learn from pore-spanning membranes? *Biochim. Biophys. Acta, Mol. Cell Res.* **2015**, *1853*, 2977–2983.
- (19) Kocun, M.; Lazzara, T. D.; Steinem, C.; Janshoff, A. Preparation of solvent-free, pore-spanning lipid bilayers: modeling the low tension of plasma membranes. *Langmuir* **2011**, *27*, 7672–7680.
- (20) Hertz, H. On contact between elastic bodies. *J. Reine Angew. Math* **1882**, *92*, 156–171.
- (21) Gumí-Audenis, B.; Sanz, F.; Giannotti, M. I. Impact of galactosylceramides on the nanomechanical properties of lipid bilayer models: an AFM-force spectroscopy study. *Soft Matter* **2015**, *11*, 5447–5454.
- (22) Butt, H.-J.; Franz, V. Rupture of molecular thin films observed in atomic force microscopy. I. Theory. *Phys. Rev. E: Stat. Phys., Plasmas, Fluids, Relat. Interdiscip. Top.* **2002**, *66*, 031601.
- (23) Franz, V.; Loi, S.; Müller, H.; Bamberg, E.; Butt, H.-J. Tip penetration through lipid bilayers in atomic force microscopy. *Colloids Surf., B* **2002**, *23*, 191–200.
- (24) Proksch, R.; Schäffer, T. E.; Cleveland, J. P.; Callahan, R. C.; Viani, M. B. Finite optical spot size and position corrections in thermal spring constant calibration. *Nanotechnology* **2004**, *15*, 1344–1350.
- (25) Israelachvili, J. N. *Intermolecular and surface forces*; Academic Press, 2015.
- (26) Tristram-Nagle, S.; Petrache, H. I.; Nagle, J. F. Structure and Interactions of Fully Hydrated Dioleoylphosphatidylcholine Bilayers. *Biophys. J.* **1998**, *75*, 917–925.
- (27) Watkins, E.; Miller, C.; Mulder, D.; Kuhl, T.; Majewski, J. Structure and orientational texture of self-organizing lipid bilayers. *Phys. Rev. Lett.* **2009**, *102*, 238101.
- (28) Gumí-Audenis, B.; Costa, L.; Redondo-Morata, L.; Milhiet, P.-E.; Sanz, F.; Felici, R.; Giannotti, M. I.; Carlà, F. In-plane molecular organization of hydrated single lipid bilayers: DPPC: cholesterol. *Nanoscale* **2018**, *10*, 87–92.
- (29) Benda, A.; Beneš, M.; Marecek, V.; Lhotský, A.; Hermens, W. T.; Hof, M. How to determine diffusion coefficients in planar phospholipid systems by confocal fluorescence correlation spectroscopy. *Langmuir* **2003**, *19*, 4120–4126.
- (30) Scomparin, C.; Lecuyer, S.; Ferreira, M.; Charitat, T.; Tinland, B. Diffusion in supported lipid bilayers: Influence of substrate and preparation technique on the internal dynamics. *Eur. Phys. J. E: Soft Matter Biol. Phys.* **2009**, *28*, 211–220.
- (31) Redondo-Morata, L.; Giannotti, M. I.; Sanz, F. AFM-Based Force-Clamp Monitors Lipid Bilayer Failure Kinetics. *Langmuir* **2012**, *28*, 6403–6410.
- (32) Berquand, A.; Levy, D.; Gubellini, F.; Le Grimmellec, C.; Milhiet, P.-E. Influence of calcium on direct incorporation of membrane proteins into in-plane lipid bilayer. *Ultramicroscopy* **2007**, *107*, 928–933.
- (33) Dimitriadis, E. K.; Horkay, F.; Maresca, J.; Kachar, B.; Chadwick, R. S. Determination of elastic moduli of thin layers of soft material using the atomic force microscope. *Biophys. J.* **2002**, *82*, 2798–2810.

Supporting Information

Compression, rupture and puncture of model membranes at the molecular scale

Oscar Saavedra V.¹, Thales F. D. Fernandes¹, Pierre-Emmanuel Milhiet^{1*}, and Costa Luca^{1**}

¹Centre de Biochimie Structurale (CBS), CNRS, INSERM, Univ Montpellier, 34090, Montpellier, France

*Correspondence: pem@cbs.cnrs.fr

**Correspondence: luca.costa@cbs.cnrs.fr

Number of pages: 7

Number of figures: 3

1 ALGORITHM TO EVALUATE THE RUPTURE FORCE

In order to evaluate the rupture force from a force curve, we developed an algorithm that works as follows (Figure S1):

- First, the force curve is low-pass filtered (Figure S1a).
- The algorithm performs a first numerical derivative (Figure S1b). A threshold, green dashed line, is used to discard non relevant values and the local minimum of the derivative is identified (eventually the maximum, if data orientation is inverse).
- The minimum of the derivative corresponds to a position in the force curve that is represented by a red dot in Figure S1c. A region defined by 20 to 30 data points centered in the red dot is then considered: it is shown in Figure S1d with two vertical green dashed lines.
- The local maximal force in the region is identified and corresponds to the rupture force F_B : red dot in Figure S1d.

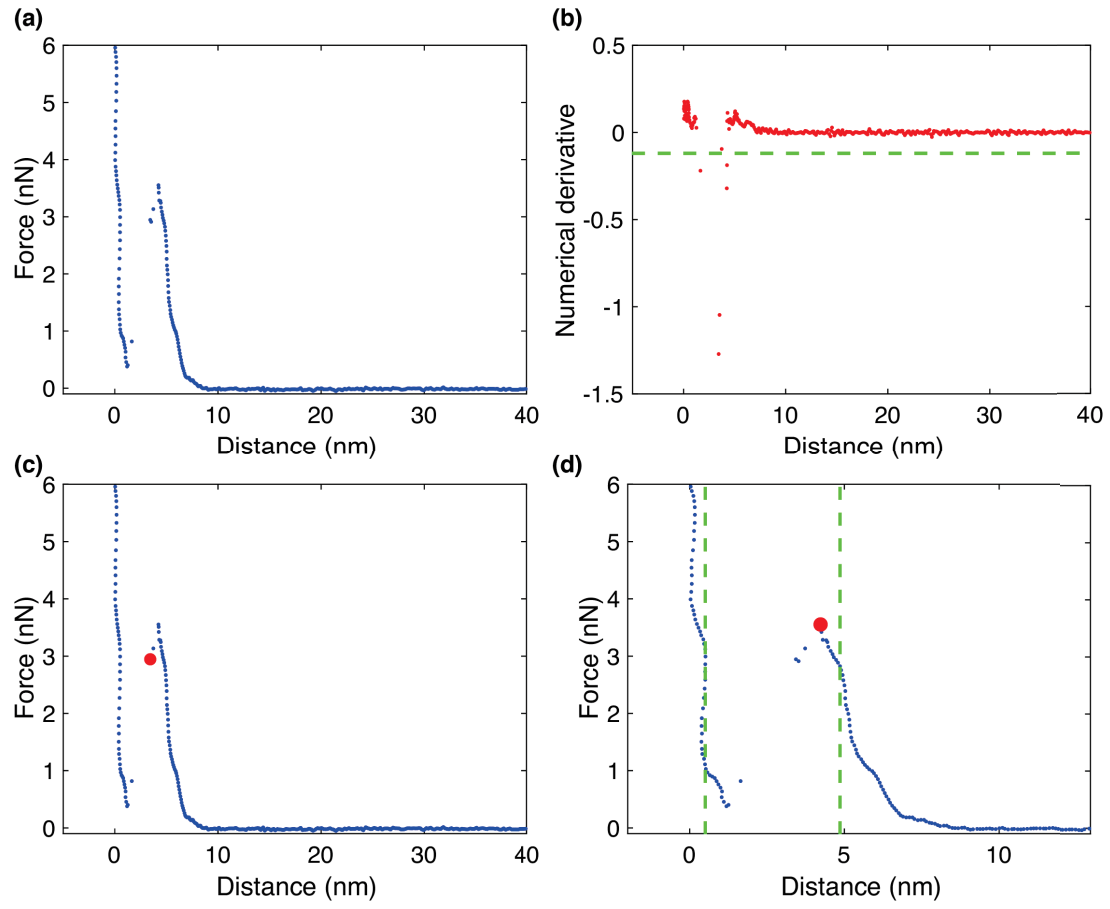


Fig. S 1: Algorithm developed to evaluate rupture forces from AFM-FS data. **(a)** Low-pass filtered force curve. **(b)** Numerical first derivative of **(a)**. **(c)** Position of the minimum of **(b)** in the force curve, represented by a red dot. **(d)** The local maximum of the force curve, corresponding to the rupture force F_B , is evaluated over a region (green dashed lines) centered in the position of the minimum of the numerical derivative.

2 YOUNG'S MODULUS AND DEBYE LENGTH EVALUATIONS

As mentioned in the main manuscript, both DOPC and DPPC Young's moduli have been determined using the Hertz model (Equation S1.2). AFM-FS experiments were performed on DOPC:DPPC (1:1) SLBs at a loading rate of $v = 1 \mu\text{m/s}$ using B20-CONT cantilevers with tip radius of 20 nm and B50-FM cantilevers with tip radius of 50 nm (both purchased from Nanotools). The contact point between tip and membrane was determined assuming the presence of 2.7 nm of water layers plus 3.6 and 4.6 nm as DOPC and DPPC thickness, respectively (1). The total thickness was added to the absolute position of the mica substrate, evaluated from the position of mechanical contact between tip and mica. Our data show the presence of the Electric Double-Layer (DL) interaction in the tip-membrane non-contact part of the curve, resulting in non-negligible forces of a few hundreds of pN once the contact is established. We took the DL effect into account modeling the tip as a sphere near a flat surface (2) (Equation S1.1). As a consequence, we have fitted the AFM-FS force *versus* distance curves independently with two different interactions as follows:

$$F_{DL}(z) = \frac{RF_Z}{\lambda_D} e^{-z/\lambda_D}, \quad \text{for } 0.1 \text{ nm} \leq z \leq 10 \text{ nm} \quad (\text{S1.1})$$

$$F_H(z) = \frac{4}{3} \frac{E}{1-\nu^2} \sqrt{R} (-z)^{\frac{3}{2}} + F_0, \quad \text{for } -\delta_{max} \leq z \leq 0 \text{ nm} \quad (\text{S1.2})$$

where z is the tip-membrane distance, λ_D is the Debye length, R is the tip radius, F_Z is an interaction constant with unity of force, E is the Young's modulus, F_0 is the interaction force at the contact point between tip and membrane and δ_{max} the maximal indentation of the SBLs. Assuming ν to be 0.5 (perfectly elastic uncompressed material), data were fitted with the Hertz model until a maximal indentation δ_{max} of 1.5 nm for DOPC and 1 nm for DPPC. DL fit was limited to tip-membrane distances higher than 1 Å to avoid to take into account non-ubiquitous short-range Van der Waals (VdW) attractive interactions (\approx to 10–20 pN, at the limit of our instrumental sensitivity). Concluding, for Equation S1.1, we left F_Z and λ_D as free parameters, whereas for Equation S1.2, only E was left as free parameter. We have evaluated $E^{\text{DOPC}} = (34 \pm 19) \text{ MPa}$ and $E^{\text{DPPC}} = (48 \pm 15) \text{ MPa}$ (Figure S2 c and e, respectively) for the 20 nm carbon probe and $E^{\text{DOPC}} = (36 \pm 19) \text{ MPa}$ and $E^{\text{DPPC}} = (58 \pm 28) \text{ MPa}$ (Figure S2 g and i, respectively) for the 50 nm carbon probe. Our values are consistent with the fact that the Young's modulus constitutes an intrinsic mechanical property of a material; therefore, it is independent of the indenter size. Moreover, our values are in agreement with data reported in the literature (3). In addition, we have determined $\lambda_D^{\text{DOPC}} = (1.6 \pm 1.4) \text{ nm}$ and $\lambda_D^{\text{DPPC}} = (1.5 \pm 1.4) \text{ nm}$ (Figure S2 d and f, respectively) for the 20 nm probe and $\lambda_D^{\text{DOPC}} = (1.3 \pm 0.6) \text{ nm}$ and $\lambda_D^{\text{DPPC}} = (1.7 \pm 0.7) \text{ nm}$ (Figure S2 h and j, respectively) for the 50 nm probe. This suggests that DOPC and DPPC head-groups have similar Debye length values close to 1.5 nm in DPBS buffer.

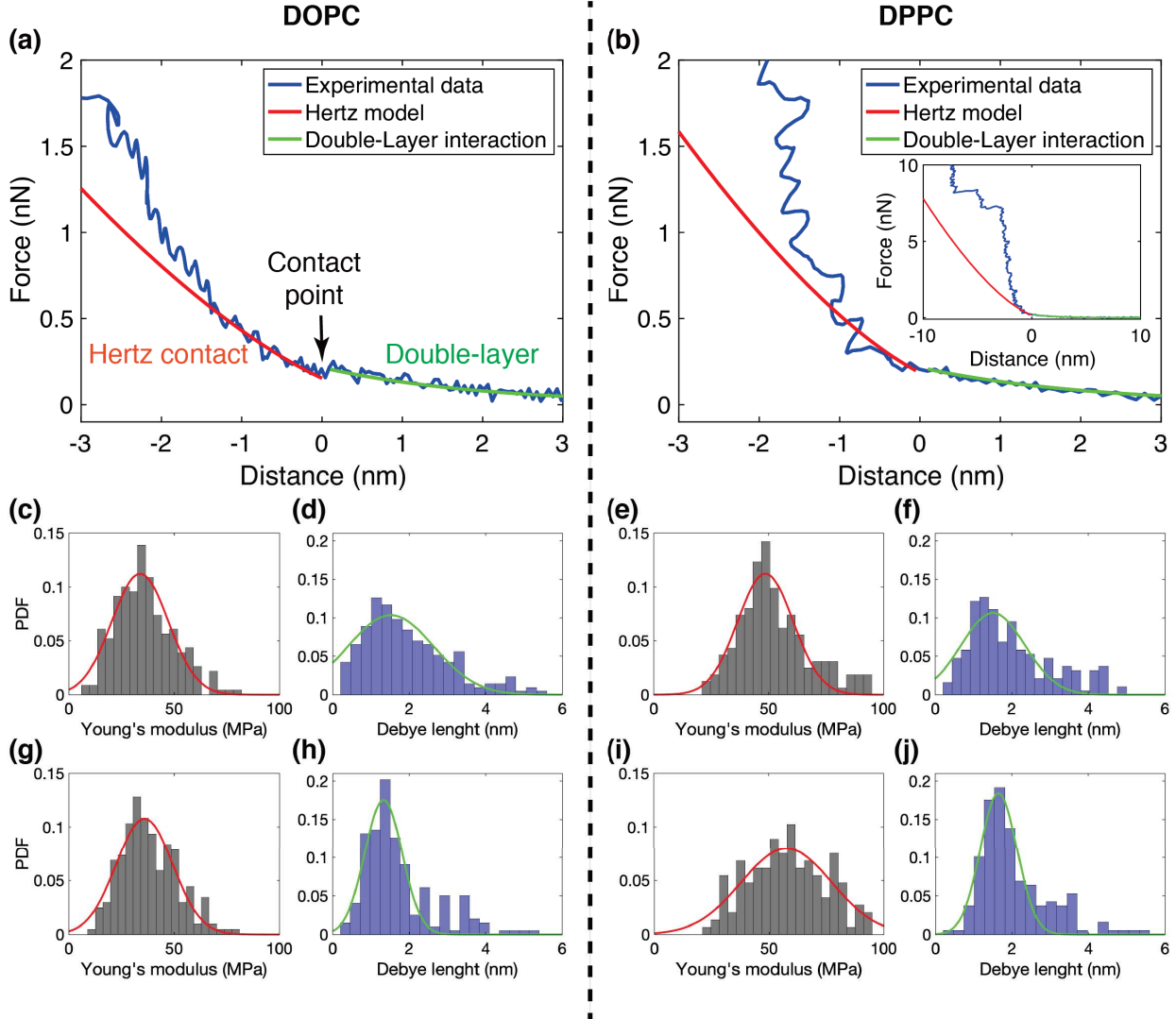


Fig. S 2: Evaluation of Young's modulus and Debye Length for DOPC (a) and DPPC (b) model membranes using an indenter with a radius of 20 nm (a,b,c,d,e,f) and 50 nm (g,h,i,j). In red the fit with Hertz model (Equation S1.2), in green the fit with DL model (Equation S1.1), the tip-membrane contact point is fixed at $z = 0$. The free parameters E and λ_D distributions over 200 curves, for both DOPC and DPPC, are displayed in the histograms. For the 20 nm indenter, $E^{\text{DOPC}} = (34 \pm 19)$ MPa and $\lambda_D^{\text{DOPC}} = (1.6 \pm 1.4)$ nm, (c) and (d), respectively and $E^{\text{DPPC}} = (48 \pm 15)$ MPa and $\lambda_D^{\text{DPPC}} = (1.5 \pm 1.4)$ nm (e) and (f), respectively. For the 50 nm indenter, $E^{\text{DOPC}} = (36 \pm 19)$ MPa and $\lambda_D^{\text{DOPC}} = (1.3 \pm 0.6)$ nm, (g) and (h), respectively and $E^{\text{DPPC}} = (58 \pm 28)$ MPa and $\lambda_D^{\text{DPPC}} = (1.7 \pm 0.7)$ nm, (i) and (j), respectively.

3 COEXISTENCE MEMBRANE PUNCTURE AND VERTICAL COMPRESSION FOR SMALL TIP INDENTERS

As mentioned in the main manuscript, when the size of the tip is small ($\approx 1\text{--}2\text{ nm}$), the molecular vertical compression in fluid phase membranes is a rare event in favour of cases where the tip can puncture the membrane in absence of rupture events (Figure 2b in the main manuscript, red curve). Fitting indentation cycles on DOPC (number of curves= 175) with the Hertz model, assuming 2 nm as tip radius (MSNL-D cantilever, Bruker), we observe that a large majority of the curves leads to a Young's modulus consistently lower ($\approx 2\text{--}3\text{ MPa}$, Figure S3a, red region) than the values reported in Figures S2c and g and, more generally, in the literature (3). It imposes a limit to the use of the Hertz model since the vertical compression of the lipid molecules occurs rarely (green region in Figure S3a). Figure S3b shows the distribution of maximal force the membrane can withstand for the same dataset. The large majority of indentation cycles show a force that is maximal at the contact point between the tip and mica (see red curve in Figure 2b of the main manuscript), suggesting that the physical mechanism involved during the indentation does not lead to a membrane rupture event anticipated by a molecular vertical compression. In other words, the tip can easily puncture the membrane, therefore encountering lower resistance (red region in Figure S3b).

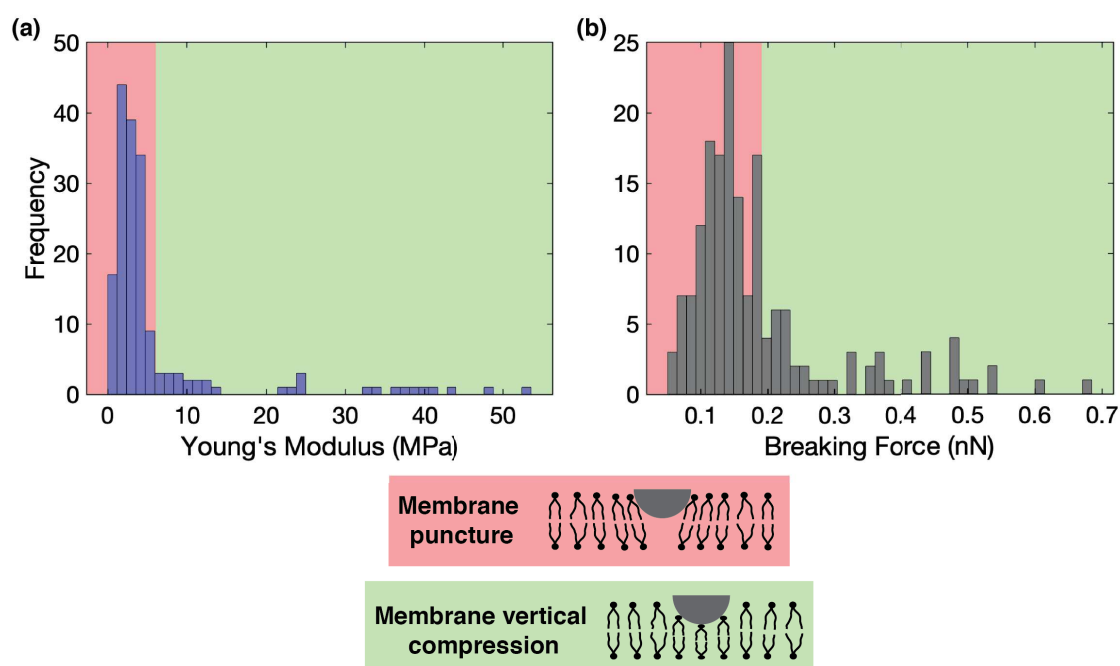


Fig. S 3: **(a)** Young's modulus distribution evaluated from indentation cycles on DOPC membranes, fitted with the Hertz contact model, using a tip with a radius of 2 nm (MSNL-D cantilever). The measured Young's modulus is ≈ 1 order of magnitude lower than the reported value of $\approx 20 - 30\text{ MPa}$. **(b)** Maximal force the membrane can withstand for the same dataset of **(a)**: in most cases (red region) it was evaluated at the contact point between the tip and the mica because the molecular vertical compression leading to membrane rupture is absent. In both **(a)** and **(b)**, the green region consists of the approach curves where molecules are vertically compressed. The red region highlights the indentation cycles showing membrane puncture.

REFERENCES

1. Tristram-Nagle, S., H. I. Petrache, and J. F. Nagle, 1998. Structure and Interactions of Fully Hydrated Dioleoylphosphatidylcholine Bilayers. *Biophysical Journal* 75:917 – 925. URL <http://www.sciencedirect.com/science/article/pii/S0006349598775800>.
2. Israelachvili, J. N., 2011. Chapter 14 - Electrostatic Forces between Surfaces in Liquids. In J. N. Israelachvili, editor, *Intermolecular and Surface Forces* (Third Edition), Academic Press, San Diego, 291 – 340. Third edition edition. URL <http://www.sciencedirect.com/science/article/pii/B9780123751829100144>.
3. Redondo-Morata, L., R. L. Sanford, O. S. Andersen, and S. Scheuring, 2016. Effect of statins on the nanomechanical properties of supported lipid bilayers. *Biophysical Journal* 111:363–372.



OPEN

Synchronous, Crosstalk-free Correlative AFM and Confocal Microscopies/Spectroscopies

Thales F. D. Fernandes, Oscar Saavedra-Villanueva, Emmanuel Margeat, Pierre-Emmanuel Milhiet[✉] & Luca Costa[✉]

Microscopies have become pillars of our characterization tools to observe biological systems and assemblies. Correlative and synchronous use of different microscopies relies on the fundamental assumption of non-interference during images acquisitions. In this work, by exploring the correlative use of Atomic Force Microscopy and confocal-Fluorescence-Lifetime Imaging Microscopy (AFM-FLIM), we quantify cross-talk effects occurring during synchronous acquisition. We characterize and minimize optomechanical forces on different AFM cantilevers interfering with normal AFM operation as well as spurious luminescence from the tip and cantilever affecting time-resolved fluorescence detection. By defining non-interfering experimental imaging parameters, we show accurate real-time acquisition and two-dimensional mapping of interaction force, fluorescence lifetime and intensity characterizing morphology (AFM) and local viscosity (FLIM) of gel and fluid phases separation of supported lipid model membranes. Finally, as proof of principle by means of synchronous force and fluorescence spectroscopies, we precisely tune the lifetime of a fluorescent nanodiamond positioned on the AFM tip by controlling its distance from a metallic surface. This opens up a novel pathway of quench sensing to image soft biological samples such as membranes since it does not require tip-sample mechanical contact in contrast with conventional AFM in liquid.

Real space observation of biomolecules at high resolution is crucial to address fundamental biological questions. In this frame, several microscopy techniques have been developed during the last decades and are currently well-established and available allowing characterizations at different lengths and timescales. Cryogenic Electron Microscopy (cryo-EM) offers nowadays the highest spatial resolution at the molecular and sub-molecular length scales but cannot image living cells in physiological conditions¹. For that, a large variety of optical-based microscopies are available, historically less resolved than cryo-EM because of the diffraction limit. However, some recently developed super-resolution techniques such as Stimulated Emission Depletion Microscopy (STED)², Stochastic Optical Reconstruction Microscopy (STORM)³, Photoactivated Localization Microscopy (PALM)⁴ and MINFLUX⁵ have bypassed the diffraction limit and improved the lateral resolution down to a few nanometers. While they do have some drawbacks both in terms of photo-toxicity or acquisition speed, their popularity nowadays reflects their coming of age. When it is to observe bio-interfaces at high resolution in physiological conditions, in a label-free configuration, Atomic Force Microscopy (AFM)⁶ and its fast video-rate version High-Speed AFM (HS-AFM)^{7,8} are outstanding techniques to obtain morphological and mechanical information at nano-scale. While all microscopies provide complementary physical and chemical information at different spatial and temporal resolutions, the challenge is now to get correlative observations of biological processes with two or more techniques that require important technological efforts.

As examples, cryo-EM and 3D super-resolution fluorescence have been coupled to aid protein localization in EM images⁹, as well as STED¹⁰, STORM^{11,12} and Super-Resolved Structured Illumination Microscopy (SR-SIM)¹³ have been successfully coupled with AFM. Combining conventional fluorescence and AFM has become increasingly popular since both techniques can work in biologically relevant conditions and they acquire complementary information: specificity mapping of proteins given by specific fluorescent probes nicely complements the high-resolution AFM images. Confocal Laser Scanning Microscopy (CLSM) and AFM have been coupled at first in 1995¹⁴ to image Langmuir-Blodgett films of 10,12-pentacosadiynoic acid. In the following decades, a large number of setups following similar operational schemes based on fixed optical axes, fixed tip position, and a

Centre de Biochimie Structurale (CBS), CNRS, INSERM, Univ Montpellier, 34090, Montpellier, France. ✉email: pem@cbs.cnrs.fr; costa@cbs.cnrs.fr

scanning sample were developed^{15–20}. In most setups, AFM and fluorescence images are acquired in a sequential manner, and correlation between images is generated afterwards^{21,22}. However, synchronicity is of high importance as it permits to follow dynamical biological processes.

In addition, it allows the acquisition of optical images while a force is applied by the AFM tip in pump and probe experiments, for instance, monitoring the response of a living cell to an AFM tip indentation or during single-molecule manipulation^{23,24}. This simultaneous modality is often not allowed due to interference and cross-talk during simultaneous image acquisition resulting in worse performance and data quality, both effects often ignored in the existing literature and only very rarely discussed^{20,25}. When coupling fluorescence (in both wide-field²⁶ and confocal²⁰ excitation schemes) with AFM, it is, therefore, of critical importance to eliminate any cross-talking between the two techniques by understanding, quantifying, and reducing the artifacts occurring during synchronous operation. We can divide artifacts into two categories:

1. AFM acquisition being affected by the excitation laser used to excite fluorescent probes. The interaction of the laser confocal spot and the AFM tip/cantilever could give rise to optomechanical/photothermal forces that can deflect the cantilever in a non-linear way which depends upon the distance from the sample. Since in time-resolved fluorescence experiments the excitation laser is continuous or pulsed at operating frequencies in the MHz regime, typically much higher than the most of cantilever resonance frequencies, the measured force (the deflection) is due to the static component of the excitation.
2. Fluorescence acquisition being affected by the presence of the AFM tip/cantilever. AFM tip luminescence gives rise to a spurious signal in the photons detection that might not be fully eliminated if there is an overlap between tip/cantilever fluorescence and the sample emission spectra.

In the case of wide-field epifluorescence, the optomechanical interactions between light and the cantilever body can result in large cantilever deflections. Cazaux *et al.* have used these deflections as a mean to mechanically synchronize AFM and optical measurements²⁶. A wide-field excitation scheme such as Total Internal Reflection excitation (TIRF) eliminates most artifacts since it limits the interaction of light only to a few hundred nanometers above the glass coverslip, where solely the tip's end is present, the cantilever being typically few microns axially farther. A large number of simultaneous experiments were reported in the last two decades using this modality^{27–31}. However, this type of illumination is not suitable for thick samples such as cells, since the tip will be positioned at the apical cellular membrane axial position, out of the evanescent excitation field.

Confocal microscopy is perfectly suited for such cellular imaging, but the interaction of the AFM tip and the confocal spot can, unfortunately, extend to a greater distance. In this work, we focus on the coupling between a confocal spot and an AFM tip/cantilever with the aim to investigate and quantify photothermal induced deflection resulting from the presence of metal coating at the cantilever backside³², radiation pressure exerted on the tip³³ due to the scattering of the confocal spot and finally tip/cantilever luminescence¹⁶. We show that all effects highly depend on the choice of the AFM tip and cantilever. We conclude that tip geometry, material, and metallic coating at the cantilever backside, as well as cantilever stiffness, are the key parameters to be taken into account. We also present how these common pitfalls can be avoided, or highly minimized, so there is no spurious cross-talk in the acquired images. As proof of principle we imaged synchronously the topography, lifetime, and fluorescence intensity of gel and fluid phases in Supported Lipid Bilayer (SLB), labeled with a BODIPY fluorescent probe. Finally, for the first time, to the best of our knowledge, we implemented a simultaneous AFM Force Spectroscopy (AFM-FS) and confocal fluorescence spectroscopy operational scheme. In this way, we probed the force and lifetime variation due to Metal Induced Energy Transfer (MIET) between the Nitrogen-Vacancy (NV) centers in a nanodiamond attached to the apex of an AFM tip and a substrate of thin gold, therefore, enabling a novel pathway of quench sensing and opening up novel non-invasive imaging modes in liquid that can be used to image soft and fragile biological specimens.

Results

The synchronous imaging acquisition setup based on confocal excitation is described by Fig. 1. The excitation source is a supercontinuum pulsed laser where an excitation band-pass filter enables the convenient switching between different excitation wavelengths for multi-color fluorescence acquisition. The light is focused by a high Numerical Aperture objective (NA = 1.4). The emitted fluorescence photons are collected by the objective, focused on a pinole, recollimated, filtered by an emission filter and finally focused on an Avalanche Photodiode (APD) connected to a Time-Correlated Single Photon Counting (TCSPC) card.

The AFM is mounted on top of an inverted microscope where the sample and the tip can be displaced independently with two XYZ piezo scanners. The synchronization of the AFM and the TCSPC card is made by routing the events (photons) with a Transistor-Transistor Logic (TTL) signal generated by the AFM electronics controller, therefore, enabling to assign a *xy/z*-position for each photon. Topography, intensity, and lifetime signals from the setup are used to construct simultaneously an AFM and two optical images, respectively. If operated in force spectroscopy mode, (AFM-FS), force, intensity, and lifetime curves versus tip-sample distance are simultaneously acquired. The lifetime was either evaluated for each image pixel by fitting a decay curve with a single exponential or, in AFM-FS mode, by amplitude weighting the decay curve (see Materials and Methods section). It is worth to notice that is crucial to use a short-pass filter (AFM laser filter) before the APD to filter out the light used in the AFM cantilever monitoring setup (AFM laser)³⁴, usually called optical beam deflection.

As previously mentioned, the interaction of the focused excitation light and the AFM tip can give rise to two different phenomena: optomechanical forces and/or tip/cantilever luminescence, where the former branches into radiation pressure and photothermal effect. Radiation pressure (Fig. 2a) will always be present in all cases since the scattering of the incoming light will generate forces due to change in momentum of light. Momentum conservation dictates that the cantilever will be deflected upwardly by this force. Photothermal deflection (Fig. 2b) is

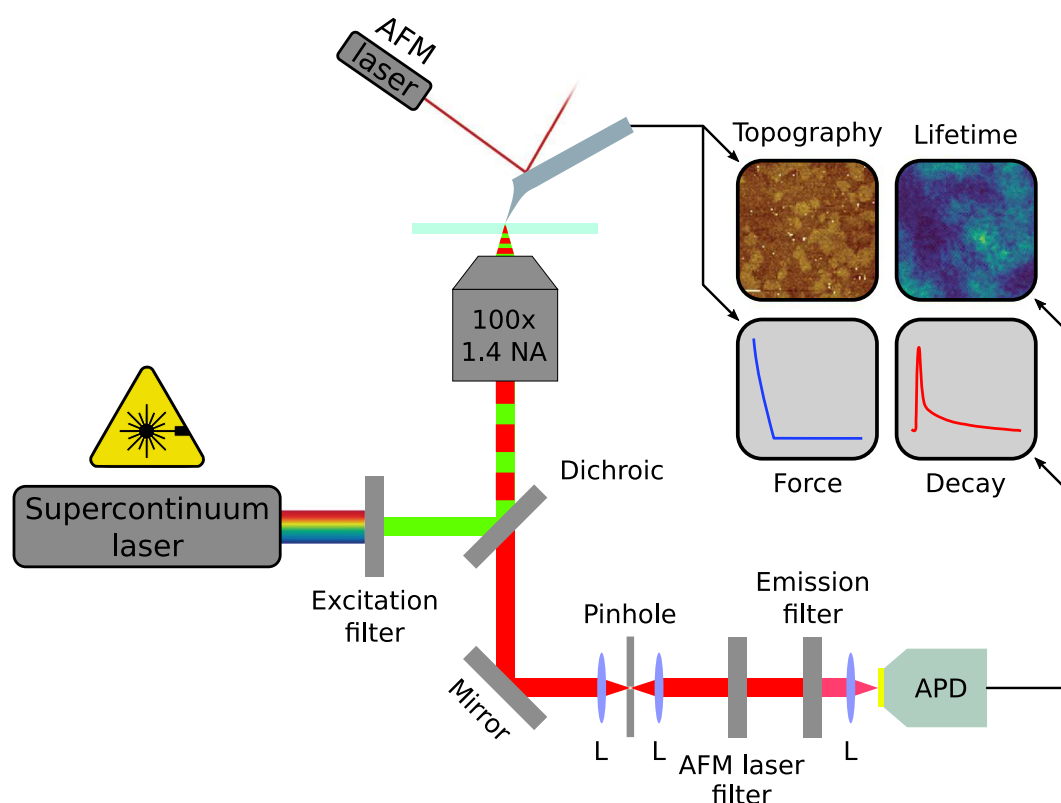


Figure 1. AFM and inverted confocal microscope setup, where the AFM and the optics are coupled by synchronizing the photons acquisition with a TTL signal from the AFM electronics controller. Convergent lenses are indicated as L.

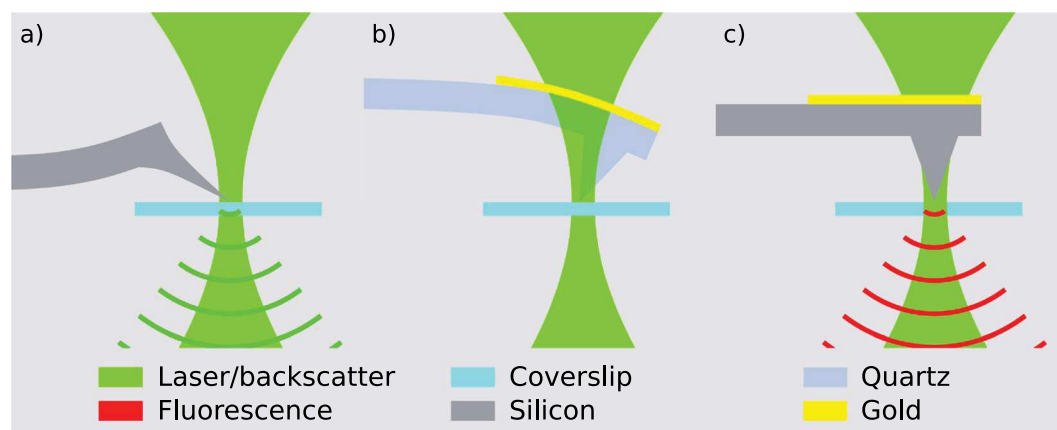


Figure 2. Possible AFM tip and confocal spot interactions: radiation pressure (a), photothermal induced deflection (b), and cantilever/tip luminescence (c).

present if the cantilever is composed of two different materials (similarly to a bimetallic strip), which is the case of metal-coated cantilevers, where a thin layer of metal is deposited onto the cantilever backside to improve reflectivity. For visible light, gold will absorb more than either silicon or silicon nitride (higher extinction coefficient) and, due to its higher thermal expansion coefficient, it will expand more when heated by the laser. This differential expansion will cause a downwards bending of the cantilever. Spurious luminescence (Fig. 2c) can arise from two sources: 1. the material of the tip/cantilever itself can present luminescence properties, as in the case of amorphous silicon nitride, particularly important at wavelengths higher than 800 nm¹⁶. 2. The coating on the cantilever backside can be luminescent as well, as for example gold that emits in the red region of the spectrum³⁵. It is worth to notice that backscattered light will occur in all possible configurations since the tip will always scatter the incoming light of the confocal spot in all directions and, therefore, for the same reason radiation pressure

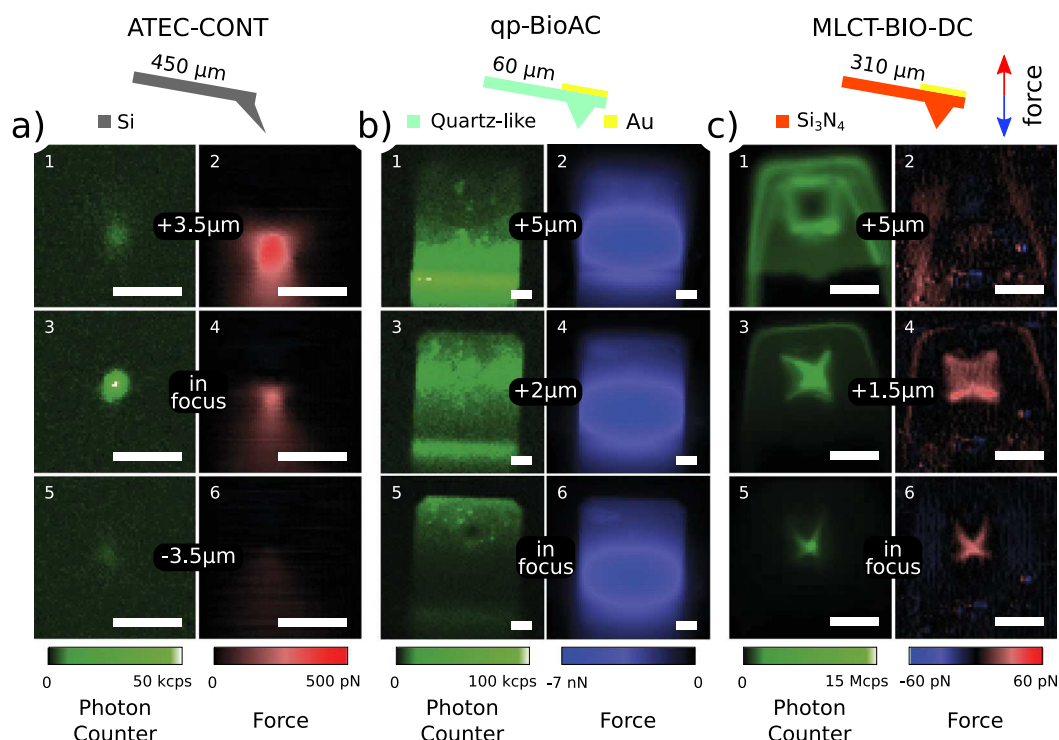


Figure 3. Simultaneous photon counts (panels 1, 3, and 5) and force (panels 2, 4, and 6) scans for three different AFM cantilevers: (a) ATEC-CONT, (b) qp-BioAC, and (c) MLCT-BIO-DC. The images were acquired using a reverse-tip image operational scheme where the confocal spot is a probe and the AFM tip and cantilever are samples to be measured. Data were collected with a 532/10 nm excitation filter, a 690/50 nm emission filter, and a laser power of 300 μ W. Subfigures 1–2, 3–4, and 5–6 were acquired at different distances from the confocal spot focal plane. The scale bar is 5 μ m for all images. In the schematic of the cantilevers, the nominal cantilever length and the red and blue arrows indicate positive and negative force directions, respectively, corresponding to the color scale in panels 2, 5, and 6. Intensity (photon counter) images (panels 1, 3, and 5) are given in counts per second (cps) and were recorded directly from the APD. The cantilever used for the qp-BioAC is the CB2 while the one for MLCT-BIO-DC is the cantilever C. The Point Spread Function (PSF) of the confocal spot is \approx 400 nm.

will always be present. However, most of the backscattered light can be easily eliminated by a notch filter when it is not already sufficiently reflected by the emission filter.

We characterized and quantified these effects by operating the AFM in the reverse-tip imaging configuration³⁶. The confocal spot is focused 4 μ m from a glass coverslip and held in place throughout the measurement. Using the *hover mode* of the AFM (see Material and Methods), the tip scans the glass coverslip in the trace scan and then, in the retrace scan, the tip follows the retrace topography vertically displaced in z by a given distance specified by the user. In this way, it is possible to make a constant height image even if the sample is inclined. In this mode, the deflection of the cantilever is monitored in the retrace scan without an active feedback. Deflection (force) and intensity (photon counter) images are acquired during scan, as shown in Fig. 3. The resulting images will be of the interaction of the confocal spot with different regions of the tip for different focal planes. In this operational scheme, the confocal spot is steady and operates as a “probe” while the AFM tip and cantilever are the samples to be measured, hence the name, reverse-tip imaging. We used three AFM cantilevers with different specifications: a protruding silicon tip (Fig. 3a), a quartz-like tip with gold coating on the cantilever backside (Fig. 3b) and silicon nitride (Si_3N_4) with a gold-coated cantilever (Fig. 3c), commercially available as ATEC-CONT (Nanosensors), qp-BioAC (Nanosensors), and MLCT-BIO-DC (Bruker), respectively. The images were acquired both with the tip in focus and out-of-focus positions to observe the different interactions of the confocal spot (300 μ W power, 532/10 nm wavelength) with the AFM tip and cantilever body.

Given the large emission spectra of silicon³⁷, silicon nitride¹⁶, and the metallic coating on the cantilever backside, in our case gold³⁵, the choice of the emission filter is not crucial if compared to fluorescence imaging of conventional organic fluorophores characterized by narrow emission spectra. In Fig. 3 we used a 690/50 nm emission filter. Panels 1, 3, and 5 show the photon intensity signal whereas panels 2, 4, and 6 display the vertical force acting on the AFM cantilever. Figure 3a shows that the ATEC-CONT has a bright central spot in the photon intensity channel that is due to tip luminescence and presents a positive force in the range of a few hundred of piconewtons. By inserting a notch filter in the emission path, no significant change in the photon intensity channel is observed, which shows that backscattering contribution is minimal and it is completely filtered out by the band-pass emission filters. Such a positive force is a direct consequence of the radiation pressure acting on the

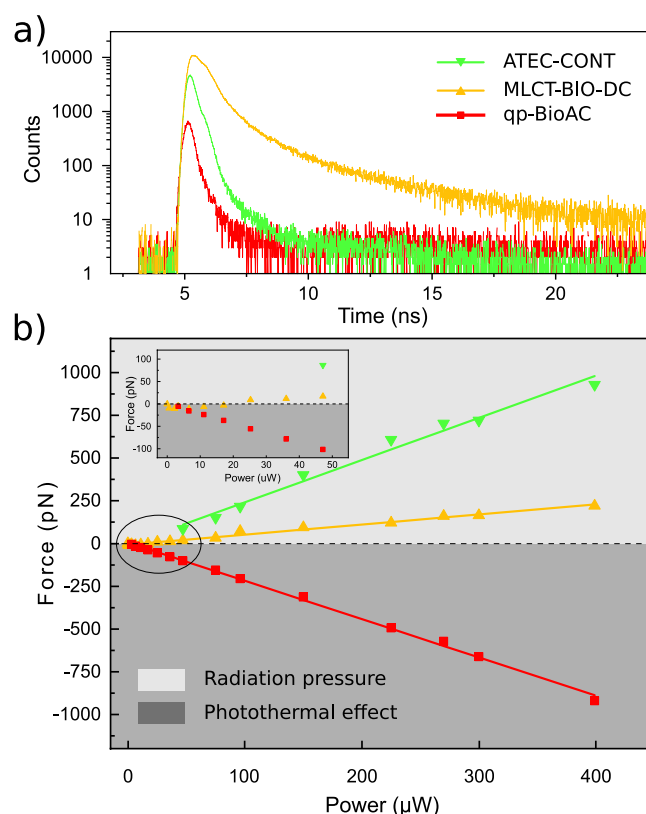


Figure 4. (a) Luminescence decay curves for different AFM cantilevers and (b) variation of the measured force as a function of the laser power. The cantilevers are qp-BioAC (red), MLCT-BIO-DC (yellow), and ATEC-CONT (green). The inset in (b) shows a zoom of the region of low power, highlighted by the ellipse. Positive force is characterized as radiation pressure while negative force is photothermal induced deflection. The slopes of the lines in (a) are: ATEC-CONT (2.47 ± 0.13 pN/μW), MLCT-BIO-DC (0.59 ± 0.02 pN/μW), and qp-BioAC (-2.24 ± 0.03 pN/μW). All curves were acquired with a 532/10 nm excitation filter, with a 690/50 nm emission filter, and 300 μW power in (a). The positive force region is colored in green to indicate the radiation pressure regime whereas the negative force region is colored in purple to indicate the photothermal regime.

cantilever due to the backscattered light. With the qp-BioAC (Fig. 3b) the situation is consistently different: the force is negative and it has a maximum modulus of ≈ 7 nN. The confocal spot interacts strongly with the gold reflective coating on the cantilever backside, as shown in the photon intensity images, Fig. 3b panels 1, 3, and 5. As a consequence, the interaction induces a differential heating that bends the cantilever downwards due to photothermal effects. The intensity signal presents no direct correlation with the force observed and is highly dependent on the cantilever bending angle. In contrast with the previous case, the tip position is characterized by a darker spot in the photon intensity image (Fig. 3b panel 5) that is due to the fact that both excitation light and gold emission have to pass through the tip, therefore through a higher quantity of material. As a consequence, we collect less fluorescence emitted by the reflective gold coating material when the tip and confocal spot are aligned. The MLCT-BIO-DC (Fig. 3c) shows a mix of radiation pressure and a mild photothermal deflection contributions in the force signal. In this case, it is also possible to observe the interaction with the tip's gold-coating but the thermal effects are not as drastic as before, leading to a positive total force acting on the cantilever when the tip and confocal spot are aligned (see Materials and Methods). The small deflection of the MLCT-BIO-DC, despite the presence of a gold coating at the cantilever's end, could be attributed to its manufacturing process, optimized to minimize probe bending due to elevated temperatures.

Given the data presented in Fig. 3, the arising question is what cantilever is worth using to reduce cross-talk between AFM and time-resolved fluorescence acquisitions in correlative experiments. Figure 4a presents time-resolved fluorescence decay curves acquired for the three AFM cantilevers of Fig. 3 with a high laser power of 300 μW to maximize signal to noise ratio for the less luminescent ones. MLCT-BIO-DC (yellow curve) has the highest intensity signal by two orders of magnitude and presents a long lifetime in comparison with the qp-BioAC (red curve) and the ATEC-CONT (green curve).

While ATEC-CONT and qp-BioAC will affect the measured lifetime of fluorescent probes characterized by a short (≈ 1 ns) lifetime, the MLCT-BIO-DC will affect a larger variety of fluorophores presenting even longer lifetimes. In addition, we monitored the variation of the spurious force as a function of the incident laser power (Fig. 4b). The force scales linearly with the power and the different cantilevers branch in the two categories depending on the nature of the optomechanical interaction: radiation pressure and photothermal induced deflection.

Cantilever	Brand	Optomechanical constant [pN/ μ W]
ATEC-CONT	Nanosensors	2.47 ± 0.13 pN/ μ W
qp-BioAC	Nanosensors	-2.24 ± 0.03 pN/ μ W
MLCT-BIO-DC	Bruker	0.59 ± 0.02 pN/ μ W

Table 1. Slopes of the fits in Fig. 4.

It is worth to notice that the photothermal deflection computed in this case, for a laser power of 300 μ W, is inferior in modulus to the 7 nN shown in Fig. 3b because in the latter case the maximum force is measured with the confocal spot focused on gold-coated cantilever backside and not on the AFM tip as in Fig. 4b, as previously mentioned. Table 1 reports the slopes from Fig. 4b, force versus laser power, which indicates the significance of the force for a given probe.

Concluding, low laser power should be used, and the relative position between the tip and the confocal spot should be held constant, leading to a change of the cantilever equilibrium position while avoiding a change of relative deflections. In addition, our data suggest that the qp-BioAC cantilevers should be employed to accurately evaluate the lifetime of the fluorescent probes within the sample (Fig. 4a). Instead, MLCT-BIO-DC cantilevers, presenting lower spurious force, are more suited for experiments where low AFM interaction forces have to be measured and in presence of a large number of fluorophores in the excitation volume, ensuring high signal to noise ratio to properly evaluate their lifetime.

The advantage of the correlative AFM-FLIM imaging mode relies on the complementarity of the two techniques. To prove that, we imaged fluid and gel phases enriched domains in biological model membranes, correlating their morphology (AFM) with their local viscosity (FLIM). We used a lipid mixture of 1,2-dipalmitoyl-sn-glycero-3-phosphocholine (DPPC), 1,2-dioleoyl-sn-glycero-3-phosphocholine (DOPC) in 1:1 molar ratio supplemented with 0.1% in volume of 2-(4,4-difluoro-5,7-dimethyl-4-bora-3a,4a-diaza-s-indacen e-3-dodecanoyl)-1-hexadecanoyl-sn-glycero-3-phosphocholine (BODIPY). For the simultaneous acquisition of AFM, confocal microscopy, and FLIM (shown in Fig. 5), we used the qp-BioAC cantilever and a laser power of 120 nW, ensuring, as previously explained, the highest accuracy for BODIPY lifetime evaluation while minimizing the spurious force during AFM acquisition.

Both topography (Fig. 5a) and fluorescence intensity (Fig. 5b) show that the DPPC enriched regions (higher thickness) have lower BODIPY concentration. Wu *et al.* showed in Giant Unilamellar Vesicles (GUVs) that high viscosity lipids present higher lifetime, hence lifetime can be used to probe directly the lipids viscosity³⁸. Figure 5c shows that DPPC enriched domains have higher lifetime when compared with DOPC domains, this is expected since DPPC is a gel-phase lipid, hence more viscous than DOPC, a fluid-phase lipid. The higher lifetime, above 3 ns, when compared to Wu *et al.* ≈ 1.8 ns³⁸, can be attributed to the fact that supported bilayers are formed on top of a substrate (glass), inducing different physical behaviors in terms of lipid diffusion and potentially local viscosity when compared to free-standing bilayers in the GUVs case. Indeed, even if the presence of a layer of buffer (2-3 nm thickness) between the lipid polar heads and the substrate generally prevents an important hindrance in lipid diffusion³⁹, it is known that the latter can be reduced as compared to giant unilamellar vesicles⁴⁰. The tip luminescence, dominated by low lifetime (< 1 ns) is not present in the simultaneous AFM-FLIM imaging (see Sections 3 and 5 of the Supplementary Information).

Minimizing tip/cantilever luminescence and optomechanical forces is relevant also in synchronous AFM-FS and fluorescence spectroscopy experiments. In this novel operational scheme, the AFM tip has fluorescent properties that can be correlated with the force measured by AFM while being approached or retracted from the sample. The force readout can be used to define the mechanical contact position between the sample and the fluorescent probe and, subsequently, the latter can be accurately placed with nanometric precision at a given distance from the sample and its lifetime can be probed.

To demonstrate that, we show the decrease of lifetime of NV centers in a diamond nanoparticle due to MIET⁴¹ while the nanodiamond is approached to a gold substrate. Figure 6 shows an example of nanopositioning and nanomanipulation of a nanodiamond attached to the apex of an AFM tip. Figure 6a,b show a plot of the decays for every pixel (z -position, axis), where the color scale represents the number of photons collected, acquired simultaneously with a force curve Fig. 6e,f. The experiments were performed in Dulbecco's Phosphate-Buffered Saline (DPBS) solution. Firstly, we approached an ATEC-CONT tip holding a nanodiamond at its apex to a gold substrate, pressed with a high force (10 nN) and held in place for 2 seconds (Fig. 6a,c,e). This allowed the nanodiamond to dislodge from the tip and to stay permanently on the gold. The tip was then retracted without the nanodiamond. This can be clearly seen from Fig. 6c, where the lifetime decreases approaching the gold and never recovers back during tip retraction from gold. The lifetime of the nanodiamond changes from 12.60 ± 0.28 ns to 11.69 ± 0.30 ns, which corresponds to a quenching efficiency of ≈ 7.2 %. In a second experiment, showed in Fig. 6b,d,f, we used a custom qp-BioAC tip (CB1) with a plateau at its end holding a stable nanodiamond at the tip's apex (see Materials and Methods section). In this configuration, the fluorescent nanodiamond is approached, pressed with lower force (5 nN), and retracted from the gold substrate without being dislodged from the AFM tip. The lower force is a requirement to avoid the loss of the nanodiamond upon contact. The lifetime and force curves are symmetric, Fig. 6d,f, showing that the interaction is reversible. The lifetime of the nanodiamond changes from 13.86 ± 0.27 ns to 13.13 ± 0.23 ns upon contact with the gold, which corresponds to a quenching efficiency of ≈ 5.5 %. The quenching in lifetime when approaching gold, or any metal, is expected due to MIET⁴¹. The radiation rate will change due to the coupling of the nanodiamond electromagnetic near-field with the plasmons of the gold. In the vertical position (x -axis) of Fig. 6e,f the approach and retract curves have been “unfolded”, where

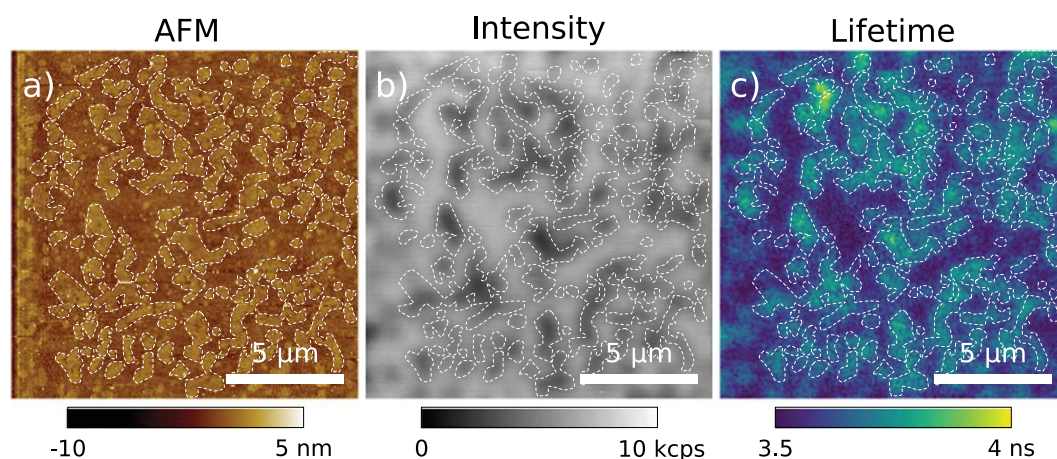


Figure 5. AFM morphology (a), fluorescence intensity (b), and lifetime (c) of DOPC:DPPE (1:1 molar ratio) labeled with 0.1% BODIPY model membranes. The three images were synchronously acquired. The scale bar is 5 μm , the power used was 120 nW with a 488/10 nm excitation filter and a 525/39 nm emission filter. The tip used was a qp-BioAC. The dashed white line serves as visual aid for the separation of the two domains.

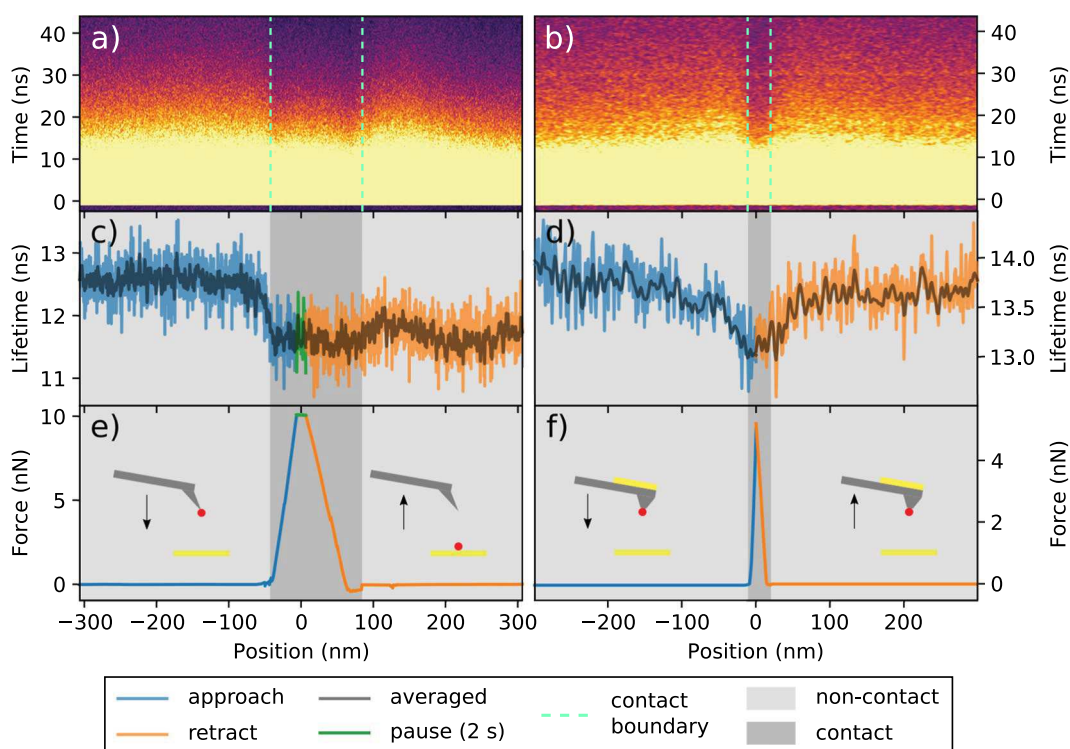


Figure 6. Simultaneous force curve and nanodiamond lifetime measurements approaching and retracting a gold substrate. Photons are synchronized with TTL from the AFM that enables the acquisition of decay curves for every z -position of the tip. (a,b) Show the tip z -position versus time (decay curves), where the color scale represents the number of photons collected. (c,d) Show the lifetime of the nanodiamond in function of the tip position. (e,f) Show the standard force curves unfolded so approach and retract curves are separated in the negative and positive axis, respectively. The blue curves in (c–f) consist of the approach whereas orange region the retract. The green curves in (c,e) constitute a region where the tip was paused for 2 seconds. The light gray region displays the non-contact (zero force) interactions whereas the darker gray consists of the contact regime. A 532/10 nm excitation filter was used with a 709/167 nm emission filter with power of 90 μW . The dark gray curves in (c,d) show the data with spatial (9 neighbors) and temporal (4 neighbors) binning (filter). The same binning is also applied to (a,b) to aid visualization. An ATEC-CONT was used in (a,c,f) whereas in (b,d,f) a modified qp-BioAC red(CB1) with a plateau was used. Tip schematics in (e,f) show an AFM tip with a nanodiamond (in red) and the gold substrate (yellow). In the retract curve of (e) the nanodiamond is left on the surface whereas in (f) it is kept at the tip's end.

approach/retract have negative/positive position values. A folded version of the force curves is presented in Section 2 of the Supplementary Information together with the lifetime curve for another nanodiamond.

Discussion

The mutual interaction of the confocal spot and the AFM tip/cantilever can give rise to a cross-talk in the AFM and/or fluorescence images. Two main forces have been explored: radiation pressure and photothermal-induced deflections. Miranda *et al.* have calculated the deformation due to laser heating on gold-coated cantilevers and found displacements of 9 nm and forces around 3 nN with ≈ 2 times less power than used in Fig. 3²⁵. Radiation pressure forces can be estimated to be in the range of few tens/hundreds of piconewtons, in agreement with our results (see Section 1 of the Supplementary Information). While in standard confocal imaging a laser power inferior to 100 μ W is usually employed, in correlative STED-AFM¹¹ a much higher power in the mW range is required, suggesting that simultaneous STED and AFM will produce optomechanical forces from several hundreds of pN to the nN range (Fig. 4b), causing large tip deflections when using soft AFM cantilevers (< 0.1 N/m stiffnesses). The inset of Fig. 4b, however, suggests that even at reasonably low laser power (10–50 μ W) optomechanical forces are present and can be quantified in few tens of pN. The same applies to the overall attractive force in the case of qp-BioAC. Those forces are not negligible and should be taken into account when measuring by AFM particularly soft interfaces such as living cells plasma membrane⁴² or when unfolding single molecules⁴³.

Moreover, the optomechanical interaction will not be constant if the alignment between the excitation laser and the AFM tip is not kept fixed during data acquisition, for instance, if the confocal spot is scanned and the tip is fixed as in the case of AFM coupled with a confocal microscope with a spinning disk operational scheme²⁴ or with some STED microscopes. While MLCT-BIO-DC minimizes optomechanical forces, quartz-like cantilevers such as qp-BioAC perform better for time-resolved fluorescence measurements due to lower tip luminescence. We have shown that using a low excitation power of 120 nW (more generally inferior to 10 μ W) it is possible to image synchronously model membrane morphology, fluorescence intensity and lifetime minimizing optomechanical spurious forces (< 10 pN) and tip and gold-coating on cantilever backside luminescence, therefore minimizing any tip-related artifact.

Concerning the nanopositioning experiment presented in Fig. 6, the lifetime decrease occurs in absence of mechanical contact between the fluorescent probe and the gold substrate, at short distances where the AFM is not sensitive enough to detect any interaction force. In perspective, this enables the possibility to obtain topographical images in liquid acquired in absence of AFM tip-sample mechanical contact. It represents an important advance when it is to image soft, fluorescently-labeled, samples that are largely deformed by conventional AFM due to their extreme softness as it occurs in the case of living cell membranes.

In our case, only a small drop (7% and 5%) in nanodiamond lifetime is observed in Fig. 6c,d, respectively. Although the change is small, uncertainty in lifetime characterization is in order of hundreds of picoseconds, therefore, the change observed is still significant. Tisler *et al.* have observed a 35% MIET efficiency when approaching a single NV center 25 nm nanodiamond attached to an AFM tip on top of graphene, a material that behaves like a metal¹⁸. In our case, the small MIET efficiency observed in Fig. 6 could be attributed to either the larger nanodiamond size (≈ 40 nm) or the more abundant number of NV centers (≈ 15) that are randomly oriented in the nanodiamond core. In the case of the experiment shown by Tisler *et al.*¹⁸ a complete lifetime spectroscopical change in respect to the nanodiamond-sample distance is not reported. Indeed, in their case, the lifetime variation was measured only when the nanodiamond was in mechanical contact with graphene or the underlining substrate.

The lifetime/force curve, where the fluorescence decay is recorded for each z-position of the tip/emitter, enable us to gain insight in the near-field non-contact interactions, as it has been shown by Buchler *et al.* in the case of a gold nanoparticle approached to a glass coverslip⁴⁴, validating the theory predicted by Drexhage⁴¹ in 1970. Only when both lifetime and force signals are acquired, the precise mechanical contact point can be identified from the AFM interaction force and, consequently, an accurate fluorescent tip-sample distance can be measured. Indeed, the full control of the emitters nano-positioning is the key for future non-invasive (sub-piconewton forces) imaging modes, where the topography is mapped by relying on the quantum exchange of energy between donors (tip) and acceptors (sample) rather than the mechanical contact usual in AFM in liquid.

In summary, our results impose important experimental constraints for synchronous operation and interference-free correlative AFM and confocal time-resolved fluorescence. In this work, we have quantified in pN/ μ W the radiation pressure and photothermal detection forces acting on AFM cantilevers composed of different materials and in the case of different tip geometries. While quartz-like AFM probes, minimizing tip luminescence, are more suited when fluorescence lifetime has to be measured, the overall optomechanical forces are minimized if radiation pressure and photothermal effect contributions are comparable, canceling each other. However, our findings allow for the synchronous collection of AFM and FLIM images as well as for the simultaneous correlation of Force Spectroscopy (AFM-FS) with fluorescence lifetime. We have shown the correlation of the topography (AFM) with the local viscosity (FLIM) in the presence of gel and fluid phase separated domains in model biological membranes labeled with a BODIPY fluorophore. Finally, we have shown that the simultaneous correlation of force and fluorescence lifetime reveals a unique potential that we have used to reversibly tune the spectroscopic properties of a fluorescent nanodiamond attached to an AFM tip once it is placed in close vicinity with a gold substrate.

Materials and Methods

Atomic Force and Confocal Microscopies. Images were acquired using a Nanowizard 4 (JPK Instruments, Bruker) equipped with a Tip Assisted Optics (TAO) module and a Vortis-SPM control unit. The AFM cantilever detection system employs an infrared low-coherence light source, with emission centered at 980 nm and further long-pass filtered at 850 nm with a Schott RG850 filter. The AFM head was mounted on a Zeiss

	Model	Wavelength [nm]	Brand
Exc.	ZET488/10x	448/10	Chroma
	ZET532/10x	532/10	Chroma
Emiss.	FF01-525/39	525/39	Semrock
	AT690/50m	690/50	Chroma
	FF01-709/167-25	709/167	Semrock

Table 2. Emission/Excitation filters.

inverted optical microscope. A custom-made confocal microscope was coupled to the AFM using a Rock-PP supercontinuum laser (Leukos) as an excitation source operating at 20 MHz (50 ns pulses of width < 100 ps). We used an oil immersion objective with a 1.4 numerical aperture (Plan-Apochromat 100x, FWD = 0.17 mm, Zeiss) and a pinhole of 100 μm diameter size (P100D, Thorlabs). We used an avalanche photodetector (SPCM-AQR-15, PerkinElmer) connected to an SPC-150 (Becker & Hickl) TCSPC card to collect fluorescence signals. The light source of the AFM detection system was filtered out in the fluorescence emission path using an ET800sp short pass filter (Chroma). The excitation laser power was measured after the objective at the sample level with a S170C microscope slide power sensor and a PM100 energy meter interface (both purchased from Thorlabs). The emission and excitation filters utilized are shown in Table 2.

During simultaneous AFM/FLIM images the AFM tip and confocal spot positions were fixed by co-aligning them. Full alignment is obtained in two steps: 1. The tip is at first roughly aligned using white field illumination and then the alignment is fine-tuned using the increase of tip luminescence. It is worth to notice that when tip and confocal spot are aligned, some AFM tips, such as qp-BioAC (Nanosensors), show colocalized tip luminescence and optical forces maxima, whereas so-called “protruding AFM tips” do not show maxima colocalization. 2. The sample is imaged and any mismatch between topography and FLIM image is adjusted by correcting the tip position.

Keeping the confocal spot and AFM tip aligned during data acquisition has the advantage to maintain constant all spurious effects resulting from synchronous operation. In addition to the tip/cantilever luminescence background and the optomechanical deflection, we mention the mirror-like effect that is due to the reflection of the incoming excitation light by the metallic coating at the cantilever backside: this results in a higher excitation intensity that is constant all over the image acquisition if confocal spot and tip are aligned, whereas it is not in case of wide-field epifluorescence or confocal spinning disk operational schemes.

Force/Lifetime curves. Acquisition of approach-retract curves with simultaneous collection of force, photon intensity (photon counter) and fluorescent nanodiamond lifetime was performed using 532/10 nm as excitation filter and 709/167 nm as emission filter with a laser excitation power of 90 μW . The number of photons emitted by the nanodiamond (> 6 ns) and collected by the objective is in the order of tens of counts per second (cps), whereas normal acquisition speeds in modern AFM can reach hundreds of kHz⁴⁵. Since hundreds or thousands of photons are needed to properly evaluate the lifetime, our acquisition bandwidth must be reduced to few tens/hundreds of Hz. Faster acquisition rates would result in the collection of too few photons (or even none) and the lifetime evaluation would be impossible. For this reason we have fixed our acquisition bandwidth to 20 Hz and performed forced curves in a quasi-static mode at a speed of 5 nm/s.

Lifetime was evaluated by amplitude weighting the decay curve for times greater than 6 ns. All measurements were performed at room temperature and under liquid conditions in Dulbecco’s Phosphate Buffer Solution (DPBS), purchased from GIBCO, without MgCl_2 and CaCl_2 (GIBCO ref. 14190-094). The tip was held constant and the sample was approached to the tip using the axial sample piezo of the TAO module. The tip-confocal alignment was performed similarly to the method described above with a key change: we focused the confocal spot when the tip is in mechanical contact with the sample surface, hence the maximum signal from the nanodiamond/gold happens at the contact point (Fig. 6).

AFM tips. qp-BioAC (tip height $\approx 7 \mu\text{m}$) and ATEC-CONT (tip height $\approx 17 \mu\text{m}$) were purchased from Nanosensors and MLCT-BIO-DC (tip height $\approx 3.5 \mu\text{m}$) was purchased from Bruker. MLCT-Bio-DC-C probes have a resonance frequency of ≈ 1 kHz, ATEC-CONT of ≈ 6 kHz and qp-BioAC of ≈ 25 kHz and ≈ 45 kHz (CB2 and CB1, respectively), all resonances measured in liquid environment. Custom tips, presenting a plateau at the tip apex, were purchased from Nanoworld: they were fabricated modifying a qp-BioAC cantilever (see Section 4 of Supplementary Information). An electron beam deposited carbon tip was grown on top of a thin layer of gold. Subsequently, a flat circular plateau of ≈ 50 nm diameter was obtained at the tip apex by means of Field Ion Beam (FIB) to aid fluorescent nanodiamond fixation and stability.

For optomechanical force characterization, a dozen tips were used to fully characterize and understand the forces employed. All probes of the same brand behaved similarly, with the same range of forces and same force/intensity distribution over the cantilever. For the approach-retract experiment with the nanodiamonds, we have collected data from tens of different probes whereas each probe had a different nanodiamond that was carefully grafted. In Fig. 6 two of such different tips were used.

Tip calibration. In all AFM experiments, the inverse optical lever sensitivity and lever stiffness of qp-BioAC and ATEC-CONT cantilevers were calibrated using a combination of a Sader⁴⁶ and thermal⁴⁷ methods (called

“contact-free” method in the JPK AFM instruments). The fundamental peak was used with a correction of 0.817 at ambient temperature and in liquid environment.

MLCT-BIO-DC triangular cantilever optical lever sensitivity was evaluated with the acquisition of an approach-retract curve (deflection versus z scanner displacement curve) on a glass rigid surface and cantilevers stiffness were quantified consequently with a thermal method.

Reverse-tip imaging. Simultaneous intensity (photon counter) and force images presented in Fig. 3 were obtained by fixing the laser focus to 4 μm from a glass coverslip and held in place throughout the measurement. We employed the *hover mode* (JPK instruments) where in the trace (forward) line the tip is in contact with the sample, whereas in the retrace (backward) line the tip is still following the topography (recorded from the trace) at a fixed distance from the sample defined by the AFM user. In this way, in the retrace image, the deflection can be monitored and can be converted to the force acting on the cantilever at a specific distance. By varying the latter, it is possible to probe the optomechanical interactions acting at different planes of the laser path.

Images were acquired using a 532/10 nm excitation filter, a measured power of 300 μW and an emission filter of 690/50 nm using 64 lines \times 64 pixels, a line rate of 6 Hz and scan size of 10 $\mu\text{m} \times$ 10 μm for ATEC-CONT probes, 15 $\mu\text{m} \times$ 15 μm for the MLCT-BIO-DC, and 30 $\mu\text{m} \times$ 30 μm for the qp-BioAC. The photon counter signal from the APD was directly connected through the input of the AFM electronics, not utilizing the TCSPC card, therefore, resulting in force and intensities images directly in the AFM software without need for any additional signal post-processing. The intensity images units are given in counts per second (cps), which correspond to the photon collection rate by the AFM electronics.

Model membranes. 1,2-dipalmitoyl-sn-glycero-3-phosphocholine (DPPC) and 1,2-dioleoyl-sn-glycero-3-phosphocholine (DOPC) were purchased from Avanti Polar Lipids Inc. 2-(4,4-difluoro-5,7-dimethyl-4-bora-3a,4a-diaza-s-indacene-3-dodecanoyl)-1-hexadecanoyl-sn-glycero-3-phosphocholine (BODIPY) was purchased from Thermofisher. Chloroform and methanol were purchased from Sigma-Aldrich. Membrane experiments were performed in DPBS buffer solution filtered before use with an inorganic membrane filter (0.22 μm pore size, Whatman International Ltd). DPPC and DOPC dissolved in chloroform:methanol (v:v 1:1) were supplemented with 0.1% BODIPY. The solvent was then evaporated to dryness under nitrogen flow to obtain a thin film spread in a glass tube. The dried lipids films were hydrated with DPBS buffer solution, previously heated at 60°C, until a final total concentration of 0.2 mM. The tube was later subjected to cycles of vortex mixing and heating at 60°C. The vesicle suspension was extruded with a polycarbonate membrane filter (100 nm pore size, Whatman, purchased from Avanti Lipids). Circular glass coverslips (2.8 cm diameter, 165 μm thick, purchased from Marienfeld) were cleaned by a cycle of sonication in KOH for 15 min, followed by a second cycle of sonication in deionized water for 15 min. Then, the glass coverslips were exposed to plasma (Expanded Plasma Cleaner PDC-002, Harrick Scientific Corporation) at high RF power level for 15 min. Supported lipid bilayers (SLBs) were obtained by vesicles fusion method^{48–50}. 300 μL of vesicles suspensions were deposited onto cleaned glass coverslips, previously mechanically fixed in an Attofluor chamber (Thermofisher), and incubated for 30 min at 70°C. Afterwards, the samples were rinsed several times with buffer solution to remove unfused vesicles, always keeping the substrates hydrated and imaged by correlative confocal-AFM after 24 hours.

FLIM of model membranes. Images were obtained using a 488/10 nm excitation filter and a 535/39 nm emission filter with a laser excitation power of 120 nW. AFM images of the membrane were acquired in contact mode using a rectangular qp-BioAC cantilever with a stiffness of 0.3 N/m at constant force of 1.5 nN at a line imaging rate of 0.25 Hz with 128 lines \times 128 pixels and with a scan size of 15 $\mu\text{m} \times$ 15 μm . Images were collected with a sample scan with the AFM tip and excitation beam kept aligned and steady. Lifetime was fitted with SPCLimage (Becker & Hickl) using a single exponential and spatial binning of 1. AFM and FLIM images were synchronized by tagging each photon read by the TCSPC card with a TLL signal (pixel/line/frame) from the AFM instrument.

Nanodiamonds and gold substrate. Circular glass coverslips (Marienfeld) were subjected to sonication cycles in acetone (5 minutes) and ethanol (5 minutes), and subsequently dried under nitrogen flow. 5 nm or 10 nm of gold were evaporated on top of coverslips by thermal evaporation method at a rate of 1 $\text{\AA}/\text{s}$ (AS053 Oerlikon thermal evaporating source). Fluorescent Nanodiamonds (FNDs) were purchased from FND Biotech (Taiwan). A solution of 40 nm diameter nanodiamonds, each containing in average 15 NV centers, at a concentration of 0.1 mg/mL was sonicated for 15 min and subsequently diluted to 0.1 $\mu\text{g}/\text{mL}$. 5 μL were deposited on both gold-coated and glass coverslips and left to dry. Finally, nanodiamonds were imaged by correlative confocal and AFM in DPBS solution.

Nanodiamond grafting. At the AFM tip apex was performed on both ATEC-CONT and qp-BioAC tips. Fluorescence images were acquired without AFM tip to pre-localize nanodiamond candidates on a glass coverslip for the grafting process. Subsequently, an AFM image with low force setpoint (\ll 1 nN) was acquired in the same area in AFM dynamic mode. The PLL-coated tip was then pressed on the selected nanodiamond for 10–20 seconds with a 1 nN setpoint³⁶. The use of PLL permanently sets the nanodiamond to be at the tip apex if low forces are used to avoid dislodging events. The modified qp-BioAC, with a circular plateau at the tip apex, ensures higher nanodiamond stability. The absence of the plateau in the ATEC-CONT makes the nanodiamond more prone to dislodgement if higher forces are used.

Received: 8 January 2020; Accepted: 14 March 2020;
Published: 27 April 2020

References

- Cheng, Y. Single-particle cryo-EM—How did it get here and where will it go. *Science* **361**, 876–880, <https://doi.org/10.1126/science.aat4346> (2018).
- Willig, K. I., Rizzoli, S. O., Westphal, V., Jahn, R. & Hell, S. W. STED microscopy reveals that synaptotagmin remains clustered after synaptic vesicle exocytosis. *Nature* **440**, 935–939, <http://www.nature.com/articles/nature04592> (2006).
- Rust, M. J., Bates, M. & Zhuang, X. Sub-diffraction-limit imaging by stochastic optical reconstruction microscopy (STORM). *Nature Methods* **3**, 793–796, <http://www.nature.com/articles/nmeth929> (2006).
- Manley, S. *et al.* High-density mapping of single-molecule trajectories with photoactivated localization microscopy. *Nature Methods* **5**, 155–157, <http://www.nature.com/articles/nmeth.1176> (2008).
- Balzarotti, F. *et al.* Nanometer resolution imaging and tracking of fluorescent molecules with minimal photon fluxes. *Science* **355**, 606–612, <https://science.sciencemag.org/content/355/6325/606> (2017).
- Dufréne, Y. F. *et al.* Imaging modes of atomic force microscopy for application in molecular and cell biology. *Nature Nanotechnology* **12**, 295–307, <https://doi.org/10.1038/nnano.2017.45>, <http://www.nature.com/articles/nnano.2017.45> (2017).
- Ando, T. High-speed atomic force microscopy coming of age. *Nanotechnology* **23**, 062001, <http://stacks.iop.org/0957-4484/23/i=6/a=062001?key=crossref.06a5980f6d107126d308c4b231dccc2> (2012).
- Nasrallah, H. *et al.* Imaging artificial membranes using high-speed atomic force microscopy. In *Atomic Force Microscopy*, 45–59, https://link.springer.com/protocol/10.1007/978-1-4939-8894-5_3 (Springer, 2019).
- Kopek, B. G., Shtengel, G., Xu, C. S., Clayton, D. A. & Hess, H. F. Correlative 3D superresolution fluorescence and electron microscopy reveal the relationship of mitochondrial nucleoids to membranes. *Proceedings of the National Academy of Sciences* **109**, 6136–6141, <https://doi.org/10.1073/pnas.1121558109> (2012).
- Harke, B., Chacko, J. V., Haschke, H., Canale, C. & Diaspro, A. A novel nanoscopic tool by combining AFM with STED microscopy. *Optical Nanoscopy* **1**, 3, <https://doi.org/10.1186/2192-2853-1-3> (2012).
- Odermatt, P. D. *et al.* High-Resolution Correlative Microscopy: Bridging the Gap between Single Molecule Localization Microscopy and Atomic Force Microscopy. *Nano Letters* **15**, 4896–4904, <https://doi.org/10.1021/acs.nanolett.5b00572> (2015).
- Dahmane, S. *et al.* Nanoscale organization of tetraspanins during HIV-1 budding by correlative dSTORM/AFM. *Nanoscale* **11**, 6036–6044, <http://xlink.rsc.org/?DOI=C8NR07269H> (2019).
- Gómez-Varela, A. I. *et al.* Simultaneous co-localized super-resolution fluorescence microscopy and atomic force microscopy: combined SIM and AFM platform for the life sciences. *Scientific Reports* **10**, 1122, <http://www.nature.com/articles/s41598-020-57885-z> (2020).
- Hillner, P., Walters, D., Lal, R., Hansma, H. & Hansma, R. Combined Atomic Force and Confocal Laser Scanning Microscope. *Microscopy and Microanalysis* **1**, 127–130, http://www.journals.cambridge.org/abstract_S1431927695111277 (1995).
- Gradinaru, C. C., Martinsson, P., Aartsma, T. J. & Schmidt, T. Simultaneous atomic-force and two-photon fluorescence imaging of biological specimens *in vivo*. *Ultramicroscopy* **99**, 235–245, <https://linkinghub.elsevier.com/retrieve/pii/S0304399104000105> (2004).
- Kassies, R. *et al.* Combined AFM and confocal fluorescence microscope for applications in bio-nanotechnology. *Journal of Microscopy* **217**, 109–116, <https://doi.org/10.1111/j.0022-2720.2005.01428.x> (2005).
- Bek, A. *et al.* Fluorescence Enhancement in Hot Spots of AFM-Designed Gold Nanoparticle Sandwiches. *Nano Letters* **8**, 485–490, <https://doi.org/10.1021/nl072602n> (2008).
- Tisler, J. *et al.* Single Defect Center Scanning Near-Field Optical Microscopy on Graphene. *Nano Letters* **13**, 3152–3156, <https://doi.org/10.1021/nl401129m> (2013).
- Tetienne, J.-P. *Un microscope de champ magnétique basé sur le défaut azote-lacune du diamant: réalisation et application à l'étude de couches ferromagnétiques ultraminces*. Ph.D. thesis, École normale supérieure de Cachan - ENS Cachan (2014).
- He, Y., GovindRao, V., Cao, J. & Lu, H. P. Simultaneous spectroscopic and topographic imaging of single-molecule interfacial electron-transfer reactivity and local nanoscale environment. *The journal of physical chemistry letters* **7**, 2221–2227, <https://doi.org/10.1021/acs.jpclett.6b00862> (2016).
- Meller, K. & Theiss, C. Atomic force microscopy and confocal laser scanning microscopy on the cytoskeleton of permeabilised and embedded cells. *Ultramicroscopy* **106**, 320–325, <https://linkinghub.elsevier.com/retrieve/pii/S0304399105002275> (2006).
- Laskowski, P. R. *et al.* High-Resolution Imaging and Multiparametric Characterization of Native Membranes by Combining Confocal Microscopy and an Atomic Force Microscopy-Based Toolbox. *ACS Nano* **11**, 8292–8301, <https://doi.org/10.1021/acs.nano.7b03456> (2017).
- Becker, K., O'Brien, E. T., Falvo, M. R. & Superfine, R. Vertical Light Sheet Enhanced Side-View Imaging for AFM Cell Mechanics Studies. *Scientific Reports* **8**, 1504, <https://doi.org/10.1038/s41598-018-19791-3> (2018).
- Efremov, Y. M. *et al.* Anisotropy vs isotropy in living cell indentation with AFM. *Scientific Reports* **9**, 5757, <http://www.nature.com/articles/s41598-019-42077-1> (2019).
- Miranda, A., Martins, M. & De Beule, P. A. A. Simultaneous differential spinning disk fluorescence optical sectioning microscopy and nanomechanical mapping atomic force microscopy. *Review of Scientific Instruments* **86**, 093705, <https://doi.org/10.1063/1.4931064> (2015).
- Cazaux, S. *et al.* Synchronizing atomic force microscopy force mode and fluorescence microscopy in real time for immune cell stimulation and activation studies. *Ultramicroscopy* **160**, 168–181, <https://doi.org/10.1016/j.ultramic.2015.10.014>, <https://linkinghub.elsevier.com/retrieve/pii/S0304399115300516> (2016).
- Sarkar, A., Robertson, R. B. & Fernandez, J. M. Simultaneous atomic force microscope and fluorescence measurements of protein unfolding using a calibrated evanescent wave. *Proceedings of the National Academy of Sciences* **101**, 12882–12886, <https://doi.org/10.1073/pnas.0403534101> (2004).
- Gump, H., Stahl, S. W., Strackharn, M., Puchner, E. M. & Gaub, H. E. Ultrastable combined atomic force and total internal fluorescence microscope. *Review of Scientific Instruments* **80**, 063704, <https://doi.org/10.1063/1.3148224> (2009).
- Ortega-Esteban, A. *et al.* Fluorescence Tracking of Genome Release during Mechanical Unpacking of Single Viruses. *ACS Nano* **9**, 10571–10579, <https://doi.org/10.1021/acs.nano.5b03020> (2015).
- Uchihashi, T., Watanabe, H., Fukuda, S., Shibata, M. & Ando, T. Functional extension of high-speed AFM for wider biological applications. *Ultramicroscopy* **160**, 182–196, <https://doi.org/10.1016/j.ultramic.2015.10.017>, <https://linkinghub.elsevier.com/retrieve/pii/S0304399115300504> (2016).
- Umakoshi, T., Fukuda, S., Iino, R., Uchihashi, T. & Ando, T. High-speed near-field fluorescence microscopy combined with high-speed atomic force microscopy for biological studies. *Biochimica et Biophysica Acta (BBA) - General Subjects* **1864**, 0–1, <https://doi.org/10.1016/j.bbagen.2019.03.011>, <https://linkinghub.elsevier.com/retrieve/pii/S0304416519300613> (2020).
- Ramos, D., Tamayo, J., Mertens, J. & Calleja, M. Photothermal excitation of microcantilevers in liquids. *Journal of Applied Physics* **99**, 124904, <https://doi.org/10.1063/1.2205409> (2006).
- Favero, I. & Karrai, K. Optomechanics of deformable optical cavities. *Nature Photonics* **3**, 201–205, <http://www.nature.com/articles/nphoton.2009.42> (2009).
- Araghi, H. Y. & Paige, M. F. Insight into diacetylene photopolymerization in Langmuir-Blodgett films using simultaneous AFM and fluorescence microscopy imaging. *Surface and Interface Analysis* **49**, 1108–1114, <https://doi.org/10.1002/sia.6284> (2017).

35. YungHui, Y. *et al.* Tip-enhanced sub-diffraction fluorescence imaging of nitrogen-vacancy centers in nanodiamonds. *Applied Physics Letters* **102**, 013102, <https://doi.org/10.1063/1.4773364> (2013).
36. Rondin, L. *et al.* Nanoscale magnetic field mapping with a single spin scanning probe magnetometer. *Applied Physics Letters* **100**, 153118, <https://doi.org/10.1063/1.3703128> (2012).
37. Li, Y. *et al.* Broadband infrared photoluminescence in silicon nanowires with high density stacking faults. *Nanoscale* **7**, 1601–1605, <https://doi.org/10.1039/C4NR05410E> (2015).
38. Wu, Y. *et al.* Molecular rheometry: direct determination of viscosity in Lo and Ld lipid phases via fluorescence lifetime imaging. *Physical Chemistry Chemical Physics* **15**, 14986, <http://xlink.rsc.org/?DOI=c3cp51953h> (2013).
39. Seantier, B., Giocondi, M.-C., Grimellec, C.L. & Milhiet, P.-E. Probing supported model and native membranes using afm. *Current Opinion in Colloid & Interface Science* **13**, 326–337, <http://www.sciencedirect.com/science/article/pii/S1359029408000046> (2008).
40. Przybylo, M. *et al.* Lipid diffusion in giant unilamellar vesicles is more than 2 times faster than in supported phospholipid bilayers under identical conditions. *Langmuir* **22**, 9096–9099, <https://doi.org/10.1021/la061934p> (2006).
41. Drexhage, K. Influence of a dielectric interface on fluorescence decay time. *Journal of Luminescence* **1–2**, 693–701, <https://linkinghub.elsevier.com/retrieve/pii/0022231370900827> (1970).
42. Costa, L. *et al.* Spectroscopic Investigation of Local Mechanical Impedance of Living Cells. *PLoS One* **9**, e101687, <https://doi.org/10.1371/journal.pone.0101687> (2014).
43. Rico, F., Gonzalez, L., Casuso, I., Puig-Vidal, M. & Scheuring, S. High-Speed Force Spectroscopy Unfolds Titin at the Velocity of Molecular Dynamics Simulations. *Science* **342**, 741–743, <https://doi.org/10.1126/science.1239764> (2013).
44. Buchler, B. C., Kalkbrenner, T., Hettich, C. & Sandoghdar, V. Measuring the Quantum Efficiency of the Optical Emission of Single Radiating Dipoles Using a Scanning Mirror. *Physical Review Letters* **95**, 063003, <https://doi.org/10.1103/PhysRevLett.95.063003> (2005).
45. Amo, C. A.v Garcia, R. Fundamental High-Speed Limits in Single-Molecule, Single-Cell, and Nanoscale Force Spectroscopies. *ACS Nano* **10**, 7117–7124, <https://doi.org/10.1021/acs.nano.6b03262> (2016).
46. Sader, J. E. *et al.* A virtual instrument to standardise the calibration of atomic force microscope cantilevers. *Review of Scientific Instruments* **87**, 093711, <https://doi.org/10.1063/1.4962866> (2016).
47. Proksch, R., Schäffer, T. E., Cleveland, J. P., Callahan, R. C. & Viani, M. B. Finite optical spot size and position corrections in thermal spring constant calibration. *Nanotechnology* **15**, 1344–1350, <http://stacks.iop.org/0957-4484/15/i=9/a=039?key=crossref.42df421f27524c77ef7045d3d62b4d36> (2004).
48. Milhiet, P. E., Vié, V., Giocondi, M.-C. & LeGrimellec, C. AFM Characterization of Model Rafts in Supported Bilayers. *Single Molecules* **2**, 109–112, [https://doi.org/10.1002/1438-5171\(200107\)2:2<109::AID-SIMO109>3.0.CO;2-L](https://doi.org/10.1002/1438-5171(200107)2:2<109::AID-SIMO109>3.0.CO;2-L) (2001).
49. Redondo-Morata, L., Giannotti, M. I. & Sanz, F. Influence of Cholesterol on the Phase Transition of Lipid Bilayers: A Temperature-Controlled Force Spectroscopy Study. *Langmuir* **28**, 12851–12860, <https://doi.org/10.1021/la302620t> (2012).
50. Gumí-Audenis, B. *et al.* In-plane molecular organization of hydrated single lipid bilayers: Dppc: cholesterol. *Nanoscale* **10**, 87–92, <https://doi.org/10.1039/C7NR07510C> (2018).

Acknowledgements

L.C. and T.F. acknowledge support from CNRS Momentum program (2017). O.S. acknowledges funding from the European Union's Horizon 2020 research and innovation program under the Marie Skłodowska-Curie grant agreement No. 721874 (SPM 2.0). This project has received funding from the Agence Nationale de la Recherche (ANR) under grant agreement ANR-17-CE09-0026-02. The CBS is a member of the France-BioImaging (FBI) and the French Infrastructure for the Integrated Biology (FRISBI), 2 national infrastructures supported by the French National Research Agency (ANR-10-INBS-04-01 and ANR-10-INBS-05 respectively). The authors acknowledge Francesco Pedaci for discussions and Martina Di Muzio and the MicroFabSpace and Microscopy Characterization Facility, Unit 7 of ICTS “NANBIOSIS” from CIBER at IBEC, for providing the gold-coated coverslips.

Author contributions

E.M., P.-E.M., L.C. and T.F.D.F. conceived the research. T.F.D.F. and L.C. conducted the experiments. T.F.D.F. analyzed the data and conceived the Python code for data analysis. T.F.D.F., O.S., L.C. and E.M. set up the instrument. All authors reviewed the manuscript.

Competing interests

The authors declare no competing interests.

Additional information

Supplementary information is available for this paper at <https://doi.org/10.1038/s41598-020-62529-3>.

Correspondence and requests for materials should be addressed to P.-E.M. or L.C.

Reprints and permissions information is available at www.nature.com/reprints.

Publisher's note Springer Nature remains neutral with regard to jurisdictional claims in published maps and institutional affiliations.



Open Access This article is licensed under a Creative Commons Attribution 4.0 International License, which permits use, sharing, adaptation, distribution and reproduction in any medium or format, as long as you give appropriate credit to the original author(s) and the source, provide a link to the Creative Commons license, and indicate if changes were made. The images or other third party material in this article are included in the article's Creative Commons license, unless indicated otherwise in a credit line to the material. If material is not included in the article's Creative Commons license and your intended use is not permitted by statutory regulation or exceeds the permitted use, you will need to obtain permission directly from the copyright holder. To view a copy of this license, visit <http://creativecommons.org/licenses/by/4.0/>.

© The Author(s) 2020

Synchronous, Crosstalk-free Correlative AFM and Confocal Microscopies/Spectroscopies - Supplementary Information

Thales F. D. Fernandes¹, Oscar Saavedra-Villanueva¹, Emmanuel
Margeat¹, Pierre-Emmanuel Milhiet^{1*}, and Luca Costa^{1**}

¹Centre de Biochimie Structurale (CBS), CNRS, INSERM, Univ
Montpellier, 34090, Montpellier, France.

*pem@cbs.cnrs.fr

**costa@cbs.cnrs.fr

March 18, 2020

1 Radiation Pressure

The radiation pressure acting upon the tip can be estimated by the change in momentum of the incident light. The radiation pressure P is defined as:

$$P = \frac{p}{c\pi R_L^2}, \quad (1)$$

where p is the laser power, c is the speed of light, and R_L is the size of the confocal spot. This pressure will act on the surface area of the AFM tip, πR_e^2 , where R_e is the effective radius of the laser cross-section interaction with the tip apex and will give rise to a force. Typical values are $p \approx 500$ uW, $R_L = 250$ nm, and $R_e = 1$ – $2\mu\text{m}$ (estimated from Fig. 3 of the main manuscript), and thus resulting in a force of a few tens or hundreds of pN, which is in the

same order of magnitude as the ones measured in our experiments (Figs. 3a and 4b of the main manuscript).

2 Approach and retract curves of nanodiamond on a gold surface

In Fig. 6 from the main manuscript, the force curves are presented “unfolded”, whereas the approach and retract curves are separated. Fig. 1d shows the conventional representation of a force curve with the approach and retract curves aligned as a function of nanodiamond-gold reciprocal distance: data were collected in a different region of the same gold substrate from Fig. 6 from the main manuscript. This helps to elucidate the fact that the system is behaving in a reversible way: approach and retract are highly correlated (superimposed) from either Figs. 1b and d. Fig. 1c shows a decay curve for the sum of all decays in Fig. 1a.

3 SLB lifetime

The presence of the tip (either ATEC or qp-BioAC) in the confocal spot results in a signal of low lifetime, < 1 ns (Fig. 4a from the main manuscript). Fig. 2a shows a decay curve from a DOPC region from Fig. 5c of the main manuscript, while Fig. 2b shows the respective phasor plot. Clearly, the decay curve presents no peak with low lifetime, indicating that the tip is not contributing with any spurious signal. This is further corroborated by the phasor plot showing data that belong to a single population and close to the semi-circle.

4 SEM image of qp-BioAC with plateau tips

As described in the Materials and Methods section of the main manuscript, the plateau tips are obtained from qp-BioAC cantilevers. An electron beam

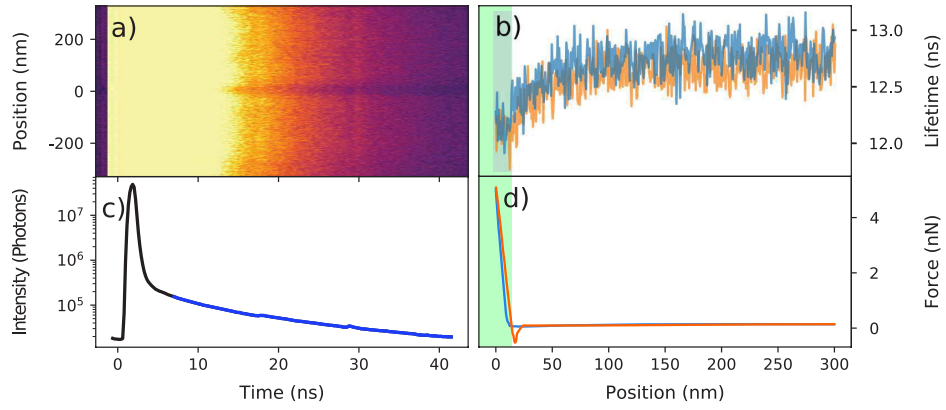


Figure 1: Simultaneous force curve and nanodiamond lifetime measurements approaching and retracting a gold substrate. (a) shows tip z -position versus time (decay curves). (b) shows the nanodiamond lifetime in function of tip position (approach and retract curves). (c) shows the decay curve for the sum of all decays in (a). (d) shows the force in function of tip position (approach and retract curves). In (b and d), cyan and orange represent approach and retract, respectively. A modified qp-BioAC with a nanodiamond on a 50 nm plateau at the tip's end was used with 90 μW laser power. The light blue region in (b and d) shows the contact regime between nanodiamond and gold.

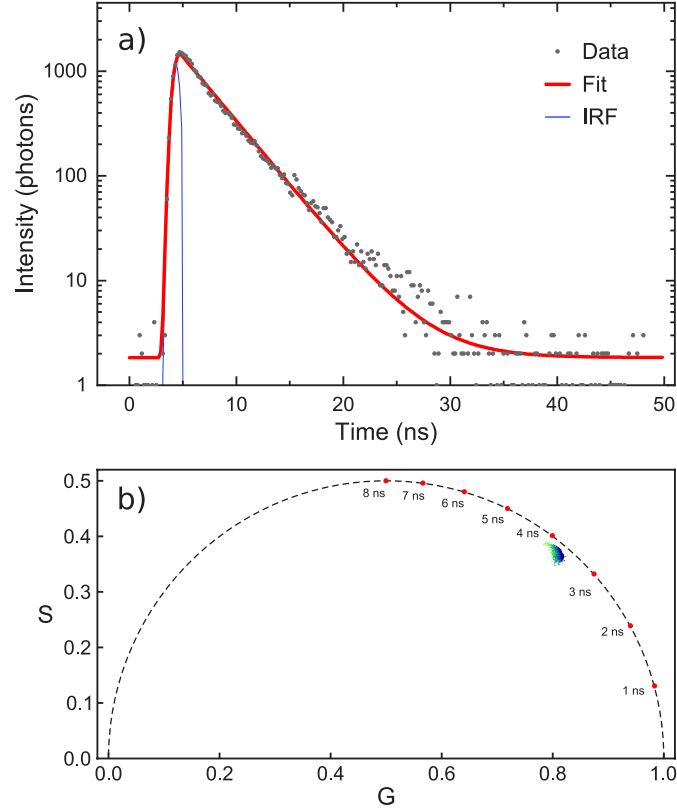


Figure 2: **(a)** Decay curve from a DOPC enriched region from Fig. 5c of the main manuscript: the blue curve is the Instrumental Response Function (IRF), black dots are experimental data and the red curve is the fit. **(b)** phasor plot of all DOPC/DPPC regions decays in Fig. 5c from the main manuscript. The power used was 120 nW, with an excitation filter of 488/10 nm and a band-pass emission filter of 525/39 nm. We used a qp-BioAC as AFM cantilever.

deposited carbon tip was grown on top of a thin layer of gold. Subsequently, a flat circular plateau of ≈ 50 nm diameter was obtained at the tip apex by means of FIB, as shown in a Scanning Electron Microscopy (SEM) image in Fig. 3.

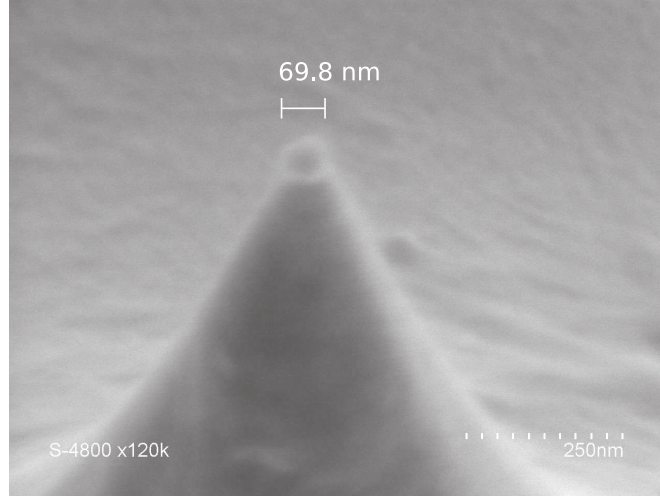


Figure 3: SEM image of a modified qp-BioAC plateau tip.

5 Lifetime distribution in DOPC/DPPC mixture

Fig. 5 of the main manuscript shows the DOPC/DPPC domains, labeled with BODIPY organic dyes, by AFM, fluorescence intensity and lifetime. Applying a mask on the AFM data, it is possible to separate the lifetimes from the two distinct enriched domains and get their distribution, which is shown in Fig. 4.

The BODIPY's lifetimes from DOPC and DPPC regions are 3.55 ± 0.07 ns and 3.71 ± 0.09 ns, respectively, leading to a ≈ 160 ps difference between the domains. This difference is in the same range as the one observed by Wu *et al.* for DOPC and DOPC-cholesterol mixtures in GUVs (ref. 38 in the main manuscript).

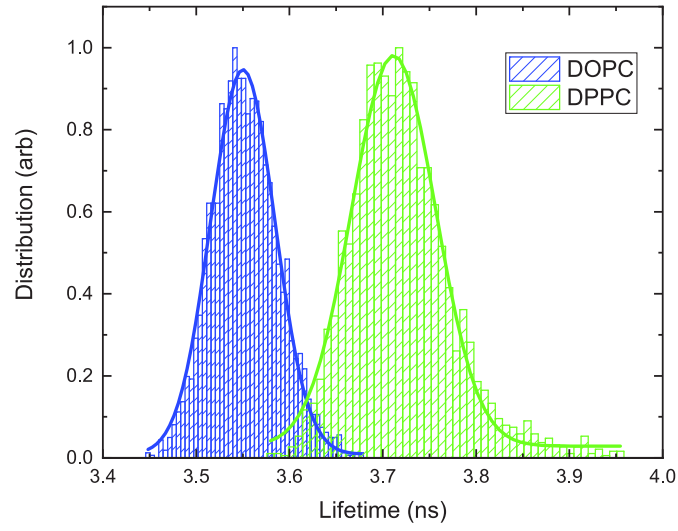
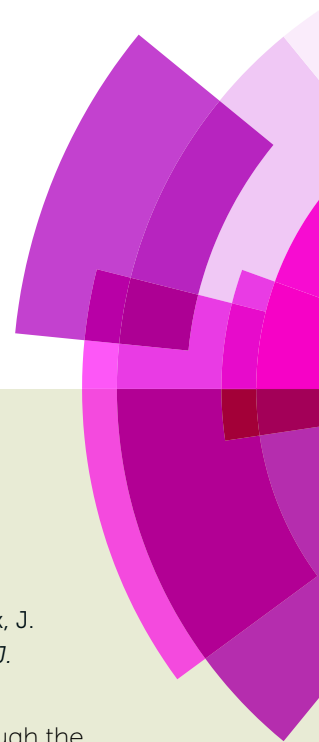


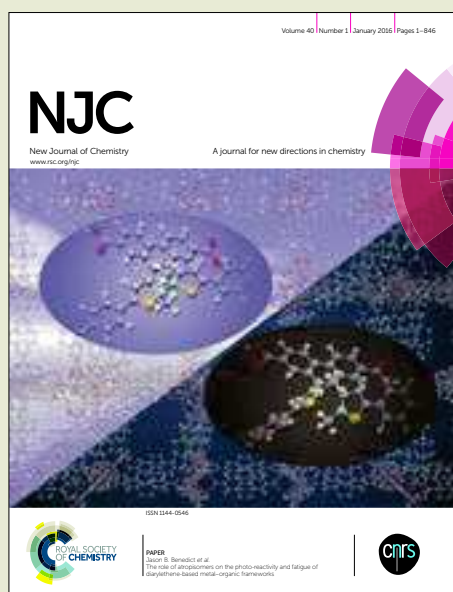
Figure 4: BODIPY lifetime distribution from DOPC (blue) and DPPC (green) domains from Fig. 5. The lifetimes of DOPC and DPPC are 3.55 ± 0.07 ns and 3.71 ± 0.09 ns, respectively.

NJC

Accepted Manuscript



This article can be cited before page numbers have been issued, to do this please use: G. Ngo, G. Félix, J. Long, L. Costa, O. Saavedra, P. Milhiet, J. Devoisselle, Y. Guari, J. Larionova and J. C. Chopineau, *New J. Chem.*, 2019, DOI: 10.1039/C9NJ00251K.



This is an Accepted Manuscript, which has been through the Royal Society of Chemistry peer review process and has been accepted for publication.

Accepted Manuscripts are published online shortly after acceptance, before technical editing, formatting and proof reading. Using this free service, authors can make their results available to the community, in citable form, before we publish the edited article. We will replace this Accepted Manuscript with the edited and formatted Advance Article as soon as it is available.

You can find more information about Accepted Manuscripts in the [author guidelines](#).

Please note that technical editing may introduce minor changes to the text and/or graphics, which may alter content. The journal's standard [Terms & Conditions](#) and the ethical guidelines, outlined in our [author and reviewer resource centre](#), still apply. In no event shall the Royal Society of Chemistry be held responsible for any errors or omissions in this Accepted Manuscript or any consequences arising from the use of any information it contains.



Journal Name

COMMUNICATION

A simple approach for controlled deposition of Prussian Blue Analogues nanoparticles on a functionalised plasmonic gold surface†

Received 00th January 20xx,
Accepted 00th January 20xx

DOI: 10.1039/x0xx00000x

www.rsc.org/

Giang Ngo,^a Gautier Félix,^{*a} Jérôme Long,^a Luca Costa,^b Oscar Saavedra V.,^b Pierre-Emmanuel Milhiet,^b Jean-Marie Devoisselle,^a Yannick Guari,^a Joulia Larionova,^a Joël Chopineau^{*a,c}

We report here a simple and efficient approach for the controlled deposition of Prussian blue analogue nanoparticles' monolayer on a gold surface functionalised with amino groups and their characterisation by Surface Plasmon Resonance spectroscopy and Atomic Force Microscopy combined with a theoretical modeling.

Prussian blue analogues (PBA) are coordination cyano-bridged networks having the general formula $A_{1-x}[M'(CN)_6]_{1-x/3}\square_x$ (A is a monovalent cation, M and M' are transition metal ions, \square is the cyanometallate vacancies), in which M and M' are connected through cyano-bridges leading to a three-dimensional face-centred cubic open-framework. The large workable combinations of transition metal ions lead to a wide family of PBA with different interesting physico-chemical properties, including magnetic behaviour,¹⁻³ electronic phase-change phenomena,⁴⁻⁶ photo-switching phenomenon,⁷⁻¹⁰ gas and ions' absorption/hydrogen storage,¹¹ and negative thermal expansion.^{12, 13} Compare to their bulk counterparts, PBA nanoparticles (NPs) exhibit unique size and shape dependent features,¹⁴ such as for instance optical,¹⁵ magnetic,^{16, 17} and elastic^{18, 19} properties, which may find potential applications in many fields²⁰ including electrode devices,²¹ electronics, optics, biology²² and medicine.^{23, 24} Considering that several of these applications require the NPs on a planar surface, the controlled deposition or patterning of PBA NPs on a surface is an important challenge.²⁵ In this line of thought, three different approaches may be cited.²⁶ The first one consists in the electrochemical deposition of Prussian blue and PBA thin films on platinum,²⁷ glassy carbon and indium-doped tin oxide,²⁸ or gold single crystals.²⁹ Other strategy involving a sequential layer-by-layer deposition on polyethylene terephthalate polymer solid surface (Melinex),

conducting to a series of magnetic and photo-magnetic PBA thin films have been developed by D. Talham's group.³⁰⁻³² This consecutive approach has been extended to design of mono and multi-layered paramagnetic and ferromagnetic PBA films directly grown on a functionalized Si(100) surface³³ or on a quartz or indium tin oxide surface.³⁴ Secondly, nanostructured PBA on a gold surface has been obtained by A. Bleuzen *and coll.* by sequential nanopatterning.³⁵ The third approach includes the homogeneous deposition of already formed PB nanoparticles on a positively charged indium tin oxide conductive glass and gold surfaces,³⁶ functionalized with amine Au electrodes³⁷ or SiO₂³⁸ surfaces.

Gold surface presents several advantages for the deposition of metal-organic framework³⁹ and particularly of the PBA NP layers and their investigation: (i) it may be easily functionalised by a self-assembled monolayer (SAM) with a variety of ligands able to anchor NPs,⁴⁰⁻⁴³ (ii) these SAM can control the deposition and dispersion of nano-objects.^{44, 45} In this work, we propose a simple method to implement and optimise the controlled deposition of a monolayer of well-dispersed $K^+/Ni^{2+}/[Fe(CN)_6]^{3-}$ PBA NPs on a large (1 cm²) gold surface functionalised with a SAM of aminoethanethiol. A particular emphasis is given on the detailed characterisation of the obtained PBA@Au materials by using SPR measurements and AFM imaging both assisted by theoretical modelling. This combined approach conducts also to original method for the measurement of PBA nanoparticles' refractive index.

^a Institut Charles Gerhardt Montpellier (ICGM), Univ Montpellier, ENSCM, CNRS, Montpellier, France. E-mail: joel.chopineau@enscm.fr, gautier.felix@umontpellier.fr

^b Centre de Biochimie Structurale (CBS), CNRS, INSERM, Univ Montpellier, France

^c Université de Nîmes Rue Georges Salan 30000 Nîmes

†Electronic Supplementary Information (ESI) available: [details of any supplementary information available should be included here]. See DOI: 10.1039/x0xx00000x

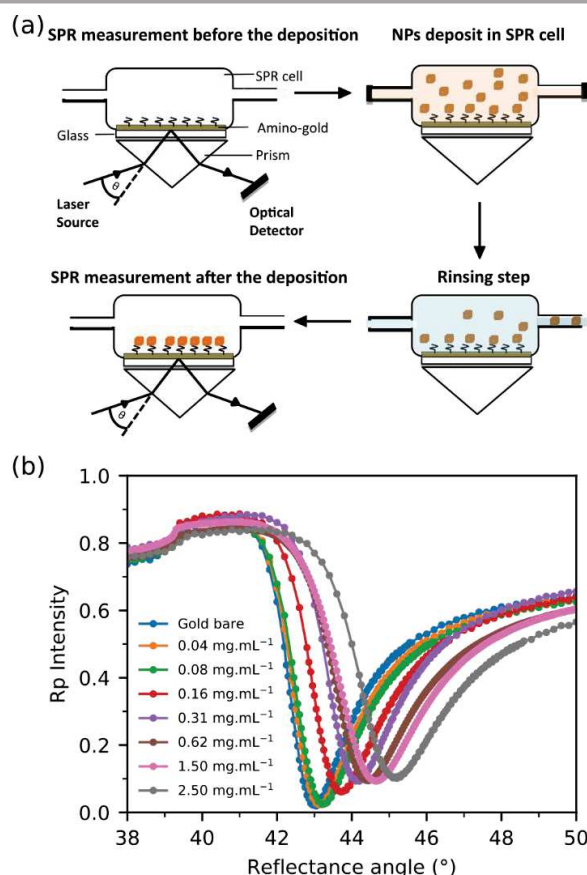


Fig. 1 (a) Scheme of NPs deposit on the amino-gold surface in SPR cell; (b) Normalized intensity of the total internal reflection of PBA NPs on the gold aminated surface for the different NPs concentrations in suspension with a *p*-polarisation of light (R_p) as a function of the internal reflection angle (SPR recordings). Lines are guide for the eyes.

K⁺/Ni²⁺/[Fe(CN)₆]³⁻ PBA NPs were synthesised by the controlled addition of the respective molecular precursors, NiCl₂·6H₂O and K₃[Fe(CN)₆], using the synthetic strategy we previously reported for other PBA to give K_{0.04}Ni[Fe(CN)₆]_{0.62}.^{18, 23} The IR spectrum (Fig. S1a, Electronic Supporting Information (ESI)) shows the typical stretching vibrations at 2166 and 2100 cm⁻¹ corresponding to the Fe^{III}-CN-Ni^{II} and Fe^{II}-CN-Ni^{II} linkages of the PBA cyano-bridged network, respectively.⁴⁶ The transmission electronic microscopy (TEM) images show the presence of PBA NPs with a well-defined cubic shape with a mean length edge equal to 35 ± 3 nm (Fig. S1b, c, ESI). A negative zeta potential of -23 mV measured for the particles indicates the presence of the [Fe(CN)₆]³⁻ moiety on the NPs' surface, which contributes to their stabilization and good dispersion in water.⁴⁷ As a simple way to anchor the NPs on a gold surface a thin layer of aminoethanethiol of about 5 Å (see ESI) has been used.^{40, 48} In our experimental conditions, pH > 7; the surface amine functions are therefore able to coordinate the Ni²⁺ ions located at the surface of the PBA nanoparticles but the presence of the electrostatic interactions between the nanoparticles and the surface cannot be excluded.

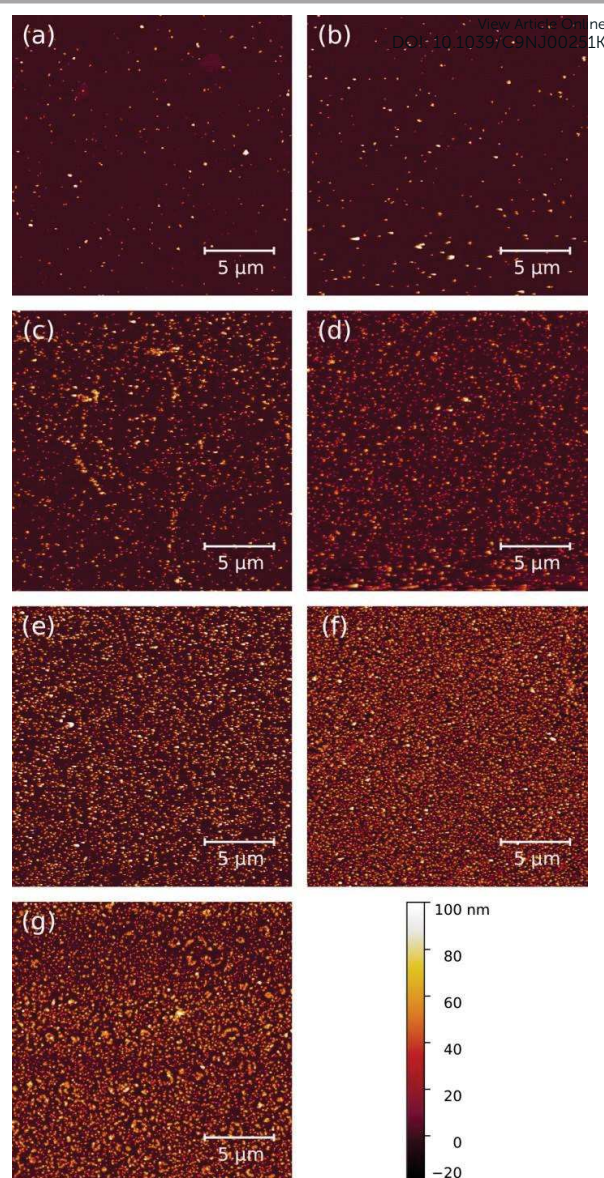


Fig. 2 AFM images with scale bar 20 x 20 μm of the PBA NPs deposit on the amino-gold surface with different initial concentrations: (a) 0.04 mg.mL⁻¹; (b) 0.08 mg.mL⁻¹; (c) 0.16 mg.mL⁻¹; (d) 0.31 mg.mL⁻¹; (e) 0.62 mg.mL⁻¹; (f) 1.50 mg.mL⁻¹; (g) 2.50 mg.mL⁻¹.

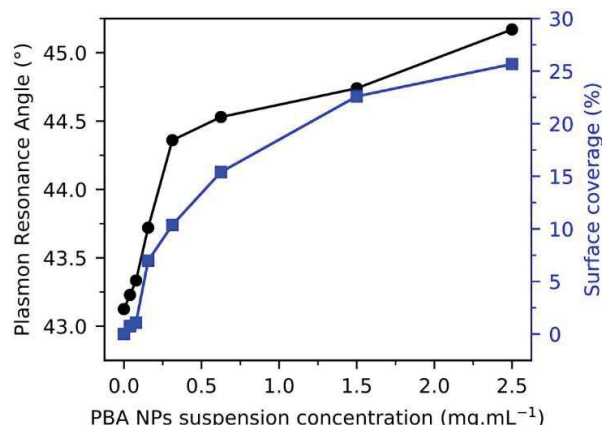


Fig. 3 Surface coverage (blue squares) and plasmon resonance angles (black circles) as a function of the NPs' concentration. Lines are guide for eyes.

The deposition of NPs suspended in water at different concentrations (0.04, 0.08, 0.16, 0.31, 0.62, 1.50 and 2.50 mg.mL⁻¹) on the amino-gold surface was conducted and monitored using a home-made SPR setup.⁴⁹ To this purpose, the slides were deposited on an optical BK-7 right angle prism to obtain the Kretschmann configuration (total internal reflection of light in *p*-polarisation). To get an optical continuity, a refractive index matching oil was used between the gold slide and the optical prism. Then, a SPR chamber (1 mL) was mounted on the amino-gold surface (Fig. 1a). The determination of the resonance angle (minimum of SPR curve) of the amino-gold surface was performed in air using the total internal reflectivity configuration with incident angles ranging between 38.00° and 50.00°. The intensity of reflected light decreases sharply to almost zero for a reflectance angle of 43.10°, this value was set as the reference resonance angle. Then, for NPs deposition, the SPR chamber was filled with 1 mL of the NPs' suspension. After 7 hours, the cell was thoroughly rinsed with 25 mL of ultrapure water, to be sure that all unbound NPs were removed. Nitrogen gas was flowed gently inside the chamber for 3 minutes to dry the surface. SPR measurements of the NPs deposited on the amino-gold surfaces were performed in air. Fig. 1b shows the SPR spectra for samples containing different amount of NPs. When the concentration of NPs in the initial suspension increases, a shift of the resonance angle from 43.22° to 45.17° was observed. The right-shift of the resonance angle is usually linked with two major phenomena, a change in the refractive index of the NPs and the amount of NPs deposited on the amino-gold surface. As the NPs refractive index is assumed to be the same for all samples, the difference in the observed resonance angles is a consequence of an augmentation of the amount of NPs deposited on the amino-gold surface. However, the SPR measurements provide an overall optical thickness of the thin deposit on the amino surface, but no information is given concerning the organization of NPs on the surface. The IR spectra of the PBA NPs deposited on the Au surface present also two peaks (2166 and 2100 cm⁻¹), confirming that PBA

structure has been preserved after deposition (see Fig. S2a, ESI). DOI: 10.1039/C9NJ00251K

Atomic Force Microscopy (AFM) was therefore used to image the NPs-amino-gold surface at the nanometre scale. Fig. 2 displays AFM images, performed in Amplitude Modulation AFM mode (AM-AFM) in ambient conditions,^{50, 51} for the 7 samples with different amount of NPs. Several AFM images were taken at different areas for 5 x 5 μm² and 20 x 20 μm². They show a homogeneous distribution of the NPs on the surface. Note that the average height shown in Fig. 2 is less than twice the height of a nanoparticle (the mean height of NPs measured in all AFM image is 40 ± 10 nm, see Fig. S3c). We can conclude that the NPs deposition on the amino-gold surface can be approximated as a discrete coverage of individual PBA NPs. A zoom of the surface dispersion and roughness (1nm for the substrate roughness) for the sample with a suspension concentration of 0.16 mg.mL⁻¹ (Fig. 2c) shows that each point in AFM image represents one nano-object (See Fig S3a, b). For each topographic AFM image, we used the Gwyddion software⁵² and the threshold method to estimate the coverage of the surface by PBA NPs. According to the initial concentration of NPs, the surface coverage increased from 0.8% to 25.7%. The SPR resonance angle values and the surface coverage as a function of the concentration of PBA NPs suspensions are exposed in Fig. 3. Both curves, which seem to have correlated behaviour, show that there are two different regimes in the coverage process: at low concentration, the evolution of the surface coverage is linear as a function of the NPs concentrations and then, the surface coverage increases moderately and tends to saturate. As it was discussed previously, the surface of NPs is negatively charged, which tends to isolate them during the deposition process, which beside the presence of amino groups at the surface can explain the homogeneous deposition of the NPs.⁴⁵ Experimental SPR resonance angle was compared to the one of simulated curves obtained by the generalised Rouard method applied to an absorbing thin-film stack.⁵³ The model allows simulating the reflectance and the transmission of a multi-layer optical system, where each layer was assumed as perfectly flat and homogeneous. The parameters of the model are the thickness of each layer and their complex refractive index (the real part is the refractive index and the imaginary part is the optical absorption). It is important to note that the optical absorption of gold in the visible wavelength domain is strongly linked to the plasmonic phenomenon. The Maxwell-Garnett equation^{54, 55} can be used to calculate an effective refractive index n_{eff} of the NPs-air mixture (See ESI), and then used as the refractive index of the NPs layer in the generalized Rouard method. Fig. 4a shows the result of simulations of the SPR spectra obtained for the same surface coverage values as those determined from the AFM experimental data (see Fig. 3). The resonance angles obtained from the experimental SPR curves were fitted using the minima of the simulated SPR curves, by the non-linear least square method coupled with a Monte-Carlo random walk with a large number of steps. For each step a random refractive index has been chosen, and kept only if the least square error was smaller. In Fig. 4b the

COMMUNICATION

Journal Name

minima of the simulated curves (red line) and the shift of resonance plasmon angles of the experimental curves (black squares) were plotted as a function of the surface coverage of NPs on the gold surface. The results of the fit (Fig. 4b) and the simulated plasmon curves of Fig. 4a gave a refractive index for the NPs of 1.44 ± 0.03 at a wavelength of 632.8 nm. In parallel, we have extracted the refractive index of the PBA NPs from a refractometry measurement of NPs–water mixture (see ESI for details). The result gave a value of 1.44 at a wavelength of 589 nm, which is in good agreement with the SPR measurement. Such as reported in Fig. 1b and Fig. 2, the right shift of the plasmon curve minima observed in Fig. 4a is induced by a rising of the surface coverage of NPs on the gold surface. Note that the intensity of the SPR experimental curves has not been taken into account to extract the refractive index of NPs because it does not influence the SPR resonance angle and then the extracted refractive index. Also, the variation of the former can be induced by the absorption of NPs and the scattering produced by the roughness of the NPs surface (see Fig. S4 and S5, ESI).

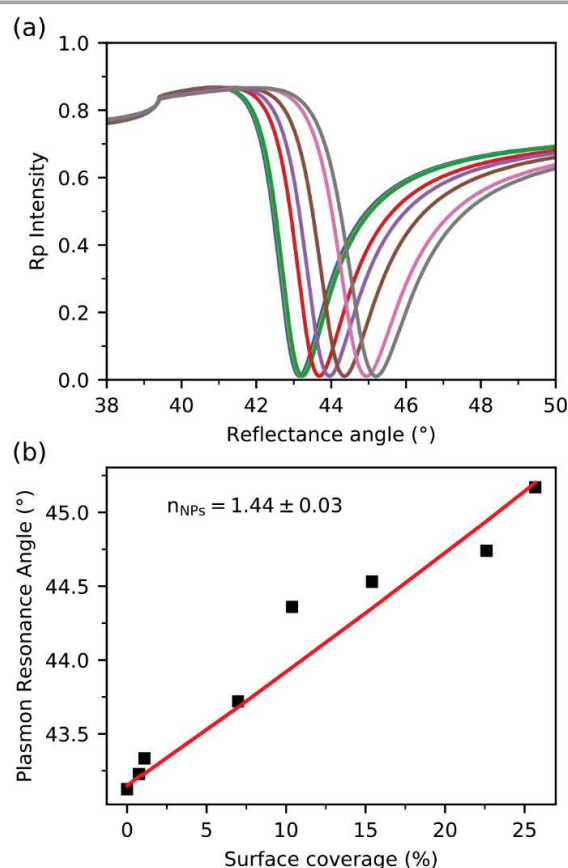


Fig. 4 (a) Plasmon curves calculated using Rouard method with surface coverage similar as the experiment; (b) Plasmonic resonance angles as a function of the surface coverage of NPs on amino-gold surface. The black squares represent the experimental points and the red curve is the fitting obtained with modelization.

In summary, we reported a simple and efficient method for a controlled chemical deposition of the PBA NPs on a gold

aminated surface. The cubic $\text{K}^+/\text{Ni}^{2+}/[\text{Fe}(\text{CN})_6]^{3-}$ NPs of 35 nm were anchored to the surface mainly via coordination bonds between the Ni^{2+} ions situated on the surface of the NPs and the available on the gold surface amino functions. The control of the NPs amount on the surface is achieved by the variation of the initial concentration of NPs in the aqueous suspensions, giving in all cases a homogeneous distribution of the NPs on the overall Au surface, as confirmed by SPR measurements and AFM imaging. The SPR data were fitted using the generalized Rouard method and the Maxwell–Garnett equation providing the determination of a refractive index for PBA NPs. This approach for NPs deposition can be easily extended to other inorganic NPs with interesting physico-chemical properties, that opens the ways for various applications.

Conflicts of interest

There are no conflicts to declare.

Acknowledgments

The CBS is a member of the France-BioImaging (FBI) and the French Infrastructure for Integrated Structural Biology (FRISBI), 2 national infrastructures supported by the French National Research Agency (ANR-10-INBS-04-01 and ANR-10-INBS-05, respectively). Oscar Saavedra acknowledges funding from the European Union's Horizon 2020 research and innovation program under the Marie Skłodowska-Curie grant agreement No. 721874 (SPM2.0).

Notes and references

- W. R. Entley and G. S. Girolami, *Science*, 1995, **268**, 397-400.
- S. Ferlay, T. Mallah, R. Ouahès, P. Veillet and M. Verdaguer, *Nature*, 1995, **378**, 701-703.
- M. Verdaguer, A. Bleuzen, V. Marvaud, J. Vaissermann, M. Seuleiman, C. Desplanches, A. Scullier, C. Train, R. Garde, G. Gelly, C. Lomenech, I. Rosenman, P. Veillet, C. Cartier and F. Villain, *Coord. Chem. Rev.*, 1999, **190–192**, 1023-1047.
- N. Shimamoto, S.-i. Ohkoshi, O. Sato and K. Hashimoto, *Inorg. Chem.*, 2002, **41**, 678-684.
- W. Kosaka, K. Nomura, K. Hashimoto and S.-i. Ohkoshi, *J. Am. Chem. Soc.*, 2005, **127**, 8590-8591.
- T. Mahfoud, G. Molnár, S. Bonhommeau, S. Cobo, L. Salmon, P. Demont, H. Tokoro, S.-i. Ohkoshi, K. Boukheddaden and A. Bousseksou, *J. Am. Chem. Soc.*, 2009, **131**, 15049-15054.
- O. Sato, T. Iyoda, A. Fujishima and K. Hashimoto, *Science*, 1996, **272**, 704-705.
- V. Escax, A. Bleuzen, J. P. Itié, P. Munsch, F. Varret and M. Verdaguer, *J. Phys. Chem. B*, 2003, **107**, 4763-4767.
- S.-i. Ohkoshi, H. Tokoro and K. Hashimoto, *Coord. Chem. Rev.*, 2005, **249**, 1830-1840.
- H. Tokoro, T. Matsuda, K. Hashimoto and S.-i. Ohkoshi, *J. App. Phys.*, 2005, **97**, 10M508.
- S. S. Kaye and J. R. Long, *J. Am. Chem. Soc.*, 2005, **127**, 6506-6507.
- K. W. Chapman, P. J. Chupas and C. J. Kepert, *J. Am. Chem. Soc.*, 2006, **128**, 7009-7014.

Journal Name

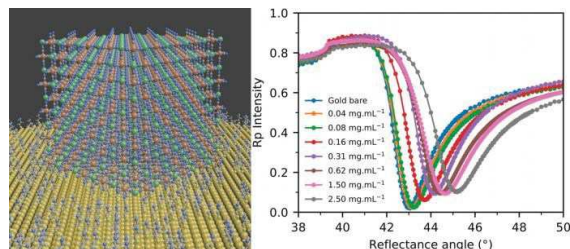
COMMUNICATION

- 13 A. L. Goodwin, K. W. Chapman and C. J. Kepert, *J. Am. Chem. Soc.*, 2005, **127**, 17980-17981.
- 14 L. Catala and T. Mallah, *Coord. Chem. Rev.*, 2017, **346**, 32-61.
- 15 D. Brinzei, L. Catala, C. Mathonière, W. Wernsdorfer, A. Gloter, O. Stephan and T. Mallah, *J. Am. Chem. Soc.*, 2007, **129**, 3778-3779.
- 16 L. Catala, T. Gacoin, J.-P. Boilot, É. Rivière, C. Paulsen, E. Lhotel and T. Mallah, *Adv. Mater.*, 2003, **15**, 826-829.
- 17 W. Kosaka, M. Tozawa, K. Hashimoto and S.-i. Ohkoshi, *Inorg. Chem. Commun.*, 2006, **9**, 920-922.
- 18 G. Félix, W. Nicolazzi, L. Salmon, G. Molnár, M. Perrier, G. Maurin, J. Larionova, J. Long, Y. Guari and A. Bousseksou, *Phys. Rev. Lett.*, 2013, **110**, 235701.
- 19 G. Félix, M. Mikolasek, H. J. Shepherd, J. Long, J. Larionova, Y. Guari, J.-P. Itié, A. I. Chumakov, W. Nicolazzi, G. Molnár and A. Bousseksou, *Eur. J. Inorg. Chem.*, 2018, **2018**, 443-448.
- 20 M. Wang, L. Yang, B. Hu, J. Liu, L. He, Q. Jia, Y. Song and Z. Zhang, *Biosens. Bioelectron.*, 2018, **113**, 16-24.
- 21 L. He, B. Cui, B. Hu, J. Liu, K. Tian, M. Wang, Y. Song, S. Fang, Z. Zhang and Q. Jia, *ACS Appl. Energy Mater.*, 2018, **1**, 3915-3928.
- 22 N. Zhou, L. Yang, B. Hu, Y. Song, L. He, W. Chen, Z. Zhang, Z. Liu and S. Lu, *Anal. Chem.*, 2018, **90**, 13624-13631.
- 23 G. Maurin-Pasturel, E. Rascol, M. Bussan, S. Sevestre, J. Lai-Kee-Him, P. Bron, J. Long, J. Chopineau, J.-M. Devoisselle, Y. Guari and J. Larionova, *Inorg. Chem. Front.*, 2017, **4**, 1737-1741.
- 24 G. Dacarro, A. Taglietti and P. Pallavicini, *Molecules*, 2018, **23**.
- 25 D. P. Goronzy, M. Ebrahimi, F. Rosei, Y. Fang, S. De Feyter, S. L. Tait, C. Wang, P. H. Beton, A. T. S. Wee, P. S. Weiss, D. F. Perepichka and Arramel, *ACS Nano*, 2018, **12**, 7445-7481.
- 26 D. R. Talham and M. W. Meisel, *Chem. Soc. Rev.*, 2011, **40**, 3356-3365.
- 27 O. Sato, Y. Einaga, T. Iyoda, A. Fujishima and K. Hashimoto, *J. Phys. Chem. B*, 1997, **101**, 3903-3905.
- 28 W. E. Buschmann, S. C. Paulson, C. M. Wynn, M. A. Girtu, A. J. Epstein, H. S. White and J. S. Miller, *Chem. Mater.*, 1998, **10**, 1386-1395.
- 29 S. Nakanishi, G. Lu, H. M. Kothari, E. W. Bohannon and J. A. Switzer, *J. Am. Chem. Soc.*, 2003, **125**, 14998-14999.
- 30 F. A. Frye, D. M. Pajerowski, S. M. Lane, N. E. Anderson, J.-H. Park, M. W. Meisel and D. R. Talham, *Polyhedron*, 2007, **26**, 2281-2286.
- 31 F. A. Frye, D. M. Pajerowski, J.-H. Park, M. W. Meisel and D. R. Talham, *Chem. Mater.*, 2008, **20**, 5706-5713.
- 32 D. M. Pajerowski, J. E. Gardner, D. R. Talham and M. W. Meisel, *New J. Chem.*, 2011, **35**, 1320-1326.
- 33 S. Tricard, C. Costa-Coquelard, S. Mazerat, E. Rivière, V. Huc, C. David, F. Miserque, P. Jegou, S. Palacin and T. Mallah, *Dalton Transactions*, 2012, **41**, 4445-4450.
- 34 M. Pyrasch and B. Tiede, *Langmuir*, 2001, **17**, 7706-7709.
- 35 V. Tranjoy, M. Faustini, D. Grosso, F. Brisset, P. Beaunier, E. Rivière, M. Putero and A. Bleuzen, *Nanoscale*, 2017, **9**, 5234-5243.
- 36 D. Jiang, L. Sun, T. Liu and W. Wang, *Anal. Chem.*, 2017, **89**, 11641-11647.
- 37 N. Zhu, X. Hao, J. Ulstrup and Q. Chi, *ACS Catal.*, 2016, **6**, 2728-2738.
- 38 G. Dacarro, P. Grisoli, M. Borzenkov, C. Milanese, E. Fratini, G. Ferraro, A. Taglietti and P. Pallavicini, *Supramol. Chem.*, 2017, **29**, 823-833.
- 39 L. He, F. Duan, Y. Song, C. Guo, H. Zhao, J.-Y. Tian, Z. Zhang, C.-S. Liu, X. Zhang, P. Wang, M. Du and S.-M. Fang, *2D Mater.*, 2017, **4**, 025098.
- 40 M. D. Porter, T. B. Bright, D. L. Allara and C. E. D. Chidsey, *J. Am. Chem. Soc.*, 1987, **109**, 3559-3568.
- 41 C. D. Bain, E. B. Troughton, Y. T. Tao, J. Evall, G. M. Whitesides and R. G. Nuzzo, *J. Am. Chem. Soc.*, 1989, **111**, 321-335.
- 42 W. Knoll, *Annu. Rev. Phys. Chem.*, 1998, **49**, 569-638.
- 43 Y. Xue, X. Li, H. Li and W. Zhang, *Nat. Commun.*, 2014, **5**, 4348.
- 44 I. U. Vakarelski, C. E. McNamee and K. Higashitani, *Colloids Surf. A*, 2007, **295**, 16-20.
- 45 C. Grunewald, M. Schmutte, C. N. Noufele, C. Graf and T. Risse, *Anal. Chem.*, 2015, **87**, 10642-10649.
- 46 Y. Guari, J. Larionova, K. Molvinger, B. Folch and C. Guérin, *Chem. Commun.*, 2006, DOI: 10.1039/b602460b, 2613-2615.
- 47 S.-J. Wang, C.-S. Chen and L.-C. Chen, *Sci. Technol. Adv. Mater.*, 2016, **14**, 044405.
- 48 C. Rossi, J. Homand, C. Bauche, H. Hamdi, D. Ladant and J. Chopineau, *Biochemistry*, 2003, **42**, 15273-15283.
- 49 R. Veneziano, C. Rossi, A. Chenal, J.-M. Devoisselle, D. Ladant and J. Chopineau, *Proc. Natl. Acad. Sci. U.S.A.*, 2013, **110**, 20473-20478.
- 50 R. García, *Amplitude Modulation Atomic Force Microscopy: GARCIA:AMPLIT.MODULATION O-BK*, Wiley-VCH Verlag GmbH & Co. KGaA, Weinheim, Germany, 2010.
- 51 G. Marinaro, M. Burghammer, L. Costa, T. Dane, F. De Angelis, E. Di Fabrizio and C. Riekel, *ACS Appl. Mater. Interfaces*, 2015, **7**, 12373-12379.
- 52 D. Nečas and P. Klapetek, *Open Physics*, 2011, **10**, 181-188.
- 53 P. Lecaruyer, E. Maillart, M. Canva and J. Rolland, *Appl. Opt.*, 2006, **45**, 8419-8423.
- 54 J. C. M. Garnett, *Phil. Trans. R. Soc. Lond. A*, 1904, **203**, 385-420.
- 55 R. Rupp, *Opt. Commun.*, 2000, **182**, 273-279.

Graphical abstract:

View Article Online
DOI: 10.1039/C9NJ00251K

Surface Plasmon Resonance monitoring of Prussian Blue Analogue nanoparticles anchored on Gold-Cysteamine substrate



A simple approach for controlled deposition of Prussian Blue Analogues nanoparticles on a functionalised plasmonic gold surface†

Giang Ngo,^a Gautier Félix,^{*a} Jérôme Long,^a Luca Costa,^b Oscar Saavedra V.,^b Pierre-Emmanuel Milhiet,^b Jean-Marie Devoisselle,^a Yannick Guari,^a Joulia Larionova,^a Joël Chopineau^{*a,c}

Materials

All chemical reagents were purchased and used without further purification: Potassium ferricyanide (Acros Organics, 99%), Nickel (II) chloride hexahydrate (Chimica, 99%), 2-aminoethanethiol hydrochloride (Sigma Aldrich, 98%). Ultra-pure water was obtained from a MilliQ apparatus (Millipore).

Gold coated glass slides (including 2 ± 0.5 nm thickness of chromium layer and 47 ± 1 nm thickness of gold layer) (size: 2.5 x 3.7 cm) were obtained from Femto (Besançon, France).

Synthesis of 35 nm $K^+/Ni^{2+}/[Fe(CN)_6]^{3-}$ PBA nanoparticles.

The two aqueous solutions of reactants: $NiCl_2 \cdot 6H_2O$ (16 mM, 50 mL) and $K_3[Fe(CN)_6]$ (17 mM, 50 mL) were added simultaneously to 100 mL of MilliQ water using a two-syringe infusion pump (KdScientific KDS200) with a fixed addition rate at $4 \text{ mL} \cdot \text{min}^{-1}$, under vigorous stirring at 25°C.

After completion of the addition, the solution was stirred for one hour and then centrifuged at $35700 \times g$ during 10 min. The supernatant was removed and $K^+/Ni^{2+}/[Fe(CN)_6]^{3-}$ nanoparticles were recovered by centrifugation and washed with MilliQ water (3 times) and ethanol (1 time), finally dried under vacuum. In a typical experiment, about 100 mg of nanoparticles were obtained.^{1,2}

Amino coated gold surfaces

Cysteamine (aminoethane thiol) anchoring on glass was formed by immersing the gold coated glass slides overnight in an ethanol solution containing 5 mM of cysteamine hydrochloride³. The glass slides were thoroughly rinsed with MilliQ water and the surface was neutralised by immersing the slides in 35 mL of NaOH solution (0.1M) for 10 min. After thoroughly rinsing with water, the amino coated glass slides were dried under nitrogen flow.

In situ $K^+/Ni^{2+}/[Fe(CN)_6]^{3-}$ NPs deposition on Cysteamine-modified Gold surface (AuCyst) for Surface Plasmon Resonance measurements

Nanoparticles colloidal suspensions in MilliQ water were supplied at different concentrations: 2.50; 1.50; 0.62; 0.31; 0.16; 0.08 and 0.04 mg.mL⁻¹. The scheme (Fig. 1 (a)) describes the method used for assembling nanoparticles on the gold-coated glass slide using a homemade SPR PTFE cell. In this device, the glass slide was mounted on the SPR flow cell (1 mL in volume) with the amino coated layer facing the interior of the cell. After 8 hours of nanoparticles deposition, MilliQ water was injected to rinse the cell. The cell was then dried by flowing nitrogen gas. SPR measurements were performed at the air interface.

Characterization methods

Physical characterization. The hydrodynamic diameter and zeta potential of the nanoparticles were measured on a Nano ZS Zetasizer (Malvern, UK).

Transmission Electron Microscopy (TEM, JEOL 1200 EX II and LaB6 JEOL 1400 Plus) was used to determine the morphology of single PBA nanoparticles. Samples for TEM measurements were deposited from suspensions on copper grids. NPs size distribution histograms were determined using enlarged TEM micrographs taken at magnification of 100K on a statistical sample of ca. 200 NPs.

Fourier transformed infra-red (FTIR) spectroscopy. Infrared spectra in transmission mode of nanoparticles were recorded in a dried KBr matrix formatted as disks on Spectrum Two FT-IR spectrophotometer (Spectrum 100, Perkin Elmer, US).

Attenuated total reflection (ATR)-FTIR. The deposition of PBA NPs on amino-gold, ATR-FTIR measurements were performed using attenuated total reflection accessory on a Spectrum Two FT-IR Spectrophotometer. A background without sample was acquired prior measurements.

Powder X-ray diffraction. The powder X-ray diffraction pattern (XRDP) was recorded in the interval $2\theta = 10-80^\circ$ at room temperature with the XPERTpro Panalytical diffractometer mounted in a Debye-Scherrer configuration and equipped with a Cu K α radiation. The XRDP planar configuration with fixed sample and rotation diffraction angle was used.

Surface plasmon resonance (SPR) experiments and calculations. For performing SPR measurements, the SPR cell was mounted on the SPR bench. One side of the cover glass is coated with gold (inside of the cell) while the other was colligated to a right angle prism (N-BK7, 20 mm) by using an appropriate matching index oil (Invoil 704, BCP Instruments, France). Plasmon excitation was achieved via a p-polarised light from a standard 632.8 nm HeNe laser. A lock-in amplifier (including pre-amplifier and chopper) was equipped in order to maximize the signal-to-noise ratio and reject stray light. The SPR cell coupled to the prism was mounted on a precise goniometer stage for precise control of incoming and reflected light beam. The incidence angle was monitored between 38° and 50° by rotating the sample

cell and detector turntable motors with 0.05° steps. The control of the spectrometer was done via WASPLAS software. The obtained data were analysed using the generalised Rouard method and Maxwell-Garnett equation in a homemade python code, in order to determine the refractive index of NPs. For the simulation, we have taken a multi-layer system with the following composition: an infinite glass layer (to modelise the prism), a chromium layer of 2 nm, a gold layer of 47 nm, a layer of PBA NPs, an infinite layer of air. To be approximated as a homogeneous and flat layer, the NPs were considered as defect in a matrix (in our case the air). The height of this layer is the average of the NPs height on the surface, extracted from AFM measurements.

The Maxwell-Garnett equation allows calculating the effective refractive index n_{eff} of a matrix with punctual defect. It is important to note that the refractive index and the dielectric constant of a material are linked as follows:

$$\epsilon_{material} = n_{material}^2 \quad (1)$$

In this paper, the effective layer is composed by a matrix (dielectric constant: ϵ_m) of air with NPs defects (dielectric constant: ϵ_{NP}), with a volumic fraction of NPs in the matrix f .

$$\epsilon_{eff} = \epsilon_m \frac{2f(\epsilon_{NP} - \epsilon_m) + \epsilon_{NP} + 2\epsilon_m}{2\epsilon_m + \epsilon_{NP} + f(\epsilon_m - \epsilon_{NP})} \quad (2)$$

The volumic fraction of NPs is proportional to the surface coverage of NPs on the gold surface.

The absorption of NPs is taken into account in the complex refractive index of NPs, in Fig. S4 the refractive index is $1.44 + 0.1i \pm 0.04$. For Fig. S3, the roughness of the surface is taken into account by a modification of the Fresnel coefficient of the layer such as it was done in ref 4.

Fit of the resonance angle of SPR spectra. To fit the resonance angle of experimental SPR spectra (minimum angle) the non-linear least square method coupled with a Monte Carlo random walk was used. First, the refractive range for the Monte Carlo random walk is chosen (in our case, between 1.0 and 2.0). The first step of the algorithm is to select a (random or not) refractive index for the NPs and calculated the associated theoretical SPR curves. Then the least-square error between the experimental SPR minimum spectra and the theoretical ones is calculated. The second step of the algorithm is to use a recursive loop where N ($N=1\,000\,000$, for instance) refractive indexes are selected one by one. For each new refractive index, the theoretical SPR curves have been calculated as well as the least-square error between the experimental SPR minimum spectra and the theoretical ones. When the least-square error from the new refractive index was smaller than the least-square error from the old one, the new refractive index was kept. This simulation has been done several times (1000 for instance) and the refractive index associated with the smallest gives the optimal fit parameter. To calculate the error, the numerical standard deviation has been calculated. The error of the refractive index was calculated using the least-square density of probability (which depends on the standard deviation) and the Metropolis algorithm.

Refractometry. A Bellingham + Stanley RFM-T refractometer was used to extract the refractive index of NPs from the effective refractive index of a NPs/water mixture. Using the volumic fraction and the effective refractive index in the Maxwell-Garnett equation, we were able to work out the refractive index of NPs. The volumic fraction of NPs in water was calculated using the weighting mass of NPs, the water volume and the density of NPs. A refractive index of 1.44 was found for the NPs.

Atomic force microscopy (AFM). AFM images were obtained in ambient conditions using a Nanowizard 4 AFM (JPK Instruments, Germany) equipped with a Vortis SPMControl electronics and an Ultraspeed cantilever holder. Data were collected in Amplitude Modulation AFM mode (AM-AFM mode)⁵ using AC160TS cantilevers (Olympus probes, Japan) with nominal resonance frequency ≈ 300 kHz, with scan size of $20\ \mu\text{m} \times 20\ \mu\text{m}$ (Figure 2 of the main manuscript) and $5\ \mu\text{m} \times 5\ \mu\text{m}$ (Figure S3) both with 512×512 pixels. The cantilever free oscillation amplitude was set to approximately 10 nm and the setpoint amplitude to $\approx 75\%$ of it. The scan speed was set to 0.75 – 1 second per line. Data analysis as well as the evaluation of the surface coverage was carried out using Gwyddion Software^{6, 7}. Surface coverage was evaluated dividing the total NPs area, evaluated through the definition of a height threshold, by the total area of the full AFM image.

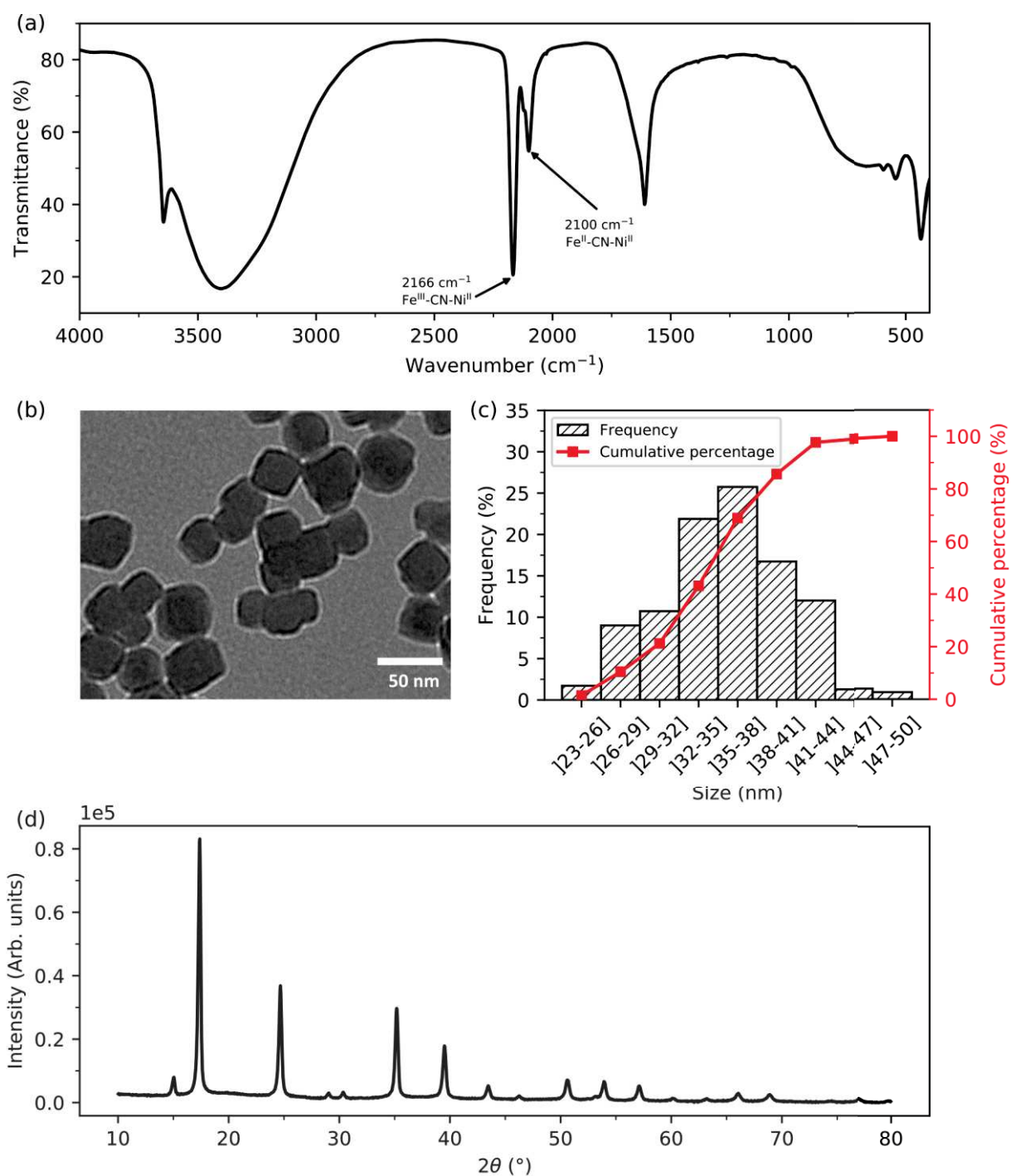


Fig. S1 Characterization of $\text{K}^+/\text{Ni}^{2+}/[\text{Fe}(\text{CN})_6]^{3-}$ PBA NPs (a) Comparison of infrared spectra between PBA NPs and amino/gold surface, collected by transmission FTIR; (b) TEM image; (c) PBA NPs size distribution determined by TEM measurement; (d) X-Ray diffraction pattern of PBA NPs.

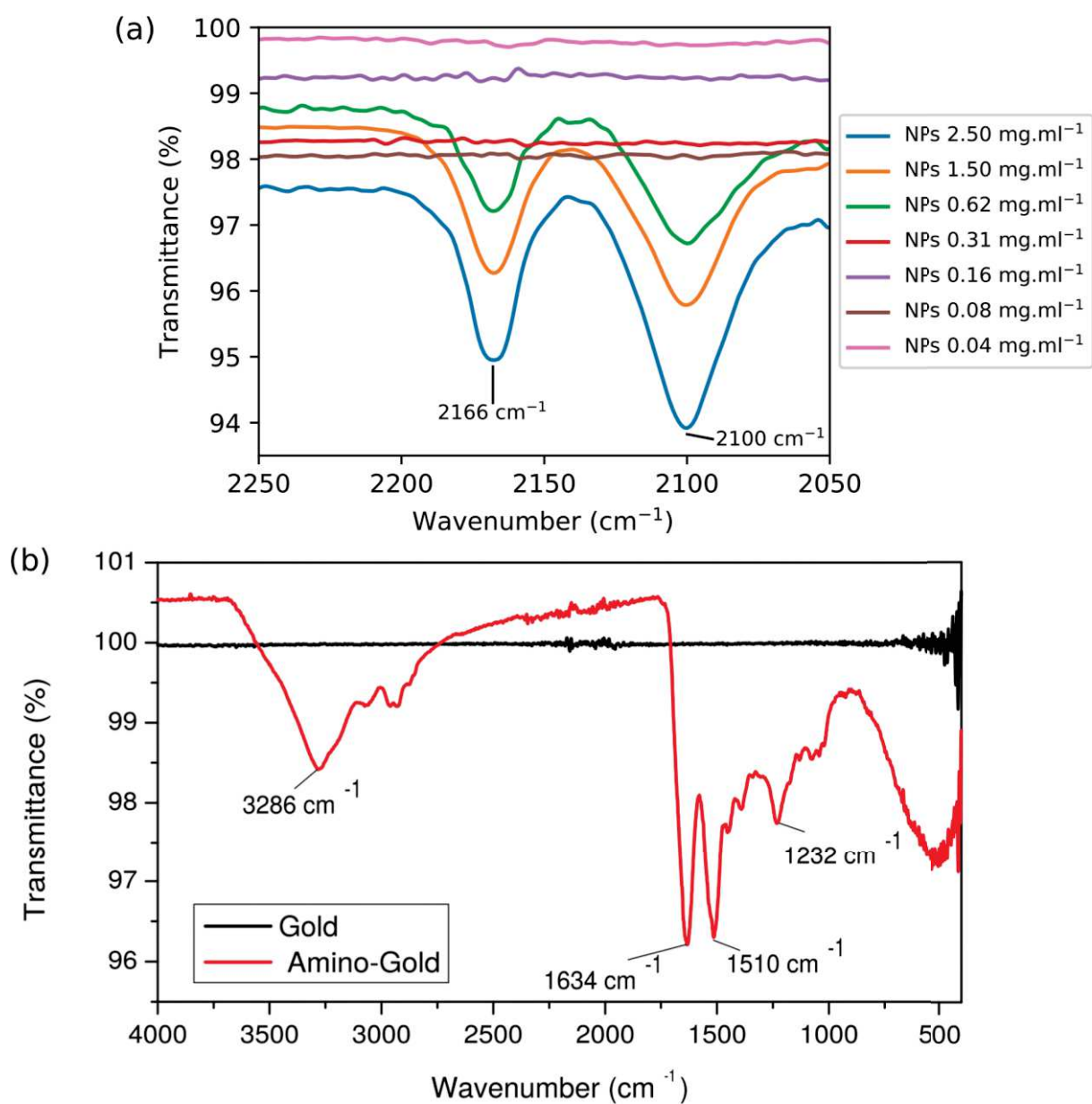


Fig. S2 (a) Infrared spectra of NPs deposited on amino-gold surface at different concentrations collected by ATR-FTIR (The amino-gold surface was taken as ATR-FTIR reference background); (b) Infrared spectra of gold and amino-gold substrat collected by ATR-FTIR (reference: air).

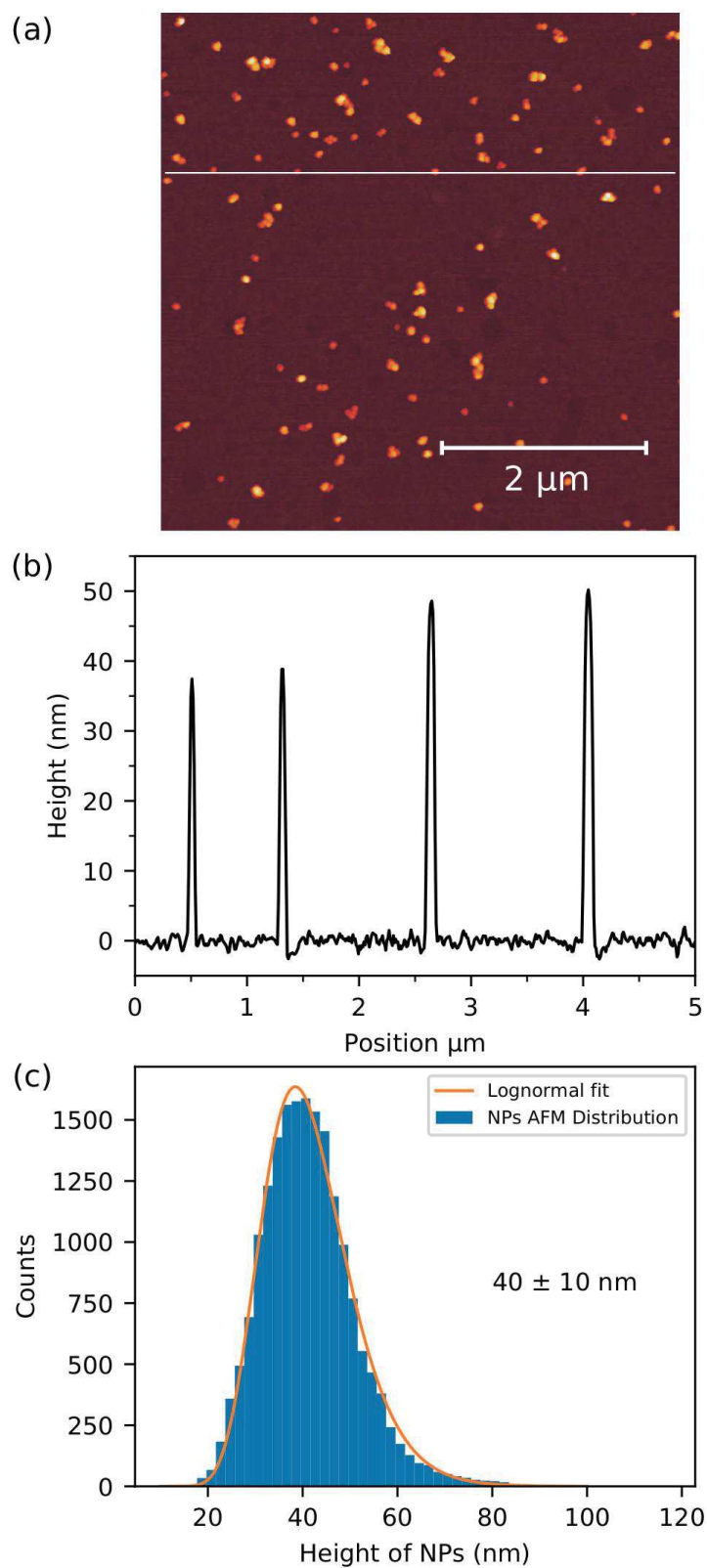


Fig. S3 AFM Topographical image (scale bar 2 μm) with indicated cross-section (a) and its height profile (b) for NPs deposited on amino-gold surface at 0.16 mg.mL^{-1} concentration; (c) Size distribution of NPs measured with all topographic AFM image.

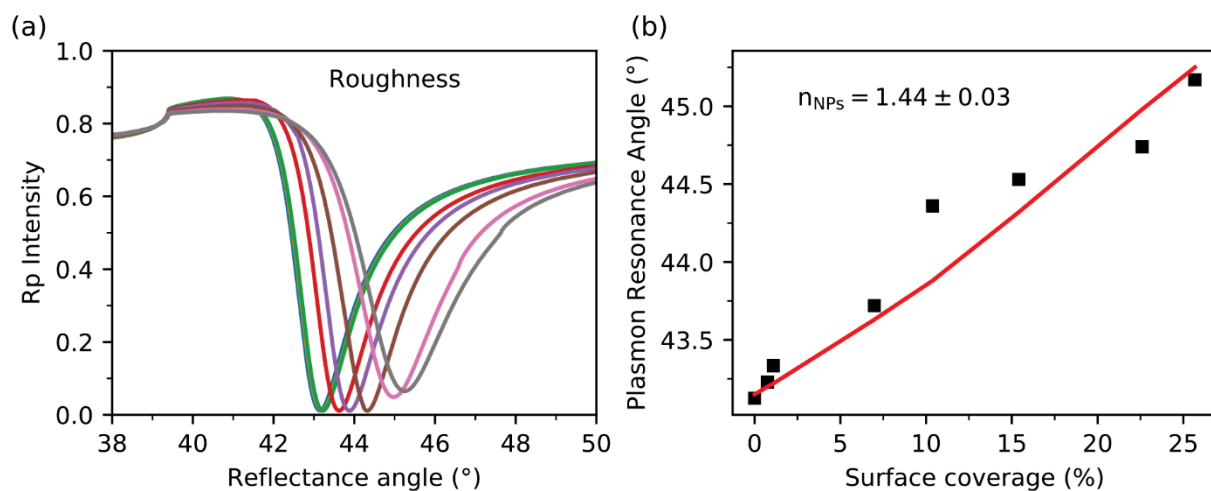


Fig. S4 (a) Plasmon curves with surface roughness calculated using Rouard method; (b) Plasmon resonance angles represented as a function of the surface coverage of NPs on amino-gold surface.

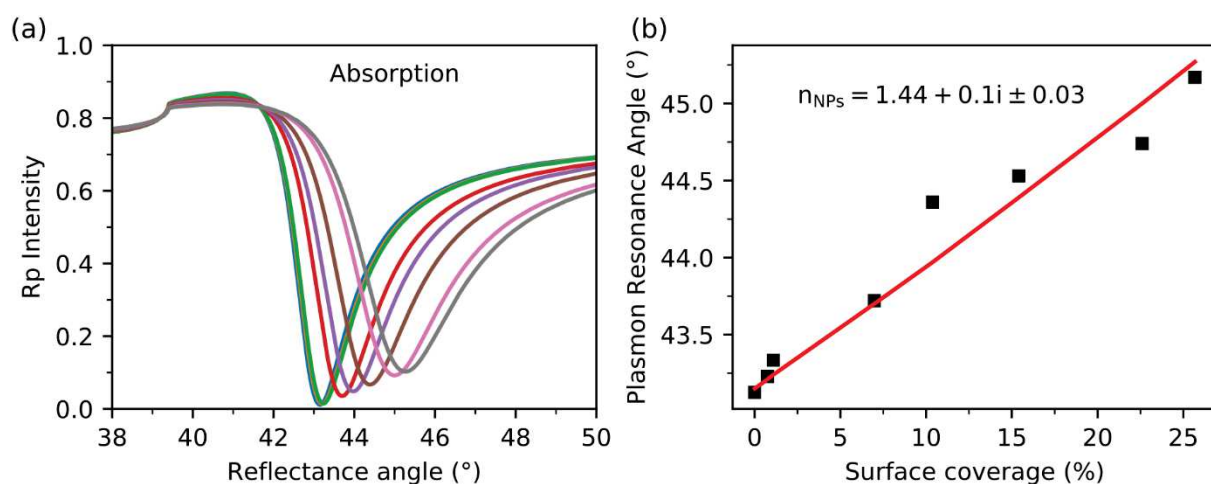


Fig. S5 (a) Plasmon curves with absorption calculated using Rouard method; (b) Plasmon resonance angles represented as a function of the surface coverage of NPs on amino-gold surface.

The CBS is a member of the France-BioImaging (FBI) and the French Infrastructure for Integrated Structural Biology (FRISBI), 2 national infrastructures supported by the French National Research Agency (ANR-10-INBS-04-01 and ANR-10-INBS-05, respectively). Oscar Saavedra acknowledges funding from the European Union's Horizon 2020 research and innovation program under the Marie Skłodowska-Curie grant agreement No. 721874 (SPM2.0).

1. G. Félix, W. Nicolazzi, L. Salmon, G. Molnár, M. Perrier, G. Maurin, J. Larionova, J. Long, Y. Guari and A. Bousseksou, *Phys. Rev. Lett.*, 2013, **110**, 235701.
2. G. Maurin-Pasturel, E. Rascol, M. Busson, S. Sevestre, J. Lai-Kee-Him, P. Bron, J. Long, J. Chopineau, J.-M. Devoisselle, Y. Guari and J. Larionova, *Inorg. Chem. Front.*, 2017, **4**, 1737-1741.
3. C. Rossi, J. Homand, H. Hamdi, C. Bauche, D. Ladant and J. Chopineau, *Biochemistry*, 2003, **42**, 15273-15283.
4. G. Léron del and R. Romestain, *Applied Physics Letters*, 1999, **74**, 2740-2742.
5. R. García, *Amplitude Modulation Atomic Force Microscopy: GARCIA:AMPLIT.MODULATION O-BK*, Wiley-VCH Verlag GmbH & Co. KGaA, Weinheim, Germany, 2010.
6. D. Nečas and P. Klapetek, *Open Physics*, 2011, **10**, 181-188.
7. A. Theodoratou, L. Costa, L. Bonnet, C. Blanc, V. Lapinte, P. Etienne, P.-E. Milhiet, J.-J. Robin, J. Oberdisse, J. Chopineau and A. Aubert-Pouëssel, *European Polymer Journal*, 2019, **111**, 161-169.

Bibliography

- [1] H. T. McMahon and J. L. Gallop, “Membrane curvature and mechanisms of dynamic cell membrane remodelling,” *Nature*, vol. 438, no. 7068, p. 590, 2005.
- [2] M. Murate and T. Kobayashi, “Revisiting transbilayer distribution of lipids in the plasma membrane,” *Chemistry and Physics of Lipids*, vol. 194, pp. 58 – 71, 2016. Memorial Issue for Robert Bittman.
- [3] J. D. Nickels, J. C. Smith, and X. Cheng, “Lateral organization, bilayer asymmetry, and inter-leaflet coupling of biological membranes,” *Chemistry and Physics of Lipids*, vol. 192, pp. 87 – 99, 2015. ORNL workshop on Biomembranes.
- [4] G. J. Doherty and H. T. McMahon, “Mediation, Modulation, and Consequences of Membrane-Cytoskeleton Interactions,” *Annual Review of Biophysics*, vol. 37, pp. 65–95, may 2008.
- [5] A. Kusumi, C. Nakada, K. Ritchie, K. Murase, K. Suzuki, H. Murakoshi, R. S. Kasai, J. Kondo, and T. Fujiwara, “Paradigm shift of the plasma membrane concept from the two-dimensional continuum fluid to the partitioned fluid: High-speed single-molecule tracking of membrane molecules,” *Annual Review of Biophysics and Biomolecular Structure*, vol. 34, no. 1, pp. 351–378, 2005. PMID: 15869394.
- [6] S. J. Singer and G. L. Nicolson, “The Fluid Mosaic Model of the Structure of Cell Membranes,” *Science*, vol. 175, pp. 720 LP – 731, feb 1972.
- [7] M. Rao and S. Mayor, “Active organization of membrane constituents in living cells,” *Current Opinion in Cell Biology*, vol. 29, pp. 126–132, 2014.

- [8] K. Simons and W. L. C. Vaz, “Model Systems, Lipid Rafts, and Cell Membranes,” *Annual Review of Biophysics and Biomolecular Structure*, vol. 33, pp. 269–295, may 2004.
- [9] M. Edidin, “Lipids on the frontier: a century of cell-membrane bilayers,” *Nature Reviews Molecular Cell Biology*, vol. 4, no. 5, pp. 414–418, 2003.
- [10] K. Simons and E. Ikonen, “Functional rafts in cell membranes,” *Nature*, vol. 387, no. 6633, pp. 569–572, 1997.
- [11] E. Sezgin, I. Levental, S. Mayor, and C. Eggeling, “The mystery of membrane organization: composition, regulation and roles of lipid rafts,” *Nature Reviews Molecular Cell Biology*, vol. 18, no. 6, pp. 361–374, 2017.
- [12] L. J. Pike, “Rafts defined: A report on the keystone symposium on lipid rafts and cell function,” *Journal of Lipid Research*, vol. 47, pp. 1597–1598, jul 2006.
- [13] R. Macháň and M. Hof, “Lipid diffusion in planar membranes investigated by fluorescence correlation spectroscopy,” *Biochimica et Biophysica Acta (BBA) - Biomembranes*, vol. 1798, no. 7, pp. 1377–1391, 2010.
- [14] A. Kusumi, C. Nakada, K. Ritchie, K. Murase, K. Suzuki, H. Murakoshi, R. S. Kasai, J. Kondo, and T. Fujiwara, “Paradigm Shift of the Plasma Membrane Concept from the Two-Dimensional Continuum Fluid to the Partitioned Fluid: High-Speed Single-Molecule Tracking of Membrane Molecules,” *Annual Review of Biophysics and Biomolecular Structure*, vol. 34, pp. 351–378, may 2005.
- [15] D. M. Engelman, “Membranes are more mosaic than fluid,” *Nature*, vol. 438, no. 7068, pp. 578–580, 2005.
- [16] H. T. McMahon and E. Boucrot, “Membrane curvature at a glance,” *Journal of Cell Science*, vol. 128, no. 6, pp. 1065–1070, 2015.
- [17] S. Attwood, Y. Choi, and Z. Leonenko, “Preparation of dopc and dppc supported planar lipid bilayers for atomic force microscopy and atomic force spectroscopy,” *International Journal Of Molecular Sciences*, vol. 14, no. 2, pp. 3514–3539, 2013.

- [18] S. W. Hui, R. Viswanathan, J. A. Zasadzinski, and J. N. Israelachvili, “The structure and stability of phospholipid bilayers by atomic force microscopy,” *Biophysical journal*, vol. 68, pp. 171–178, jan 1995.
- [19] F. Dekkiche, M. Corneci, A.-M. Trunfio-Sfarghiu, B. Munteanu, Y. Berthier, W. Kaabar, and J.-P. Rieu, “Stability and tribological performances of fluid phospholipid bilayers: Effect of buffer and ions,” *Colloids and Surfaces B: Biointerfaces*, vol. 80, no. 2, pp. 232 – 239, 2010.
- [20] Y. Fang and J. Yang, “The growth of bilayer defects and the induction of interdigitated domains in the lipid-loss process of supported phospholipid bilayers,” *Biochimica et Biophysica Acta (BBA) - Biomembranes*, vol. 1324, no. 2, pp. 309 – 319, 1997.
- [21] S. Garcia-Manyes, L. Redondo-Morata, G. Oncins, and F. Sanz, “Nanomechanics of Lipid Bilayers: Heads or Tails?,” *Journal of the American Chemical Society*, vol. 132, pp. 12874–12886, sep 2010.
- [22] M. M. Kozlov, P. I. Kuzmin, and S. V. Popov, “Formation of cell protrusions by an electric field: a thermodynamic analysis,” *European Biophysics Journal*, vol. 21, no. 1, pp. 35–45, 1992.
- [23] S. Leikin, M. M. Kozlov, N. L. Fuller, and R. P. Rand, “Measured effects of diacylglycerol on structural and elastic properties of phospholipid membranes,” *Biophysical journal*, vol. 71, pp. 2623–2632, nov 1996.
- [24] T. Harayama and H. Riezman, “Understanding the diversity of membrane lipid composition,” *Nature Reviews Molecular Cell Biology*, vol. 19, no. 5, pp. 281–296, 2018.
- [25] F. Campelo, H. T. McMahon, and M. M. Kozlov, “The Hydrophobic Insertion Mechanism of Membrane Curvature Generation by Proteins,” *Biophysical Journal*, vol. 95, no. 5, pp. 2325–2339, 2008.
- [26] H. T. McMahon, M. M. Kozlov, and S. Martens, “Membrane Curvature in Synaptic Vesicle Fusion and Beyond,” *Cell*, vol. 140, no. 5, pp. 601–605, 2010.

- [27] T. Kirchhausen, “Three ways to make a vesicle,” *Nature Reviews Molecular Cell Biology*, vol. 1, no. 3, pp. 187–198, 2000.
- [28] D. Jensen and R. Schekman, “Copii-mediated vesicle formation at a glance,” *Journal of Cell Science*, vol. 124, no. 1, pp. 1–4, 2011.
- [29] H. T. McMahon and E. Boucrot, “Molecular mechanism and physiological functions of clathrin-mediated endocytosis,” *Nature Reviews Molecular Cell Biology*, vol. 12, no. 8, pp. 517–533, 2011.
- [30] Y. Rao and V. Haucke, “Membrane shaping by the Bin/amphiphysin/Rvs (BAR) domain protein superfamily,” *Cellular and Molecular Life Sciences*, vol. 68, no. 24, pp. 3983–3993, 2011.
- [31] C. Mim and V. M. Unger, “Membrane curvature and its generation by bar proteins,” *Trends in biochemical sciences*, vol. 37, p. 526—533, December 2012.
- [32] D. Stamenović and N. Wang, “Invited Review: Engineering approaches to cytoskeletal mechanics,” *Journal of Applied Physiology*, vol. 89, pp. 2085–2090, nov 2000.
- [33] J. Alcaraz, L. Buscemi, M. Grabulosa, X. Trepas, B. Fabry, R. Farré, and D. Navajas, “Microrheology of Human Lung Epithelial Cells Measured by Atomic Force Microscopy,” *Biophysical Journal*, vol. 84, no. 3, pp. 2071–2079, 2003.
- [34] C. Zhu, G. Bao, and N. Wang, “Cell Mechanics: Mechanical Response, Cell Adhesion, and Molecular Deformation,” *Annual Review of Biomedical Engineering*, vol. 2, pp. 189–226, aug 2000.
- [35] F. Rico, P. Roca-Cusachs, N. Gavara, R. Farré, M. Rotger, and D. Navajas, “Probing mechanical properties of living cells by atomic force microscopy with blunted pyramidal cantilever tips,” *Phys. Rev. E*, vol. 72, p. 021914, Aug 2005.
- [36] I. Sokolov, M. E. Dokukin, and N. V. Guz, “Method for quantitative measurements of the elastic modulus of biological cells in AFM indentation experiments,” *Methods*, vol. 60, no. 2, pp. 202–213, 2013.
- [37] J. Dai and M. P. Sheetz, “Membrane Tether Formation from Blebbing Cells,” *Biophysical Journal*, vol. 77, no. 6, pp. 3363–3370, 1999.

- [38] B. Seantier, M.-C. Giocondi, C. L. Grimellec, and P.-E. Milhiet, “Probing supported model and native membranes using AFM,” *Current Opinion in Colloid & Interface Science*, vol. 13, no. 5, pp. 326–337, 2008.
- [39] T. Bhatia, P. Husen, J. Brewer, L. A. Bagatolli, P. L. Hansen, J. H. Ipsen, and O. G. Mouritsen, “Preparing giant unilamellar vesicles (GUVs) of complex lipid mixtures on demand: Mixing small unilamellar vesicles of compositionally heterogeneous mixtures,” *Biochimica et Biophysica Acta (BBA) - Biomembranes*, vol. 1848, no. 12, pp. 3175–3180, 2015.
- [40] R. Kwok and E. Evans, “Thermoelasticity of large lecithin bilayer vesicles,” *Biophysical journal*, vol. 35, p. 637—652, September 1981.
- [41] J. R. Henriksen and J. H. Ipsen, “Measurement of membrane elasticity by micropipette aspiration,” *The European Physical Journal E*, vol. 14, no. 2, pp. 149–167, 2004.
- [42] Faucon, J.F., Mitov, M. D., Méléard, P., Bivas, I., and Bothorel, P., “Bending elasticity and thermal fluctuations of lipid membranes. theoretical and experimental requirements,” *J. Phys. France*, vol. 50, no. 17, pp. 2389–2414, 1989.
- [43] P. Méléard, T. Pott, H. Bouvrais, and J. Ipsen, “Advantages of statistical analysis of giant vesicle flickering for bending elasticity measurements,” *The European physical journal. E, Soft matter*, vol. 34, p. 116, October 2011.
- [44] D. M. Haverstick and M. Glaser, “Visualization of Ca^{2+} -induced phospholipid domains,” *Proceedings of the National Academy of Sciences*, vol. 84, no. 13, pp. 4475–4479, 1987.
- [45] D. Haverstick and M. Glaser, “Visualization of domain formation in the inner and outer leaflets of a phospholipid bilayer,” *The Journal of Cell Biology*, vol. 106, pp. 1885 – 1892, 1988.
- [46] C. Dietrich, L. A. Bagatolli, Z. N. Volovyk, N. L. Thompson, M. Levi, K. Jacobson, and E. Gratton, “Lipid Rafts Reconstituted in Model Membranes,” *Biophysical Journal*, vol. 80, no. 3, pp. 1417–1428, 2001.

- [47] Y. Zhou, C. K. Berry, P. A. Storer, and R. M. Raphael, "Peroxidation of polyunsaturated phosphatidyl-choline lipids during electroformation," *Biomaterials*, vol. 28, no. 6, pp. 1298 – 1306, 2007.
- [48] N. F. Morales-Pennington, J. Wu, E. R. Farkas, S. L. Goh, T. M. Konyakhina, J. Y. Zheng, W. W. Webb, and G. W. Feigenson, "GUV preparation and imaging: Minimizing artifacts," *Biochimica et Biophysica Acta (BBA) - Biomembranes*, vol. 1798, no. 7, pp. 1324–1332, 2010.
- [49] I. Khan, A. Elhissi, M. Shah, M. A. Alhnan, and W. Ahmed, "9 - Liposome-based carrier systems and devices used for pulmonary drug delivery," in *Woodhead Publishing Series in Biomaterials* (J. P. B. T. B. Davim and M. Tribology, eds.), pp. 395–443, Woodhead Publishing, 2013.
- [50] S. Vemuri and C. T. Rhodes, "Preparation and characterization of liposomes as therapeutic delivery systems: a review," *Pharmaceutica Acta Helvetiae*, vol. 70, no. 2, pp. 95–111, 1995.
- [51] L. Picas, P.-E. Milhiet, and J. Hernández-Borrell, "Atomic force microscopy: A versatile tool to probe the physical and chemical properties of supported membranes at the nanoscale," *Chemistry and Physics of Lipids*, vol. 165, no. 8, pp. 845–860, 2012.
- [52] S. Tristram-Nagle, H. I. Petrache, and J. F. Nagle, "Structure and interactions of fully hydrated dioleoylphosphatidylcholine bilayers," *Biophysical Journal*, vol. 75, no. 2, pp. 917 – 925, 1998.
- [53] A. A. Brian and H. M. McConnell, "Allogeneic stimulation of cytotoxic t cells by supported planar membranes," *Proceedings of the National Academy of Sciences*, vol. 81, no. 19, pp. 6159–6163, 1984.
- [54] A. R. Burns, D. J. Frankel, and T. Buranda, "Local Mobility in Lipid Domains of Supported Bilayers Characterized by Atomic Force Microscopy and Fluorescence Correlation Spectroscopy," *Biophysical Journal*, vol. 89, no. 2, pp. 1081–1093, 2005.

- [55] S. Chiantia, J. Ries, N. Kahya, and P. Schwille, “Combined AFM and Two-Focus SFCS Study of Raft-Exhibiting Model Membranes,” *ChemPhysChem*, vol. 7, pp. 2409–2418, nov 2006.
- [56] A. Berquand, D. Lévy, F. Gubellini, C. Le Grimmellec, and P.-E. Milhiet, “Influence of calcium on direct incorporation of membrane proteins into in-plane lipid bilayer,” *Ultramicroscopy*, vol. 107, no. 10, pp. 928–933, 2007.
- [57] K. J. Seu, A. P. Pandey, F. Haque, E. A. Proctor, A. E. Ribbe, and J. S. Hovis, “Effect of Surface Treatment on Diffusion and Domain Formation in Supported Lipid Bilayers,” *Biophysical Journal*, vol. 92, pp. 2445–2450, apr 2007.
- [58] M.-C. Giocondi, B. Seantier, P. Dosset, P.-E. Milhiet, and C. Le Grimmellec, “Characterizing the interactions between GPI-anchored alkaline phosphatases and membrane domains by AFM,” *Pflügers Archiv - European Journal of Physiology*, vol. 456, no. 1, pp. 179–188, 2008.
- [59] B. Gumí-Audenis, L. Costa, L. Ferrer-Tasies, I. Ratera, N. Ventosa, F. Sanz, and M. I. Giannotti, “Pulling lipid tubes from supported bilayers unveils the underlying substrate contribution to the membrane mechanics,” *Nanoscale*, vol. 10, no. 30, pp. 14763–14770, 2018.
- [60] S. Pace, P. Gonzalez, J.-M. Devoisselle, P.-E. Milhiet, D. Brunel, and F. Cunin, “Grafting of monoglyceride molecules for the design of hydrophilic and stable porous silicon surfaces,” *New J. Chem.*, vol. 34, pp. 29–33, 2010.
- [61] B. Gumí-Audenis, L. Costa, L. Redondo-Morata, P.-E. Milhiet, F. Sanz, R. Felici, M. I. Giannotti, and F. Carlà, “In-plane molecular organization of hydrated single lipid bilayers: Dppc:cholesterol,” *Nanoscale*, vol. 10, pp. 87–92, 2018.
- [62] E. T. Castellana and P. S. Cremer, “Solid supported lipid bilayers: From biophysical studies to sensor design,” *Surface Science Reports*, vol. 61, no. 10, pp. 429–444, 2006.
- [63] R. P. Richter, R. Bérat, and A. R. Brisson, “Formation of Solid-Supported Lipid Bilayers: An Integrated View,” *Langmuir*, vol. 22, pp. 3497–3505, apr 2006.

- [64] M. Tanaka and E. Sackmann, “Polymer-supported membranes as models of the cell surface,” *Nature*, vol. 437, no. 7059, pp. 656–663, 2005.
- [65] S. Steltenkamp, M. Müller, M. Deserno, C. Hennesthal, C. Steinem, and A. Janschhoff, “Mechanical properties of pore-spanning lipid bilayers probed by atomic force microscopy,” *Biophysical journal*, vol. 91, pp. 217–26, 08 2006.
- [66] P. E. Milhiet, V. Vié, M.-C. Giocondi, and C. Le Grimmellec, “Afm characterization of model rafts in supported bilayers,” *Single Molecules*, vol. 2, no. 2, pp. 109–112, 2001.
- [67] H. A. Rinia, R. A. Demel, J. P. J. M. van der Eerden, and B. de Kruijff, “Blistering of Langmuir-Blodgett Bilayers Containing Anionic Phospholipids as Observed by Atomic Force Microscopy,” *Biophysical Journal*, vol. 77, no. 3, pp. 1683–1693, 1999.
- [68] M. P. Levy D., “Imaging of transmembrane proteins directly incorporated within supported lipid bilayers using atomic force microscopy. in: Sousa a., kruhlak m. (eds) nanoimaging. methods in molecular biology (methods and protocols),” *Methods in molecular biology (Clifton, N.J.)*, vol. 950, pp. 1–10, 2013.
- [69] A. C. Simonsen and L. A. Bagatolli, “Structure of spin-coated lipid films and domain formation in supported membranes formed by hydration,” *Langmuir*, vol. 20, pp. 9720–9728, oct 2004.
- [70] R. Richter, A. Mukhopadhyay, and A. Brisson, “Pathways of Lipid Vesicle Deposition on Solid Surfaces: A Combined QCM-D and AFM Study,” *Biophysical Journal*, vol. 85, no. 5, pp. 3035–3047, 2003.
- [71] E. Reimhult, M. Zäch, F. Höök, and B. Kasemo, “A Multitechnique Study of Liposome Adsorption on Au and Lipid Bilayer Formation on SiO₂,” *Langmuir*, vol. 22, pp. 3313–3319, mar 2006.
- [72] B. Seantier, C. Breffa, O. Félix, and G. Decher, “In Situ Investigations of the Formation of Mixed Supported Lipid Bilayers Close to the Phase Transition Temperature,” *Nano Letters*, vol. 4, pp. 5–10, jan 2004.

- [73] E. Abbe, “Beiträge zur Theorie des Mikroskops und der mikroskopischen Wahrnehmung,” *Archiv für Mikroskopische Anatomie*, vol. 9, no. 1, pp. 413–468, 1873.
- [74] E. Betzig, G. H. Patterson, R. Sougrat, O. W. Lindwasser, S. Olenych, J. S. Bonifacio, M. W. Davidson, J. Lippincott-Schwartz, and H. F. Hess, “Imaging intracellular fluorescent proteins at nanometer resolution,” *Science*, vol. 313, no. 5793, pp. 1642–1645, 2006.
- [75] R. M. Hochmuth, N. Mohandas, and P. L. Blackshear Jr, “Measurement of the elastic modulus for red cell membrane using a fluid mechanical technique,” *Biophysical journal*, vol. 13, pp. 747–762, aug 1973.
- [76] O. Et-Thakafy, N. Delorme, C. Gaillard, C. Mériadec, F. Artzner, C. Lopez, and F. Guyomarc’h, “Mechanical Properties of Membranes Composed of Gel-Phase or Fluid-Phase Phospholipids Probed on Liposomes by Atomic Force Spectroscopy,” *Langmuir*, vol. 33, pp. 5117–5126, may 2017.
- [77] S. Dahmane, C. Doucet, A. Le Gall, C. Chamontin, P. Dosset, F. Murcy, L. Fernandez, D. Salas, E. Rubinstein, M. Mougél, M. Nollmann, and P.-E. Milhiet, “Nanoscale organization of tetraspanins during hiv-1 budding by correlative dstorm/afm,” *Nanoscale*, vol. 11, pp. 6036–6044, 2019.
- [78] P. Hinterdorfer and Y. F. Dufrêne, “Detection and localization of single molecular recognition events using atomic force microscopy,” *Nature Methods*, vol. 3, no. 5, pp. 347–355, 2006.
- [79] L. A. Chtcheglova and P. Hinterdorfer, “Simultaneous AFM topography and recognition imaging at the plasma membrane of mammalian cells,” *Seminars in Cell & Developmental Biology*, vol. 73, pp. 45–56, 2018.
- [80] T. Ando, N. Kodera, E. Takai, D. Maruyama, K. Saito, and A. Toda, “A high-speed atomic force microscope for studying biological macromolecules,” *Proceedings of the National Academy of Sciences*, vol. 98, no. 22, pp. 12468–12472, 2001.

- [81] N. Kodera, D. Yamamoto, R. Ishikawa, and T. Ando, “Video imaging of walking myosin V by high-speed atomic force microscopy,” *Nature*, vol. 468, no. 7320, pp. 72–76, 2010.
- [82] T. Ando, “High-speed atomic force microscopy coming of age,” *Nanotechnology*, vol. 23, p. 062001, jan 2012.
- [83] T. Ando, “High-speed atomic force microscopy,” *Microscopy*, vol. 62, pp. 81–93, feb 2013.
- [84] E. Moeendarbary and A. R. Harris, “Cell mechanics: principles, practices, and prospects,” *WIREs Systems Biology and Medicine*, vol. 6, no. 5, pp. 371–388, 2014.
- [85] S. Ebnesajjad, “18 - properties of tetrafluoroethylene homopolymers,” in *Fluoroplastics (Second Edition)* (S. Ebnesajjad, ed.), vol. 1, pp. 396 – 440, Oxford: William Andrew Publishing, second edition ed., 2015.
- [86] L. Picas, F. Rico, and S. Scheuring, “Direct measurement of the mechanical properties of lipid phases in supported bilayers,” *Biophysical Journal*, vol. 102, pp. L01–L03, Jan 2012.
- [87] L. Redondo-Morata, R. L. Sanford, O. S. Andersen, and S. Scheuring, “Effect of statins on the nanomechanical properties of supported lipid bilayers,” *Biophysical Journal*, vol. 111, no. 2, pp. 363–372, 2016.
- [88] O. Et-Thakafy, N. Delorme, C. Gaillard, C. Mériadec, F. Artzner, C. Lopez, and F. Guyomarc’h, “Mechanical properties of membranes composed of gel-phase or fluid-phase phospholipids probed on liposomes by atomic force spectroscopy,” *Langmuir*, vol. 33, pp. 5117–5126, may 2017.
- [89] R. Lakes, “Foam structures with a negative Poisson’s ratio,” *Science*, vol. 235, pp. 1038+, may 1987.
- [90] J. N. Grima, S. Winczewski, L. Mizzi, M. C. Grech, R. Cauchi, R. Gatt, D. Attard, K. W. Wojciechowski, and J. Rybicki, “Tailoring graphene to achieve negative poisson’s ratio properties,” *Advanced Materials*, vol. 27, no. 8, pp. 1455–1459, 2015.

- [91] R. Gatt, M. Vella Wood, A. Gatt, F. Zarb, C. Formosa, K. M. Azzopardi, A. Casha, T. P. Agius, P. Schembri-Wismayer, L. Attard, N. Chockalingam, and J. N. Grima, “Negative Poisson’s ratios in tendons: An unexpected mechanical response,” *Acta Biomaterialia*, vol. 24, pp. 201–208, 2015.
- [92] M. S. Stetsenko, “Determining the elastic constants of hydrocarbons of heavy oil products using molecular dynamics simulation approach,” *Journal of Petroleum Science and Engineering*, vol. 126, pp. 124 – 130, 2015.
- [93] A. Janshoff and C. Steinem, “Mechanics of lipid bilayers: What do we learn from pore-spanning membranes?,” *Biochimica et Biophysica Acta (BBA) - Molecular Cell Research*, vol. 1853, no. 11, Part B, pp. 2977 – 2983, 2015. Mechanobiology.
- [94] W. Rawicz, K. Olbrich, T. McIntosh, D. Needham, and E. Evans, “Effect of chain length and unsaturation on elasticity of lipid bilayers,” *Biophysical Journal*, vol. 79, no. 1, pp. 328–339, 2000.
- [95] L. Landau, E. Lifshitz, A. Kosevich, J. Sykes, L. Pitaevskii, and W. Reid, *Theory of Elasticity: Volume 7*. Course of theoretical physics, Elsevier Science, 1986.
- [96] H. Hertz, “On contact between elastic bodies,” *J. Reine Angew. Math*, vol. 92, pp. 156–171, 1882.
- [97] P. Roca-Cusachs, V. Conte, and X. Trepac, “Quantifying forces in cell biology,” *Nature Cell Biology*, vol. 19, no. 7, pp. 742–751, 2017.
- [98] M. Dembo and Y.-L. Wang, “Stresses at the cell-to-substrate interface during locomotion of fibroblasts,” *Biophysical Journal*, vol. 76, no. 4, pp. 2307–2316, 1999.
- [99] S. R. Polio, K. E. Rothenberg, D. Stamenovic, and M. L. Smith, “A micropatterning and image processing approach to simplify measurement of cellular traction forces,” *Acta biomaterialia*, vol. 8, p. 82—88, January 2012.
- [100] M. Bergert, T. Lendenmann, M. Zündel, A. E. Ehret, D. Panozzo, P. Richner, D. K. Kim, S. J. P. Kress, D. J. Norris, O. Sorkine-Hornung, E. Mazza, D. Poulikakos, and A. Ferrari, “Confocal reference free traction force microscopy,” *Nature Communications*, vol. 7, no. 1, p. 12814, 2016.

- [101] Y. Huang, C. Schell, T. B. Huber, A. N. Şimşek, N. Hersch, R. Merkel, G. Gommer, and B. Sabass, “Traction force microscopy with optimized regularization and automated bayesian parameter selection for comparing cells,” *Scientific Reports*, vol. 9, no. 1, p. 539, 2019.
- [102] W. R. Legant, J. S. Miller, B. L. Blakely, D. M. Cohen, G. M. Genin, and C. S. Chen, “Measurement of mechanical tractions exerted by cells in three-dimensional matrices,” *Nature Methods*, vol. 7, no. 12, pp. 969–971, 2010.
- [103] J. Steinwachs, C. Metzner, K. Skodzek, N. Lang, I. Thievesten, C. Mark, S. Münster, K. E. Aifantis, and B. Fabry, “Three-dimensional force microscopy of cells in biopolymer networks,” *Nature Methods*, vol. 13, no. 2, pp. 171–176, 2016.
- [104] J. L. Tan, J. Tien, D. M. Pirone, D. S. Gray, K. Bhadriraju, and C. S. Chen, “Cells lying on a bed of microneedles: An approach to isolate mechanical force,” *Proceedings of the National Academy of Sciences*, vol. 100, no. 4, pp. 1484–1489, 2003.
- [105] M. Gupta, B. R. Sarangi, J. Deschamps, Y. Nematbakhsh, A. Callan-Jones, F. Margadant, R.-M. Mège, C. T. Lim, R. Voituriez, and B. Ladoux, “Adaptive rheology and ordering of cell cytoskeleton govern matrix rigidity sensing,” *Nature Communications*, vol. 6, no. 1, p. 7525, 2015.
- [106] S. Ghassemi, G. Meacci, S. Liu, A. A. Gondarenko, A. Mathur, P. Roca-Cusachs, M. P. Sheetz, and J. Hone, “Cells test substrate rigidity by local contractions on submicrometer pillars,” *Proceedings of the National Academy of Sciences*, vol. 109, no. 14, pp. 5328–5333, 2012.
- [107] A. V. Taubenberger, D. W. Huttmacher, and D. J. Muller, “Single-cell force spectroscopy, an emerging tool to quantify cell adhesion to biomaterials,” *Tissue engineering. Part B, Reviews*, vol. 20, p. 40–55, February 2014.
- [108] I. Casuso, F. Rico, and S. Scheuring, “Biological afm: Where we come from - where we are - where we may go,” *Journal of Molecular Recognition*, vol. 24, no. 3, pp. 406–413, 2011.

- [109] O. Campas, T. Mammoto, S. Hasso, R. A. Sperling, D. O’Connell, A. G. Bischof, R. Maas, D. A. Weitz, L. Mahadevan, and D. E. Ingber, “Quantifying cell-generated mechanical forces within living embryonic tissues,” *Nature Methods*, vol. 11, no. 2, pp. 183–189, 2014.
- [110] F. Serwane, A. Mongera, P. Rowghanian, D. A. Kealhofer, A. A. Lucio, Z. M. Hockenbery, and O. Campas, “In vivo quantification of spatially varying mechanical properties in developing tissues,” *Nature Methods*, vol. 14, no. 2, pp. 181–186, 2017.
- [111] M. E. Dolega, M. Delarue, F. Ingremeau, J. Prost, A. Delon, and G. Cappello, “Cell-like pressure sensors reveal increase of mechanical stress towards the core of multicellular spheroids under compression,” *Nature Communications*, vol. 8, no. 1, p. 14056, 2017.
- [112] C. Arbore, L. Perego, M. Sergides, and M. Capitanio, “Probing force in living cells with optical tweezers: from single-molecule mechanics to cell mechanotransduction,” *Biophysical Reviews*, vol. 11, no. 5, pp. 765–782, 2019.
- [113] M.-C. Zhong, X.-B. Wei, J.-H. Zhou, Z.-Q. Wang, and Y.-M. Li, “Trapping red blood cells in living animals using optical tweezers,” *Nature Communications*, vol. 4, no. 1, p. 1768, 2013.
- [114] B. González-Bermúdez, G. V. Guinea, and G. R. Plaza, “Advances in Micropipette Aspiration: Applications in Cell Biomechanics, Models, and Extended Studies,” *Biophysical Journal*, vol. 116, no. 4, pp. 587–594, 2019.
- [115] D. Leckband, “Surface Force Apparatus Measurements of Molecular Forces in Biological Adhesion BT - Handbook of Molecular Force Spectroscopy,” pp. 1–22, Boston, MA: Springer US, 2008.
- [116] D. Balleza, M. Sacchi, G. Vena, D. Galloni, G. Puia, P. Facci, and A. Alessandrini, “Effects of neurosteroids on a model membrane including cholesterol: A micropipette aspiration study,” *Biochimica et Biophysica Acta (BBA) - Biomembranes*, vol. 1848, no. 5, pp. 1268–1276, 2015.
- [117] P. H. Jones, O. M. Maragò, and G. Volpe, *Optical Tweezers: Principles and Applications*. Cambridge University Press, 2015.

- [118] J. Y. Shao and R. M. Hochmuth, “Micropipette suction for measuring piconewton forces of adhesion and tether formation from neutrophil membranes,” *Biophysical Journal*, vol. 71, no. 5, pp. 2892–2901, 1996.
- [119] D. P. Theret, M. J. Levesque, M. Sato, R. M. Nerem, and L. T. Wheeler, “The Application of a Homogeneous Half-Space Model in the Analysis of Endothelial Cell Micropipette Measurements,” *Journal of Biomechanical Engineering*, vol. 110, pp. 190–199, aug 1988.
- [120] J. N. ISRAELACHVILI and G. E. ADAMS, “Direct measurement of long range forces between two mica surfaces in aqueous KNO₃ solutions,” *Nature*, vol. 262, no. 5571, pp. 774–776, 1976.
- [121] J. N. Israelachvili and D. Tabor, “The measurement of van der Waals dispersion forces in the range 1.5 to 130 nm,” *Proceedings of the Royal Society of London. A. Mathematical and Physical Sciences*, vol. 331, pp. 19–38, nov 1972.
- [122] J. Israelachvili, Y. Min, M. Akbulut, A. Alig, G. Carver, W. Greene, K. Kristiansen, E. Meyer, N. Pesika, K. Rosenberg, and H. Zeng, “Recent advances in the surface forces apparatus (SFA) technique,” *Reports on Progress in Physics*, vol. 73, p. 036601, jan 2010.
- [123] G. Binnig, C. F. Quate, and C. Gerber, “Atomic force microscope,” *Phys. Rev. Lett.*, vol. 56, pp. 930–933, Mar 1986.
- [124] O. Saavedra V., T. F. D. Fernandes, P.-E. Milhiet, and L. Costa, “Compression, Rupture, and Puncture of Model Membranes at the Molecular Scale,” *Langmuir*, vol. 36, pp. 5709–5716, jun 2020.
- [125] “Resolution, Noise, and Sensitivity,” oct 2010.
- [126] C. L. Cheung, J. H. Hafner, and C. M. Lieber, “Carbon nanotube atomic force microscopy tips: Direct growth by chemical vapor deposition and application to high-resolution imaging,” *Proceedings of the National Academy of Sciences*, vol. 97, no. 8, pp. 3809–3813, 2000.

- [127] J. Martinez, T. D. Yuzvinsky, A. M. Fennimore, A. Zettl, R. García, and C. Bustamante, “Length control and sharpening of atomic force microscope carbon nanotube tips assisted by an electron beam,” *Nanotechnology*, vol. 16, pp. 2493–2496, sep 2005.
- [128] “Instrumental and Conceptual Aspects,” oct 2010.
- [129] R. Lal and S. A. John, “Biological applications of atomic force microscopy,” *American Journal of Physiology-Cell Physiology*, vol. 266, no. 1, pp. C1–C21, 1994. PMID: 8304408.
- [130] J. L. Hutter and J. Bechhoefer, “Calibration of atomic-force microscope tips,” *Review of Scientific Instruments*, vol. 64, no. 7, pp. 1868–1873, 1993.
- [131] H. J. Butt and M. Jaschke, “Calculation of thermal noise in atomic force microscopy,” *Nanotechnology*, vol. 6, pp. 1–7, jan 1995.
- [132] J. E. Sader, I. Larson, P. Mulvaney, and L. R. White, “Method for the calibration of atomic force microscope cantilevers,” *Review of Scientific Instruments*, vol. 66, pp. 3789–3798, jul 1995.
- [133] J. E. Sader, J. W. M. Chon, and P. Mulvaney, “Calibration of rectangular atomic force microscope cantilevers,” *Review of Scientific Instruments*, vol. 70, pp. 3967–3969, sep 1999.
- [134] S. Liu and Y. Wang, “Chapter 6 - A Review of the Application of Atomic Force Microscopy (AFM) in Food Science and Technology,” vol. 62, pp. 201–240, Academic Press, 2011.
- [135] “Theory of Amplitude Modulation AFM,” oct 2010.
- [136] X. Zhou, R. Zhuo, P. Wen, and F. Li, “Amplitude modulation atomic force microscopy based on higher flexural modes,” *AIP Advances*, vol. 7, p. 125319, dec 2017.
- [137] H. Grubmüller, B. Heymann, and P. Tavan, “Ligand Binding: Molecular Mechanics Calculation of the Streptavidin-Biotin Rupture Force,” *Science*, vol. 271, pp. 997 LP – 999, feb 1996.

- [138] E. Evans and K. Ritchie, “Dynamic strength of molecular adhesion bonds,” *Biophysical journal*, vol. 72, pp. 1541–1555, apr 1997.
- [139] R. Merkel, P. Nassoy, A. Leung, K. Ritchie, and E. Evans, “Energy landscapes of receptor–ligand bonds explored with dynamic force spectroscopy,” *Nature*, vol. 397, no. 6714, pp. 50–53, 1999.
- [140] L. Redondo-Morata, M. I. Giannotti, and F. Sanz, “Structural impact of cations on lipid bilayer models: Nanomechanical properties by AFM-force spectroscopy,” *Molecular Membrane Biology*, vol. 31, no. 1, pp. 17–28, 2014.
- [141] B. Gumí-Audenis, F. Sanz, and M. I. Giannotti, “Impact of galactosylceramides on the nanomechanical properties of lipid bilayer models: an afm-force spectroscopy study,” *Soft Matter*, vol. 11, pp. 5447–5454, 2015.
- [142] S. Garcia-Manyes, G. Oncins, and F. Sanz, “Effect of ion-binding and chemical phospholipid structure on the nanomechanics of lipid bilayers studied by force spectroscopy,” *Biophysical Journal*, vol. 89, no. 3, pp. 1812–1826, 2005.
- [143] H.-J. Butt and V. Franz, “Rupture of molecular thin films observed in atomic force microscopy. i. theory,” *Physical Review E*, vol. 66, p. 031601, Sep 2002.
- [144] S. Loi, G. Sun, V. Franz, and H.-J. Butt, “Rupture of molecular thin films observed in atomic force microscopy. ii. experiment,” *Physical Review E*, vol. 66, p. 031602, Sep 2002.
- [145] V. Franz, S. Loi, H. Müller, E. Bamberg, and H.-J. Butt, “Tip penetration through lipid bilayers in atomic force microscopy,” *Colloids and Surfaces B: Biointerfaces*, vol. 23, no. 2-3, pp. 191–200, 2002.
- [146] R. Proksch, T. E. Schäffer, J. P. Cleveland, R. C. Callahan, and M. B. Viani, “Finite optical spot size and position corrections in thermal spring constant calibration,” *Nanotechnology*, vol. 15, pp. 1344–1350, Aug 2004.
- [147] J. N. Israelachvili, “Chapter 14 - electrostatic forces between surfaces in liquids,” in *Intermolecular and Surface Forces (Third Edition)* (J. N. Israelachvili, ed.), pp. 291 – 340, San Diego: Academic Press, third edition ed., 2011.

- [148] L. Redondo-Morata, M. I. Giannotti, and F. Sanz, “Afm-based force-clamp monitors lipid bilayer failure kinetics,” *Langmuir*, vol. 28, pp. 6403–6410, 2012.
- [149] A. Berquand, D. Levy, F. Gubellini, C. Le Grimmellec, and P.-E. Milhiet, “Influence of calcium on direct incorporation of membrane proteins into in-plane lipid bilayer,” *Ultramicroscopy*, vol. 107, no. 10-11, pp. 928–933, 2007.
- [150] E. Watkins, C. Miller, D. Mulder, T. Kuhl, and J. Majewski, “Structure and orientational texture of self-organizing lipid bilayers,” *Physical Review Letters*, vol. 102, no. 23, p. 238101, 2009.
- [151] B. Gumí-Audenis, L. Costa, L. Redondo-Morata, P.-E. Milhiet, F. Sanz, R. Felici, M. I. Giannotti, and F. Carlà, “In-plane molecular organization of hydrated single lipid bilayers: Dppc: cholesterol,” *Nanoscale*, vol. 10, no. 1, pp. 87–92, 2018.
- [152] A. Benda, M. Beneš, V. Marecek, A. Lhotský, W. T. Hermens, and M. Hof, “How to determine diffusion coefficients in planar phospholipid systems by confocal fluorescence correlation spectroscopy,” *Langmuir*, vol. 19, no. 10, pp. 4120–4126, 2003.
- [153] C. Scomparin, S. Lecuyer, M. Ferreira, T. Charitat, and B. Tinland, “Diffusion in supported lipid bilayers: Influence of substrate and preparation technique on the internal dynamics,” *The European Physical Journal E*, vol. 28, no. 2, pp. 211–220, 2009.
- [154] E. K. Dimitriadis, F. Horkay, J. Maresca, B. Kachar, and R. S. Chadwick, “Determination of elastic moduli of thin layers of soft material using the atomic force microscope,” *Biophysical journal*, vol. 82, no. 5, pp. 2798–2810, 2002.
- [155] R. Desgarceaux, Z. Santybayeva, E. Battistella, A. L. Nord, C. Braun-Breton, M. Abkarian, O. M. Maragò, B. Charlot, and F. Pedaci, “High-Resolution Photonic Force Microscopy Based on Sharp Nanofabricated Tips,” *Nano Letters*, vol. 20, pp. 4249–4255, jun 2020.
- [156] E.-L. Florin, A. Pralle, J. K. Heinrich Hörber, and E. H. K. Stelzer, “Photonic Force Microscope Based on Optical Tweezers and Two-Photon Excitation for Biological Applications,” *Journal of Structural Biology*, vol. 119, no. 2, pp. 202–211, 1997.

- [157] T. F. D. Fernandes, O. Saavedra, E. Margeat, P.-E. Milhiet, and L. Costa, “Synchronous, Crosstalk-free Correlative AFM and Confocal Microscopies/Spectroscopies,” *Scientific Reports*, vol. 10, no. 1, p. 7098, 2020.
- [158] K. I. Willig, S. O. Rizzoli, V. Westphal, R. Jahn, and S. W. Hell, “STED microscopy reveals that synaptotagmin remains clustered after synaptic vesicle exocytosis,” *Nature*, vol. 440, no. 7086, pp. 935–939, 2006.
- [159] M. J. Rust, M. Bates, and X. Zhuang, “Sub-diffraction-limit imaging by stochastic optical reconstruction microscopy (STORM),” *Nature Methods*, vol. 3, no. 10, pp. 793–796, 2006.
- [160] S. Manley, J. M. Gillette, G. H. Patterson, H. Shroff, H. F. Hess, E. Betzig, and J. Lippincott-Schwartz, “High-density mapping of single-molecule trajectories with photoactivated localization microscopy,” *Nature Methods*, vol. 5, no. 2, pp. 155–157, 2008.
- [161] F. Balzarotti, Y. Eilers, K. C. Gwosch, A. H. Gynnå, V. Westphal, F. D. Stefani, J. Elf, and S. W. Hell, “Nanometer resolution imaging and tracking of fluorescent molecules with minimal photon fluxes,” *Science*, vol. 355, no. 6325, pp. 606–612, 2017.
- [162] K. Meller and C. Theiss, “Atomic force microscopy and confocal laser scanning microscopy on the cytoskeleton of permeabilised and embedded cells,” *Ultramicroscopy*, vol. 106, no. 4, pp. 320–325, 2006.
- [163] P. R. Laskowski, M. Pfreundschuh, M. Stauffer, Z. Ucurum, D. Fotiadis, and D. J. Müller, “High-Resolution Imaging and Multiparametric Characterization of Native Membranes by Combining Confocal Microscopy and an Atomic Force Microscopy-Based Toolbox,” *ACS Nano*, vol. 11, pp. 8292–8301, aug 2017.
- [164] C. M. Stroh, A. Ebner, M. Geretschlager, G. Freudenthaler, F. Kienberger, A. S. M. Kamruzzahan, S. J. Smith-Gill, H. J. Gruber, and P. Hinterdorfer, “Simultaneous Topography and Recognition Imaging Using Force Microscopy,” *Biophysical Journal*, vol. 87, no. 3, pp. 1981–1990, 2004.

- [165] C. Stroh, H. Wang, R. Bash, B. Ashcroft, J. Nelson, H. Gruber, D. Lohr, S. M. Lindsay, and P. Hinterdorfer, “Single-molecule recognition imaging microscopy,” *Proceedings of the National Academy of Sciences*, vol. 101, no. 34, pp. 12503–12507, 2004.
- [166] A. Dazzi and C. B. Prater, “AFM-IR: Technology and Applications in Nanoscale Infrared Spectroscopy and Chemical Imaging,” *Chemical Reviews*, vol. 117, pp. 5146–5173, apr 2017.
- [167] P. Lasch and D. Naumann, “Spatial resolution in infrared microspectroscopic imaging of tissues,” *Biochimica et Biophysica Acta (BBA) - Biomembranes*, vol. 1758, no. 7, pp. 814–829, 2006.
- [168] E. C. Mattson, M. Unger, S. Clède, F. Lambert, C. Policar, A. Imtiaz, R. D’Souza, and C. J. Hirschmugl, “Toward optimal spatial and spectral quality in widefield infrared spectromicroscopy of IR labelled single cells,” *Analyst*, vol. 138, no. 19, pp. 5610–5618, 2013.
- [169] R. K. Reddy, M. J. Walsh, M. V. Schulmerich, P. S. Carney, and R. Bhargava, “High-Definition Infrared Spectroscopic Imaging,” *Applied Spectroscopy*, vol. 67, pp. 93–105, jan 2013.
- [170] C. R. Findlay, R. Wiens, M. Rak, J. Sedlmair, C. J. Hirschmugl, J. Morrison, C. J. Mundy, M. Kansiz, and K. M. Gough, “Rapid biodiagnostic ex vivo imaging at 1 μm pixel resolution with thermal source FTIR FPA,” *Analyst*, vol. 140, no. 7, pp. 2493–2503, 2015.
- [171] A. Dazzi, F. Glotin, and R. Carminati, “Theory of infrared nanospectroscopy by photothermal induced resonance,” *Journal of Applied Physics*, vol. 107, p. 124519, jun 2010.
- [172] B. Lahiri, G. Holland, and A. Centrone, “Chemical Imaging Beyond the Diffraction Limit: Experimental Validation of the PTIR Technique,” *Small*, vol. 9, pp. 439–445, feb 2013.
- [173] S. Clède, F. Lambert, C. Sandt, S. Kascakova, M. Unger, E. Harté, M.-A. Plamont, R. Saint-Fort, A. Deniset-Besseau, Z. Gueroui, C. Hirschmugl, S. Lecomte, A. Dazzi,

- A. Vessières, and C. Policar, “Detection of an estrogen derivative in two breast cancer cell lines using a single core multimodal probe for imaging (SCoMPI) imaged by a panel of luminescent and vibrational techniques,” *Analyst*, vol. 138, no. 19, pp. 5627–5638, 2013.
- [174] G. Latour, L. Robinet, A. Dazzi, F. Portier, A. Deniset-Besseau, and M.-C. Schanne-Klein, “Correlative nonlinear optical microscopy and infrared nanoscopy reveals collagen degradation in altered parchments,” *Scientific Reports*, vol. 6, no. 1, p. 26344, 2016.
- [175] T. Forster, “Energiewanderung und Fluoreszenz,” *Naturwissenschaften*, vol. 33, no. 6, pp. 166–175, 1946.
- [176] T. Förster, “Zwischenmolekulare Energiewanderung und Fluoreszenz,” *Annalen der Physik*, vol. 437, pp. 55–75, jan 1948.
- [177] J. R. Lakowicz, ed., *Introduction to Fluorescence*, pp. 1–26. Boston, MA: Springer US, 2006.
- [178] “Energy Transfer BT - Principles of Fluorescence Spectroscopy,” pp. 443–475, Boston, MA: Springer US, 2006.
- [179] R. M. Clegg, “Fluorescence resonance energy transfer,” *Current Opinion in Biotechnology*, vol. 6, no. 1, pp. 103–110, 1995.
- [180] X. F. Wang and B. Herman, *Fluorescence Imaging Spectroscopy and Microscopy*. Chemical Analysis: A Series of Monographs on Analytical Chemistry and Its Applications, Wiley, 1996.
- [181] K. H. Drexhage, “Iv interaction of light with monomolecular dye layers,” vol. 12 of *Progress in Optics*, pp. 163 – 232, Elsevier, 1974.
- [182] A. I. Chizhik, J. Rother, I. Gregor, A. Janshoff, and J. Enderlein, “Metal-induced energy transfer for live cell nanoscopy,” *Nature Photonics*, vol. 8, no. 2, pp. 124–127, 2014.
- [183] J. Enderlein, “Single-molecule fluorescence near a metal layer,” *Chemical Physics*, vol. 247, no. 1, pp. 1 – 9, 1999.

- [184] N. Karedla, A. I. Chizhik, I. Gregor, A. M. Chizhik, O. Schulz, and J. Enderlein, “Single-molecule metal-induced energy transfer (smmiet): Resolving nanometer distances at the single-molecule level,” *ChemPhysChem*, vol. 15, no. 4, pp. 705–711, 2014.
- [185] A. Zelená, S. Isbaner, D. Ruhlandt, A. Chizhik, C. Cassini, A. S. Klymchenko, J. Enderlein, A. Chizhik, and S. Köster, “Time-resolved MIET measurements of blood platelet spreading and adhesion,” *Nanoscale*, vol. 12, no. 41, pp. 21306–21315, 2020.
- [186] P. Bharadwaj and L. Novotny, “Spectral dependence of single molecule fluorescence enhancement,” *Optics Express*, vol. 15, no. 21, pp. 14266–14274, 2007.
- [187] A. Ghosh, A. Sharma, A. I. Chizhik, S. Isbaner, D. Ruhlandt, R. Tsukanov, I. Gregor, N. Karedla, and J. Enderlein, “Graphene-based metal-induced energy transfer for sub-nanometre optical localization,” *Nature Photonics*, vol. 13, no. 12, pp. 860–865, 2019.
- [188] K. Y. Han, D. Wildanger, E. Rittweger, J. Meijer, S. Pezzagna, S. W. Hell, and C. Eggeling, “Dark state photophysics of nitrogen-vacancy centres in diamond,” *New Journal of Physics*, vol. 14, 2012.
- [189] G. Yuan, D. E. Gómez, N. Kirkwood, K. Boldt, and P. Mulvaney, “Two Mechanisms Determine Quantum Dot Blinking,” *ACS Nano*, vol. 12, pp. 3397–3405, apr 2018.
- [190] F. Jelezko and J. Wrachtrup, “Single defect centres in diamond: A review,” *physica status solidi (a)*, vol. 203, no. 13, pp. 3207–3225, 2006.
- [191] M. W. Doherty, N. B. Manson, P. Delaney, F. Jelezko, J. Wrachtrup, and L. C. L. Hollenberg, “The nitrogen-vacancy colour centre in diamond,” *Physics Reports*, vol. 528, no. 1, pp. 1–45, 2013.
- [192] M. Chipaux, K. J. van der Laan, S. R. Hemelaar, M. Hasani, T. Zheng, and R. Schirhagl, “Nanodiamonds and Their Applications in Cells,” *Small*, vol. 14, p. 1704263, jun 2018.

- [193] D. Ramos, J. Tamayo, J. Mertens, and M. Calleja, “Photothermal excitation of microcantilevers in liquids,” *Journal of Applied Physics*, vol. 99, no. 12, p. 124904, 2006.
- [194] I. Favero and K. Karrai, “Optomechanics of deformable optical cavities,” *Nature Photonics*, vol. 3, no. 4, pp. 201–205, 2009.
- [195] R. KASSIES, K. O. VAN DER WERF, A. LENFERINK, C. N. HUNTER, J. D. OLSEN, V. SUBRAMANIAM, and C. OTTO, “Combined AFM and confocal fluorescence microscope for applications in bio-nanotechnology,” *Journal of Microscopy*, vol. 217, no. 1, pp. 109–116, 2005.
- [196] Y. Yung Hui, Y.-C. Lu, L.-J. Su, C.-Y. Fang, J.-H. Hsu, and H.-C. Chang, “Tip-enhanced sub-diffraction fluorescence imaging of nitrogen-vacancy centers in nanodiamonds,” *Applied Physics Letters*, vol. 102, no. 1, p. 13102, 2013.
- [197] L. Rondin, J.-P. Tetienne, P. Spinicelli, C. Dal Savio, K. Karrai, G. Dantelle, A. Thiaville, S. Rohart, J.-F. Roch, and V. Jacques, “Nanoscale magnetic field mapping with a single spin scanning probe magnetometer,” *Applied Physics Letters*, vol. 100, no. 15, p. 153118, 2012.
- [198] Y. Li, Z. Liu, X. Lu, Z. Su, Y. Wang, R. Liu, D. Wang, J. Jian, J. H. Lee, H. Wang, Q. Yu, and J. Bao, “Broadband infrared photoluminescence in silicon nanowires with high density stacking faults,” *Nanoscale*, vol. 7, no. 5, pp. 1601–1605, 2015.
- [199] Y. Wu, M. Štefl, A. Olzyńska, M. Hof, G. Yahioğlu, P. Yip, D. R. Casey, O. Ces, J. Humpolíčková, and M. K. Kuimova, “Molecular rheometry: direct determination of viscosity in lo and ld lipid phases via fluorescence lifetime imaging,” *Phys. Chem. Chem. Phys.*, vol. 15, pp. 14986–14993, 2013.
- [200] M. Przybylo, J. Sýkora, J. Humpolíčková, A. Benda, A. Zan, and M. Hof, “Lipid Diffusion in Giant Unilamellar Vesicles Is More than 2 Times Faster than in Supported Phospholipid Bilayers under Identical Conditions,” *Langmuir*, vol. 22, pp. 9096–9099, oct 2006.
- [201] J. E. Sader, R. Borgani, C. T. Gibson, D. B. Haviland, M. J. Higgins, J. I. Kilpatrick, J. Lu, P. Mulvaney, C. J. Shearer, A. D. Slattey, P.-A. Thorén, J. Tran, H. Zhang,

- H. Zhang, and T. Zheng, “A virtual instrument to standardise the calibration of atomic force microscope cantilevers,” *Review of Scientific Instruments*, vol. 87, no. 9, p. 93711, 2016.
- [202] C. A. Amo and R. Garcia, “Fundamental High-Speed Limits in Single-Molecule, Single-Cell, and Nanoscale Force Spectroscopies,” *ACS Nano*, vol. 10, pp. 7117–7124, jul 2016.
- [203] K. H. Drexhage, “Influence of a dielectric interface on fluorescence decay time,” *Journal of Luminescence*, vol. 1-2, pp. 693–701, 1970.
- [204] J. Tisler, T. Oeckinghaus, R. J. Stöhr, R. Kolesov, R. Reuter, F. Reinhard, and J. Wrachtrup, “Single defect center scanning near-field optical microscopy on graphene,” *Nano Letters*, vol. 13, no. 7, pp. 3152–3156, 2013.